Control of detachment in the divertor region of tokamaks: impact of wall geometry, particle, and energy sources

Hao Yang

Aix*Marseille université
Socialement engagée

NNT/NL : 2023AIXM0085/010ED353

THÈSE DE DOCTORAT

Soutenue à Aix-Marseille Université
le 20 mars 2023 par

Hao YANG

Control of detachment in the divertor region of tokamaks: impact of wall geometry, particle, and energy sources

Discipline
Sciences pour l'Ingénieur

Spécialité
Fusion magnétique

École doctorale
ED 353 Sciences pour l'Ingénieur

Laboratoire/Partenaires de recherche
CEA, IRFM
M2P2, CNRS, Aix Marseille University
PIIM, CNRS, Aix Marseille University

Composition du jury

Giuseppe Calabrò Università de la Tuscia	Rapporteur
Paolo Innocente CNR à RFX, Padoue	Rapporteur
Claudia Negulescu Université de Toulouse	Examinatrice
Olivier Février l'EPFL/SPC de Lausanne	Examinateur
Laure Vermare CNRS, LPP, Ecole Polytechnique	Examinatrice
Eric Serre CNRS, laboratoire M2P2	Président du jury
Jérôme Bucalossi IRFM CEA	Encadrant CEA
Guido Ciraolo IRFM CEA	Directeur de thèse
Hugo Bufferand IRFM CEA	Invité

cea irfm M2P2 UMR 7340 CNRS - Aix-Marseille Université - Centrale Marseille PIIM

Affidavit

Je soussigné, Hao Yang, déclare par la présente que le travail présenté dans ce manuscrit est mon propre travail, réalisé sous la direction scientifique de Guido Ciraolo et Jérôme Bucalossi, dans le respect des principes d'honnêteté, d'intégrité et de responsabilité inhérents à la mission de recherche. Les travaux de recherche et la rédaction de ce manuscrit ont été réalisés dans le respect à la fois de la charte nationale de déontologie des métiers de la recherche et de la charte d'Aix-Marseille Université relative à la lutte contre le plagiat.

Ce travail n'a pas été précédemment soumis en France ou à l'étranger dans une version identique ou similaire à un organisme examinateur.

Fait à Marseille le 06 janvier 2023

YANG Hao
杨昊

Liste de publications et participation aux conférences

Liste des publications réalisées dans le cadre du projet de thèse:

1. H. Yang, G. Ciraolo, J. Bucalossi, et al. “Numerical modeling of the impact of leakage under divertor baffle in WEST”. in: *Nuclear Materials and Energy* (2022), p. 101302. ISSN: 2352-1791. DOI: https://doi.org/10.1016/j.nme.2022.101302. URL: https://www.sciencedirect.com/science/article/pii/S2352179122001831

2. H. Bufferand, J. Bucalossi, G. Ciraolo, et al. “Progress in edge plasma turbulence modelling—hierarchy of models from 2D transport application to 3D fluid simulations in realistic tokamak geometry”. In: *Nuclear Fusion* 61.11 (Oct. 2021), p. 116052. DOI: 10.1088/1741-4326/ac2873. URL: https://dx.doi.org/10.1088/1741-4326/ac2873

3. J. Bucalossi, J. Achard, O. Agullo, et al. “Operating a full tungsten actively cooled tokamak: overview of WEST first phase of operation”. In: *Nuclear Fusion* 62.4 (Feb. 2022), p. 042007. DOI: 10.1088/1741-4326/ac2525. URL: https://dx.doi.org/10.1088/1741-4326/ac2525

4. S. Di Genova, A. Gallo, N. Fedorczak, et al. “Modelling of tungsten contamination and screening in WEST plasma discharges”. In: *Nuclear Fusion* 61.10 (Sept. 2021), p. 106019. DOI: 10.1088/1741-4326/ac2026. URL: https://dx.doi.org/10.1088/1741-4326/ac2026

5. H Bufferand, J Balbin, S Baschetti, et al. “Implementation of multi-component Zhdanov closure in SOLEDGE3X”. in: *Plasma Physics and Controlled Fusion* 64.5 (Mar. 2022), p. 055001. DOI: 10.1088/1361-6587/ac4fac. URL: https://dx.doi.org/10.1088/1361-6587/ac4fac

6. Nicolas Rivals, Patrick Tamain, Yannick Marandet, et al. “SOLEDGE3X full vessel plasma simulations for computation of ITER first-wall fluxes”. In: *Contributions to Plasma Physics* 62.5-6 (2022), e202100182. DOI: https://doi.org/10.1002/ctpp.202100182. eprint: https://onlinelibrary.wiley.com/doi/pdf/10.1002/ctpp.202100182. URL: https://onlinelibrary.wiley.com/doi/abs/10.1002/ctpp.202100182

7. Rémi Delaporte-Mathurin, Hao Yang, Julien Denis, et al. “Fuel retention in WEST and ITER divertors based on FESTIM monoblock simulations”. In: *Nuclear Fusion* 61.12 (Oct. 2021), p. 126001. DOI: 10.1088/1741-4326/ac2bbd. URL: https://dx.doi.org/10.1088/1741-4326/ac2bbd

8. E. Laribi, E. Serre, P. Tamain, et al. “Impact of negative triangularity on edge plasma transport and turbulence in TOKAM3X simulations”. In: *Nuclear Materials and Energy* 27 (2021), p. 101012. ISSN: 2352-1791. DOI: https://doi.org/10.1016/j.nme.2021.101012. URL: https://www.sciencedirect.com/science/article/pii/S2352179121000880

9. Nicolas Rivals, Patrick Tamain, Yannick Marandet, et al. “Impact of enhanced far-SOL transport on first wall fluxes in ITER from full vessel edge-plasma simulations”. In: *Nuclear Materials and Energy* 33 (2022), p. 101293. ISSN: 2352-1791. DOI: https://doi.org/10.1016/j.nme.2022.101293. URL: https://www.sciencedirect.com/science/article/pii/S2352179122001740

10. G. Ciraolo, S. Di Genova, H. Yang, et al. “Interpretative modeling of impurity transport and tungsten sources in WEST boundary plasma”. In: *Nuclear Fusion* 61.12 (Oct. 2021), p. 126015. DOI: 10.1088/1741-4326/ac2439. URL: https://dx.doi.org/10.1088/1741-4326/ac2439

Participation aux conférences et écoles d’été au cours de la période de thèse:

1. 2021 EPS conferences, June 21–25, 2021

2. 2022 25th PSI conference, June 13–17, 2022

3. 14th Carolus Magnus Summer School on Plasma and Fusion Energy Physics, 20/09/2021 - 01/10/2021, Forschungszentrum Jülich, Germany

Résumé

Dans les machines de fusion magnétique de prochaine génération, comme DEMO, une grande partie de la puissance injectée et produite par les réactions de fusion doit être dissipée avant que le plasma n'entre en contact avec la paroi au niveau de composants appelés " cibles " dans le divertor. Le détachement du plasma est l'une des solutions envisagées pour protéger les tuiles des cibles en maintenant le front de rayonnement à une certaine distance de la cible. Ceci permet d'évacuer sous forme de rayonnement la majeure partie de la puissance de chauffage sur une plus grande surface et de maintenir le flux de chaleur à des niveaux compatibles avec leur design.

Ce travail de thèse se concentre sur l'étude des caractéristiques du plasma détaché dans différentes configurations divertor de deux tokamaks : " TCV ", situé en Suisse, et " WEST " situé à Cadarache, en France. Le détachement doit être contrôlé en temps réel pour garantir à la fois une production d'énergie continue par le réacteur, et une durée de vie longue pour composants face au plasma. Pour développer des méthodes de contrôle de rétroaction fiables, la première étape consiste à sélectionner les bonnes variables de contrôle et les bons actionneurs (injection de gaz, d'impureté, etc.). A l'aide de simulations numériques de bord et de modèles réduits, cette thèse vise à trouver la variable de contrôle la plus appropriée qui sera utilisée dans un système de rétroaction pour contrôler les actionneurs disponibles dans les réacteurs de fusion. Des simulations numériques 2D sont obtenues en utilisant le code de transport SOLEDGE3X-EIRENE avec des paramètres d'entrée spécialement définis pour reproduire les scénarios expérimentaux. Pour obtenir ces paramètres, une méthode de contrôle par rétroaction sur le profil du plasma a été développée comme un outil permettant de déterminer les coefficients de transport radial du plasma de bord à partir des données expérimentales. Les résultats des simulations sont comparés aux mesures expérimentales disponibles et montrent un bon accord.

Les impacts de la forme géométrique de la paroi (comme le degré de fermeture du divertor), de la quantité d'impuretés injectées, et de la puissance d'entrée sont discutés. Les résultats de la simulation montrent que le cas avec un divertor plus fermé montre de meilleures performances pour piéger les particules neutres, avec une pression neutre plus élevée près de la cible. L'augmentation à la fois de la pression de neutres ou de la concentration en impuretés dans le divertor entraîne une plus grande dissipation de puissance, et facilite l'accès au régime détaché. Un divertor plus fermé, ainsi que l'injection d'azote peuvent permettre au plasma de se détacher avec une densité plasma dans la région centrale plus faible (jusqu'à 24%) dans les cas que nous avons examinés. Les valeurs seuils à partir desquelles le plasma détache pour les paramètres tels que le flux de chaleur sur la paroi et la hauteur du front de rayonnement ne sont pas significativement affectés par la modification de la fermeture

du baffle ou la concentration d'impuretés. Une puissance d'entrée plus élevée peut augmenter de manière significative le seuil de détachement en termes de densité du plasma en amont, de la pression neutre du divertor, du flux de particules cibles, etc. La dépendance des résultats numériques pour quelques quantités physiques est également analysée à l'aide de modèles réduits pour trouver les observables qui affectent principalement le processus de détachement.

Enfin, les avantages relatifs des différentes observables au regard la contrôlabilité du détachement sont analysés. Un nouveau critère pour le détachement est proposé, fournissant un bon indicateur de l'état de détachement optimal dans tous les scénarios de plasma analysés (les situations avec différents degré de fermeture du divertor, concentration d'impuretés, et puissance d'entrée). Plusieurs stratégies de contrôle du détachement du divertor sont conçues en fonction des variables de contrôle choisies et comparées aux méthodes de contrôle existantes. La robustesse d'une stratégie de contrôle du tokamak WEST est étudiée par des simulations numériques, et sera testée dans de futures expériences.

Mots clés: modélisation numérique, plasmas de bord, détachement du divertor, contrôle, fermeture du divertor, impureté, mode L, mode H

Abstract

In the next step magnetic fusion devices like DEMO, a large fraction of power, more than 95%, needs to be dissipated before the plasma impacts the dedicated regions on the wall, the so-called divertor targets. The divertor detachment is one of the solutions envisaged to protect target tiles by keeping the radiation front detached from the target, thus radiating most of the heating power on a larger surface, keeping the heat flux deposit on the target at a manageable level, and reducing the sputtering and accumulation of impurities.

The present work is devoted to investigating the strategies to control detachment in the tokamak single null divertor configuration, which is planned for the International Thermonuclear Experimental Reactor (ITER) experiment presently in construction at Cadarache. The detachment must be feedback controlled in real-time to guarantee the continuous production of energy by the reactor and a long life of the plasma-facing components. To develop reliable feedback control methods, the first step is to use good control variables and actuators. With the help of edge numerical simulations and reduced models, this thesis aims to find the more appropriate control variable that will be used in a feedback scheme to adjust the actuators available in fusion reactors. 2D numerical simulations are obtained using SOLEDGE3X-EIRENE transport code with input parameters specially defined to reproduce the experimental scenarios in tokamaks, and more precisely in the TCV tokamak located in Switzerland and the WEST tokamak located in Cadarache, France. Profile feedback control has been developed as an interpretative tool to extract edge plasma transport coefficients from experimental data. Simulation results are compared with available experimental measurements and show good agreement. Modeling density scan is performed via adjusting deuterium gas puffing or impurity seeding to achieve different levels of detachment.

The impacts of wall geometry (like divertor closure), impurities, and input power on detachment have been discussed. Simulation results show that the case with a more closed divertor has better performance in trapping the neutral particles and has higher neutral pressure near the target. Increasing the neutral pressure or impurity concentration in the divertor leads to greater power dissipation, thus facilitating the access to the detached regime. Both considering more closed divertor configurations and increasing nitrogen seeding will induce the divertor detachment at lower upstream separatrix density, up to 24% in the cases we have considered. The threshold values of variables like target heat flux, and radiation front height in the divertor for detachment are found to be not significantly affected by the change of divertor closure and impurities concentration. Higher input power can significantly increase the detachment threshold in upstream plasma density, divertor neutral pressure, target

particle flux, etc. The dependence of numerical results from few physical quantities is also analyzed with the help of reduced models to find the observables that mostly affect the detachment process.

Finally, the relative advantage of the different observables regarding detachment controllability is evaluated. A new criterion for detachment is proposed, which provides a good indicator of the optimal detachment condition in all the analyzed plasma scenarios (the situations with different levels of divertor closure, impurities concentration, and input power). Several strategies for controlling the divertor detachment have been designed based on good control variables and compared with existing control methods. The robustness of a control strategy for WEST tokamak has been investigated by numerical simulations, and it will be tested in future experiments.

Keywords: numerical modeling, edge plasma, divertor detachment, control, divertor closure, nitrogen seeding, L-mode, H-mode

Acknowledgments

Over the past three years, I have been on an incredible journey filled with joy, excitement, and unforgettable memories. This journey would not have been possible without the important support and help of many people, and for that, I am deeply grateful.

I want to express my sincere appreciation to my advisors, Dr. Guido Ciraolo, Dr. Jérôme Bucalossi, and Dr. Hugo Bufferand for their unwavering support, encouragement, and guidance throughout my entire graduate journey. Their wisdom, patience, and expertise were invaluable in shaping my research and helping me grow as a scholar.

I also want to thank my committee members, Dr. Giuseppe Calabrò, Dr. Paolo Innocente, Dr. Claudia Negulescu, Dr. Olivier Février, Dr. Laure Vermare, and Dr. Eric Serre for their constructive feedback and insightful comments that greatly improved my thesis.

I am grateful to my collaborators, Gloria Falchetto, Nicolas Fedorczak, Patrick Tamain, Eric Nardon, Gallo Alberto, Stephane Vartanian, Bernard Pégourié, Yannick Marandet, Rémi Delaporte-Mathurin, James P Gunn, Davide Galassi, Stuart Henderson, Holger Reimerdes, Sophie Gorno, Filippo Bagnato, and Christian Theiler for their helpful discussions and assistance in the laboratory. Their contributions were instrumental in the completion of this research.

I would also like to thank my colleagues and friends, Elias Laribi, Julio Balbin Arias, Emily Bourne, Robin Varennes, Eléonore Geulin, Mathieu Peret, Manuel Scotto D'Abusco, Valeria Ostuni, Nicolas Rivals, Julien Denis, Raffael Eller-Düll, Stefano Di Genova, Virginia Quadri, Galazka Krzysztof, Tullio Barbui, Shengyu Shi, Luca Cappelli, Shuqi Xu, Yifan Peng, Shengli Chen, Chunhui Dang, Nan Jiang, Jiaqing Kou, and others for their continuous support, encouragement, and understanding during the ups and downs of this challenging academic journey.

I would like to give a special thanks to my family, especially my parents, for their love, support, and encouragement throughout my academic journey. Their belief in me and their constant encouragement kept me motivated and focused on my goals.

Lastly, I want to acknowledge CEA and AMU for hosting me during my PhD, and all the individuals whose contributions, whether big or small, made this research possible.

Thank you all for making this thesis a reality.

Table of contents

Acronyms

SOL

Scrape-Off-Layer. 22, 25, 31, 39–41, 44–46, 66, 69, 83, 90, 96, 110, 114, 116–118, 124, 128, 129, 133, 135, 147–150, 169, 177, 178, 202, 206, 208, 209, 213–218, 223, 225, 227, 228, 232, 234

LCFS

Last Closed (magnetic) Flux Surface. 22, 23, 41, 54

PFR

Private Flux Region. 22, 42, 59, 63, 66, 70, 83, 90, 101, 103, 116, 117, 148–150, 208, 215, 223, 227

L-mode

Low-confinement mode. 24, 25, 29, 58, 59, 63, 66, 70, 82, 89, 101, 105, 135, 206, 207, 216

H-mode

High-confinement mode. 24, 25, 29, 82, 86, 87, 101, 129, 135

ITER

International Thermonuclear Experimental Reactor. 24–26, 58, 159

DEMO

DEMOnstration power plant. 24, 26, 27, 58, 159, 173

LP

Langmuir Probe. 26, 41, 43, 52, 66, 72, 74, 91, 167, 169, 229

XPR

X-Point Radiator. 27, 77, 78, 80, 166, 223, 233–235

TCV

Tokamak à Configuration Variable. 27, 29, 57, 82–86, 90, 94–96, 99–103, 129, 130, 133–135, 145, 156, 158, 160, 161, 163–166, 171, 174, 176–178, 201, 206, 208, 209, 211–213, 232

LOS

Lines Of Sight. 27, 53–55

WEST

W-tungsten Environment in Steady-state Tokamak. 27, 29, 43, 48, 52–56, 58–63, 65–72, 76, 77, 79–81, 86, 96, 97, 99–101, 103–105, 115, 116, 118, 119, 127–130, 133–135, 147, 156, 158, 160–163, 165–169, 174, 175, 177, 178, 201, 206, 207, 209–211, 216, 218, 223, 228, 234–236

SMBI

Supersonic Molecular Beam Injection. 28

2PM

Two-Point Model. 28, 29, 44–47, 49, 51, 106, 115–117, 121–125, 129, 138, 160, 177

LSN

Lower-Single-Null. 29, 58, 59, 61, 66, 68, 71, 77, 83, 85, 89, 101, 103–106, 108, 114, 126–129, 213

USN

Upper-Single-Null. 29, 101, 103–106, 108, 126, 128, 129

OMP

Outer Mid-Plane. 42–44, 48, 49, 51, 63, 64, 70–72, 85–89, 91–93, 101, 108, 109, 117, 126–129, 154, 155, 167, 205, 206, 209–212, 218, 219, 223, 232, 233

IR

bolometric Infra-Red. 43, 167

DoD

Degree of Detachment. 49–51

PFU

Plasma-Facing Units. 52

ICRH

Ion Cyclotran Radiofrequency Heating . 61

CEI

Core-Edge-Interface. 61, 62, 68, 84–86, 90, 108, 205

DBS

Doppler Back Scattering. 72, 73

HFS

High Field Side. 83, 209, 214, 217–219

LFS

Low Field Side. 83, 108, 160, 209, 214, 217–219, 223

NBI

Neutral-Beam Injection. 84, 90, 147

TS

Thomson Scattering. 86, 88, 167

CXRS

Charge eXchange Recombination Spectroscopy. 86, 88, 89

ELM

Edge Localized Mode. 90, 135

MAR

Molecular Activated Recombination. 94

NSFA

ramped Nitrogen Seeding starting From an Attached case. 135, 136, 141, 143, 170

NSFD

ramped Nitrogen Seeding starting From a Detached case. 135, 136, 141, 170

FOPDT

First-Order Plus Dead Time. 202

FRF

Frequency Response Function. 202

Symbols

B_ϕ

toroidal magnetic field. 21, 25, 58, 61, 68, 71, 82, 126, 147, 148, 199, 213, 214, 216–219, 223, 224, 234, 235

B_θ

poloidal magnetic field. 21, 147, 214

I_p

plasma current. 22, 60, 61, 66–68, 71, 82, 126, 213

q_s

safety factor. 23, 160, 163, 167

ψ_N

normalized poloidal magnetic flux coordinate. 23, 24, 61, 64, 68, 70, 71, 77, 84, 86, 89, 163, 218, 225

$J_{\parallel,\mathrm{i}}$

parallel ion saturation current density. 26, 27, 70, 72, 74, 168, 169

$n_\mathrm{e,sep}$

upstream separatrix electron density. 28, 42–44, 48–51, 62, 69, 72, 75–80, 82, 86, 93–96, 98–100, 105–109, 112–114, 126–133, 135, 137–141, 143, 144, 147–153, 160–163, 201, 202, 204, 205, 209, 211, 215–225, 228, 229, 231, 234–236

$D_\perp$

radial mass diffusivity. 32, 40, 41, 63, 64, 70, 71, 86, 89, 105, 205, 206

$\nu_\perp$

radial momentum diffusivity. 34, 63, 86, 206

$\chi_\perp$

radial heat flux diffusivity. 34, 63, 86, 89, 90, 105, 205, 206, 208

λ_q

decay length of heat flux. 42–44, 117–119, 121, 123, 160, 163, 167

$n_{\mathrm{e,int,X}}$

line-integral density in the edge plasma channel that is pointing in the X-point region. 55, 66, 67, 133, 228

c_{Z}

impurity concentration. 135

E_{θ}

poloidal electron field. 147, 148, 214, 223

R_{D}

ratio of detachment. 162, 163, 165–169, 171–176, 178

$T_{\mathrm{e,sep}}$

upstream separatrix electron temperature. 205, 209

E_{ψ}

radial electron field. 214, 219, 223

Units

If there is no specific mention of units, S.I. (Système International) units are used. Following the convention generally accepted in the subject, temperatures are written in unit electron volts [eV]. When we mention temperatures in T[K], the transfer relationship is like T[K] = T[eV]e/k, here $e = 1.602 \times 10^{-19}$ C is the electronic charge, $k = 1.381 \times 10^{-23}\,\mathrm{J\,K^{-1}}$ is the Boltzmann constant. In some reference papers, kT[K] and eT[eV] are possibly written in T[J].

1. Introduction

Sommaire

1.1. Thermonuclear fusion

Nuclear fusion is the process of combining two light nuclei into a single, heavier nucleus, which releases energy. For example, when two isotopes of hydrogen (deuterium and tritium) are fused, they produce a helium nucleus and a neutral particle, releasing 17.6 MeV of energy per reaction [11] :

$$ {}_1\mathrm{D}^2 + {}_1\mathrm{T}^3 \rightarrow {}_2\mathrm{He}^4(3.5\ \mathrm{MeV}) + {}_0\mathrm{n}^1(14.1\ \mathrm{MeV}) \tag{1.1} $$

The nuclei of deuterium and tritium need high enough energy to overcome mutual repulsion due to their positive charges, and the cross-section reaches the peak value at 100 keV. Presently, the Equation 1.1 is the most promising fusion reaction compared with D–D, D–He^3 as shown in Figure 1.1.

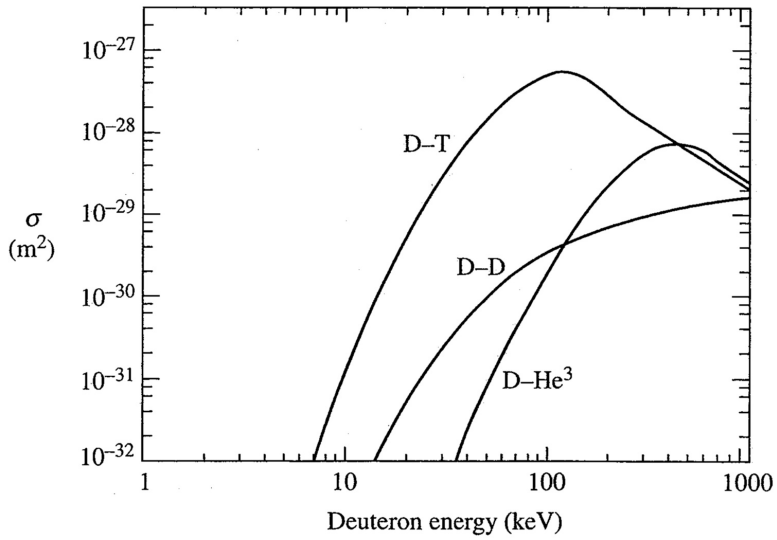

FIGURE 1.1. : Cross-sections for the reactions D–T, D–D and D–He^3. Figure from reference [11].

The particles need to be maintained in the reacting region with a sufficiently large product of confinement time and density to reach a positive power balance to maintain the reaction continuously. With high enough confinement, the plasma temperature can be maintained with α-particle heating (mostly absorbed by the plasma) from the reaction. The external heating is then no more needed. When the reaction reaches this threshold point, the so-called ignition is realized. The ignition requires the product of density (n), temperature (T), and energy confinement time (τ_E) exceeds the critical value which is developed from the so-called Lawson criterion :

$$nT\tau_E > 3 \times 10^{21}\,\mathrm{m}^{-3}\,\mathrm{keVs} \tag{1.2}$$

Such high value is still hard to realize. Some solutions are under investigation, like magnetic confinement (Tokamak, Stellarator) and Inertial confinement (LMJ, NIF, etc.).

Deuterium is a fairly abundant isotope of hydrogen, with 1 deuterium atom for every 6700 hydrogen atoms in the ocean, which means that the sea is a potential source of extremely large amounts of deuterium. Tritium is rarer on Earth, while it can be produced artificially through nuclear reactions. The simplest way is to use lithium to react with neutrons to generate tritium, and deuterium can also generate tritium by absorbing neutrons. Nuclear fusion does not produce long-term and high-level nuclear radiation that occurs in nuclear fission. Humans have already achieved uncontrolled nuclear fusion, such as the explosion of a hydrogen bomb. Inventing a device that can effectively control the process of fusion and make the energy output continuously and stably would be an ideal choice in the future.

1.2. Tokamak

The tokamak is an experimental device that uses a powerful magnetic field to confine plasma in the shape of a torus to achieve controlled nuclear fusion. As shown in Figure 1.2, at the center of the tokamak is a vacuum chamber with circular section. The coils poloidally wound around the vacuum chamber can generate a toroidal magnetic field $\mathbf{B}_\phi$; the inner poloidal coils (the so-called central solenoid) can induce a plasma current by induction with constant magnetic flux change, and the current can generate a poloidal field $\mathbf{B}_\theta$; the outer poloidal coils, which are toroidally wound around the vacuum chamber can contribute to the poloidal field and shape the plasma. The toroidal magnetic field $\mathbf{B}_\phi$ is usually much stronger than poloidal field $\mathbf{B}_\theta$, leading to the helical magnetic field $\mathbf{B}$ being primarily aligned in the toroidal direction, as shown below.

$$\mathbf{B} = \mathbf{B}_\phi + \mathbf{B}_\theta \tag{1.3}$$

The toroidal $\mathbf{B}_\phi$ is not homogeneous in the tokamak, $B_\phi \sim 1/R$, R is the horizontal distance from the central axis of the machine. The gradient of magnetic field in the R direction and curved magnetic field line in the toroidal direction can lead to up-down separation of ions and electrons due to drifts (Section B). The separation of ions and electrons can generate an electric field in the vertical direction and make plasma move to the wall in the presence of toroidal magnetic field $\mathbf{B}_\phi$. The poloidal $\mathbf{B}_\theta$ plays an important role in preventing the separation of ions and electrons. The helical magnetic field $\mathbf{B}$ thus presents better confinement for particles. However, the confinement is still not satisfied due to instabilities generate turbulence transport and thus reducing the energy confinement time. At the end of the last century, superconducting technology was used in the tokamak device to facilitate long discharge operations in tokamak.

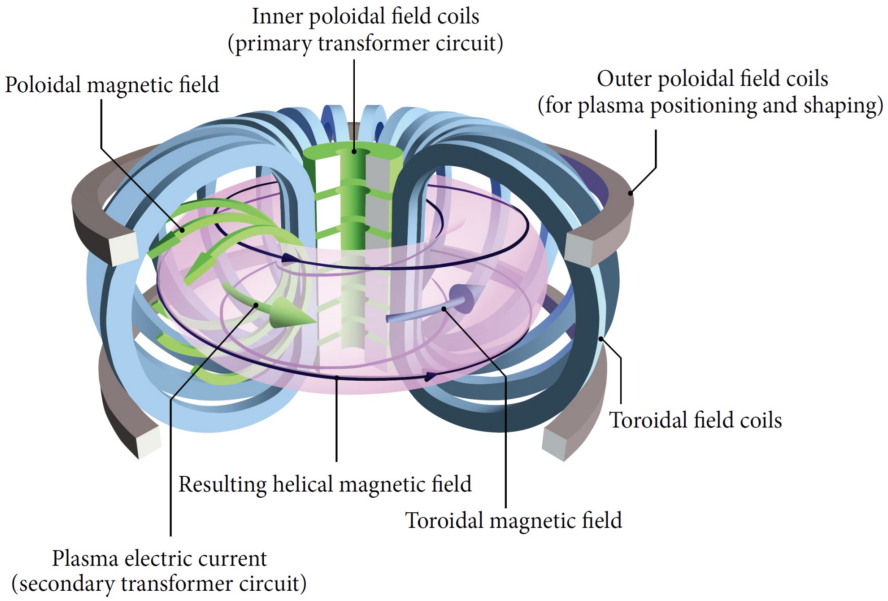

FIGURE 1.2. : Schematic of a tokamak chamber and magnetic configuration. Figure from reference [12].

1.3. Divertor and scrape-off layer

The plasma domain in a tokamak is usually separated into two regions : the core region and the *Scrape-Off-Layer* (SOL) region by the *Last Closed (magnetic) Flux Surface* (LCFS) (also called separatrix) which is the outermost flux surface untouched by solid surface. In the early stage of tokamak study, limiters were applied to contact with plasma to protect the wall as shown in Figure 1.3. The particles have very high velocity along the field line and can reach the sound speed at the entrance of a very thin layer (sheath) near the wall due to the strong sink function (Section 2.3.1). The sheath forms at the limiter side that interact with plasma, leading to high particle loss velocity, making the particles can only move cross-field for a very short distance beyond the radial limitation of limiter. Outside the LCFS, the layer due to short diffuse distance of edge plasma is the so-called SOL.

The divertor is now more frequently applied in tokamak as it can keep plasma-wall interaction some distance from the main plasma, and reduce the impact of impurities on the core region. The configuration is generated by using an external conductor with current $\mathbf{I}_D$, which keeps the consistent direction as plasma current ($\mathbf{I}_p$), as divertor configuration on a poloidal cut shown in Figure 1.4. Here, *Private Flux Region* (PFR) indicates the region surrounded by target plate and two divertor legs. The poloidal magnetic field strength equals zero at X-point. It is found that the edge plasma can strongly influence the system and be critical in the dependence of boundary conditions.

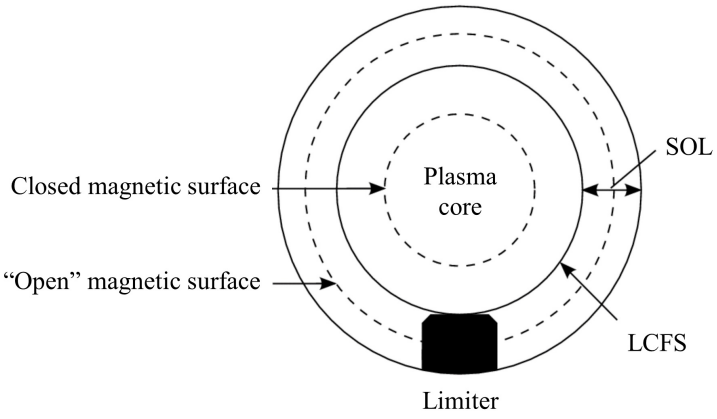

FIGURE 1.3. : Limiter configuration on a poloidal cut.

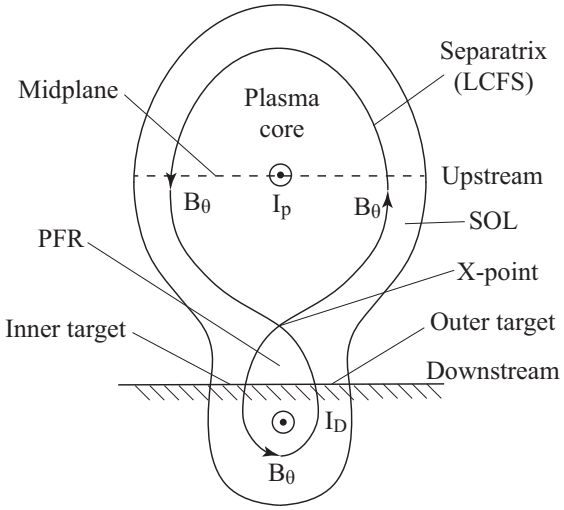

FIGURE 1.4. : Divertor configuration on a poloidal cut.

The safety factor q_s is used to evaluate the stability of the plasma in tokamak, which is approximately evaluated by Equation 1.4 in the machine with large aspect ratio and circular cross-section. The aspect ratio is defined as R/a, where R is the major radius of the torus and a is the minor radius of the (circular) LCFS. However, r in Equation 1.4 means the minor radius of any particular (circular) flux surface [13]. The plasma appears unstable if $q_s \leq 2$ at the edge (LCFS) [11].

$$q_s \approx \frac{r B_\phi}{R B_\theta} \tag{1.4}$$

The normalized poloidal flux ψ_N is usually used as perpendicular coordinate and given by

$$\psi_N = \frac{\psi - \psi_0}{\psi_{sep} - \psi_0} \tag{1.5}$$

where ψ_0 is the poloidal flux value at the magnetic axis, ψ_{sep} is the value at the separatrix and ψ represent the poloidal flux value at measured location. One can clearly see that for the point on the separatrix $\psi_N = 1$, for the point inside separatrix $\psi_N < 1$, and for the point outside separatrix $\psi_N > 1$.

1.4. Modes of confinement

Low-confinement mode (L-mode) is the earliest mode operated in tokamak devices. It presents relatively low confinement in plasma energy and particles compared with other modes. In 1982, the *High-confinement mode* (H-mode) was discovered in ASDEX tokamak. When the heating power (from the neutral beam) was increased and surpassed a certain threshold value, the plasma went into improved energy and particle confinement state spontaneously [14]. This observation is different from the conventional L-mode, the reason is still not yet fully understood, a transport barrier (the region where the turbulence transport is locally reduced) was found in the plasma confinement region near the separatrix as shown in Figure 1.5. Due to its potential to improve the confinement, H-mode is one of the desired operating regimes for future tokamak operations like *International Thermonuclear Experimental Reactor* (ITER) or *DEMOnstration power plant* (DEMO) [15]. Experimental results show that minimum heating power is required to provoke an L-mode into the H-mode regime [16]. L-H threshold power is found to be largely independent of diverter geometry [17].

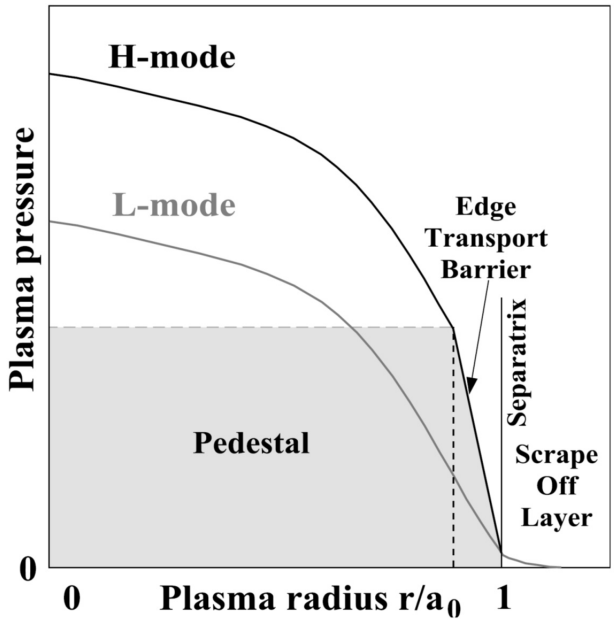

FIGURE 1.5. : Typical pressure profiles observed in L- and H-mode phases. Figure from reference [18].

Improved energy confinement mode (I-mode) was also investigated by certain

devices. This mode can be achieved by using unfavorable magnetic direction and consequent drifts (ion moves in the direction from the active X-point to center due to the gradient of toroidal magnetic field $\mathbf{B}_\phi$), following the H-mode access and keeping the H-mode power threshold high. It presents H-mode-like high-energy confinement and L-mode-like relatively poor particle confinement simultaneously [19, 20]. The transport barrier in edge energy without the one in particle can benefit the reactor performance, prevent impurity core accumulation and facilitate the removal of fusion ash [21]. I-mode shows the potential to be a credible solution alternative to H-mode for the operation of the tokamak.

1.5. Plasma regimes and detachment

In future fusion reactors, the core plasma can reach very high temperatures (more than 1×10^8 °C). A challenge is to avoid such hot plasma destruct wall material. In divertor configuration, a high level of heating power leaves the confined region and enters the SOL, finally depositing on a relatively narrow surface on the wall. The heat flux can easily exceed the wall material limitation, for ITER it is less than 10 MW/m^2 [22]. To realize long pulse discharge operations in reactors, a large fraction of power needs to be dissipated before the heat flux arrives at the divertor target, and maintain the target heat load at a manageable level.

Detachment is one of the explored solutions to protect target tiles. It was initially found in the experiment. As shown in Figure 1.6, with increasing pedestal density (or upstream density), the plasma will go through different regimes :

- **Sheath-limited regime.** The temperature gradient along the field line is very small. The change of SOL mainly happens in the sheath.
- **High recycling regime.** Strong temperature gradient along the field line, faster rise (decrease) of target density (temperature), and most of the particle sources come from the neutrals recycled from the wall.
- **Detached regime.** When pedestal density (or upstream density) is raised above a certain threshold, the target temperature becomes very low (few eV), and the neutrals coming from the target are less probably ionized in the neighborhood of their origin, thus the ionization front can move away from the target. When the target temperature is below 2 eV, recombination can play a role in decreasing the plasma density at the target.

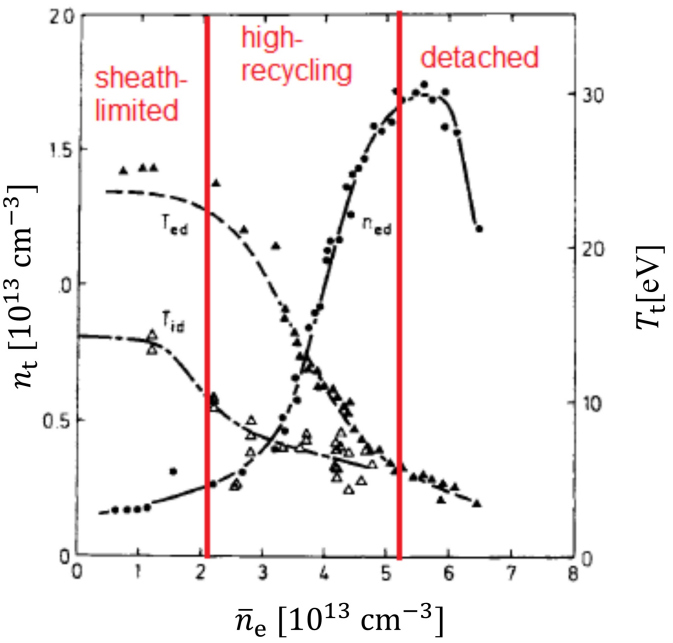

FIGURE 1.6. : Evolution of electron temperature, ion temperature, and plasma density at the target as a function of bulk plasma density $\bar{n}_e$ in the tokamak ASDEX [23]. The distinction between the three regimes is underlined with red vertical lines.

Therefore, the plasma in detached regime can keep the radiation front some distance from the target and radiate most of the heating power (about 60%–75% in ITER, and more than 95% in DEMO [24]) in a larger surface, thus keeping the heat flux deposit at the target at a manageable level. Detachment can be realized by raising the plasma density, injecting impurities, or changing the input power. However, strong detachment may lead to a reduction in core performance, so it is important to control detachment at a proper level. More investigation needs to be done to know better about how to control the detached regime.

1.6. Detachment control and challenges

There are several detachment control methods have been developed based on different control variables :

- The particle flux. Presently, the more feasible strategy to control detachment is to use the rollover characteristic of parallel ion saturation current density $J_{\parallel,i}$ at the divertor target when divertor plasma detaches as shown in Figure 1.7. It is attractive as the $J_{\parallel,i}$ can be easily measured by *Langmuir Probe*s (LPs). This method has been verified in tokamaks like Tore Supra [25], JET [26], EAST [27], DIII-D [28], and KSTAR [29]. However, variable impurities concentration and

input power can significantly change the $J_{\parallel,i}$ rollover threshold, which raises challenges in realizing reliable detachment control with $J_{\parallel,i}$ (Section 5.2). These limitations can largely reduce the feasibility of applying the control strategy based on analyzing the evolution of $J_{\parallel,i}$ in future DEMO devices, as the impurity seeding is found to be a necessary step to facilitate detachment in high heating power cases. The flexibility of changing the input power should also be allowed in an ideal detachment control strategy to give some operation space for target tile protection in the transition stage and controlling the burning plasma.

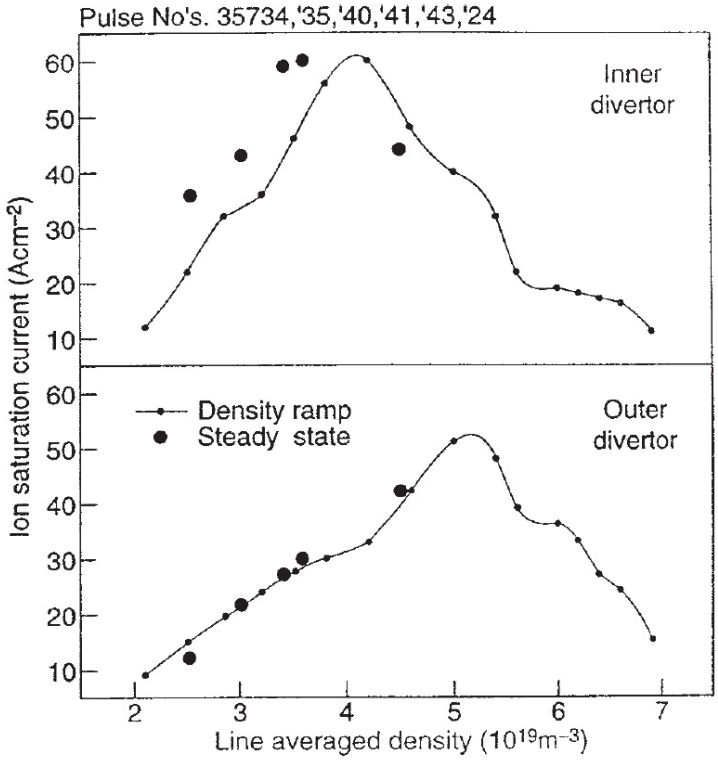

FIGURE 1.7. : Rollover of measured peak ion fluxes at the inner and outer divertors for a density ramp in L mode of JET when plasma detached. Figure from reference [30].

- The radiation front or radiation center. The height of the impurity emission front or *X-Point Radiator* (XPR) from the divertor target was employed to control detachment in *Tokamak à Configuration Variable* (TCV) [31] and in ASDEX Upgrade [32]. However, this method requires an effective real-time diagnostic system with high enough spatial resolution. For example, the TCV used multi-spectral imaging diagnostic MANTIS [33] to analyze the location of the CIII emission front. The ASDEX Upgrade used a number of *Lines Of Sight* (LOS) across the divertor to analyze the XPR position. Such control strategies are difficult to be reproduced in devices with shorter divertor legs, such as *W-tungsten Environment in Steady-state Tokamak* (WEST).

- The radiated power. The control of radiated power or the fraction between radiated power and input power was applied in AUG [34], JT-60U [35], and EAST [36], to manage the divertor heat flux, by using bolometer diagnostic or absolute extreme ultraviolet (AXUV) channels [37].

There are also some instability issues that need to be concerned about. For example, bifurcation is usually found in high input power cases. It can make the divertor plasma unstable during the transition from the attached to the detached regime. To control the detachment, we need to make the plasma skip this unstable period as quickly as possible [38]. In H-mode operation, it has been found that achieving both ELM suppression and detachment simultaneously is challenging in many available devices [39]. Other instability issues may arise due to slight changes in the magnetic configuration. The ideal detachment control strategy needs to be developed based on analyzing one or several variables that are highly related to the detachment level, in order to improve control performance under various situations with varying impurity concentration, heating power, or configuration. The main objective of this thesis is to find a better detachment control strategy, particularly focusing on identifying the improved control variables.

Feedback control is typically employed during detachment control, and one crucial factor is the time delay. Once the system state is measured using diagnostic methods, the feedback controller needs to analyze the data in real time and send commands to the executor, such as the gas injection signal. Excessive time delay in this process can make the system difficult to control. In a tokamak such as EAST, the interval between when the injection signal is sent and when the density starts to grow is ~ 50 ms for gas puffing pulse but only ~ 5 ms for *Supersonic Molecular Beam Injection* (SMBI) [40]. The time delay in changing the input power is typically a few milliseconds. Concerning the diagnostic aspect, it is important to address the relatively high noise level present in the signal. The signal must be carefully processed to provide useful information to the feedback controller. Additionally, due to the limited capacity to remove particles from the tokamak device and considering the wall as a potential source of particles, the plasma density does not exhibit the same sensitivity to an equal increase or decrease in the gas puff rate. Consequently, when designing a feedback controller, it is necessary to rapidly reduce the gas puff to zero if the plasma state, such as the $n_{e,sep}$, exceeds the set value.

1.7. Outline

This thesis is devoted to further understanding the detached plasma regime and its control which is a challenge that needs to be solved to give insights into operating the long pulse plasma in the next-generation tokamak. It is organized as follows.

In Chapter 2, edge plasma physics and its diagnostics are introduced. It is provided a brief illustration of plasma transport in a magnetic field and plasma-wall interaction. *Two-Point Model* (2PM) is presented, which can be helpful in understanding plasma

regimes. The essential aspects of fluid equations that describe the edge plasma are also presented.

In Chapter 3, the numerical modeling process is introduced. We use the edge plasma simulation code called SOLEDGE3X-EIRENE. Then we discuss the influence of simulation setups including the treatment of transport coefficients, drifts, and recycling coefficients. The understanding of the sensitivity to the setup can help us to build promising edge plasma simulation models close to the experimental results. The numerical simulation is mainly performed on devices : WEST and TCV. The L-mode (in WEST) and H-mode (in TCV) cases have been reproduced with *Lower-Single-Null* (LSN) (in both) and *Upper-Single-Null* (USN) (in WEST) magnetic configurations. Based on the basic case, density scans have been performed to cover the plasma in different regimes, especially the detached one. Obtaining the evolution process of plasma from attached to detached can be helpful in understanding the physics and characteristics of plasma, and knowing how the plasma can be controlled.

In Chapter 4, the impact of divertor closure, impurity seeding, and input power on detachment onset have been investigated. This can help us understand the physics better and find detachment-dependent parameters which are critical for stable detachment control. The 2PM was also studied and used SOLEDGE3X simulation data as input to facilitate the physical understanding and identify the key points that are relevant to the detachment.

In Chapter 5, we discuss the strategies to control detachment. A new criterion for detachment is proposed, which provides a good indicator of the optimal detachment condition in all the analyzed plasma scenarios (the situations with different levels of divertor closure, impurities concentration, and input power). Several strategies for controlling the divertor detachment have been designed based on good control variables and compared with existing control methods. The robustness of a control strategy for WEST tokamak has been investigated by time-dependent numerical simulations, and it will be tested in future experiments.

2. Tokamak edge plasma physics

Sommaire

2.1. High-collisionality in edge plasma

The plasma resistivity, denoted as η_s, is proportional to $T_e^{-3/2}$. Low or high resistivity is associated with relatively hot or cold plasma, respectively. Additionally, the collisionality of the plasma can help differentiate between the two temperature regimes. Hot plasma exhibits low collisionality, whereas colder plasma demonstrates higher collisionality. One way to estimate the collisionality is by comparing typical scales :

- The length of the magnetic field line $L_\parallel$, associated with the parallel transport, proportional to the physical size of the machine (major radius of the tokamak R), usually in a scale of 100 m.

- The particle mean free path λ_c, associated with the thermalization process due to Coulombian collisions between plasma particles, can be evaluated by

$$\lambda_{ee} \approx \lambda_{ii} \approx \frac{10^{16} T^2}{n_e}, \tag{2.1}$$

where, λ in unit [m], temperature T in unit [eV] and the number of electrons n_e in unit [m^{-3}]. The evolution of λ as a function of temperature T is shown in Figure 2.1. For relatively hot plasma (e.g. $T_e \approx 1\,\text{keV}$, $n_e \approx 1 \times 10^{19}\,m^{-3}$), $\lambda \approx 1000\,m$; for relatively cold plasma (e.g. $T_e \approx 50\,\text{eV}$, $n_e \approx 1 \times 10^{19}\,m^{-3}$), $\lambda \approx 2.5\,m$.

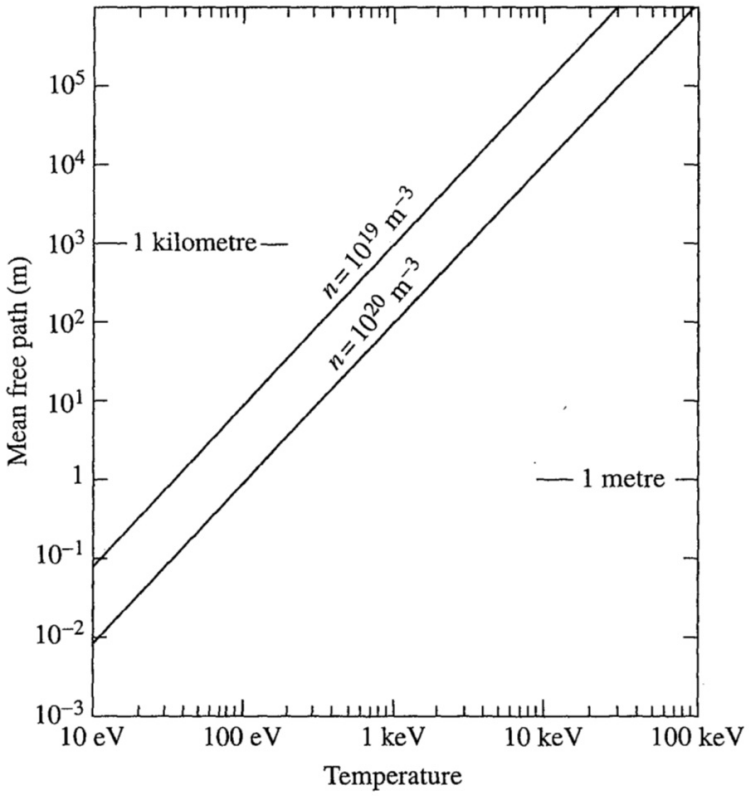

FIGURE 2.1. : Graphs of the electron mean free path against temperature. The ion mean free path is approximately equal to the electron mean path at the same temperature. Figure from reference [11].

Thus :

$$\text{Hot plasma :} \quad \lambda_c \gg L_\parallel$$
$$\text{Cold plasma :} \quad \lambda_c \ll L_\parallel$$

Here, we focus on the description of the plasma in SOL which is typical cold plasma with high collisionality. This description can be done with different levels of precision, either tracking all ionized particles following the Lorentz equation or using fluid

equations to describe collective transport. The fluid description can be properly used in cold plasma to make a good approximation.

2.2. Fluid equations

In this thesis, we mainly use the edge transport code SOLEDGE3X (Section 3.1) to perform numerical simulations. Mass, momentum, and energy balance are solved for arbitrary edge plasma composition in the SOLEDGE3X [5].

2.2.1. Particle balance

The particle balance described by the continuity equation for all charge states of ion species is shown below :

$$\frac{\partial n_\alpha}{\partial t} + \nabla \cdot (n_\alpha \mathbf{v}_\alpha) = S_{\mathrm{n},\alpha} \tag{2.2}$$

The n_α is ion density, $\mathbf{v}_\alpha$ is ion velocity and $S_{\mathrm{n},\alpha}$ is a volume source of ions (due to ionisation and recombination of neutrals). The $\mathbf{v}_\alpha$ can be decomposed as follow :

$$\mathbf{v}_\alpha = v_{\parallel,\alpha}\mathbf{b} + \mathbf{v}_{\perp,\alpha} \tag{2.3}$$

Here, the $\mathbf{b} = \mathbf{B}/B$ represents a unit vector aligned with the magnetic field; the $v_{\parallel,\alpha}$ is parallel velocity determined by the parallel momentum balance discussed in Section 2.2.2; the $\mathbf{v}_{\perp,\alpha}$ is the perpendicular velocity determined from the perpendicular momentum balance and drift ordering is applied. The cross-field transport, which comes from collision, turbulence is emulated by radial mass diffusivity $D_\perp$. The perpendicular velocity $\mathbf{v}_{\perp,\alpha}$ can be described as :

$$\mathbf{v}_{\perp,\alpha} = -D_{\perp,\alpha}\frac{\nabla_\perp n_\alpha}{n_\alpha} = -D_{\perp,\alpha}\nabla_\perp \log n_\alpha \tag{2.4}$$

Because of quasi-neutrality plasma, the electron density is computed by :

$$n_\mathrm{e} = \sum_\mathrm{i} Z_\mathrm{i} n_\mathrm{i} \tag{2.5}$$

2.2.2. Momentum balance

The momentum balance for each species is described by the equation below :

$$\begin{aligned}\frac{\partial}{\partial t}(m_\alpha n_\alpha \mathbf{v}_\alpha) + \nabla \cdot (m_\alpha n_\alpha \mathbf{v}_\alpha \otimes \mathbf{v}_\alpha) \quad &= \quad -\nabla p_\alpha + Z_\alpha e n_\alpha (\mathbf{E} + \mathbf{v}_\alpha \times \mathbf{B}) \\ &\quad -\nabla \cdot \overline{\overline{\Pi}}_\alpha + \mathbf{R} + \mathbf{S}_{\Gamma,\alpha}\end{aligned} \tag{2.6}$$

The $\mathbf{R}$ is the friction force computed by the multi-species Zhdanov closure [41] ; $\mathbf{S}_{\Gamma,\alpha}$ is the external momentum source (due to ionization and recombination process) ; $\overline{\overline{\Pi}}_\alpha$ is the stress tensor can be decomposed as follow :

$$\overline{\overline{\Pi}} = \overline{\overline{\Pi}}_\parallel + \overline{\overline{\Pi}}_\angle + \overline{\overline{\Pi}}_\perp \tag{2.7}$$

Here

- $\overline{\overline{\Pi}}_\parallel$ gathers parallel collisional contribution including parallel ion viscosity effects.
- $\overline{\overline{\Pi}}_\angle$ gathers gyroviscous terms which are not linked to collisions but to diamagnetic effects in the fluid description. This part is important for the so-called diamagnetic cancellation.
- $\overline{\overline{\Pi}}_\perp$ gathers perpendicular collisional contribution. It is usually neglected.

In SOLEDGE3X, the three parts of stress tensor are treated as follows : the perpendicular part is neglected ($\overline{\overline{\Pi}}_\perp \approx 0$). The diamagnetic part $\overline{\overline{\Pi}}_\angle$ is taken into account assuming ideal diamagnetic cancellation, that is considering the divergence of the diamagnetic stress tensor cancels the advection of velocity by diamagnetic velocity. Instead, one only keeps the advection by second order of ∇B drift (all drift velocities are defined in the perpendicular momentum balance section). The parallel stress tensor is kept and assumed to be in the form :

$$\overline{\overline{\Pi}}_\parallel = \pi_\parallel \left(\mathbf{b} \otimes \mathbf{b} - \frac{1}{3}\overline{\overline{I}} \right), \tag{2.8}$$

where

$$\pi_\parallel = -3\nu_0 \left(\nabla_\parallel v_{\alpha,\parallel} - \boldsymbol{\kappa} \cdot \mathbf{v}_{\alpha,\perp} - \frac{1}{3}\nabla \cdot \mathbf{v}_\alpha \right) \tag{2.9}$$

Here, $\boldsymbol{\kappa} = (\mathbf{b}\cdot\nabla)\mathbf{b}$ denotes the magnetic curvature. This kind of expression for the parallel viscous stress tensor can be found in [42-44]. The $\pi_\parallel$ variable can be seen as expressing the departure from an isotropic Maxwellian since $\pi_\parallel = p_\parallel - p_\perp$ in the Braginskii expansion. The divergence of $\overline{\overline{\Pi}}_\parallel$ gives :

$$\nabla \cdot \overline{\overline{\Pi}}_\parallel = \left[\nabla \cdot (\pi_\parallel \mathbf{b}) \right] \mathbf{b} + \pi_\parallel \boldsymbol{\kappa} - \frac{1}{3}\nabla \pi_\parallel \tag{2.10}$$

Taking the parallel projection of Equation 2.6 gives an equation for parallel momentum :

$$\frac{\partial}{\partial t}\left(m_\alpha n_\alpha v_{\alpha,\parallel} \right) + \nabla \cdot \left(m_\alpha n_\alpha v_{\alpha,\parallel} \mathbf{v}_\alpha \right) = -\nabla_\parallel p_\alpha + Z_\alpha e n_\alpha E_\parallel - \mathbf{b} \cdot \nabla \cdot \overline{\overline{\Pi}}_\alpha + R_\parallel + S_{\Gamma,\alpha,\parallel} \tag{2.11}$$

The parallel projection of the divergence of the stress tensor (parallel viscous part) gives :

$$\mathbf{b}\cdot\nabla\cdot\overline{\overline{\Pi}}_{\parallel} = \nabla\cdot(\pi_{\parallel}\mathbf{b}) - \frac{1}{3}\nabla_{\parallel}\pi_{\parallel} = \frac{2}{3}\nabla_{\parallel}\pi_{\parallel} + \pi_{\parallel}\nabla\cdot\mathbf{b} \tag{2.12}$$

For simulations ran in transport mode, a radial momentum diffusivity $\nu_{\perp}$ is added to emulate cross-field transport of velocity by turbulence. This extra-term can be added to the viscous tensor as :

$$\mathbf{b}\cdot\nabla\cdot\overline{\overline{\Pi}}_{\perp} = \nabla\cdot\left(n_{\alpha}\nu_{\perp,\alpha}\nabla_{\perp}v_{\alpha,\parallel}\right) \tag{2.13}$$

2.2.3. Power balance

The total energy of each species :

$$\mathscr{E}_{\alpha} = \frac{3}{2}en_{\alpha}T_{\alpha} + \frac{1}{2}m_{\alpha}n_{\alpha}v_{\alpha}^2 \tag{2.14}$$

The power balance for each species can be described by the equation below :

$$\frac{\partial\mathscr{E}_{\alpha}}{\partial t} + \nabla\cdot\left((\mathscr{E}_{\alpha}+p_{\alpha})\mathbf{v}_{\alpha} + \overline{\overline{\Pi}}_{\alpha}\cdot\mathbf{v}_{\alpha} + \mathbf{q}_{\alpha}\right) = \mathbf{v}_{\alpha}\cdot(en_{\alpha}\mathbf{E}_{\alpha}+\mathbf{R}) + Q + S_{\mathrm{e},\alpha} \tag{2.15}$$

Here, $\mathbf{q}_{\alpha}$ represents the heat flux and can be written as :

$$\mathbf{q}_{\alpha} = q_{\alpha,\parallel}\mathbf{b} + \mathbf{q}_{\alpha,\angle} + \mathbf{q}_{\alpha,\perp}, \tag{2.16}$$

where

- $q_{\alpha,\parallel}$ is the collisional heat flux. Its expression is provided by Zhdanov closure. In the most simple form, it can be given by a Fourier law for the thermal part plus a contribution due to the difference of parallel velocities in between species.
- $\mathbf{q}_{\alpha,\angle}$ is the diamagnetic heat flux. It takes a $\mathbf{b}\times\nabla T$ expression. In our case, we consider an ideal "diamagnetic cancellation" (see below) and assume the divergence of the diamagnetic heat flux cancels the advection of thermal energy by diamagnetic drift.
- $\mathbf{q}_{\alpha,\perp}$ is the collisional cross-field heat flux. It is negligible. However, for simulations run in transport mode, it can be used to emulate cross-field heat flux due to turbulence. In that case, it will take the form of a Fourier law :

  $$\mathbf{q}_{\alpha,\perp} = -n_{\alpha}\chi_{\perp,\alpha}\nabla_{\perp}T_{\alpha}, \tag{2.17}$$

  where the thermal conductivity $\chi_{\perp}$ must be adjusted to match turbulence effective transport.

2.3. Plasma-wall interaction

2.3.1. Sheath

The fluid equations (Section 2.2) describe the evolution of plasma in the edge. In addition, the boundary conditions that get involved with plasma-wall interaction need to be specially treated.

The electrons have very high thermal velocities compared with ions, leading to negative charge on the wall. The electric field triggered by negative charge adjusts spontaneously to prevent further accumulation of charge, in the end making ion and electron loss to the wall equally and reach steady state. This process mainly happened in a narrow region close to the wall with a width of few Deby lengths. This plasma-wall interacts narrow region is the so-called sheath. Outside the sheath, the plasma is quasi-electrically neutral. The plasma in the sheath is nearly collisionless due to the scale of sheath being much smaller than the mean free path of the particles.

Bohm criterion

Far away from the wall, we assume the electrostatic potential is zero, and plasma is in a quasi-neutral state. The electric field (caused by negative charge on the wall) repels electrons and accelerates ions, the evolution of electrostatic potential as a function of distance from source to solid surface (wall) is shown in Figure 2.2. Here, $\Delta\phi_{\mathrm{sf}}$ is the potential of the wall relative to the sheath edge ('s' for sheath, 'f' for floating), estimated to be $-3kT_{\mathrm{e}}/e$. The potential of pre-sheath $\Delta\phi_{\mathrm{se}}$ is about $-0.7kT_{\mathrm{e}}/e$, for D-plasma.

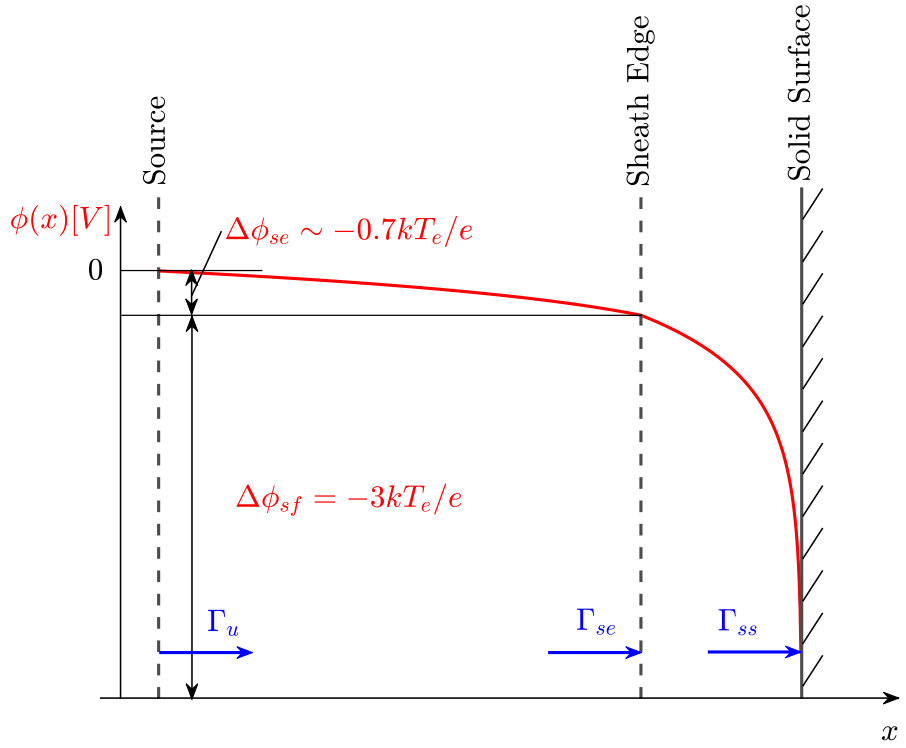

FIGURE 2.2. : Potential drop and particle flux in sheath model.

Now, we start with the simplest case : ions are assumed to be cold ($T_\mathrm{i} = 0$), and depart from the source (upstream of sheath edge), fall collisionless with zero velocity ($v_\mathrm{u} = 0$). With the function of electric field, ions satisfy particle conservation and energy conservation :

$$n_\mathrm{i}(x)\, v_\mathrm{i}(x) = n_\mathrm{i,se}\, v_\mathrm{i,se} \tag{2.18}$$

$$\frac{1}{2} m_\mathrm{i} v_\mathrm{i}^2(x) = -e\phi(x) \tag{2.19}$$

So we can obtain the ion density :

$$n_\mathrm{i}(x) = n_\mathrm{i,se} \sqrt{\frac{\phi_\mathrm{se}}{\phi(x)}} \tag{2.20}$$

For ions, the loss process strongly distorts the ordinary Maxwellian distribution due to no backward-going ions at the sheath. However, electrons have the same mean speed as ions, which is very small compared with thermal mean velocity $\langle v_\mathrm{e} \rangle$, and it can be supposed to satisfy Maxwellian distribution with Boltzmann factor (Section A.4).

$$n_\mathrm{e}(x) = n_\mathrm{e,se} \exp\left(\frac{e(\phi(x) - \phi_\mathrm{se})}{kT_\mathrm{e}} \right) \tag{2.21}$$

$n_{e,se} = n_{i,se} = n_{se}$ due to quasi-neutral plasma outside sheath edge. We can obtain an equation for the plasma potential in the vicinity of the sheath entrance. This leads to the so-called Bohm criterion for the ion entrance speed to the sheath. With $\mathbf{E} = -\nabla\phi$, and $\boldsymbol{\nabla} \cdot \boldsymbol{E} = e\left(n_i - n_e\right)/\varepsilon_0$, the 1D Poisson equation is given by

$$\begin{aligned} \frac{\mathrm{d}^2\phi}{\mathrm{d}x^2} &= -\frac{e}{\varepsilon_0}\left(n_i - n_e\right) \\ &= -\frac{e}{\varepsilon_0} n_{se}\left[\sqrt{\frac{\phi_{se}}{\phi(x)}} - \exp\left(\frac{e(\phi(x)-\phi_{se}}{kT_e}\right)\right] \end{aligned} \tag{2.22}$$

For the region inside the sheath, we define $\Delta \equiv \phi_{se} - \phi(x) (> 0)$, we can expand the items below :

$$\sqrt{\frac{\phi_{se}}{\phi(x)}} \approx 1 + \frac{1}{2}\frac{\Delta}{\phi_{se}} = 1 - \frac{1}{2}\frac{\Delta}{|\phi_{se}|} \tag{2.23}$$

$$\exp\left(\frac{e(\phi(x)-\phi_{se}}{kT_e}\right) \approx 1 - \frac{e\Delta}{kT_e} \tag{2.24}$$

Thus

$$\frac{\mathrm{d}^2\Delta}{\mathrm{d}x^2} \approx \frac{en_{se}\Delta}{\varepsilon_0}\left(\frac{e}{kT_e} - \frac{1}{2|\phi_{se}|}\right) \tag{2.25}$$

The physical result asks for a non-oscillatory Δ, so the Bohm criterion requires :

$$\frac{e}{kT_e} \geq \frac{1}{2|\phi_{se}|} \tag{2.26}$$

Combine with Equation 2.19, we have the ion velocity at sheath entrance :

$$v_{i,se} \geq c_s = \sqrt{\frac{kT_e}{m_i}}, \tag{2.27}$$

where c_s represents the sound speed. In hot plasma ($T_i \approx T_e$), the sound speed can be modified as :

$$c_s = \sqrt{\frac{kT_e + \gamma kT_i}{m_i}}, \tag{2.28}$$

where γ is the adiabatic coefficient, for an isothermal flow, $\gamma = 1$; for adiabatic flow, $\gamma = 5/3$–3, depending on the collisionality in the sheath [45].

Particle flux

In this section, we discuss the particle flux of electrons and ions toward the wall. Due to the potential well, ions are accelerated toward the wall, and only a negligible fraction of ions can escape the drag of electric field. So nearly all the ions can reach the wall (conservation of particle flux). In Figure 2.2, we present the particle flux at different

positions : Γ_u represents the one from source; Γ_{se} represents the one enter the sheath edge; Γ_{ss} represents the one reach the solid surface (wall). Due to the conservation of ion particle flux. They follow the relationships like following.

$$\Gamma_{i,u} = \Gamma_{i,se} = \Gamma_{i,ss} = n_{se} c_s \tag{2.29}$$

For electrons, the electron flux between sheath edge and wall is still conserved, due to the electric charge balance in sheath region in steady state. However, some part of electrons is repelled by electric field before entering the sheath edge, leading to the reduction of electron flux entering sheath edge as shown in the following equation.

$$\Gamma_{e,u} > \Gamma_{e,se} = \Gamma_{e,ss} \tag{2.30}$$

Because of velocity of electrons in sheath still remains the Maxwellian, plus the one-way flux we discussed in Section A.2, the electron flux reaching the wall can be written as :

$$\Gamma_{e,ss} = \frac{1}{4} n_{ss} \langle v_{ss} \rangle = n_{se} \sqrt{\frac{kT_e}{2\pi m_e}} \exp\left(\frac{e\Delta\phi_{sf}}{kT_e}\right) \tag{2.31}$$

Heat flux

Now, we consider the heat flux to the wall. For ions, we assume it satisfies the drift Maxwellian distribution function (Section A.3) with drift velocity c_s, the ion heat flux can be evaluated by :

$$\begin{aligned} q_{i,se} &= \left(\frac{5}{2} kT_i + \frac{1}{2} m_i c_s^2\right) \Gamma_{i,se} \\ &= \gamma_i kT_i \Gamma_{i,se} \ (\gamma_i = 3.5, \text{assuming } T_e = T_i, \text{isothermal flow}) \end{aligned} \tag{2.32}$$

The electrons almost follow the ordinary Maxwellian distribution due to the drift velocity being smaller than its thermal velocity. Considering one-way heat flux as Equation A.12, electron enter sheath needs to overcome ϕ_{sf} and ϕ_{se}, even though this part of the power will transfer to ion in the sheath. So, we have the net electron power flow at the sheath edge :

$$q_{e,se} = \gamma_e kT_e \Gamma_{e,se} \tag{2.33}$$

$$\gamma_e = 2 + \frac{|e\phi_{sf}|}{T_e} + \frac{|e\phi_{se}|}{T_e} \approx 2 + 3 + 0.7 = 5.7 \tag{2.34}$$

The total energy flux caused by ions and electrons deposited on the solid surface is

$$q_{ss} = q_{e,ss} + q_{i,ss} = q_{e,se} + q_{i,se} = \left(\gamma_e kT_e + \gamma_i kT_i\right) \Gamma_{se} = \gamma kT \Gamma_{se} \tag{2.35}$$

Here, we assume $T_e = T_i = T$, and $\gamma \approx 7$–8 is applied. This equation represents the heat flux that is lost from the plasma.

2.3.2. Plasma recycling

When the plasma interacts with a solid surface, the recombination process occurs. Thus the solid surface is like a sink for the plasma. Most of the ions and electrons recombine on the solid surface and will later be reinjected into the plasma as neutrals. The mass balance between the outflux of ions and electrons and the influx of neutrals is referred to as plasma recycling. However, the recycling process is not instantaneous and the trapped-trapped process happens for the particles from the plasma [46].

2.4. Atomic and molecular physics

In the SOL, the existence of atomic and molecular can not be neglected, the main reactions occurring between the species and their relative rate coefficients are shown in Figure 2.3. Neutral particles recycled from the wall mostly interact with plasma electrons through collisions. The main effects are ionization and molecular dissociation, there is also excitation reactions ($e + H^0 \rightarrow H^\star + e$). These processes can cause power exhaust in the SOL. A Monte Carlo code like EIRENE can evaluate this phenomenon.

One needs to notice that the molecules have a really small mean free path, can easily dissociate near the wall. The most important reaction to describe the SOL behavior is thus the ionization denoted by (6) in Figure 2.3, charge exchange denoted by (7). When the temperature is high ($> 20\,eV$), their coefficients are comparable, while at low temperatures, the charge exchange is dominant.

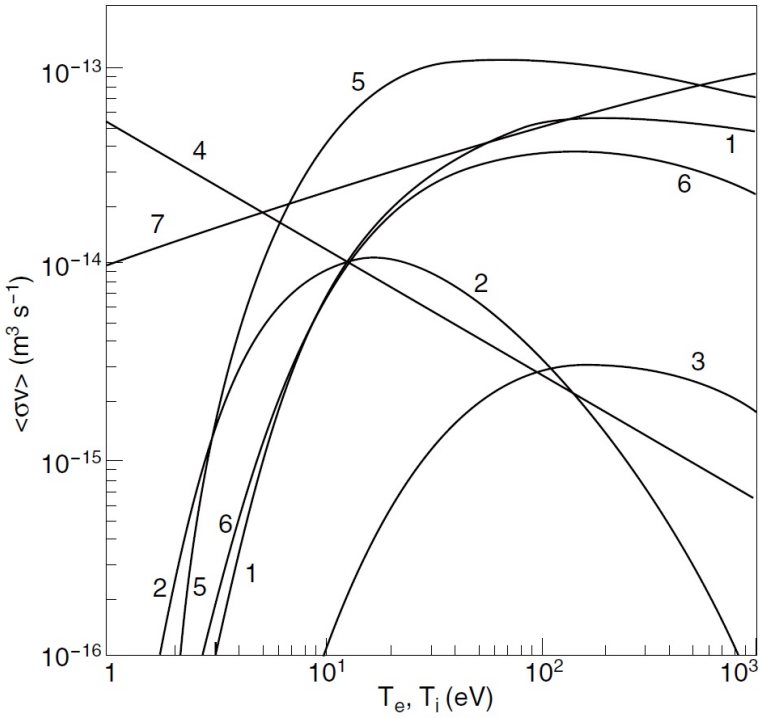

FIGURE 2.3. : The rate coefficients for atomic and molecular hydrogen. The numbered reactions are (1) : $e + H_2 \rightarrow H_2^+ + 2e$, (2) : $e + H_2 \rightarrow 2H^0 + e$, (3) : $e + H_2 \rightarrow H^0 + H^+ + 2e$, (4) : $e + H_2^+ \rightarrow 2H^0$, (5) : $e + H_2^+ \rightarrow H^0 + H^+ + e$, (6) : $e + H^0 \rightarrow H^+ + 2e$, and charge exchange (7) : $H^0 + H^+ \rightarrow H^+ + H^0$. Figure from references [13, 47].

2.5. Scrape-off layer width

2.5.1. Relating density scrape-off length λ_n to diffusion

The plasma particles collisions within the density gradient can lead to cross-field transport. We can use Fick's law to describe this diffusive motion :

$$\Gamma_\perp = -D_\perp \frac{dn}{dr}, \tag{2.36}$$

where, Γ is the particle flux density [$m^{-2}s^{-1}$], $D_\perp$ is the cross-field diffusion coefficient [m^2s^{-1}], and $dn/dr \approx -n/\lambda_n$, λ_n is the characteristic radial scale length of density. $D_\perp$ is still difficult to be calculated from the first principles, usually obtained from the experiment, in an order of 1 $m^{-2}s^{-1}$ (empirical). Being clear about these coefficients is very important in predicting the confinement properties of magnetic plasmas. Due to strong enough plasma collisionality (low temperature) in the SOL, the neo-classical effects (e.g. banana orbits) can be ignored. The charged particles will follow the magnetic field. We can 'straighten out' the SOL as shown below :

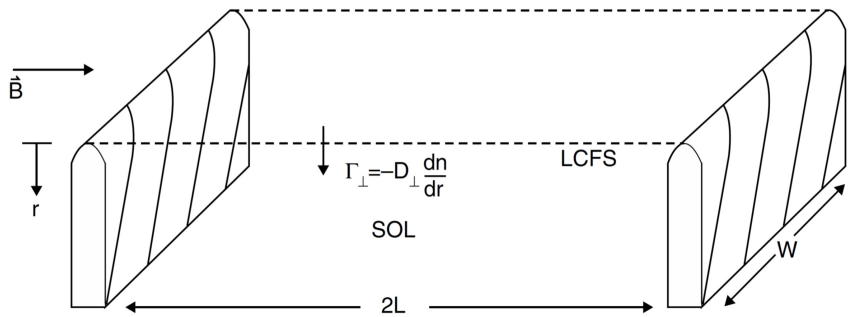

FIGURE 2.4. : The SOL 'straightened out'. Figure from reference [13].

The SOL here is limited by two opposite solid surfaces (inner and outer divertor target) at each end, LCFS or separatrix on the top, vessel wall on the bottom, width w which is perpendicular to both parallel magnetic field direction and the radial cross-field direction r. In a divertor case $w = 2\pi R B_\theta / B$, where R is the major radius, B_θ is the poloidal magnetic field strength, B is total magnetic field strength. $2L$ in Figure 2.4 represents the parallel connection length of SOL from inner to outer target, thus $2L = 2\pi R q_{95}$, q_{95} is the safety factor. For the simple SOL, the total particle out-flow from the confined plasma, crossing the LCFS into the SOL is given by :

$$\phi_\perp = - D_\perp^{\mathrm{SOL}} \frac{dn}{dr}\bigg|_{\mathrm{sep}} 2Lw \quad [\mathrm{particles\,s^{-1}}] \tag{2.37}$$

Due to $dn/dr \approx -n/\lambda_\mathrm{n}$, we have :

$$\phi_\perp = D_\perp^{\mathrm{SOL}} \left(n_{\mathrm{sep}}/\lambda_\mathrm{n}\right) 2Lw \tag{2.38}$$

The total particle flow that arrives at two targets is :

$$\phi_\parallel = 2w \int_{\mathrm{r=sep}}^{\infty} n c_\mathrm{s}\, dr \tag{2.39}$$

This result is exact if $c_\mathrm{s}(r)$ is constant and if $n(r)$ is actually exponential :

$$n(r) = n_{\mathrm{sep}} \exp(-r/\lambda_\mathrm{n}) \tag{2.40}$$

Supposing there are no other particle sources or sinks, and $\phi_\perp = \phi_\parallel$, we can get :

$$\lambda_\mathrm{n} = \left(D_\perp^{\mathrm{SOL}} L/c_\mathrm{s}\right)^{1/2} \tag{2.41}$$

The λ_n can be evaluated from $n(r)$, which is measured by LPs. Thus $D_\perp$ can be estimated in the experiment.

2.5.2. Estimate decay length of parallel heat flux λ_q

From density and temperature exponential profiles

With upstream separatrix density $n_{e,sep}$, the density profile can be written as Equation 2.42, here, r represents the radial outward distance from separatrix. The exponential profile is found to be roughly close to the experimental one.

$$n(r) = n_{sep} \exp(-r/\lambda_n) \tag{2.42}$$

Similarly, the temperature profiles can be represented as

$$T(r) = T_{sep} \exp(-r/\lambda_T) \tag{2.43}$$

As discussed in Section 2.6.1, in isothermal plasma, the density drop by a factor of 2 from upstream to the sheath edge. The heat flux can be written as :

$$q_{e,\parallel}(r) = \frac{1}{2} n c_s \gamma_e k T_e \tag{2.44}$$

$$q_{i,\parallel}(r) = \frac{1}{2} n c_s \gamma_i k T_i \tag{2.45}$$

Considering c_s given by Equation 2.28, supposing $T_e = T_i = T$, we can have the simple relation :

$$\frac{1}{\lambda_{q_{e,\parallel}}} = \frac{1}{\lambda_{q_{i,\parallel}}} = \frac{1}{\lambda_n} + \frac{3}{2\lambda_T} \tag{2.46}$$

$\lambda_{q_\parallel}$ here describe the decay length of parallel heat flux at the *Outer Mid-Plane* (OMP) (no flux expansion considered), can be evaluated by λ_n and λ_T. Both decay lengths can be obtained by fitting with experimental radial profile at the OMP.

Also, through Equation 2.59, when target temperature is much small compared with the upstream temperature ($T_{eu} \geq T_{et}$), the heat flux can be evaluated as

$$T_{eu}^{7/2} \sim \frac{7 q_{\parallel cond} L}{2 k_{0e}} \tag{2.47}$$

So heat flux can be related to the temperature directly in a rough estimation. Following the same analysis, we can also obtain another format of λ_q :

$$\lambda_{q_\parallel} \sim \frac{2}{7} \lambda_T \tag{2.48}$$

From target Gaussian profile

In divertor configuration, heat flux partially diffuses across the divertor legs into the PFR. The competition of heat transport between parallel and perpendicular parts in the divertor volume can be approximated with Gaussian width S, and the target heat flux profile can be described as Equation 2.49 from [48] :

$$q(\bar{s}) = \frac{q_0}{2} \exp\left[\left(\frac{S}{2\lambda_q f_x}\right)^2 - \frac{\bar{s}}{\lambda_q f_x}\right] \operatorname{erfc}\left(\frac{S}{2\lambda_q f_x} - \frac{\bar{s}}{S}\right) + q_{BG}, \tag{2.49}$$

where $\bar{s} = s - s_0$, s represents the target coordinate and s_0 represents the strike point position. f_x represents the flux expansion factor. The target heat flux can be measured at the target through LPs or *bolometric Infra-Red* (IR) diagnostics. To compare with other decay lengths from profiles at the OMP, the parallel heat flux is usually remapped to the OMP, fitted with Equation 2.49 (suppose $f_x = 1$), the λ_q, S and q_{BG} can be obtained. An example is shown in Figure 2.5 which based on the data of WEST simulation (Section 3.2.1.3, no drifts) with $n_{e,sep} = 2.60 \times 10^{19}$ m^{-3}.

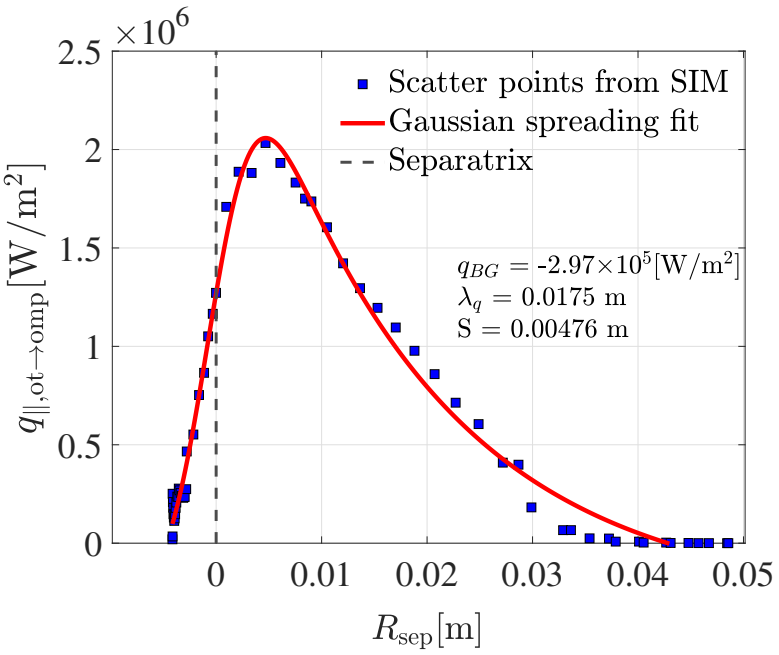

FIGURE 2.5. : The parallel heat flux at the outer target remapped at the OMP, and fitted with Gaussian spreading.

Comparasion of λ_q

From the discussion above, there are three ways to evaluate the characteristic decay length of heat flux through Equation 2.46, 2.48, and 2.49. Now we use the WEST simulation data introduced in Section 3.2.1.3 but with no drifts, to compare the evolution of heat flux decay length obtained in three methods as a function of $n_{e,sep}$, see Figure 2.6. The difference of T_e and T_i is considered. One can observe that $\lambda_q \sim \frac{2}{7}\lambda_T$ gives generally lower value than other two methods, λ_q calculated by λ_{T_e} is lower than the one calculated by λ_{T_i}. When $n_{e,sep} > 2.47 \times 10^{19}$ m^{-3}, λ_q obtained by Gaussian spreading fit is the highest. The difference between $\lambda_{q,Gaussian}$ and λ_q evaluated based on λ_T is significant, especially in the detached regime. This can be explained as extra power loss associated with plasma-neutral interactions (e.g. the charge exchange process),

leading to a flatter heat flux profile at the target [49]. Overall, the increase of λ_q with $n_{e,sep}$ is observed in all the evaluation methods.

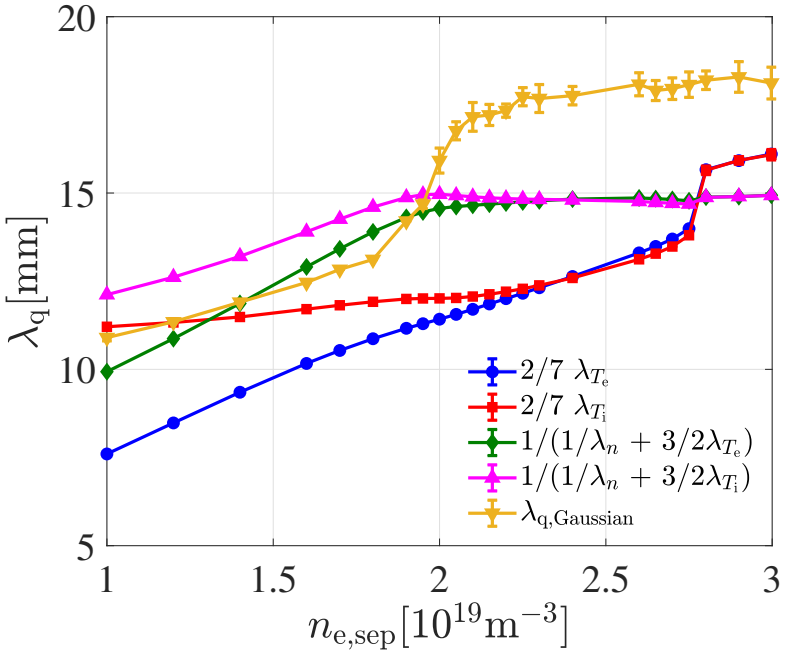

FIGURE 2.6. : Evolution of heat flux decay length obtained in three methods.

2.6. Characteristics of plasma regimes

Before talking about plasma regimes, we introduce the 2PM that can be helpful in understanding the characteristics of plasma regimes.

2.6.1. Two-point model

Basic two-point model

This section describes the basic 2PM of the divertor SOL. The divertor SOL is 'straightened out' for the purpose of simple modeling as shown in Figure 2.7. We use the subscript 'u' and 't' to indicate the upstream and target, respectively. The upstream location is usually chosen to be at the OMP.

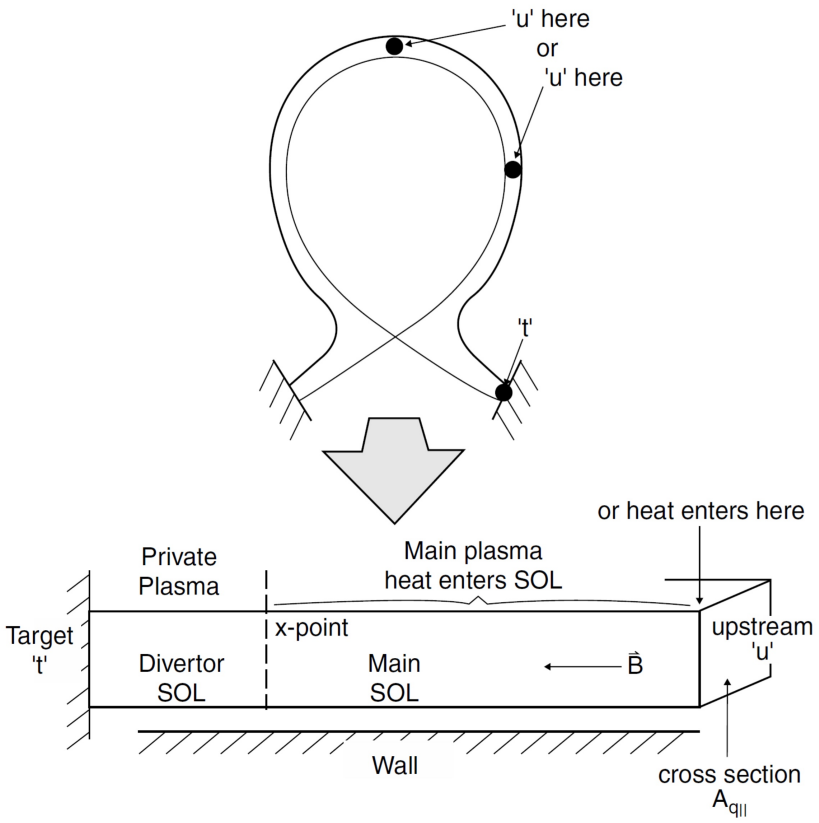

FIGURE 2.7. : The divertor SOL is 'straightened out' for the purpose of simple modeling. Figure from reference [13].

The 2PM can be derived from the fluid equations (Section 2.2) after some simplification and following the principal assumptions :

1. Particle balance. It is assumed that the parallel plasma flow is in a very thin layer between the upstream and target. The flow velocity increases from zero at the upstream and reaches sound speed at the entrance of target (particle sink). In the thin layer, plasma is fully ionized. The neutrals recycled from the targets will be ionized in a thin layer immediately in front of the target, along the same field line. There is no cross-field particle flow for neutrals or ions. Also, there is no volume recombination.

2. Pressure balance. It is assumed that there is no friction between the plasma flow in the thin ionization region and the target and no viscous effects. Thus throughout the entire length of each SOL flux tube, we have a constant total pressure $p+nmv^2$. $T_e = T_i$ is assumed, thus the plasma (static) pressure $p = nkT_e + nkT_i = 2nkT$. $v = 0$ at upstream, while at the target, $v_t = c_{st} = (2kT_t/m_i)^{1/2}$. Therefore, we have the total pressure between upstream and target :

$$n_t\left(2kT_t + mv_t^2\right) = 2n_u kT_u \tag{2.50}$$

or

$$2n_t T_t = n_u T_u \tag{2.51}$$

3. Power balance. Since the plasma velocity is very small along most part of flux tube before entering the divertor, thus the heat convection can be neglected, and suppose the heat flux is carried by the conduction. Considering one-way heat flux (Equation A.12), and collisions between charged particles, we can obtain thermal conductivity $K_\parallel = \kappa_0 T^{5/2}$, Equation (9.46) in [13]. The thermal conduction can also be described as

$$q_{\parallel \mathrm{cond}} = -\kappa_0 T^{5/2} \frac{dT}{ds_\parallel} \tag{2.52}$$

Where coefficients κ_0 for electrons and ions are $\kappa_{0e} \simeq 2000, \kappa_{0i} \approx 60$ [13]. The parallel ion heat conductivity is quite small, can be neglected. Thus we have

$$T_u^{7/2} = T_t^{7/2} + \frac{7}{2} q_\parallel \frac{L}{\kappa_{0e}} \tag{2.53}$$

For $q_\parallel$, we have the Equation 2.35 shown again as below :

$$q_\parallel = q_t = \gamma n_t k T_t c_{st} \tag{2.54}$$

To summarize, we thus have the simple 2PM as shown below :

$$\begin{aligned} 2n_t T_t &= n_u T_u \\ T_u^{7/2} &= T_t^{7/2} + \frac{7}{2} \frac{q_\parallel L}{\kappa_{0e}} \\ q_\parallel &= \gamma n_t k T_t c_{st} \end{aligned} \tag{2.55}$$

Extended two-point model

The basic 2PM is a simplified model relating the upstream and target conditions in SOL, which can help us to predict the target quantities ($T_{e,t}$, n_t, etc.) with the knowing of upstream quantities (n_u, p_u, $q_{\parallel u}$, etc.). However, various processes are excluded from the principal assumptions for the basic 2PM. The plasma in SOL may experience power losses due to radiation and charge exchange, momentum loss due to the frictional collisions with neutrals, viscous forces, and volume recombination, as well as parallel heat power partly carried by conduction, etc. These processes can become important when detachment happens. To introduce these effects qualitatively in the 2PM, we use the volumetric transfer terms for power and momentum f_{power}, f_{mom} to approximately describe the fraction of power and momentum remained until the plasma reaches the target, and use parallel heat conduction factor f_{cond} to approximately describe

the fraction of the parallel power carried by conduction. In addition, the temperature of ion and electron is no longer assumed to be equivalent as what we have done in the basic 2PM, and the toroidal flux expansion, R_t/R_u is not equal to 1 but depends on the cases considered. By taking the effects above into account, the basic 2PM can be extended to give a better performance in predicting the condition of detachment, so we have the so-called extended 2PM [50] composed by Equations (2.56)–(2.66). Certain parameters in the extended 2PM strongly correlate with the target or upstream conditions. For example the f_{power}, f_{mom} are mainly influenced by the condition on the divertor target and postulated to be a function of target temperature $T_{e,t}$ [50]. These parameters show significant non-constant properties under the variation of plasma state.

$$q_{\parallel t} R_t = f_{\text{power}} q_{\parallel u} R_u \tag{2.56}$$

$$p_t^{\text{total}} = f_{\text{mom}} p_u^{\text{total}} \tag{2.57}$$

$$q_{\parallel \text{cond}} = f_{\text{cond}} q_{\parallel u} \tag{2.58}$$

$$T_{eu}^{7/2} - T_{et}^{7/2} = \frac{7 q_{\parallel \text{cond}} L}{2 k_{0e}} \tag{2.59}$$

$$q_{\parallel u} = \frac{q_{95} P_{\text{in,sol}}}{4\pi a \lambda_q} \tag{2.60}$$

$$q_{\parallel t} = 7.5 n_t k T_{et} c_{st} \tag{2.61}$$

$$p^{\text{total}} = (1 + M^2) n_e k T_e (1 + \frac{\tau}{z}) \tag{2.62}$$

$$c_{st} = \sqrt{(1 + \tau_t / z_t)\, k T_{e,t} / m_f} \tag{2.63}$$

$$\tau \equiv \frac{T_i}{T_e} \tag{2.64}$$

$$z \equiv \frac{n_e}{\sum_\alpha n_a} = \frac{n_e}{n_i} \tag{2.65}$$

$$z_t = M_t = 1 \tag{2.66}$$

2.6.2. Plasma regimes comparison

The plasma regimes can be separated into three regimes : sheath-limited, high recycling, and detached as briefly introduced in Section 1.5. Here, we will show the

differences between the plasma regimes in a more detailed way through WEST simulation. The density scan was applied going from very low $n_{e,sep}$ to high $n_{e,sep}$ to cover three plasma regimes, based on the WEST simulation case #54903 (Section 3.2.1.2). Figure 2.8 shows the comparison of the plasma density, electron temperature, and total pressure profiles at the OMP and the outer divertor target, estimate how those parameters change during the process from sheath-limited to high-recycling regime, in the end, detached. In Figure 2.8 (a)–(c), the electron temperature and total pressure profiles almost match between the OMP and the outer divertor target : $T_t = T_u$, $P_t = P_u$, and upstream density ($n_{e,sep}$) is higher than target density by a factor of two : $n_t = n_u/2$. This phenomenon can be explained by using the total pressure conservation equation, which can write as

$$n_u T_u \left(1 + M_u^2\right) = n_t T_t \left(1 + M_t^2\right) \tag{2.67}$$

Following Bohm boundary condition (Section 2.3.1), it is restricted that the Mach number at the target $M_t = 1$. We can assume that the upstream point coincides with the stagnation point, so $M_u = 0$. We thus obtain finally $n_t = n_u/2$. This regime, in which the temperature gradient along the field line is very small, is referred to as sheath limited regime. In Figure 2.8 (d)–(f), when we ramp the $n_{e,sep}$ to a higher level, the temperature gradient along the field line becomes significant, T_e at the target is reduced below 10 eV, but the pressure conservation is still maintained. This regime is referred to as high recycling regime. In Figure 2.8 (g)–(h), the n_u is raised above a certain threshold, the total pressure gradient alone the field line becomes significant, T_e at the target also becomes very low, this regime is referred to as detached regime.

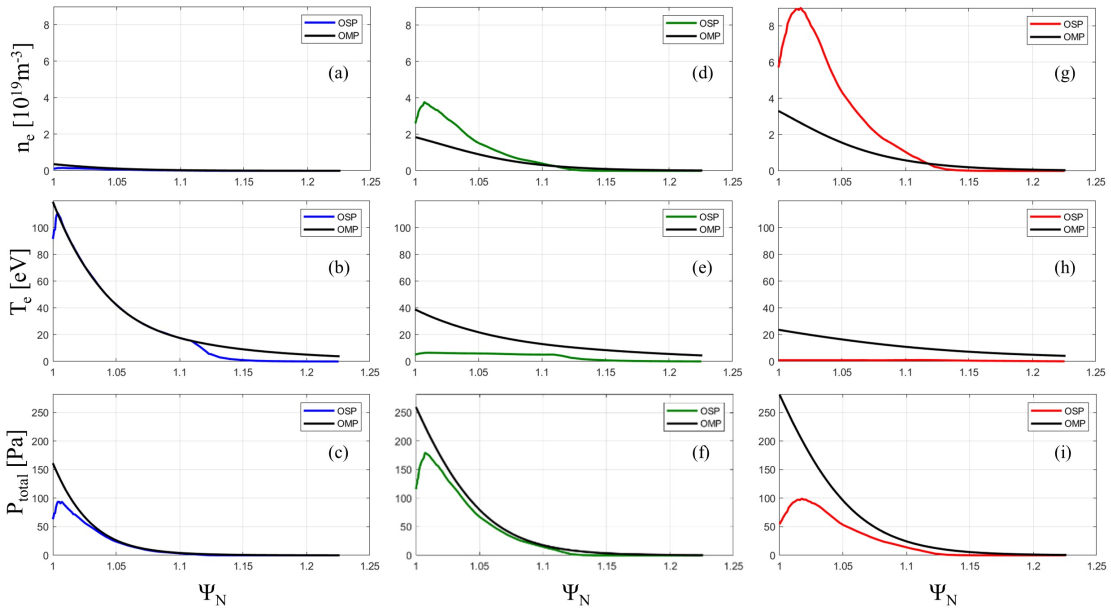

FIGURE 2.8. : The three columns from left to right correspond to the $n_{e,sep}$ from low to high value : $n_{e,sep} = 3.60 \times 10^{18}$ m^{-3}, $n_{e,sep} = 1.85 \times 10^{19}$ m^{-3}, and $n_{e,sep} = 3.30 \times 10^{19}$ m^{-3}. The three rows from top to bottom show the comparison of the electron density, temperature, and total pressure profiles at the OMP and the outer divertor target. The curves in colors (blue, green, and red) represent the profiles at the target, while the black curves represent the profiles at the OMP.

2.6.3. Degree of detachment

According to the theory of the 2PM (Section 2.6.1), the plasma density at the target $n_t \propto n_u^3$ and the parallel electron flux at the target $\Gamma_{e,t} \propto n_u^2$ in high recycling regime [13]. Here, n_u represents the upstream density, also noted as $n_{e,sep}$. Since the inner divertor detaches at a lower n_u than the outer divertor under standard conditions, the outer divertor is considered as the critical location to evaluate the *Degree of Detachment* (DoD) [51]. The DoD is defined as

$$\mathrm{DoD} = \frac{\phi_t^{\mathrm{calculated}}}{\phi_t^{\mathrm{measured}}}, \tag{2.68}$$

where $\phi_t^{\mathrm{measured}}$ is the measured electron flux at the target and $\phi_t^{\mathrm{calculated}}$ is the electron flux predicted by the 2PM. The evolution of parallel electron flux and DoD as a function of $n_{e,sep}$ are shown in Figure 2.9. One can find that the electron flux initially increases linearly with raised $n_{e,sep}$ in sheath-limited regime, then the electron flux increases proportionally to $n_{e,sep}^2$ in high-recycling regime, it rolls over at $n_{e,sep} = 2.28 \times 10^{19}$ m^{-3}, steps into the detached regime. The value of DoD is not fixed, but normally we make the curve of predicted electron flux proportional to $n_{e,sep}^2$ (blue

line) moved to be fitted with the curve of measured electron flux (black line) as much as possible in high-recycling regime on purpose. So in high recycling regime, DoD ≈ 1. When the plasma fully detached, DoD $\gg 1$. It can be observed that the DoD varies from 0.31 to 4.72, in the range of $n_{e,sep}$ investigated. For the later analysis, we choose three cases with different $n_{e,sep}$ on behalf of three stages of plasma regime : sheath-limited regime, high-recycling regime, and detached regime, as marked in Figure 2.9.

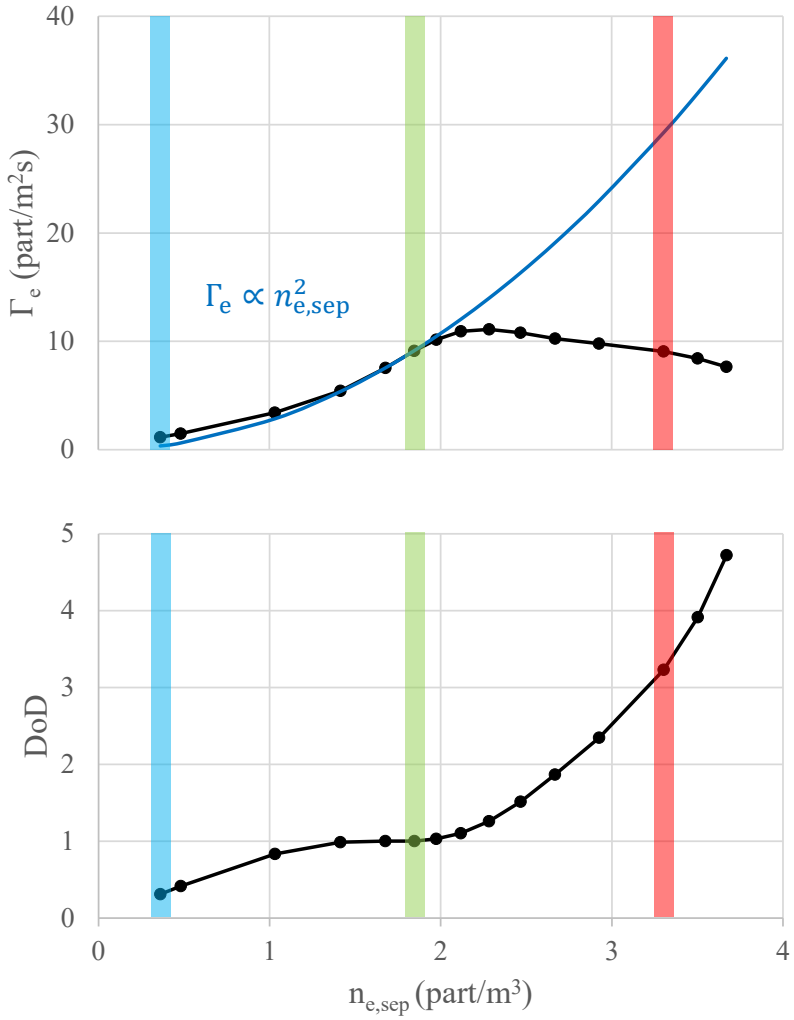

FIGURE 2.9. : The top subfigure shows the evolution of peak parallel electron flux at the outer target (black line) and reference electron flux proportional to $n_{e,sep}^2$ predicted by the 2PM (blue line). The bottom subfigure shows the evolution of DoD at the outer target (black line). The columnar regions represent three $n_{e,sep}$ from low to high : $n_{e,sep} = 3.60 \times 10^{18}$ m^{-3} (blue), $n_{e,sep} = 1.85 \times 10^{19}$ m^{-3} (green), $n_{e,sep} = 3.30 \times 10^{19}$ m^{-3} (red). More details about the electron density, temperature, and total pressure profiles at the OMP and the outer divertor target of the cases marked by the columnar regions can be checked in Figure 2.8.

2.7. Experiment diagnostics for tokamak plasma

There are a lot of experimental measurement diagnostics available, here we mainly introduce the methods that will be frequently used in the work of this thesis. In the feedback control study, the time delay of the diagnostic can be very important to

consider. One also needs to notice that the data in simulation can usually be obtained directly, but it is not always the case in the experiment.

2.7.1. Langmuir probes

Using the LPs embedded within the *Plasma-Facing Units* (PFU) that compose the divertor is the best method to characterize the plasma parameters in the vicinity of the separatrix strike points at the divertor target [52].

LPs at the target can offer the measurements of electron temperature T_e, ion saturation current I_{sat}, floating potential V_f and the sheath expansion factor α_{sheath} through fitting with the LPs current–voltage (I–V) characteristic curve, as shown in Equation 2.69. Then the parallel ion current density can be calculated following Equation 2.70. Electron density n_e can be calculated by Equation 2.72. Parallel heat flux can be evaluated by Equation 2.73.

$$I(V) = I_{sat}\left[1 - exp(\frac{V - V_f}{T_e})\right] + \frac{\Delta I}{\Delta V}V \tag{2.69}$$

$$J_{\parallel,i} = \frac{I_{sat}}{A_{LP}\sin\alpha} \tag{2.70}$$

$$c_s = \sqrt{\frac{e(T_e + T_i)}{m_i}} \tag{2.71}$$

$$n_e = \frac{J_{\parallel,i}}{ec_s} \tag{2.72}$$

$$q_\parallel = J_{\parallel,i}(\gamma T_e + E_{pot}) \tag{2.73}$$

Where A_{LP} is the tip area of the LPs. c_s is the sound speed defined as Equation 2.71, assuming that $T_e = T_i$, because T_i is usually not available. $\gamma = 5$ is the sheath heat transmission factor. $E_{pot} = 13.6 + 2.2\,eV$ is the potential energy includes the hydrogen ionisation energy and half of the molecular binding energy [53].

However, the target temperature $T_{e,t}$ measurements can be overestimated when the plasma progress into detachment (with target temperature below 5 eV). The sensitivity in temperature will decrease, indicates that the temperature from LPs is not the best control input to control detachment [28, 54].

2.7.2. Baratron gauge

The neutral pressure at the positions like midplane, baffle and pump can be measured by baratron gauge. Figure 2.10 shows the measurement of baffle and pump pressure in WEST. The tube marked in red represents the Baratron gauge, which is connected to the chamber wall through a relatively long tube but does not measure the pressure at the port location directly.

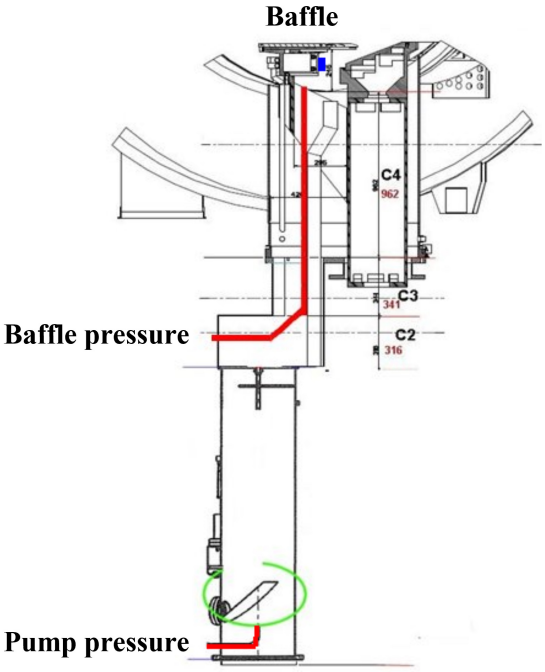

FIGURE 2.10. : Baratron absolute capacitive gauge (the part related to the divertor) in WEST.

The long tube is used to shield the gauge from the tokamak magnetic field [55]. The neutral pressure drops quickly in the conducting tube between the Baratron gauge and the port due to the conversion of energetic atomic neutrals to thermal molecules. To relate the measurements from the gauges to the pressure at the port location, we use a 0D-model [56, 57], Equations 2.74 and 2.75.

$$n_{\mathrm{mol}}^{\mathrm{gauge}} = \frac{n_{\mathrm{atom}}^{0}}{\sqrt{2}}\sqrt{\frac{T_{\mathrm{atom}}^{0}}{T_{\mathrm{wall}}}} + n_{\mathrm{mol}}^{0}\sqrt{\frac{T_{\mathrm{mol}}^{0}}{T_{\mathrm{wall}}}} \tag{2.74}$$

$$p_{\mathrm{gauge}} = n_{\mathrm{mol}}^{\mathrm{gauge}} T_{\mathrm{wall}}, \tag{2.75}$$

where $n_{\mathrm{mol}}^{\mathrm{gauge}}$ is the molecule density at the gauge. n_{atom}^{0} and T_{atom}^{0} are the neutral atom density and temperature at the port. n_{mol}^{0} and T_{mol}^{0} are the neutral molecule density and temperature at the port, respectively. T_{wall} is the temperature of the Baratron tube.

2.7.3. Bolometry

The bolometry diagnostic can help evaluate the power radiation in tokamak. In WEST there are two bolometric cameras in two horizontal ports, and they are located at the same toroidal location. Each camera supplies 8 LOS, so the whole plasma cross-section is covered by 16 LOS as shown in Figure 2.11. Each bolometer is calibrated and returns the radiated power integrated along the line of sight. The diagnostic can be

operated typically with a sampling rate of 8 ms. Through data processing in [58], the radiated power in bulk, divertor or total one can be constructed based on the data from each LOS with time delay ~ 1 ms.

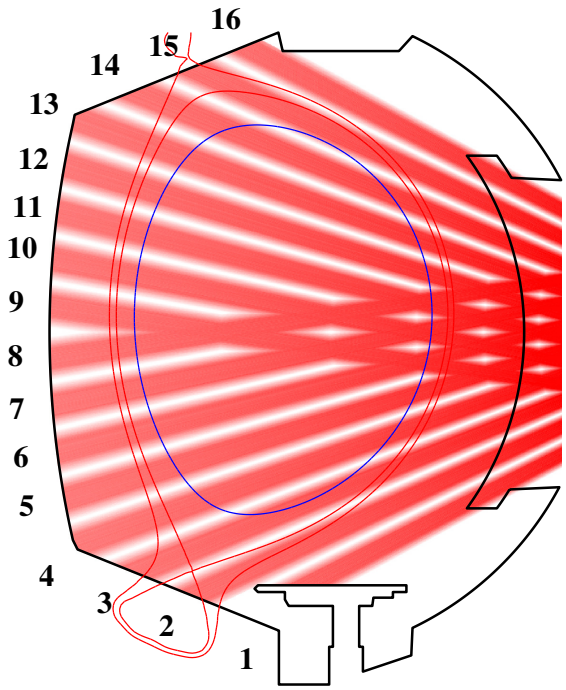

FIGURE 2.11. : Bolometer basis with magnetic equilibrium of #54903 at t = 8 s in WEST.

2.7.4. Reflectometer

The edge profile reflectometer provides radial profiles of density and density fluctuations at the edge of the plasma (outside the LCFS to the pedestal region). There are 2 channels swept reflectometer that cover the frequency range 50–75 GHz (V band) and 75–110 GHz (W band) in X-mode polarization. The time resolution is flexible and can be reduced to 3 µs. The accessibility of X-mode depends on the magnetic field as shown in Figure 2.12. When the toroidal magnetic field in the center of the vacuum vessel is smaller than 2.8 T, there is no measurement.

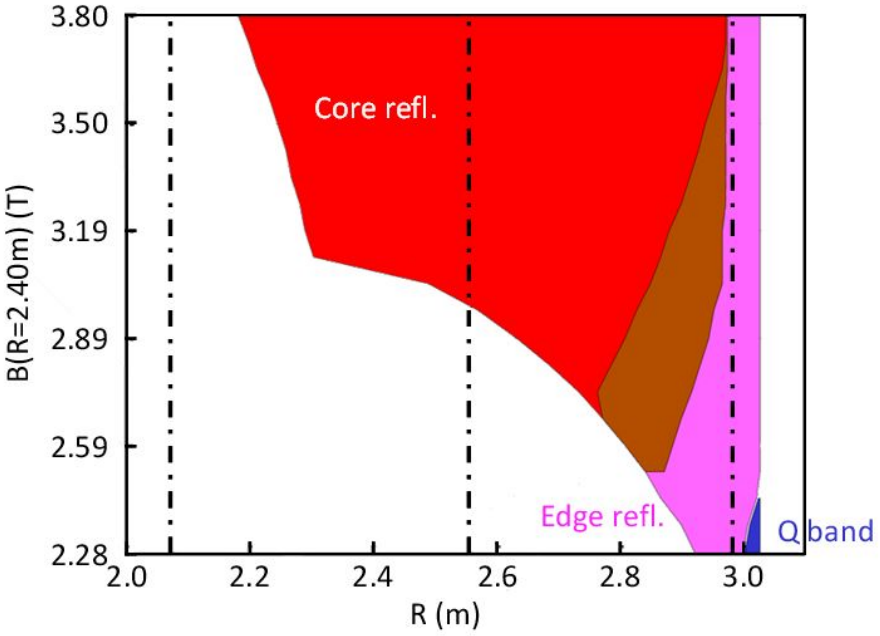

FIGURE 2.12. : The accessibility of reflectometer diagnostic depends on the magnetic field in WEST.

2.7.5. Interferometry

Interferometry diagnostic can provide the measurement of electron density along the LOS reaching through the plasma. In WEST, there are 10 Far Infrared (FIR) laser beams through the plasma (8 equatorial port bulk plasma channels + 2 vertical port edge plasma channels) as shown in Figure 2.13. Two wavelengths are used : 194.7 µm and 118.6 µm (DCN and H2O laser sources). The measurement is refreshed every 10 µs, while the result consistency will be checked and then sent to the WEST real-time shared memory network to be used for control and protection by other systems at the sampling time of 1 ms [59]. In this thesis, we evaluate the line-integral density $n_{\mathrm{e,int,X}}$ [number of particles/m^{-2}] over channel 1 (green line in Figure 2.13), which is pointing in the X-point region.

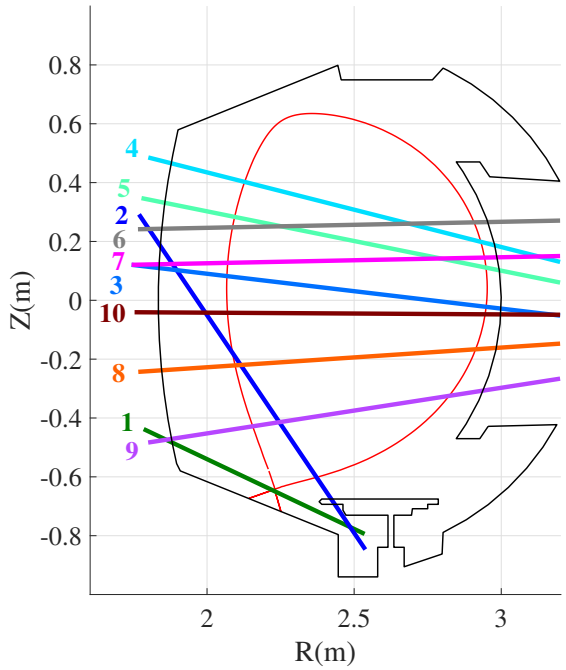

FIGURE 2.13. : Beam chord trajectories versus the magnetic separatrix surface (red curve) in WEST.

3. Numerical modeling of edge plasma transport

Sommaire

3.1. Simulation codes and SOLEDGE3X-EIRENE

There are several plasma edge simulation codes that handle the balance equations similar to Section 2.2 and consider the effects of the magnetic field, including SOLEDGE2D [60], SOLPS-ITER [61-63], UEDGE [64, 65], EDGE2D [66, 67] TOKAM3X [68] and BOUT++ [69, 70].

The simulations work in this thesis employed the latest developed SOLEDGE3X code in 2D transport mode. This code is capable of running in both transport and turbulence modes [60, 68]. The multi-species plasma fluid model is derived using the approach by Zhdanov [41]. SOLEDGE3X is coupled with EIRENE to handle kinetic neutrals. It inherits the specific characteristics of SOLEDGE2D, and uses an immersed boundary method to drive Bohm boundary conditions (Section 2.3.1) at the interface between the plasma and solid surfaces. This allows the code to handle flexible wall geometries like divertor baffles and enables simulations of the plasma up to the wall [71].

3.2. Numerical modeling

3.2.1. WEST L-mode simulation

In this section, we will introduce WEST tokamak briefly, and then try to reproduce WEST L-mode plasma background through SOLEDGE3X-EIRENE simulation and make it match the reference one from the experiment. For LSN configurations, two experimental discharges #54903 and #56420 are selected to perform modeling work, as they can represent the attached and detached plasma. Two cases are basically following the same way to define the simulation setups, but the simulation of #56420 includes the consideration of drifts and ballooning. One needs to notice that drifts and ballooning are not necessary setups to simulate detached plasma, the inclusion of drifts and ballooning is just trying to have a better description of diffusion coefficients map following the impact of drifts and turbulence. After we obtain the correct basic simulation cases, the density scan is applied to investigate the plasma behavior in different regimes.

3.2.1.1. The WEST tokamak

The WEST was transformed from the Tore Supra tokamak by changing a carbon limiter to a tungsten divertor configuration [3, 72]. It is a MA class superconducting full tungsten tokamak (plasma current $I_p = 0.5$–1 MA, toroidal field $B_\phi = 3.7$ T, major radius $R = 2.5$ m, minor radius $a = 0.5$ m), equipped with two up-down symmetric divertors. The magnetic system consists of 18 superconducting toroidal field coils, and 9 conventional copper poloidal field coils. In a top view of the tokamak, the toroidal magnetic field and the plasma currents are directed clockwise. Various magnetic configurations such as lower single null, upper single null, and double null can be performed in WEST. WEST is designed to operate a steady-state long pulse up to 1000 s and offer support to ITER operation and DEMO conceptual activities.

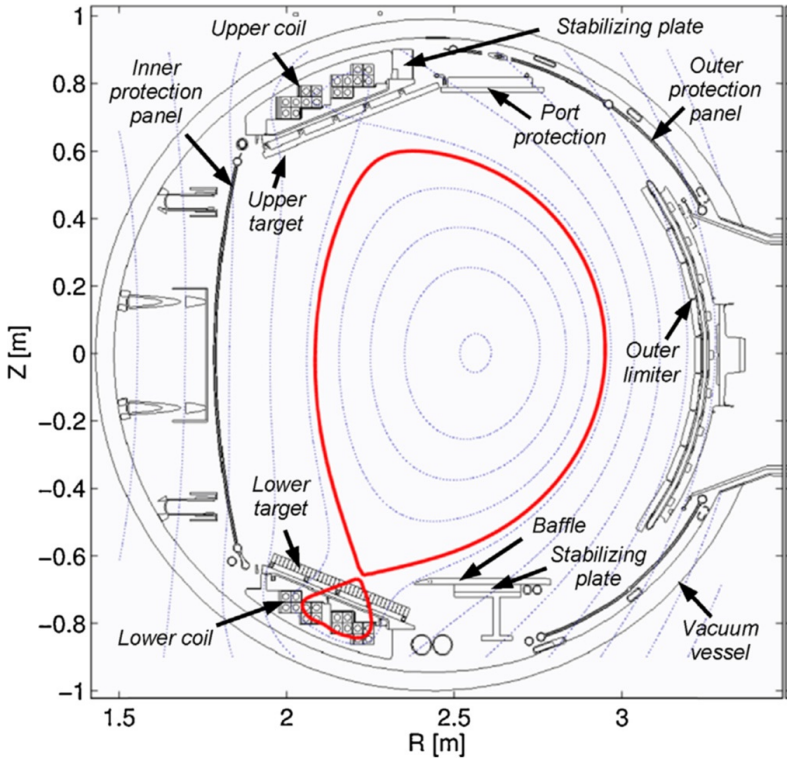

FIGURE 3.1. : Cross section of the vacuum vessel in WEST. Figure from reference [72].

3.2.1.2. Simulation setups based on attached case

The L-mode discharge #54903 at $t = 8\,\mathrm{s}$ of the C4 campaign in WEST was selected as a reference attached case for the numerical modeling work. A relatively stable state at $t = 8\,\mathrm{s}$ can be observed from its temporal evolution as shown in Figure 3.2. The operational parameters are shown in Table 3.1. The LSN magnetic configuration and the wall geometry are shown in Figure 3.3 with the gas puff position sets inside the PFR, and the pump position sets under the baffle. The mesh in Figure 3.4 is made based on the wall geometry and LSN magnetic configuration as shown in Figure 3.3.

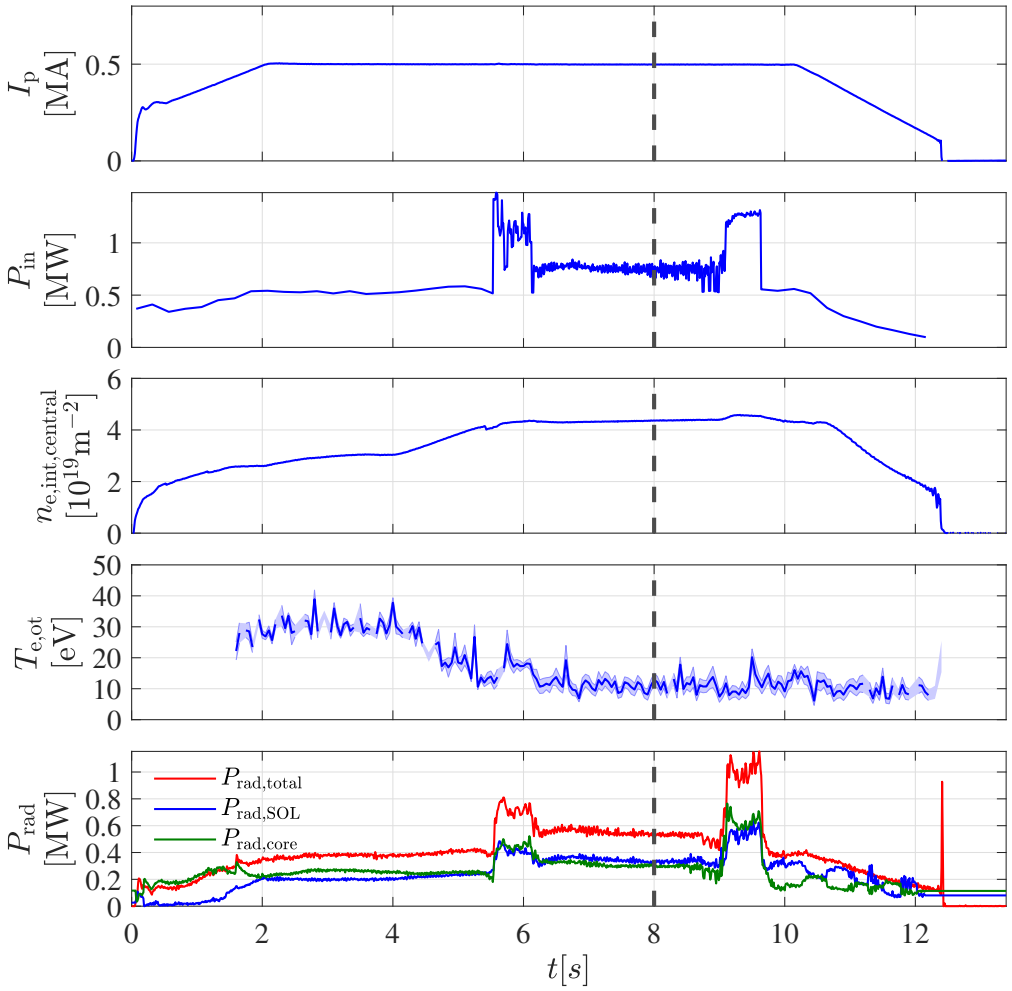

FIGURE 3.2. : Temporal evolution of plasma current (I_p), total input power (P_{in}), central line integral density ($n_{e,int,central}$), peak electron temperature at the outer target ($T_{e,ot}$), power radiation (P_{rad}) in WEST discharge #54903.

Major radius R_0 (m)	2.5
Minor radius a (m)	0.4
Plasma current I_p (MA)	0.5
Toroidal field B_ϕ (T) at R_0	3.6
Ohmic heating power $P_{\text{in,Ohmic}}$ (MW)	0.52
ICRH heating power $P_{\text{in,ICRH}}$ (MW)	0.24
Core radiated power $P^{\text{exp}}_{\text{rad,core}}$ (MW)	0.22
Upstream separatrix density $n_{\text{e,sep}}$ (10^{19}m^{-3})	1.64
Gas puff rate ($\text{Pa}\,\text{m}^3\,\text{s}^{-1}$)	0.719

TABLE 3.1. : The operational parameters of WEST discharge #54903 at $t = 8\,\text{s}$ in C4 campaign. The power delivered to the core plasma comes from Ohmic heating and *Ion Cyclotran Radiofrequency Heating* (ICRH). Core radiated power $P^{\text{exp}}_{\text{rad,core}}$ represents the radiation inside the *Core-Edge-Interface* (CEI) with $\psi_N = 0.88$ (Figure 3.3).

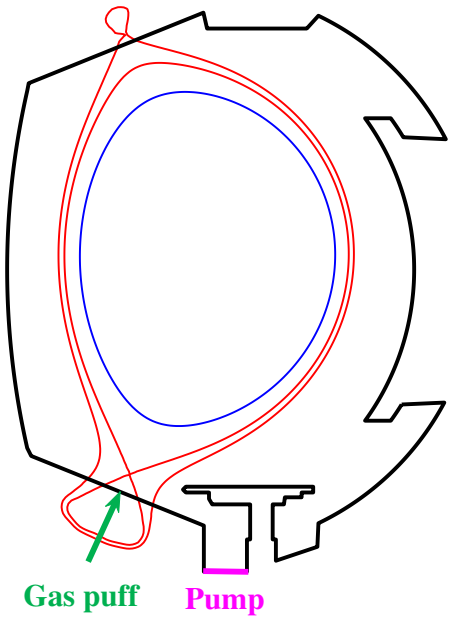

FIGURE 3.3. : WEST LSN magnetic configuration comes from the discharge #54903 at $t = 8\,\text{s}$, with wall geometry in the poloidal cross-section. The black solid curve represents the chamber wall, the red solid curves represent the first and second separatrix, the blue solid curve represents the CEI, the green arrow represents the gas puff position, and the magenta line represents the pump position.

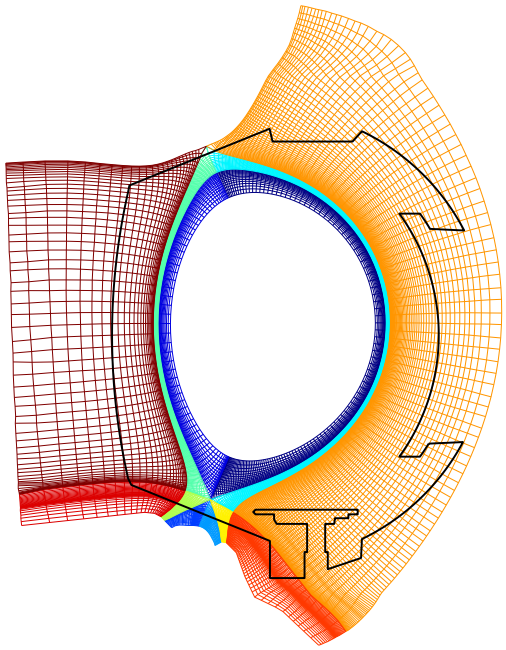

FIGURE 3.4. : SOLEDGE mesh grid based on magnetic configuration of #54903 at $t = 8\,\mathrm{s}$ in WEST. Domain decomposition is used to handle complex magnetic configurations such as closed and open field lines and private flux.

The experimental total input power $P_{\mathrm{in}}^{\mathrm{exp}} = P_{\mathrm{in,Ohmic}} + P_{\mathrm{in,ICRH}} \approx 0.76\,\mathrm{MW}$, the core radiated power inside the CEI $P_{\mathrm{rad,core}}^{\mathrm{exp}}$ is about 0.22 MW (evaluated by bolometer method [73]), as shown in Table 3.1. The input power to the edge region $P_{\mathrm{in,edge}}^{\mathrm{exp}}$ is calculated by subtracting the $P_{\mathrm{rad,core}}^{\mathrm{exp}}$ from the $P_{\mathrm{in}}^{\mathrm{exp}}$. As this discharge is performed with low heating power and inside a W-covered chamber, the influence of impurities is very small, so the simulation in this section is supposed to have no impurity, only pure deuterium. Considering that part of the energy is inevitably radiated by impurities, the radiated power in the computational domain is expected to be lower compared to reality, so the final input power of the simulation domain $P_{\mathrm{in,edge}}^{\mathrm{sim}}$ is set as 0.5 MW. The input power is split evenly between electron and ion from the core boundary.

In discharge #54903 during the time from 7 s to 9 s, the upstream $n_{\mathrm{e,sep}}$ is relatively stable. From the experimental upstream density profile (red curve with error bars) as shown in Figure 3.5, we can obtain $n_{\mathrm{e,sep}} \approx 1.64 \times 10^{19}\,\mathrm{m}^{-3}$. The $n_{\mathrm{e,sep}}$ feedback control via adjusting the gas puff rate (deuterium gas fuelling is the only external source of particles) is applied in the simulation to maintain the consistent $n_{\mathrm{e,sep}}$ as the experiment. The gas puff rate keeps decreasing linearly from 7 s to 9 s indicating a gradually saturated wall. The gas puff rate at $t = 8\,\mathrm{s}$ is around $0.719\,\mathrm{Pa\,m^3\,s^{-1}} \approx 3.47 \times 10^{20}\,\mathrm{D\ atoms\,s^{-1}}$ which can represent the averaged value that maintains the stable state. The recycling coefficient of the main chamber wall is supposed to be 1,

and the recycling coefficient of the pump is set as 0.95 to allow a deuterium gas puff rate around 3×10^{20} atoms s^{-1} which is close to the experimental gas puff level. This case is mainly prepared to analyze the impact of leakage from the aspect of neutrals transport and detachment (Section 4.1.1), thus we consider only pure deuterium plasma and no drift effects to isolate the possible influence from drifts and impurities. The influence of drifts and impurities will be investigated in the next sections. Typical values $\alpha_e = 0.2$ and $\alpha_i = 2$ are applied in the flux limiter [74].

The setup of transport coefficients in the radial direction is critical in representing the confinement properties of edge plasma. However, since the transport coefficients are still difficult to be described from the first principle, they are obtained from the experimental measurements. The classic WEST L-mode setups are $D_\perp = 0.3\,m^2s^{-1}$, $\chi_{\perp,e} = \chi_{\perp,i} = 1\,m^2s^{-1}$, which have been applied in some WEST simulation works and give promising result compared to the experiment. Here, we would like to describe the transport coefficients in a more precise way. The solution is profile feedback control, which can be used to match the radial profiles at the OMP with the experimental ones by automatically adjusting the transport coefficients, Section C. This tool can help us to extract edge transport coefficients from experimental data. In discharge #54903, we have the upstream electron density profile at the OMP from reflectometry diagnostic, but the temperature profile is unavailable. Therefore, we only control the radial mass diffusivity $D_\perp$, and suppose the radial heat flux diffusivity for electrons and ions $\chi_{\perp,e} = \chi_{\perp,i} = D_\perp/0.3$, to maintain the proportional relationship with the WEST classic L-mode setups $D_\perp = 0.3\,m^2s^{-1}$, $\chi_{\perp,e} = \chi_{\perp,i} = 1\,m^2s^{-1}$. The radial momentum diffusivity is constant as $\nu_\perp = 0.3\,m^2s^{-1}$. In the simulation domain, the transport coefficients are poloidally constant, except for the location inside the PFR, transport coefficients are the same as the value at the separatrix. To realize profile feedback, we initially start the simulation with given radial diffusivities (WEST classic L-mode diffusivities or pre-defined one) at the OMP, after a fixed number of iterations (e.g.1000), the profile feedback algorithm will compare the difference between the simulation result and target one, and propose the new radial diffusivities which will be applied in the next iteration until the result is converged. Finally, $D_\perp$ profile calculated by the feedback control at the OMP is shown in Figure 3.6, and the radial density profile is well matched with the experimental one as shown in Figure 3.5.

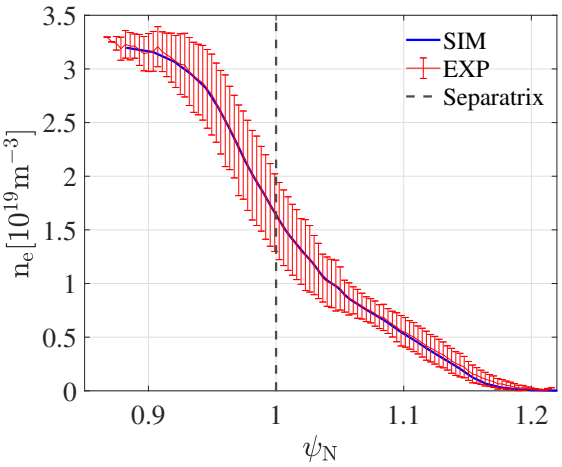

FIGURE 3.5. : Radial profile of electron density at the OMP, comparing between the experimental measurements (reflectometry method, red curve with error bars) and the SOLEDGE3X-EIRENE simulation (blue curve). The dashed line represents the position of separatrix. ψ_N is the normalized poloidal magnetic flux.

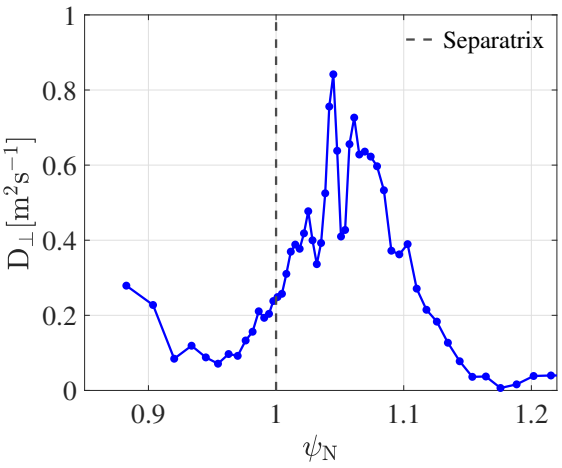

FIGURE 3.6. : Evolution of $D_\perp$ as a function of ψ_N at the OMP, controlled by the feedback function to match simulational density profile with the experimental data.

The 2D maps of electron density and temperature in the simulation domain are shown in Figure 3.7. Some results are compared with available experimental data, one can observe that the comparison between the simulation case and the experimental one shows a good match in the density, temperature, and heat flux profiles at the outer target, Figure 3.8.

One needs to notice that, the simulation of the basic case is performed with a closed baffle, which is not fully consistent with the situation of the experimental one as the discharge #54903 in the C4 campaign had reduced divertor closure with leakage at the

bottom of the outer baffle (Figure 4.1). Further analysis in Section 4.1.1 shows that the simulation yields a higher target temperature and parallel heat flux when there is a leakage, as there is less momentum and power dissipation. If we consider this aspect into account, the simulation of the basic case with a closed baffle has the potential to achieve an even better match with the experimental data for the target profiles.

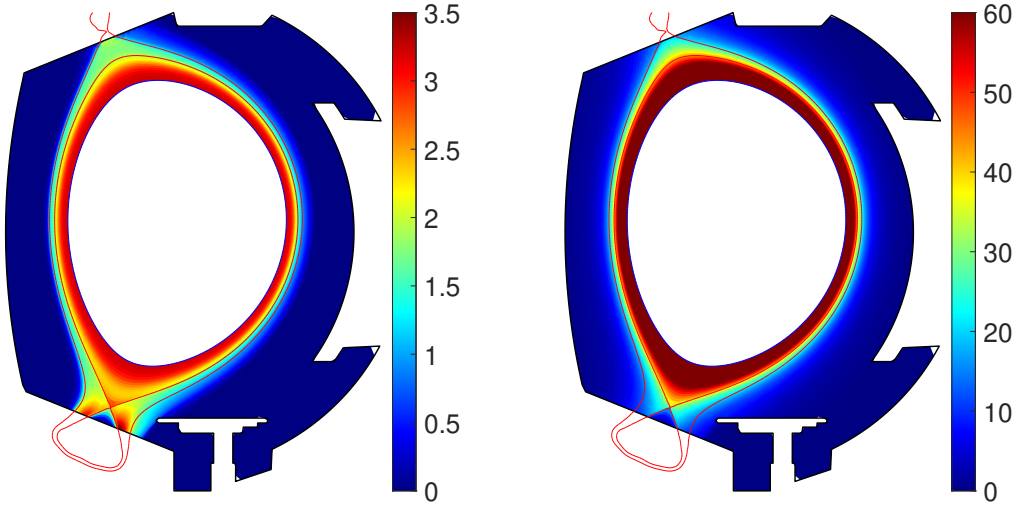

(a) $n_e[10^{19}\mathrm{m}^{-3}]$ (b) $T_e[\mathrm{eV}]$

FIGURE 3.7. : 2D maps of WEST basic simulation case (matched with experiment) for electron density, electron temperature.

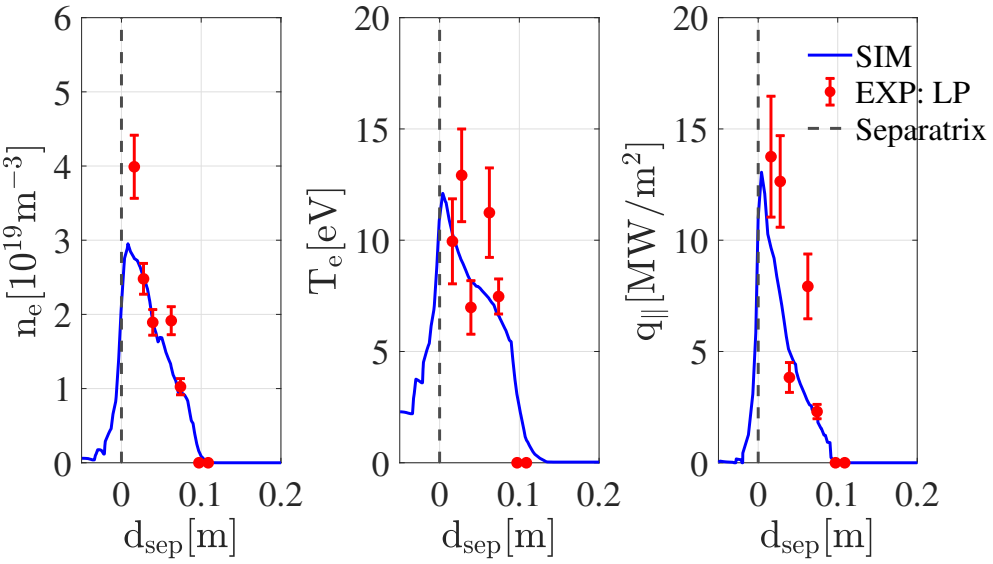

FIGURE 3.8. : The electron density, electron temperature, parallel heat flux profiles at the outer target, comparing between the experimental measurements (LPs, red dot with error bar) and the SOLEDGE3X-EIRENE simulation (blue curve). The dashed line represents the position of separatrix. d_{sep} is the radial distance from the outer strike point, negative values are in the PFR, and positive values are in the SOL.

3.2.1.3. Simulation setups based on detached case

The L-mode discharge #56420 of the C5 campaign in WEST was selected as a reference detached case for the numerical modeling work. Figure 3.9 shows the evolution of plasma current (I_p), input power (P_{in}, pure ohmic heating), line integral density near X-point ($n_{e,int,X}$), peak electron temperature at the outer target ($T_{e,ot}$), power radiation (P_{rad}) as a function of time t in this discharge. One can see that at $t = 7.3$ s, the line integral density near X-point is pretty high, and the target temperature becomes very low (≈ 5 eV measured by LPs, hit the lower limit of measurements). The visible camera shows a detachment of the radiation front (Figure 3.15a), thus, we consider the plasma detached at $t = 7.3$ s, and take the operational parameters of this moment (Table 3.2) as a reference to simulate detached plasma. The corresponding LSN magnetic configuration and the wall geometry are shown in Figure 3.10 with the gas puff position sets in the Outboard Movable Limiter to allow for midplane injection, and the pump position sets under the baffle. The mesh in Figure 3.11 is made based on the wall geometry and LSN magnetic configuration (Figure 3.10). Typical values $\alpha_e = 0.2$ and $\alpha_i = 2$ are applied in the flux limiter [74].

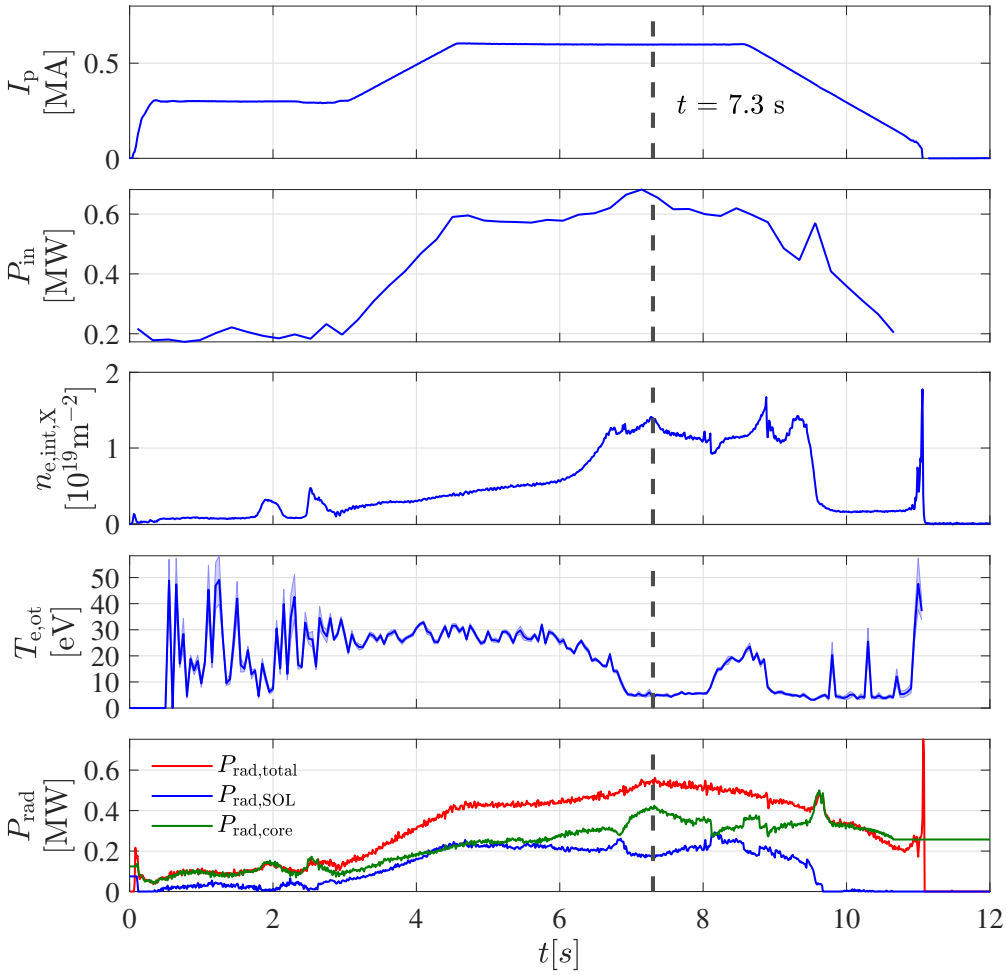

FIGURE 3.9. : Evolution of plasma current (I_p), input power (P_{in}), line integral density near X-point ($n_{e,int,X}$), peak electron temperature at the outer target ($T_{e,ot}$), power radiation (P_{rad}) as a function of time in WEST discharge #56420.

Major radius R_0 (m)	2.5
Minor radius a (m)	0.4
Plasma volume (m^3)	15
Plasma current I_p (MA)	0.6
Toroidal field B_ϕ (T) at R_0	3.6
Heating power P_{in}^{exp} (MW)	0.663
Core radiated power $P_{rad,core}^{exp}$ (MW)	0.177
Upstream separatrix density (1e19/m^3)	2.47

TABLE 3.2. : The operational parameters of WEST discharge #56420 at $t = 7.3$ s in C5 campaign. Core radiated power $P_{rad,core}^{exp}$ represents the radiation inside the CEI with $\psi_N = 0.82$ (Figure 3.10).

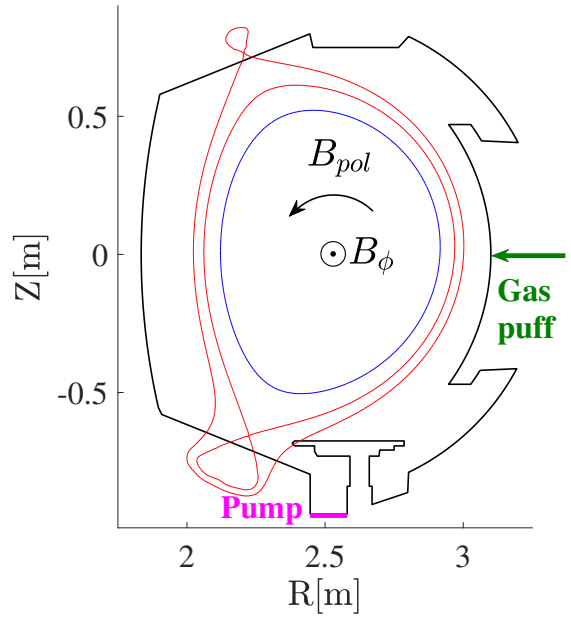

FIGURE 3.10. : WEST LSN magnetic configuration comes from the discharge #56420 at $t = 7.3$ s, with wall geometry in the poloidal cross-section. The black solid curve represents the chamber wall, the red solid curves represent the first and second separatrix, the blue solid curve represents the CEI, the green arrow represents the gas puff position, the magenta line represents the pump position.

Several operational parameters are shown in Table 3.2, we know that the total input power P_{in}^{exp} is about 0.663 MW, the core radiated power $P_{rad,core}^{exp}$ inside the CEI is about 0.177 MW (evaluated by bolometer method [73]). The input power of edge region

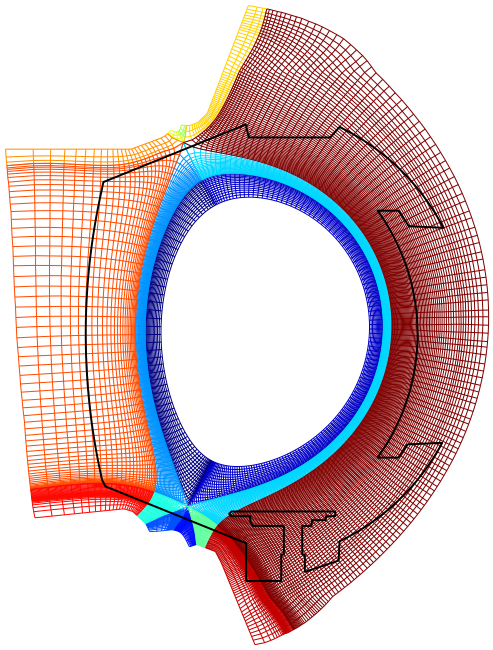

FIGURE 3.11. : WEST mesh.

$P^{\mathrm{exp}}_{\mathrm{in,edge}}$ is calculated by subtracting the $P^{\mathrm{exp}}_{\mathrm{rad,core}}$ from the $P^{\mathrm{exp}}_{\mathrm{in}}$. As this discharge is performed with relatively low heating power (pure ohmic) and inside a W-covered chamber, the influence of impurities can be very small. The simulation in this section is supposed to have no impurity, only pure deuterium. Considering that part of the energy is inevitably radiated by impurities, the radiated power in the computational domain is expected to be lower compared to reality, so the final input power of simulation domain $P^{\mathrm{sim}}_{\mathrm{in,edge}}$ is set as 0.45 MW, about $0.9 \times (P^{\mathrm{exp}}_{\mathrm{in}} - P^{\mathrm{exp}}_{\mathrm{rad,core}})$. The input power is equally shared between electrons and ions from the core boundary. Later converged simulation results show that the total radiation power in the SOL is about 0.15 MW (only from deuterium), the experimental radiation in the SOL measured by the bolometer method is around 0.18 MW (from deuterium and impurities). Considering that we suppose 0.036 MW is radiated by impurities in SOL and subtract this part when evaluating the input power for the simulation domain, the 0.03 MW difference between experiment and simulation is consistent with the prediction, also in another way verify that the input power setup has been properly defined.

From the experimental upstream density profile (red curve with error bars) as shown in Figure 3.12, we can obtain $n_{\mathrm{e,sep}} = 2.47 \times 10^{19}\,\mathrm{m}^{-3}$. The $n_{\mathrm{e,sep}}$ feedback control via adjusting the gas puff rate is applied in the simulation to maintain the consistent $n_{\mathrm{e,sep}}$ as the experiment. The gas puff rate keeps decreasing linearly in the discharge #56420 around $t = 7.3\,\mathrm{s}$ indicating a gradually saturated wall, thus the recycling coefficient of the main chamber wall is supposed to be 1. The pumping speed is set as $35\,\mathrm{m}^3\mathrm{s}^{-1}$ (equivalent to recycling coefficient ≈ 0.95), as this choice yields a reasonable

gas puff level (6.5×10^{20} D atoms s^{-1}) with respect to the experimental data (around 1.2 Pa m^3 s^{-1} $\approx 6.0 \times 10^{20}$ D atoms s^{-1}). The difference in gas puff rate between the simulation and the experiment is below 10%.

The radial diffusivities are calculated using profile feedback control, following the same procedures described in Section 3.2.1.2. However, a different approach is used to propagate these diffusivities to the entire simulation domain. In order to have a better description of the diffusivities in 2D, we consider introducing the so-called ballooning transport in which perpendicular transport is enhanced in the vicinity of the OMP observed from experiments [75, 76], and investigated in some modeling work [77-79]. In our simulations, the ballooning is described by rescaling 2D transport coefficients following the equation below [80].

$$D_{\perp,\mathrm{local}} = D_{\perp,\mathrm{omp}} \left(\frac{B_{\mathrm{omp}}}{B_{\mathrm{local}}} \right)^{b} \tag{3.1}$$

$D_{\perp,\mathrm{omp}}$ and B_{omp} represent the transport coefficients and total magnetic field strength at the OMP. B_{local} represents the total magnetic field strength at the local poloidal position, at the same poloidal flux surface (consistent ψ_{N} value) as the OMP values represented by the subscript 'omp'. To calculate the transport coefficients for the location inside the PFR, $D_{\perp,\mathrm{omp}}$ is replaced by $D_{\perp,\mathrm{sep}}$. b represents the ballooning exponent. b has been scanned from 0 to 3 in WEST simulation, showing that b value has a significant influence on the target density, particle flux, and heat flux (Section E.1.3). $b = 1$ is found to give good agreements between simulation results and available experimental results such as the parallel ion current density $J_{\parallel,\mathrm{i}}$. To realize profile feedback, we initially start the simulation with given radial diffusivities (WEST classic L-mode diffusivities or pre-defined one) at the OMP, after a fixed number of iterations (e.g.1000), the profile feedback algorithm will compare the difference between the simulational and experimental profiles, and propose the new radial diffusivities which will be applied in the next iteration until the result is converged. Finally, $D_{\perp}$ profile calculated by the feedback control at the OMP is shown in Figure 3.13, and the radial density profile is well matched with the experimental one as shown in Figure 3.12.

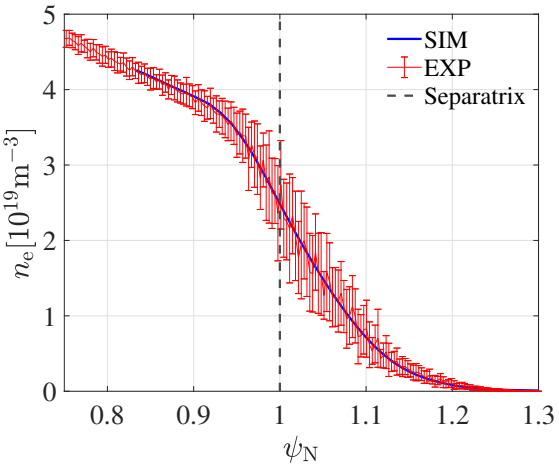

FIGURE 3.12. : Experimental radial profile of edge electron density (red curve with error bars) measured by the reflectometry method, together with the corresponding result of SOLEDGE3X-EIRENE simulation (blue curve), the dashed line represents the position of separatrix.

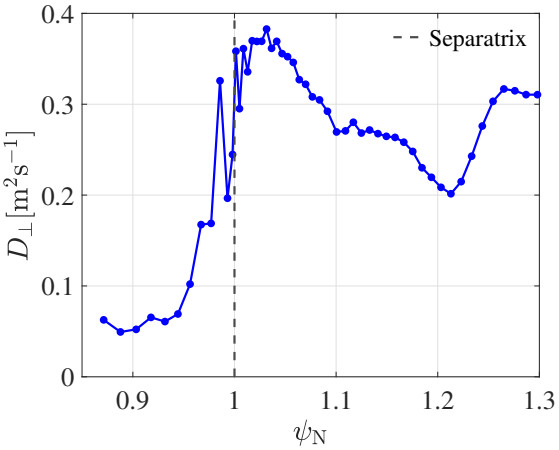

FIGURE 3.13. : Evolution of $D_\perp$ as a function of ψ_N at the OMP, controlled by the feedback function to match with the experimental density profile.

In order to have a better description of cross-field transport, the drift effects due to $\mathbf{E} \times \mathbf{B}$ drift, ∇B drift, and Curvature are considered in the simulation. In a top view of WEST, the toroidal magnetic field $\mathbf{B}_\phi$ and the plasma currents $\mathbf{I}_p$ are directed clockwise. The direction of ion ∇B drift points downwards and corresponds to the favorable magnetic field direction in the LSN magnetic configuration.

The 2D maps of electron density and temperature in the simulation domain are shown in Figure 3.14. Some results are compared with available experimental data, one can observe that the comparison between the simulational data and experimental data shows :

- Consistent 2D maps of radiation, with the significant detachment of radiation front, Figure 3.15, indicates that detachment is realized in the simulation.
- Relatively well matched perpendicular velocity, Figure 3.16. One needs to note that measurements of perpendicular velocity are mainly available at low $n_{e,sep}$. The measurements at $t = 7.3$ s, corresponding to a high $n_{e,sep} = 2.47 \times 10^{19}\,m^{-3}$, are not available. Therefore, lower $n_{e,sep}$ cases with consistent setups (fixed input power, diffusion map, etc.) are used to compare with experimental data. The perpendicular velocity in the experiment is mainly contributed by $\mathbf{E} \times \mathbf{B}$ drift velocity and measured by *Doppler Back Scattering* (DBS) at the OMP, so we compare it with the $\mathbf{E} \times \mathbf{B}$ drift velocity from simulations.
- Good match in the parallel ion current density $J_{\parallel,i}$ profile at the inner and outer targets, Figure 3.17.
- Difference in the electron temperature profile at the inner and outer targets, Figure 3.18. In this case, the target temperature predicted by simulation is about 2 eV, but the data given by LPs is about 4 eV at the outer target. The reason is that the target temperature in the experiment is measured by LPs which usually overestimates temperature when $T_e < 5$ eV (explained in Section 2.7.1). However, at the inner target, the T_e measured by LPs can reach 10 eV, with some distance from separatrix, while, T_e remains about 2 eV at the same location in simulation, the reason is not quite clear. For the target density and heat flux which are calculated based on the temperature and saturate current obtained from LPs, they will be influenced by the overestimated temperature in detached plasma.

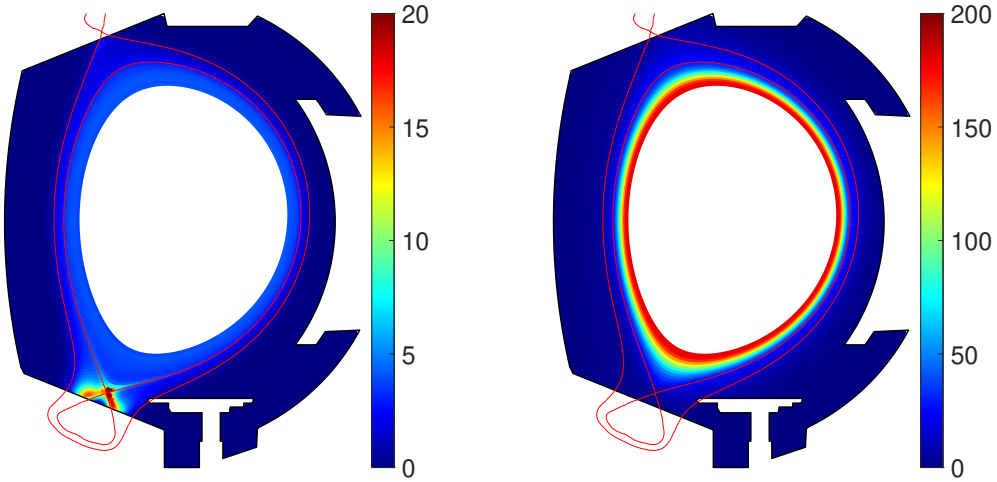

(a) $n_e[10^{19}m^{-3}]$ (b) T_e[eV]

FIGURE 3.14. : 2D maps of electron density and temperature from WEST basic simulation case.

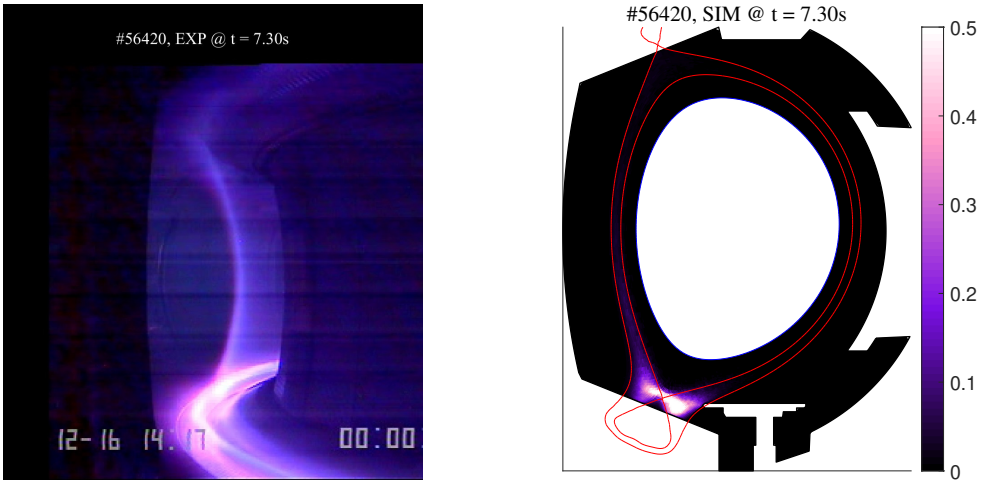

(a) P_{rad} in experiment (b) P_{rad} [MW/m^3] in simulation

FIGURE 3.15. : Radiation comparison between experiment and simulation, both have consistent upstream density.

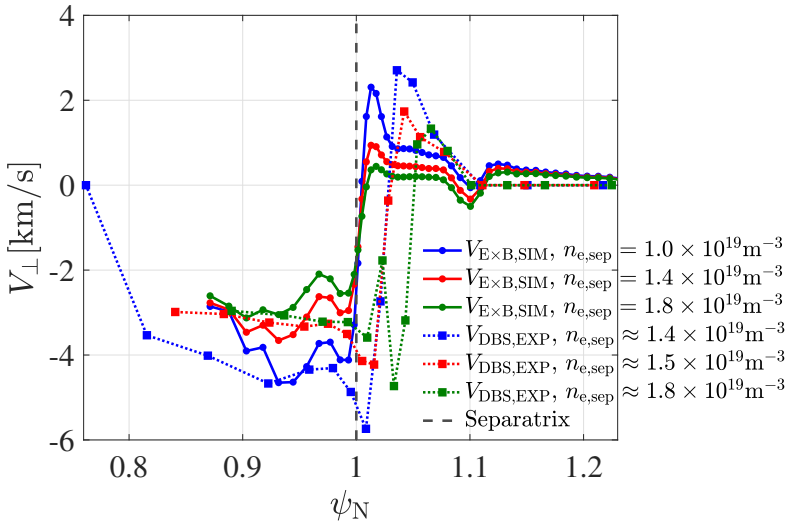

FIGURE 3.16. : Experimental radial profile of perpendicular velocity $V_{\mathrm{E\times B}}$ measured by DBS (dashed curve), together with the corresponding result of SOLEDGE3X-EIRENE simulation (solid curve), the dashed line represents the position of separatrix.

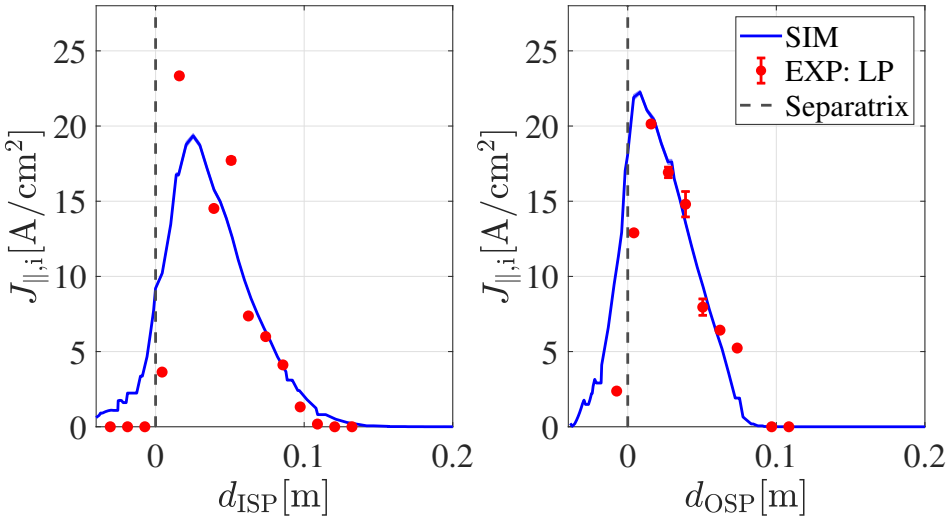

FIGURE 3.17. : Experimental $J_{\parallel,i}$ profile (red dot with error bar) at the inner and outer divertor targets measured by the LPs, and the corresponding simulational results (blue curve). The dashed line represents the position of separatrix.

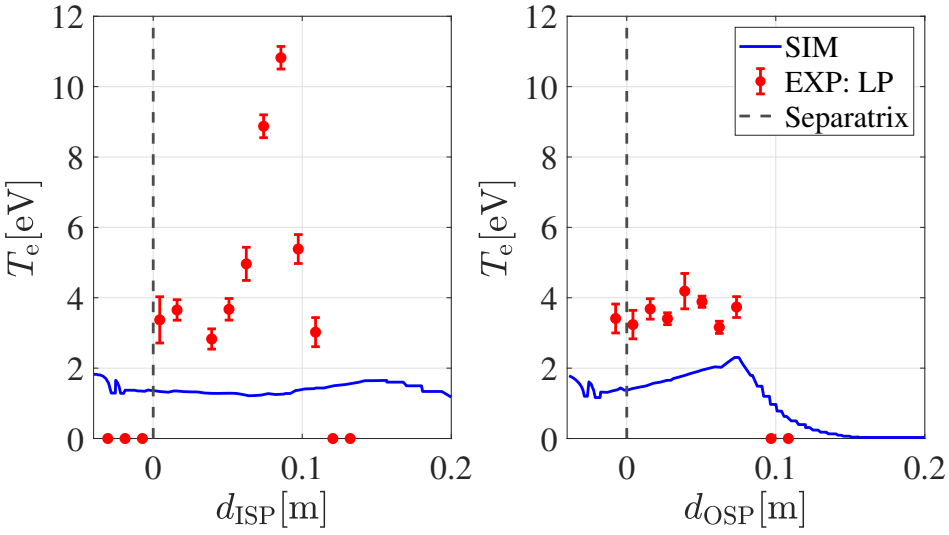

FIGURE 3.18. : Experimental inner and outer divertor target profile of electron temperature T_e (red dot with error bar) measured by the LPs, and the corresponding result of SOLEDGE3X simulation (blue curve). The dashed line represents the position of separatrix.

3.2.1.4. Plasma density scan

In Section 3.2.1.3, we have obtained a basic simulation case that properly describes the experimental edge plasma, especially the detached moment. In order to make the simulation results cover different plasma states, from the sheath limited regime to

the detached regime, the density scan is applied going from $n_{\mathrm{e,sep}} = 1.0 \times 10^{19}\,\mathrm{m}^{-3}$ to $3.5 \times 10^{19}\,\mathrm{m}^{-3}$. The change in upstream density can result in the evolution of multiple parameters as shown in Figure 3.19. Here, T_{sep} is the upstream separatrix temperature. $\hat{T}_{\mathrm{e,t}}$ is the peak electron temperature at the target. $\hat{n}_{\mathrm{e,t}}$ is the peak electron density at the target. $\hat{\Gamma}_{\parallel,\mathrm{e,t}}$ is the peak parallel electron flux at the target. $\hat{q}_{\parallel,\mathrm{t}}$ is the peak parallel heat flux at the target. $P^{\mathrm{sim}}_{\mathrm{rad,edge}}$ is the total radiated power in the simulation domain. $P^{\mathrm{sim}}_{\mathrm{in,edge}}$ is the total input power. Here we use subscripts 'it' and 'ot' to indicate the inner and outer targets, respectively. One can observe that the increasing $n_{\mathrm{e,sep}}$ with constant input power can lead to some effects :

- The corresponding gas puff ramped up.
- The separatrix temperature T_{sep}, peak target temperature $\hat{T}_{\mathrm{e,t}}$, and heat flux $\hat{q}_{\parallel,\mathrm{t}}$ keep on decreasing.
- The target density generally increased, except the one at the outer target presents a small well around $n_{\mathrm{e,sep}} = 2.3 \times 10^{19}\,\mathrm{m}^{-3}$, and the one at the inner target shows slight rollover after $n_{\mathrm{e,sep}} = 2.5 \times 10^{19}\,\mathrm{m}^{-3}$.
- The rollover of particle flux $\hat{\Gamma}_{\parallel,\mathrm{e,t}}$, the inner one rolls over earlier than the outer one but has lower amplitude.
- Higher fraction of the power is radiated with a fixed input power $P^{\mathrm{sim}}_{\mathrm{in,edge}}$.

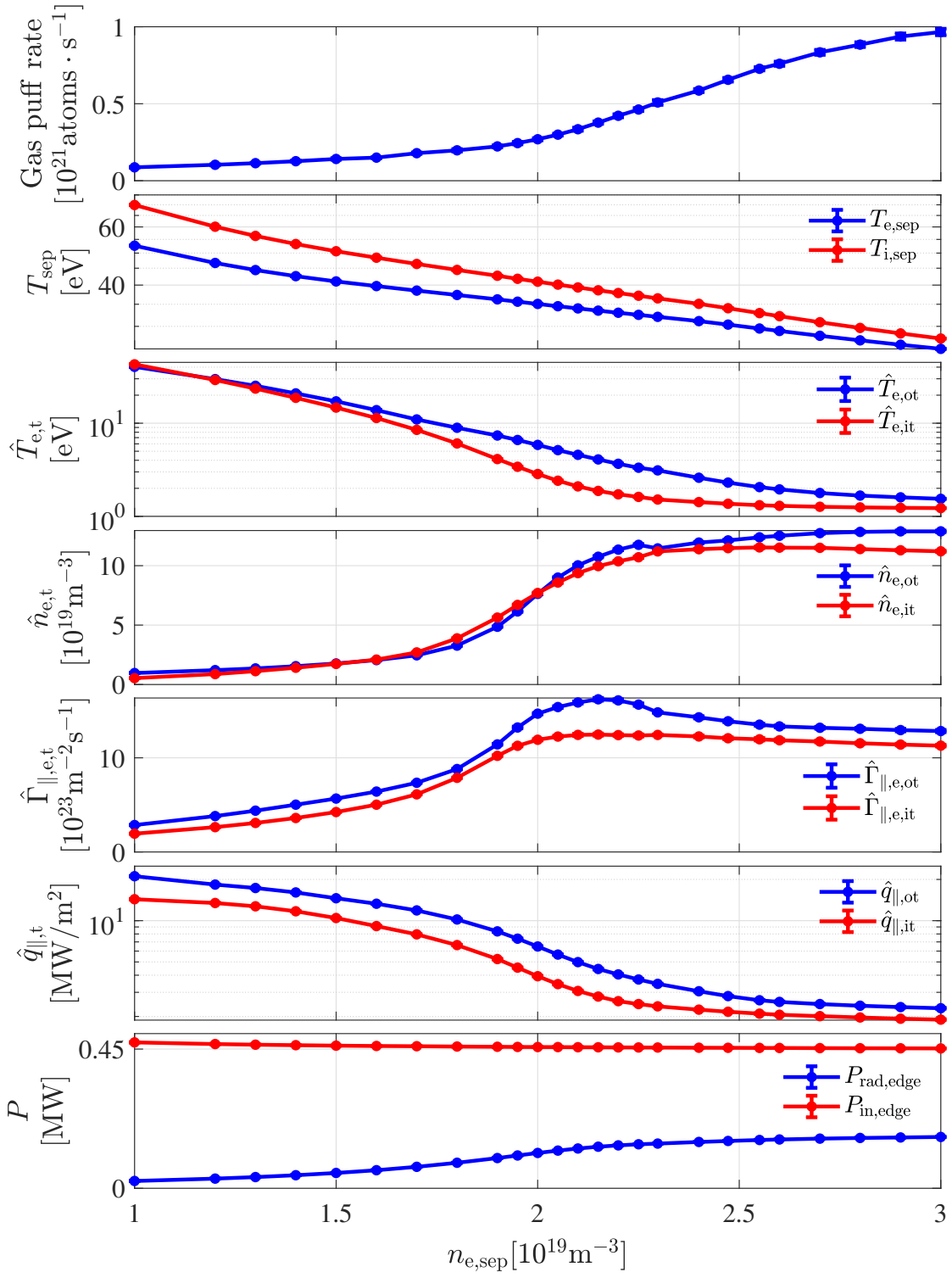

FIGURE 3.19. : Evolution of several simulated fields as a function of $n_{\text{e,sep}}$ in steady-state WEST simulations.

3.2.1.5. Analysis of simulated plasma and comparison with experiments

Bolometry signal The bolometry diagnostic has been briefly introduced in Section 2.7.3. There are 16 lines of sight in the cross-section, and the divertor region of LSN is covered by channel 2 and 3, as shown in Figure 2.11. In this section, the WEST simulation data (based on discharge #56420 in Section 3.2.1.3) will be compared with experimental data in terms of bolometry diagnostics. Thanks to the synthetic diagnostic tool named SYNDI [58], which offers the possibility to perform bolometry diagnostics based on the 2D power radiation data in simulations, we can relate the simulation results to the experimental ones.

Here, we mainly focus on the two channels that cover the divertor region. However, in the SOLEDGE3X simulation, we lack the description of radiation in the core region. The absence of radiation from the core can influence the signal of channel 3, making it difficult to compare with the experiment. Additionally, the WEST simulation case we analyze here is a pure D case, excluding the influence of impurities. Typically, a large part of the radiation is contributed by impurities, as discussed in Section 4.2. In order to make a promising comparison between simulation and experiment, we add extra radiation $P_{\mathrm{rad}} = 5.65 \times 10^4\,\mathrm{Wm}^{-3}$ on the ring between $\psi_{\mathrm{N}} = 0.67$ and 0.82 to represent part of core radiation that can influence channel 3 (as shown in Figure 3.20). We also increased the bolometer output of SYNDI by a factor of 2, considering the reduced radiation due to the lack of impurities. These adjustments enable the no drifts case to have bolometer signals in channel 2 and channel 3 that are close to the experimental ones at $n_{\mathrm{e,sep}} = 2.47 \times 10^{19}\,\mathrm{m}^{-3}$.

We can obtain the evolution of bolometer signal as a function of $n_{\mathrm{e,sep}}$ after processing our existing density scan cases with SYNDI tools. Combining with the time evolution of $n_{\mathrm{e,sep}}$ in experimental discharge #56420 from $t = 5\,\mathrm{s}$ to $t = 7.2\,\mathrm{s}$ (Figure 28), and supposing the plasma in the experiment can reach an approximately steady state within a very short time duration (few ms) when the gas puff is gradually increased with constant input power and plasma current. We can thus obtain the evolution of bolometer signals as a function of time and $n_{\mathrm{e,sep}}$ for both experiment and simulation as shown in Figure 3.21 and 3.22. The simulation case with and without drifts is taken into account. It can be observed that the signal is lower in the simulation compared with the experiment when plasma is attached (low $n_{\mathrm{e,sep}}$), and a generally good match when plasma detached. However, in the simulation with no drift, there exists a sharp increase of signal value when $n_{\mathrm{e,sep}} \geq 2.80 \times 10^{19}\,\mathrm{m}^{-3}$. The sudden increase in signal value can also be observed in the experiment result, the simulation and experiment have a very close $n_{\mathrm{e,sep}}$ threshold, but the magnitude of the experimental increase is not as very high as the simulation. The case with drifts can not reproduce such kind of sudden increase in signal when $n_{\mathrm{e,sep}}$ is high or the plasma is deeply detached. The sudden increase of bolometer signal can be explained as the presence of XPR, which is discussed in Section G.2. The reason for no XPR in the case with drifts is that the neutrals are hard to penetrate into the X-point region, as discussed in Section E.2.3. The XPR seems difficult to be reproduced in the simulation with drifts, but it is relatively easier to observe in the experiment. The physics that makes this kind of

difference needs to be investigated further.

The sum of signals from two channels is plotted in Figure 3.23. One can observe that the simulation with drifts has a better match with the experimental one in terms of signal summation.

The bolometer can be an ideal diagnostic method to know about the divertor situation. The sum of channel 2 and channel 3 signals shows a linear relationship with $n_{e,sep}$. The bolometer disgnostic is good to be implemented into the feedback control system as it also has a very low time delay (7 ms). The presence of XPR is usually combined with a sudden increase of signal in channel 3 and a sudden decrease of signal in channel 2, which shows the potential of bolometer in controlling XPR or deeper detached plasma.

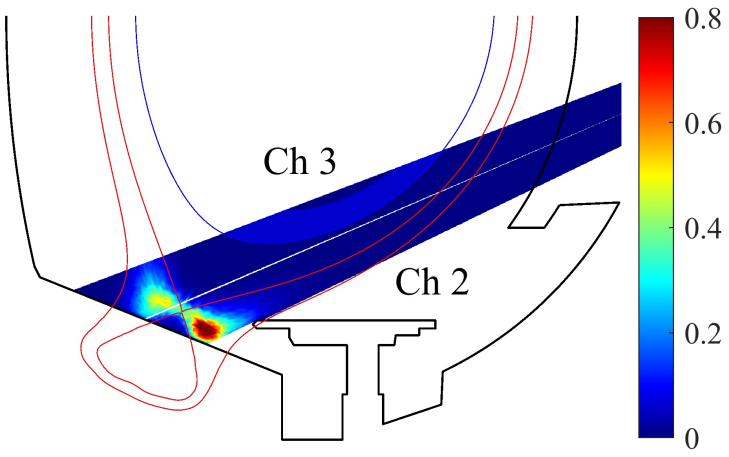

FIGURE 3.20. : The contour of radiation [MW/m^3], with channel 2 and channel 3 marked.

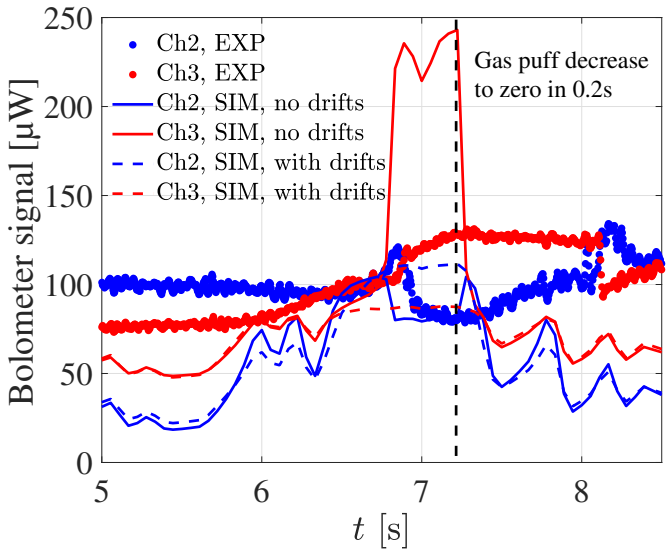

FIGURE 3.21. : Evolution of bolometer signal (Channel 2 and Channel 3) as a function of time in WEST discharge #56420, compared with simulation results.

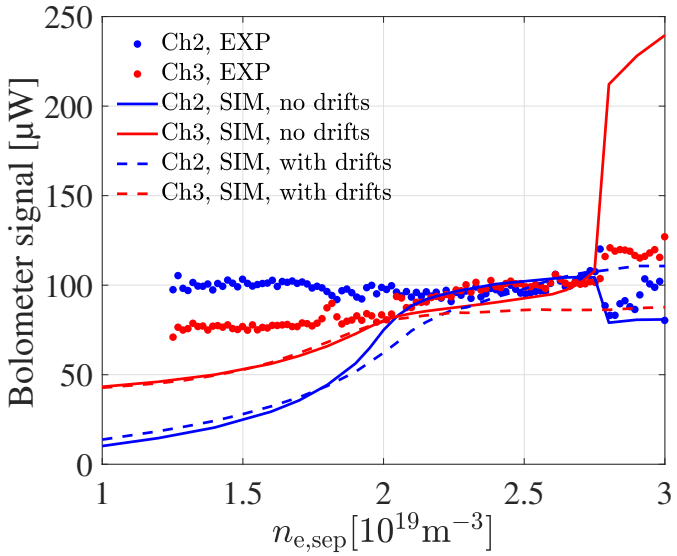

FIGURE 3.22. : Evolution of bolometer signal (Channel 2 and Channel 3) as a function of $n_{e,sep}$ in WEST discharge #56420, compared with simulation results.

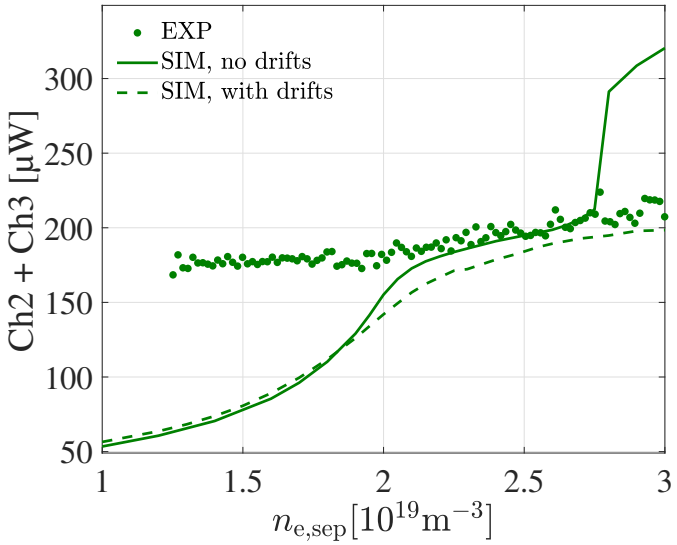

FIGURE 3.23. : Evolution of sum of bolometer signals (Channel 2 + Channel 3) as a function of $n_{e,sep}$ in WEST discharge #56420, compared with simulation results.

Line-integral density The line-integral density over channel 1 which is pointing in the X-point region (Figure 3.24) given by interferometric measurements in WEST experiment (#56420) is compared with the simulation cases. We can obtain the evolution of line-integral density as a function of time and $n_{e,sep}$ in Figure 3.25 and 3.26, respectively. One can observe that the line-integral density generally keeps a monotonic increase with $n_{e,sep}$. However, the integral density starts to saturate when the plasma is deeply detached, due to strong recombination that happens when the temperature near X-point is low enough and triggered by very high $n_{e,sep}$. The saturation of line-integral density occurs with the presence of XPR in no drifts case. While all the pure D cases, both with and without drifts, show an overestimate of the line-integral density near the X-point in the detached regime, the case with drifts exhibits a line-integral density value that is closer to the experimental measurements compared to the case without drifts. This difference between simulation and experiment can be explained by the lack of impurities in the simulation, this part still needs to be investigated further. The line-integral density near X-point shows a good potential to control detached plasma as it still shows sensitivities when plasma is detached.

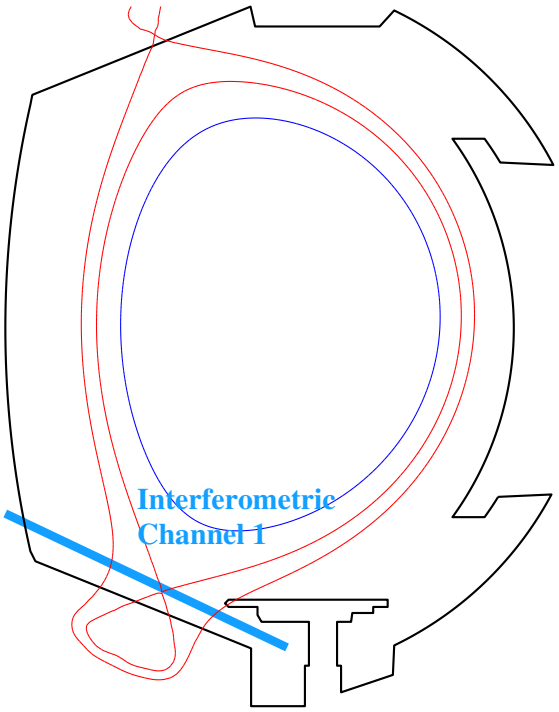

FIGURE 3.24. : Channel 1 of interferometric measurements in WEST.

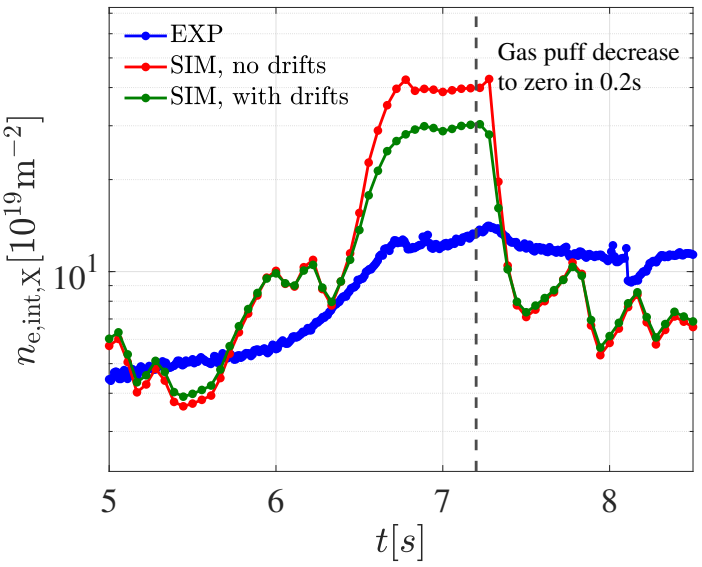

FIGURE 3.25. : Evolution of line integral density as a function of time.

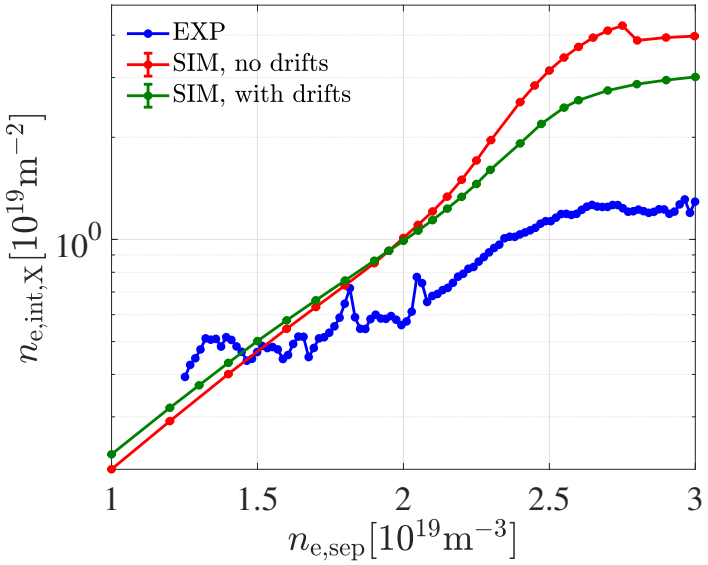

FIGURE 3.26. : Evolution of line integral density as a function of $n_{e,sep}$.

3.2.2. TCV H-mode simulation

3.2.2.1. The TCV tokamak

TCV [81, 82] is a medium-sized tokamak with plasma current I_p up to 1 MA, toridal field B_ϕ = 1.4 T, major radius R = 0.88 m, minor radius a = 0.25 m. The magnetic system consists of 16 toroidal field coils and 16 independently powered poloidal field coils. TCV has very high flexibility to vary the plasma shape with different magnetic configurations (e.g. limited, single null, double null, super-X, snowflakes). The first wall of TCV is almost fully (> 95%) covered with graphite tiles, thus carbon becomes the main plasma impurity. Graphite can not only bear very high temperatures but also mitigate the degradation risk of core plasma performance (low-Z material like C has lower influence than high-Z material like W). However, Graphite is not suitable to be used for future reactors due to big amount of hydrogen isotope retention [83]. In addition, TCV has performed extensive experimental discharges in investigating the impact of divertor closure by changing the length of the baffles [84, 85] and also the impact of nitrogen seeding on L-mode [86] and H-mode [17] cases.

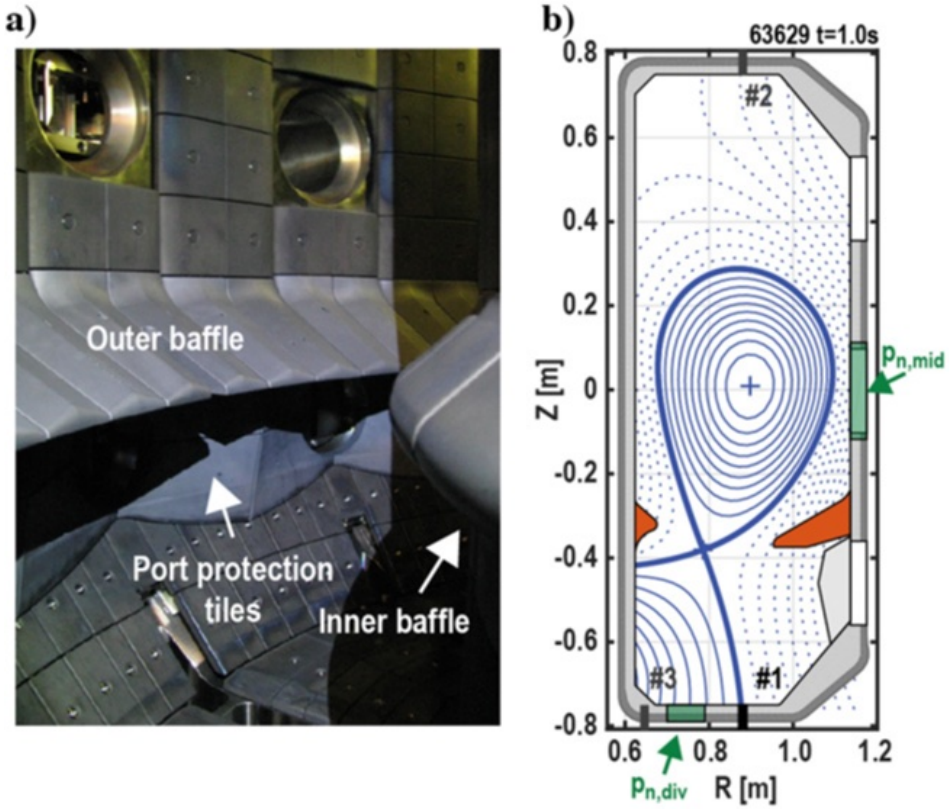

FIGURE 3.27. : (a) Interior of the TCV vacuum vessel and (b) poloidal cross-section of a standard single-null configuration in the baffled TCV vessel. Highlighted are the *High Field Side* (HFS) and *Low Field Side* (LFS) baffles (orange), gas valves (black) and ports equipped with baratrons (green). Figure from reference [85].

3.2.2.2. Simulation setups of basic case

To investigate the properties of H-mode case, the TCV discharge #70690, a typical type-I ELMy H-Mode, was selected as the experimental reference. The operational parameters are shown in Table 3.3. The discharge was performed in a LSN magnetic configuration, and the wall geometry is shown in Figure 3.28. The D_2 gas fuelling was injected near the outer separatrix at the outer target, and the N_2 seeding was injected in the PFR. The turbo pumps have a negligible effect on particle balance in the vessel during discharges since the sink of particles is dominated by the graphite wall tiles. The recycling coefficient of deuterium on the entire wall is set to 0.99 as this choice yielded reasonable gas puff levels with respect to the experiments [56]. The recycling coefficient of nitrogen is estimated to range from 0.3 to 0.5, based on spectroscopic measurements [87]. The recycling coefficient of carbon lies within the same range to obtain a reasonable radiated power in the SOL [88]. Here, the recycling coefficients of nitrogen and carbon were set to 0.5. However, we start this section by considering a case without nitrogen seeding, and carbon is therefore the only impurity that is

simulated. The physical and chemical sputtering is estimated through the Bohdansky and Roth model [89] in EIRENE with the plasma background provided by SOLEDGE3X. The mesh used in the simulation is shown in Figure 3.29.

Major radius R_0 (m)	0.89
Minor radius a (m)	0.25
Plasma current I_p (MA)	0.21
Toroidal field B_t (T) at R_0	1.39
Total heating power $P_\mathrm{in}^\mathrm{exp}$ (kW)	510
Core radiated power $P_\mathrm{rad,core}^\mathrm{exp}$ (kW)	80
Main impurity	Carbon

TABLE 3.3. : The operational parameters of TCV discharge #70690 at $t = 1$ s. The total heating power $P_\mathrm{in}^\mathrm{exp}$ represents the power delivered to the core plasma from Ohmic heating and *Neutral-Beam Injection* (NBI). Core radiated power $P_\mathrm{rad,core}^\mathrm{exp}$ represents the radiation inside the CEI with $\psi_\mathrm{N} = 0.75$ (Figure 3.28).

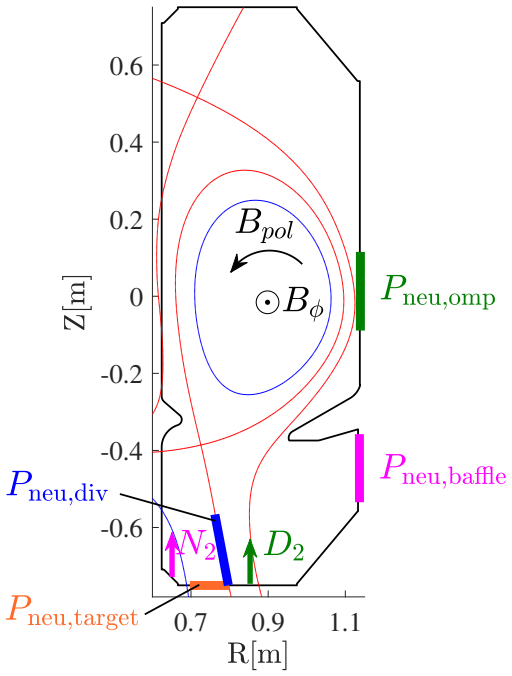

FIGURE 3.28. : TCV LSN magnetic configuration comes from TCV discharge #70690 at $t = 1$ s, with wall geometries in a poloidal cross-section. The black solid line represents the graphite wall, the red solid curves represent the first and second separatrices, the blue circle represents the CEI, the green arrow represents the deuterium gas puff position ($R = 0.88$ m), the magenta arrow represents the nitrogen seeding position ($R = 0.65$ m). The line averaged neutral pressure measured at the positions near OMP, baffle, divertor, and target. The $P_{\mathrm{neu,div}}$ is not available in the experimental measurements.

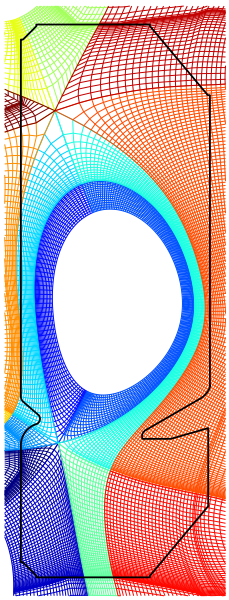

FIGURE 3.29. : SOLEDGE3X mesh grid based on magnetic configuration of #70690 at $t = 1$ s in TCV.

Thomson Scattering (TS) measurements [90] of upstream electron density and temperature profiles, and *Charge eXchange Recombination Spectroscopy* (CXRS) measurements [91] of the upstream ion temperature profile are shown in Figure 3.30. The TS measurements yield an upstream separatrix electron density, $n_{e,sep} \approx 1.36 \times 10^{19}\,m^{-3}$. In the simulations, $n_{e,sep}$ is controlled by feedback adjustments of the D_2 gas puff rate to match the experimental value. We measured $T_e \approx 405\,eV$ at the CEI. T_i, despite the relatively large experimental uncertainties, lies within the same range as T_e. Therefore, $T_{e,CEI} = T_{i,CEI} = 405\,eV$ was set as the simulation temperature boundary condition.

To simulate the H-mode case, non-constant diffusion coefficients are a mandatory choice. Feedback control of the transport coefficients at the OMP is applied (Section C). As we have the experimental upstream n_e and T_e profiles (Figure 3.30), the radial mass diffusivity $D_\perp$ and the radial heat flux diffusivity for electrons $\chi_{\perp,e}$ can be controlled separately. The ion-to-electron temperature ratio $\tau = T_i/T_e$ increases with radius, with $\tau = 1 \rightarrow 2.5$ in the edge plasma ($0.64 < \psi_N < 1$) based on the data from several machines, see, for example, Figure 7 in [92]. The simulation assumes the radial heat flux diffusivity for ions $\chi_{\perp,i}$ is higher than $\chi_{\perp,e}$ in the pedestal as $\chi_{\perp,i} = 2\chi_{\perp,e}$ inside the separatrix, $\chi_{\perp,i} = \chi_{\perp,e}$ outside the separatrix to reproduce τ profile approximately matched with experiment. The radial momentum diffusivity is assumed constant as $\nu_\perp = 0.2\,m^2s^{-1}$. The transport coefficients for impurity ions are consistent with those for the main ions. After determining the transport coefficients at the OMP, we need to propagate it to the whole simulation domain. In order to have a better description of the diffusivities in 2D, we consider introducing the so-called ballooning transport as described in the WEST simulation setups (Section 3.2.1.3). However, directly applying this diffusive map to simulations would lead to a peak target density overestimation by a factor of about 2 compared with the experimental value in TCV

case. This overestimation does not seem to be directly caused by the introduction of ballooning transport, but rather by the competition of particle and heat transport between parallel and perpendicular parts in the divertor volume [48]. Therefore, we chose to enhance the diffusivities by a factor of 10 in the divertor region and make the target profiles (density, heat flux) approximately consistent with experimental data, similarly to as done in [93, 94]. Moreover, based on the enhancement of diffusivities in the divertor, the ballooning exponent b was scanned from 0 to 3 (Section E.1.3), showing that different b values can impact the peak temperature and integral particle flux at the targets. A higher value of b results in a lower peak temperature at the inner target and a higher peak temperature at the outer target. Additionally, it leads to a narrower width while maintaining a similar peak particle flux at both targets. These effects have an impact on the carbon sputtering rate. A value $b = 1$ was found to result in a good match between the experiment and simulation with respect to the C^{6+} density at the OMP, as shown in Figure 3.31.

We first take H-mode like non-constant diffusivities at the OMP [95] as a reference to make the initial diffusion map and perform the simulation, then the profile feedback control process will automatically find the closest diffusivities that make the simulation profiles fit with the target profile shape at the OMP. The resulting diffusivity profile at the OMP is shown in Figure 3.32.

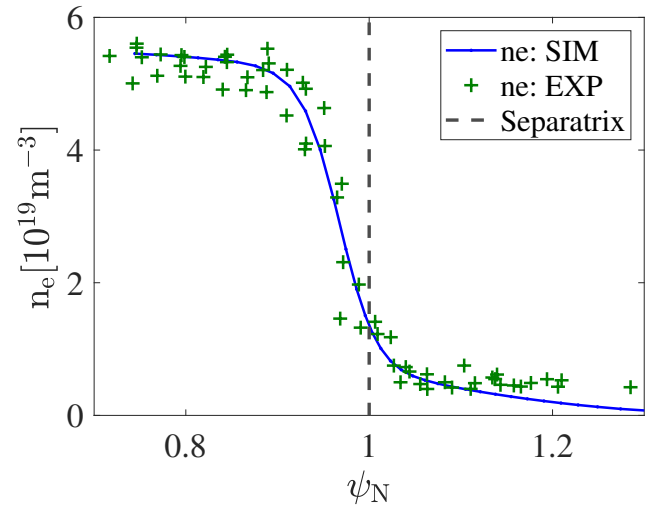

(a) Radial profiles of electron density at the OMP.

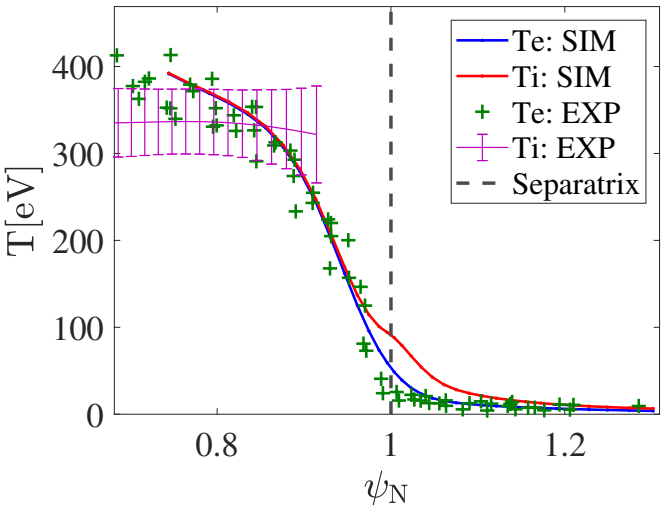

(b) Radial profiles of temperature at the OMP.

FIGURE 3.30. : Radial profiles of density and temperature at the OMP, comparing the experimental measurements of n_e and T_e (raw data measured by TS, represented by the green plus sign) and T_i (measured by CXRS, raw data fitted with a spline and represented by the purple curve with error bars showing uncertainties of the fit) with the SOLEDGE3X-EIRENE simulation (blue and red curves). The dashed line represents the position of separatrix.

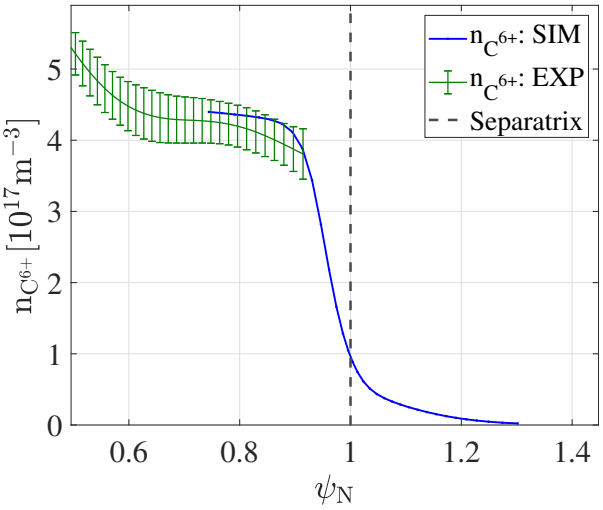

FIGURE 3.31. : Radial profiles of C^{6+} density at the OMP, comparing the experimental measurements (CXRS, raw data fitted with a spline and represented by the green curve with error bars showing uncertainties of the fit) with the SOLEDGE3X-EIRENE simulation (blue curve). The dashed line represents the position of separatrix.

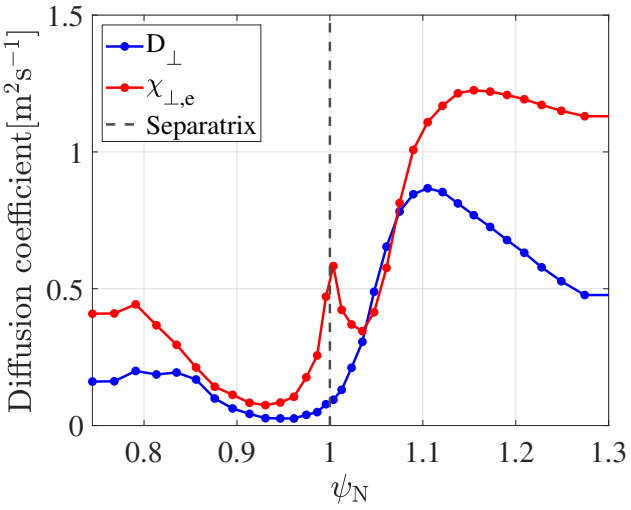

FIGURE 3.32. : Profiles of $D_\perp$ and $\chi_{\perp,e}$ as a function of ψ_N at the OMP, controlled by the feedback function to match the experimental density and temperature profile.

L-mode experiments have demonstrated that drifts mainly affect the plasma state at the inner target, with detachment being more easily achieved in the presence of the favorable magnetic field (the direction of ion ∇B drift points downwards in the LSN magnetic configuration) compared to the unfavorable one (reversed ∇B direction) [86, 96]. Although drifts were not activated in the simulations due to the challenge in convergence with low diffusion coefficients, drifts (particularly $\mathbf{E} \times \mathbf{B}$ drift) would

improve the agreement by displacing the density peak at the outer target towards the PFR. The **E** × **B** drift is responsible for notable cross-field transport in the divertor region, pointing from the outer SOL into the main plasma (and into the private plasma below the X-point) in the favorable magnetic field [80].

Since a significant amount of power is expelled during *Edge Localized Mode*s (ELMs), the simulation focuses on inter-ELMs condition and finds the total heating power going to the SOL is $P^{\mathrm{sim}}_{\mathrm{in,edge}} = 210\,\mathrm{kW}$ by setting the $T_{\mathrm{e,CEI}} = T_{\mathrm{i,CEI}}$ in the boundary condition and $\chi_{\perp,\mathrm{i}}/\chi_{\perp,\mathrm{e}} = 2$ in the pedestal. $P^{\mathrm{sim}}_{\mathrm{e,in,edge}} = 75\,\mathrm{kW}$, $P^{\mathrm{sim}}_{\mathrm{i,in,edge}} = 135\,\mathrm{kW}$, about 64% of total input power is carried by ions at the CEI. In the experiment, more heat in the ion channel is due to NBI. The input power $P^{\mathrm{sim}}_{\mathrm{in,edge}}$ found by the simulation code is roughly half of the experimental heating power crossing the CEI : $P^{\mathrm{exp}}_{\mathrm{in,edge}} = P^{\mathrm{exp}}_{\mathrm{in}} - P^{\mathrm{exp}}_{\mathrm{rad,core}} = 430\,\mathrm{kW}$ (Table 3.3).

The 2D maps of electron density and temperature in the simulation domain are shown in Figure 3.33. The upstream and downstream profiles, including density, temperature, and carbon concentration demonstrate a good match between experiment and simulation, as shown in Figures 3.30, 3.31, and 3.34.

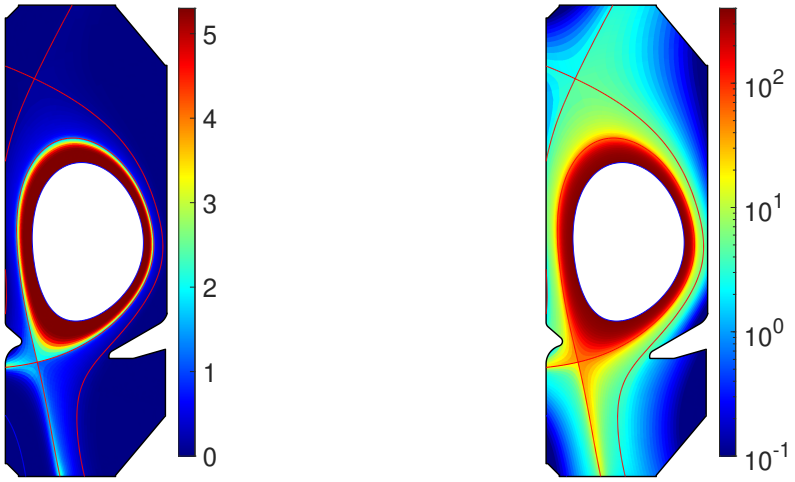

(a) $n_{\mathrm{e}}[10^{19}\mathrm{m}^{-3}]$ (b) $T_{\mathrm{e}}[\mathrm{eV}]$

FIGURE 3.33. : 2D maps of TCV basic simulation case (matched with experiment) for electron density, electron temperature.

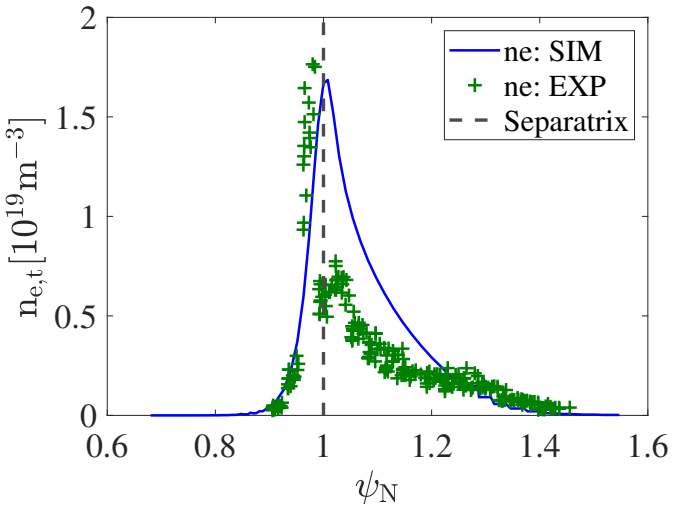

(a) The profiles of electron density at the outer target.

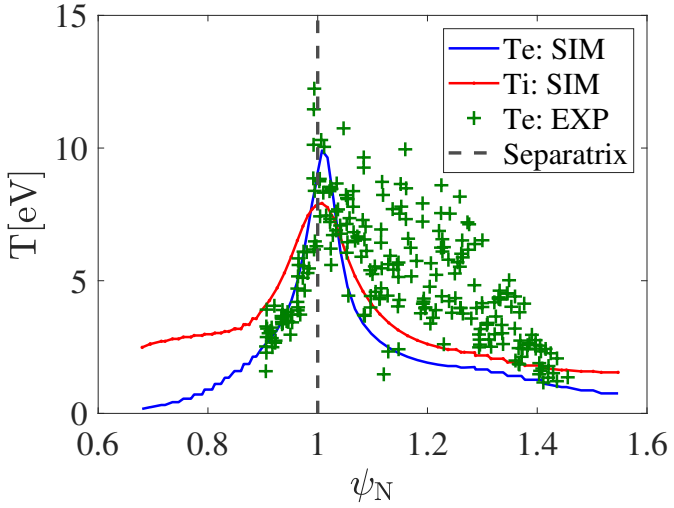

(b) The profiles of electron and ion temperature at the outer target.

FIGURE 3.34. : The density and temperature profiles at the outer target, comparing between the experimental measurements (green plus sign, data from LPs [45, 97]) and the SOLEDGE3X-EIRENE simulation (blue and red curves). The dashed line represents the position of separatrix.

We now compare the neutral pressure observed in the experiment with that predicted by the simulation. In the experiment, the neutral pressure was measured using Baratron gauges, which are connected to the two ports on the wall (near the OMP and at the target, as shown in Figure 3.28) via long tubes to shield the gauges from the magnetic field [55]. The neutral pressure drops quickly in the conducting tube between the Baratron gauge and the port due to conversion of energetic atomic neutrals to thermal molecules. It is difficult to directly compare the data from the experiment and simulation, as the simulation only covers the prediction of neutral pressure up to the wall. To relate the measurements from the gauges to the data from the port, we

can use a 0D-model presented in Section 2.7.2. Table 3.4 shows the prediction of line averaged neutral pressure at the port $P^{\mathrm{sim}}_{\mathrm{neu,port}}$, prediction of neutral pressure at the gauge $P^{\mathrm{sim}}_{\mathrm{neu,gauge}}$ (obtained after the correction with 0D-model, assuming $T_{\mathrm{wall}} = 300\,\mathrm{K}$ in the Baratron tube), and experimental neutral pressure measurements at the gauge $P^{\mathrm{exp}}_{\mathrm{neu,gauge}}$. The $P^{\mathrm{exp}}_{\mathrm{neu,gauge}}$ at the target is in the range of 34–36 mPa (the data at t = 1.07–1.1 s, considering a relatively slow response time of the entire Baratron system from 70 to 100 ms [55]). The $P^{\mathrm{exp}}_{\mathrm{neu,gauge}}$ near the OMP is below the noise level and difficult to measure. This is compatible with the very low pressure (0.7 mPa) that the simulation indicates. Overall, the agreement between the experiment and simulation is good.

Position	$P^{\mathrm{sim}}_{\mathrm{neu,port}}$ [mPa]	$P^{\mathrm{sim}}_{\mathrm{neu,gauge}}$ [mPa]	$P^{\mathrm{exp}}_{\mathrm{neu,gauge}}$ [mPa]
OMP	11.6	0.7	< 10
Target	364.0	36.8	34–36

TABLE 3.4. : The neutral pressure from simulation values and experimental measurements.

The heat flux on the entire wall was analyzed as the simulation enables the estimation of plasma conditions in the far scrape-off layer and up to the first wall (see Figure 3.35). The analysis revealed a relatively high heat flux near the inner and outer strike points and at the inner baffle tip, while it was negligible at other positions. In addition, the imbalance between inner and outer targets was noticeable, with the inner target experiencing a higher parallel heat flux by a factor of 2–3.

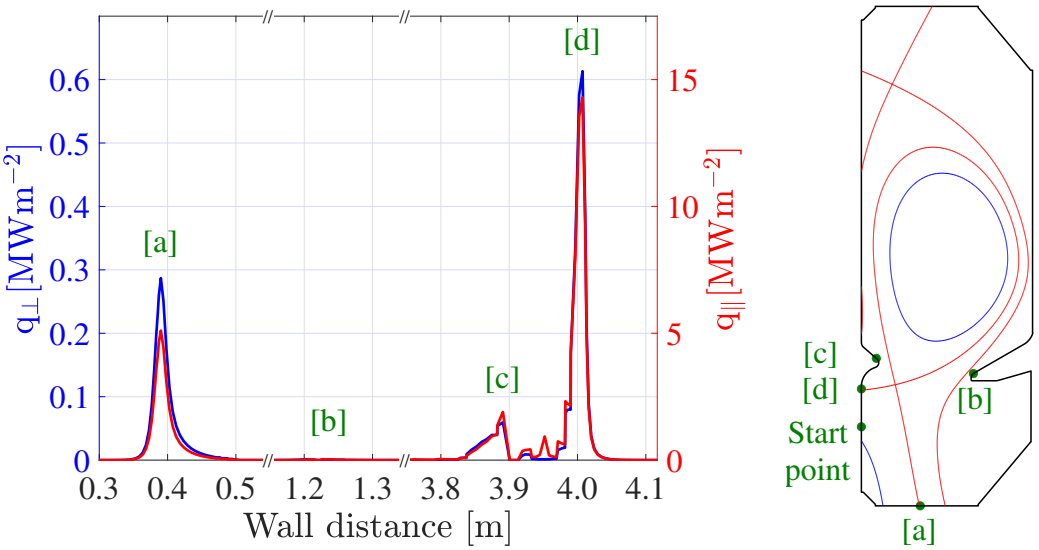

FIGURE 3.35. : The perpendicular and parallel heat flux on the wall as a function of distance, which is integrated counterclockwise along the wall, departs from the start point (figure on the right). Peak heat fluxes occur : [a] near the outer strike point, [c] near the inner baffle tip, and [d] near the inner strike point. The perpendicular and parallel heat flux from 0.5 m to 3.8 m (including [b] near the outer baffle tip) is negligible.

3.2.2.3. Upstream separatrix density scan

The initial simulation setups showed good agreement between the simulations and the measurements. We now investigate the role of the OMP separatrix density on the divertor state. We scan the separatrix density from $n_{\mathrm{e,sep}} = 1.0 \times 10^{19}\,\mathrm{m}^{-3}$ to $3.0 \times 10^{19}\,\mathrm{m}^{-3}$, while employing a feedback-controlled deuterium gas puff rate in the simulations. The input power ($P^{\mathrm{sim}}_{\mathrm{e,in,edge}} = 75\,\mathrm{kW}$, $P^{\mathrm{sim}}_{\mathrm{i,in,edge}} = 135\,\mathrm{kW}$), diffusion coefficients, and other setups were kept unchanged.

Figure 3.36 shows the evolution of multiple parameters. Here, T_{sep} is the upstream separatrix temperature. $\langle n_{\mathrm{C,total}} \rangle_{\mathrm{div}}$ is the divertor-averaged total carbon density (sum of all charge states : $\mathrm{C}^0 \rightarrow \mathrm{C}^{6+}$, averaged along the lower part of outer divertor leg, blue line in Figure 3.28). $\hat{T}_{\mathrm{e,t}}$, $\hat{n}_{\mathrm{e,t}}$, $\hat{\Gamma}_{\parallel,\mathrm{i,t}}$ and $\hat{q}_{\parallel,\mathrm{t}}$ are the peak electron temperature, density, parallel ion flux, and parallel heat flux at the targets respectively. $P^{\mathrm{sim}}_{\mathrm{rad,edge}}$ is the total radiated power in the simulation domain. $P^{\mathrm{sim}}_{\mathrm{in,edge}}$ is the total input power entering the simulation domain. We use the subscript 'it' and 'ot' to indicate the inner and outer targets, respectively. As $n_{\mathrm{e,sep}}$ increases, we can observe that :

- The amount of deuterium that needs to be supplied through gas puff increases approximately linearly with the $n_{\mathrm{e,sep}}$.
- The upstream separatrix electron and ion temperatures, $T_{\mathrm{e,sep}}$ and $T_{\mathrm{i,sep}}$, decrease. The difference in ion and electron temperatures at the separatrix reduces due to the increased collisionality.

- The divertor-averaged total carbon density $\langle n_{\mathrm{C,total}} \rangle_{\mathrm{div}}$ increases due to a higher level of carbon sputtered from the graphite wall tiles.
- The peak particle flux rolls over only at the outer target in the range of $n_{\mathrm{e,sep}}$ investigated. With a peak target temperature lower than 2 eV at the outer target, a 90% decrease in the deposited heat flux, and momentum loss $f_{\mathrm{mom,loss}} = 1 - P_{\mathrm{total,target}} / P_{\mathrm{total,upstream}} > 0.85$, the outer divertor has reached the detached regime. To investigate the properties of detachment, the following analyses will mainly focus on the outer divertor leg. The rollover of particle flux integrated over the outer target is typically observed (along with peak particle flux rollover) to identify detachment in TCV experiments, while in the simulations, it does not exhibit a rollover within the range of $n_{\mathrm{e,sep}}$ studied. This may be due to the absence of the *Molecular Activated Recombination* (MAR) in the simulations, which were shown in [98] to play a significant role in TCV.
- Higher fraction of the power is radiated with a fixed input power $P^{\mathrm{sim}}_{\mathrm{in,edge}}$.

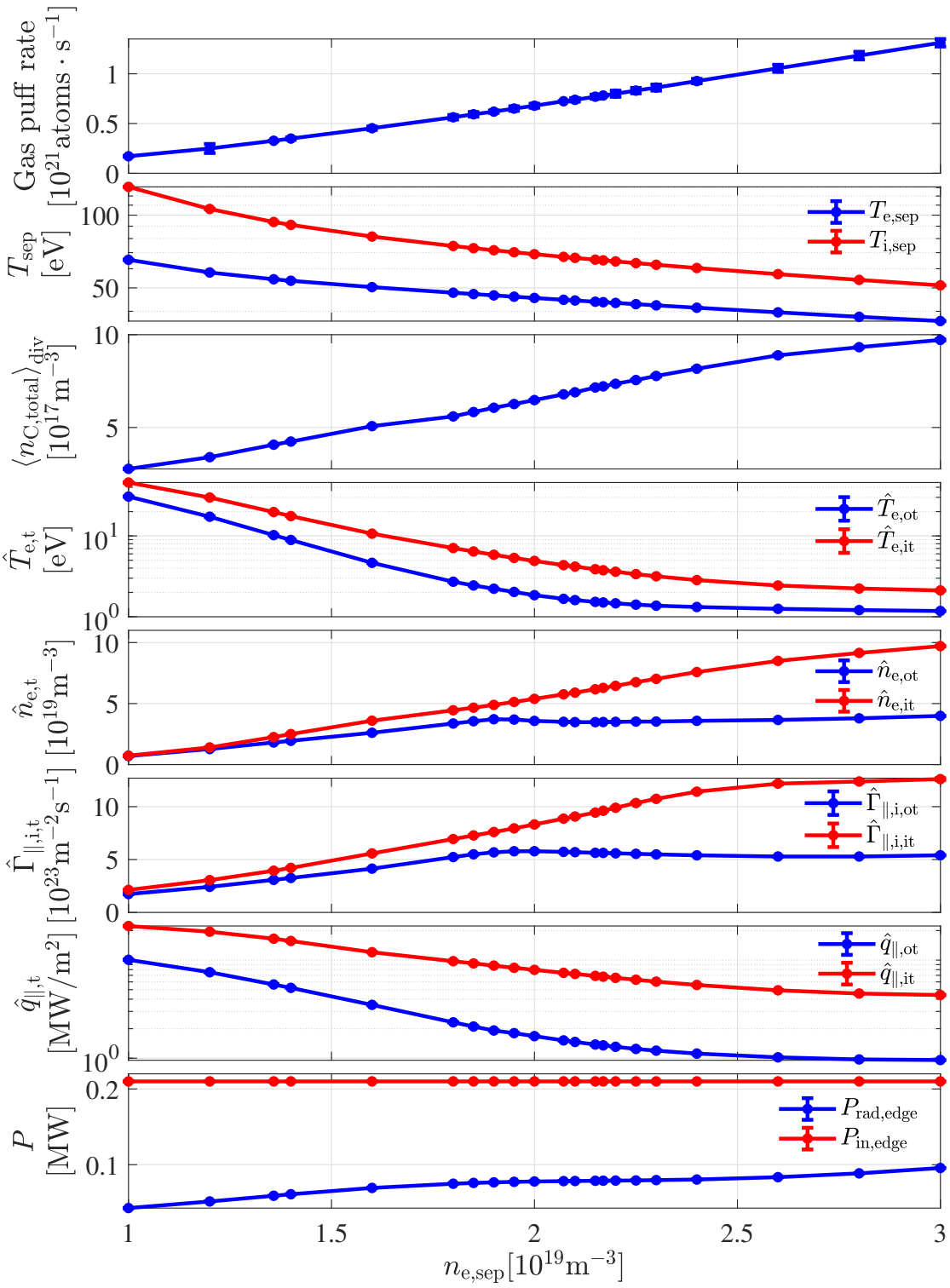

FIGURE 3.36. : Evolution of several simulated fields as a function of $n_{e,sep}$ in steady-state TCV simulations.

3.2.3. Evolution of radiation front

The energy losses by the plasma before arriving at the targets are either from neutral interactions or impurity radiation. So it is essential to look at what happens to the radiated power.

In the WEST case, with high $n_{e,sep}$, a significant increase in radiation level near the divertor is predicted by the SOLEDGE3X-EIRENE simulation, as shown in Figure 3.37. It is also observed that the radiation increases very fast : initially, it is mainly distributed near the strike points region on the divertor, then increasing plasma density by ramping the gas puff rate to a higher value, the maximum radiation region moves up off the divertor target, and two radiation centers on the inner and outer leg merged together near X-point in the detached regime.

In the TCV case, the evolution of radiation regions can also be interesting for the detachment study and can be compared with WEST, as shown in Figure 3.38. With increasing $n_{e,sep}$, the total radiated power increases gradually : initially, it is mainly distributed near the strike points region at the target, then the radiation tends to increase along the separatrix from strike-points to X-point, and in the region near the inner baffle. When $n_{e,sep}$ goes above a certain threshold ($\approx 1.80 \times 10^{19}$ m^{-3}), the radiation at the outer strike point starts to reduce, and the peak radiation region moves up along the separatrix, detaching from the outer target. However, different from the WEST case, the merger of the inner and outer leg radiation center is not obvious in TCV. In the outer divertor area (cyan polygon in Figure 3.39), the radiated power from carbon remains approximately constant (16–19 kW), with the majority being radiated by CIII ($\approx 41\%$), across the density scan with constant SOL input power.

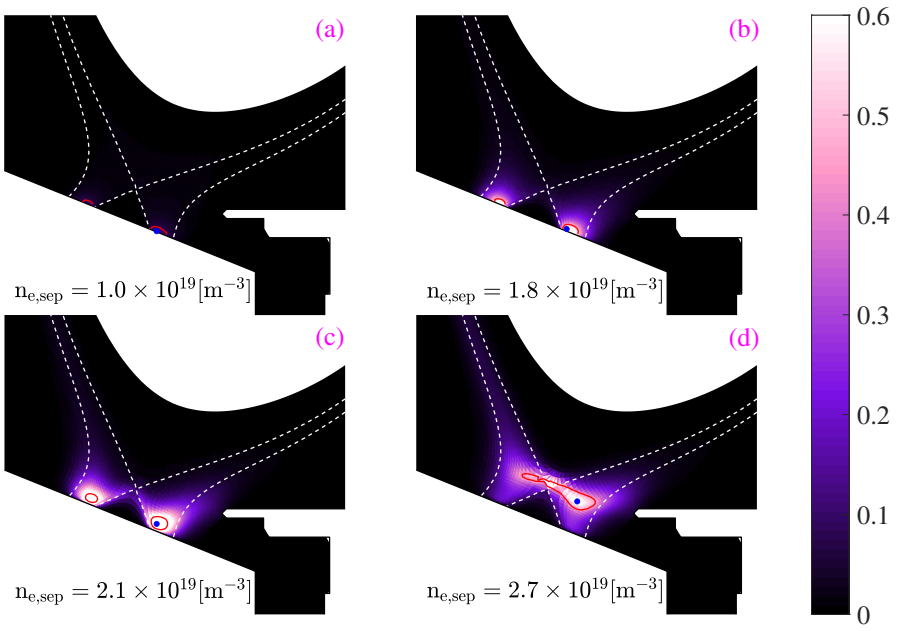

FIGURE 3.37. : Radiation power [MW/m^3] in WEST case with closed baffle. With increasing upstream $n_{e,sep}$, the main radiation regions surrounded by the radiation fronts (composed of the points that have less than 30% reduced radiation compared to the maximum radiation in the simulation domain, marked by red curve) move up off the divertor target, and two radiation centers on the inner and outer leg merged together near the X-point in the deeply detached regime. The blue dot represents the position where it has the maximum radiation. The white dashed curves represent the separatrix.

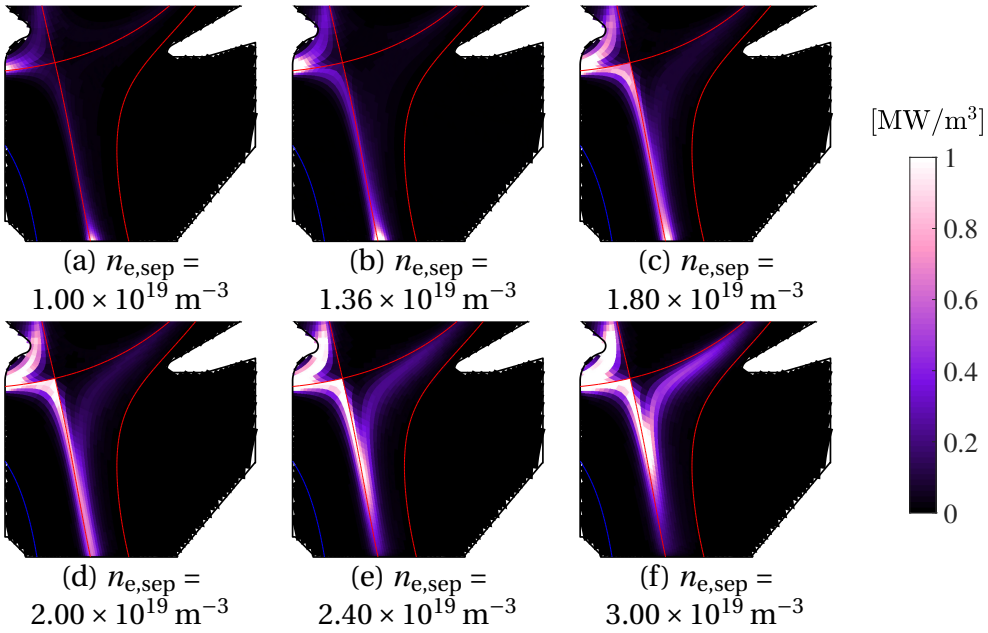

FIGURE 3.38. : 2D maps of P_{rad}, from (a) to (f) with increasing $n_{e,sep}$. In order to highlight the radiation front region, the upper limit of color bar is set as 1 MW/m^3, even if the peak value of radiation can be 10 MW/m^3, occur at the inner target, in some cases.

To evaluate the movement of the peak radiation region, there are two commonly employed options : identifying the radiation center, which corresponds to the position that shows the maximum radiation, or the radiation front, which encloses an area that covers most of the radiation. Since the location of maximum radiation will shift closer to the X-point shortly after achieving divertor detachment, identifying the radiation front becomes a more feasible option. As shown in Figure 3.39, we define the radiation front (marked by red cross) as the lowermost point of a region (enclosed by green curve) inside which the P_{rad} of each point is higher than 70% of maximum radiation in the analyzed spatial domain (marked by cyan polygon). The radiation front height $H_{rad,front}$ is used to describe the distance between the radiation front and the target. It is here defined as the vertical distance between the front and the outer target. For comparison between different devices and magnetic configurations, a normalized radiation front height $H^N_{rad,front}$ is the preferred choice, which is defined as the ratio between radiation front height $H_{rad,front}$ and X-point height $H_{X\text{-point}}$. In the case of an approximately horizontal divertor leg, the heights are replaced by the distances from the target along the leg. Therefore, $H^N_{rad,front} = 1$ corresponds to the radiation front reaching the X-point height.

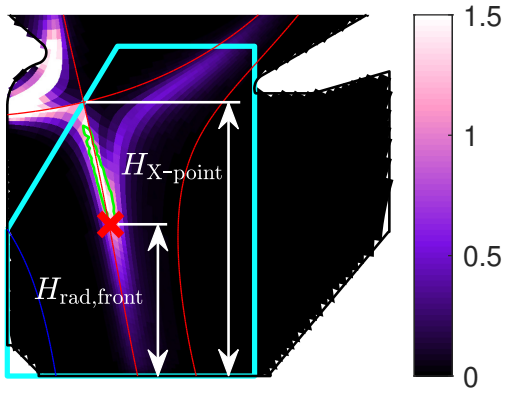

FIGURE 3.39. : 2D map of P_{rad} [MW/m^3], the same case as (f) in Figure 3.38. For the outer divertor, the radiation front (marked by red cross) is defined as the lowermost point of a region (enclosed by green curve) inside which the P_{rad} of each point is higher than 70% of maximum radiation in the analyzed spatial domain (marked by cyan polygon). The height of the radiation front $H_{\text{rad,front}}$ and the height of X-point $H_{\text{X-point}}$ are defined as the vertical distance between the outer target and the radiation front or X-point, respectively.

We now evaluate the evolution of radiation front in WEST and TCV simulations (Section 3.2.1.2 and 3.2.2, both with no drifts). As shown in Figure 3.40, one can observe that the normalized radiation front height roughly increases with $n_{\text{e,sep}}$ after its value surpasses a certain threshold. In WEST, the threshold of radiation front detachment ($n_{\text{e,sep}} \approx 1.90 \times 10^{19}\,\text{m}^{-3}$) is lower than the threshold of particle flux rollover ($n_{\text{e,sep}} \approx 2.10 \times 10^{19}\,\text{m}^{-3}$). In TCV, the threshold of radiation front detachment ($n_{\text{e,sep}} \approx 1.80 \times 10^{19}\,\text{m}^{-3}$) is also lower than the threshold of particle flux rollover ($n_{\text{e,sep}} \approx 1.95 \times 10^{19}\,\text{m}^{-3}$). Generally, the slightly lower $n_{\text{e,sep}}$ threshold of radiation front detachment compared with that of particle flux rollover is observed in both devices, indicating that the radiation front detachment can be used as a herald indicator of the rollover of particle flux in detachment control.

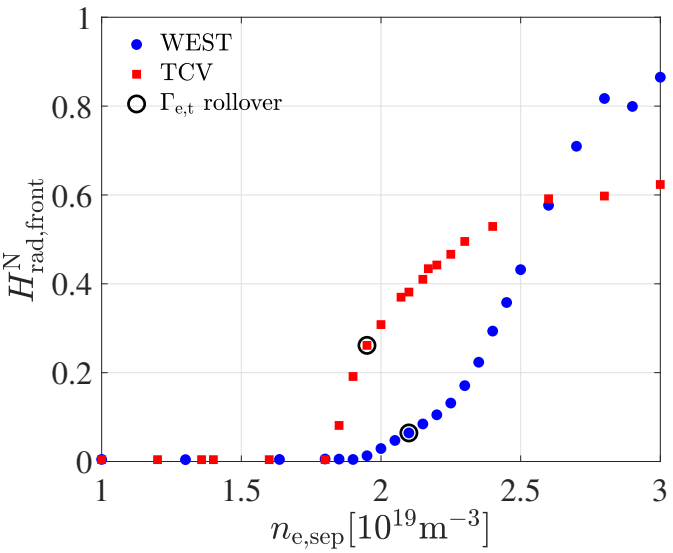

FIGURE 3.40. : Evolution of normalized radiation front height as a function of $n_{e,sep}$ in WEST and TCV. The black circle marks the point when the rollover of $\Gamma_{e,t}$ happens in each case.

3.3. Summary of simulation cases

The above sections only discussed part of the simulation cases. Table 3.5 shows a summary of all the cases that can be discussed in this thesis.

Reference discharge	#54903 at 8 s	#56420 at 7.3 s	#54896 at 8 s	#70690 at 1 s
Devise	WEST	WEST	WEST	TCV
Confinement mode	L-mode	L-mode	L-mode	H-mode
Magnetic configuration	LSN, USN	LSN	USN	LSN
Magnetic field	Forward	Forward, Reversed	Reversed	Forward
$P^{\mathrm{exp}}_{\mathrm{in,edge}}$ [MW]	0.54	0.486	0.99	0.25
$P^{\mathrm{sim}}_{\mathrm{in,edge}}$ [MW]	0.45, 0.5, 2	0.45, 2	0.92	0.21, 0.5
Drifts	NO	YES, NO	YES, NO	NO
Ballooning	NO	YES, NO	YES, NO	YES, NO
Profile feedback	YES, NO	YES, NO	YES, NO	YES, NO
$\chi_{\perp,\mathrm{i}}/\chi_{\perp,\mathrm{e}}$ inside separatrix	1	1	1	1, 2
Diff enhance in divertor	NO	NO	NO	YES, NO
R_{wall}	0.99, 1	0.99, 1	1	0.99
Pump	YES	YES	YES	NO
Impurity	none	none, O	none	C, CN
Gas puff compositions	D	D	D	D, N, DN
Gas puff position	PFR	TOP, OMP, OSP, PFR, ISP	OMP	OSP, PFR
Divertor geometry	Closed baffle, Leak baffle, No baffle	Closed baffle	No baffle	Long baffle, Short baffle
Density scan	YES	YES	NO	YES

TABLE 3.5. : The summary of all the cases and their setups discussed in this thesis.

4. Impact of wall geometry, particle, and energy sources on detachment

Sommaire

4.1. Impact of divertor closure

Wall geometry in particular baffle configuration can significantly influence detachment properties due to their effect on plasma-neutrals interactions in the divertor region. A higher neutral pressure can be achieved in a baffled divertor because fewer neutral particles can escape from it. The plasma-neutrals interaction increases with higher neutral pressure, leading to more momentum and power loss for the plasma in the baffled divertor [99]. Recent numerical and experimental studies, particularly on TCV, show that both inner and outer baffles have local effects on trapping neutral particles, but the global effect of the outer baffle is quantitatively stronger than that of the inner baffle [88]. However, it is extremely difficult to generalize these results obtained on a specific device since the wall and magnetic geometry vary significantly from

one device to another. In this regard, additional results from other devices are very helpful to progress toward a deeper comprehension of the impact of such geometries on plasma-neutrals interaction and consequently on plasma behavior.

For studying the impact of the wall geometries on divertor behavior, several studies have already been performed in other tokamak devices, for example, JET [100-102], JT-60U [103], ASDEX-Upgrade [104], DIII-D [105-110], EAST [111, 112], TCV [84, 85, 88]. One common observation is that better divertor closure can increase the neutral pressure in the divertor and facilitate access to colder divertor, and make plasma detach at lower density threshold. It is expected that the degree of divertor closure can influence the transport of neutral particles inside the main chamber, which affects the detachment onset. Knowing the exact impacts of divertor closure and understanding the physical processes behind it will be helpful for the study and control of the divertor detachment.

4.1.1. Leakage under divertor baffle in WEST

In recent experiment campaign C5 of WEST, the space between the divertor baffle and the vacuum vessel has been sealed. It is expected that this modification in baffle configuration improves the divertor pumping capability because of higher neutral pressure in the region under the baffle and close to the pump, allowing for better control of the detached plasma regime. The sealed leak under the baffle can influence the divertor closure, which refers to the degree of neutral particles escaping from the divertor [113]. Here, we discuss the impact of leakage based on considering several sizes of the leakage in the numerical investigation and then comparing with a few available experimental data to get more insight into the particle recirculation inside WEST.

Starting from the basic case (#54903 in Section 3.2.1.2), different baffle configurations from closed to open (baffle removed) are applied to make the simulation to evaluate the effects of baffle leakage, as shown in Figure 4.1. The leakage problem in WEST was due to the toroidal discontinuity of divertor baffle. Here, we put the leakage position at the bottom of the baffle to facilitate the 2D simulation, the leakage level before the WEST experimental campaign C5 is supposed to be close to or smaller than that of the baffle with small leakage, Figure 4.1b. Among the five baffle configurations, four of them are just different at the bottom part of the baffle but have the same top part in order to exclude the possible influence of recycling on the baffle [84], the remaining one removed the baffle completely. In addition, the USN case with the magnetic configuration symmetrical to the LSN one along the mid-plane shown in Figure 4.2b has been considered because it is easier to investigate the effects of open and closed baffle through the comparison between LSN closed baffle discharge and USN no baffle discharge when carrying out the experiments. For this purpose, the USN case has the same wall geometry as LSN closed baffle case, with the gas puff position inside the PFR, but the pump remained at the bottom part as it can not be changed in WEST.

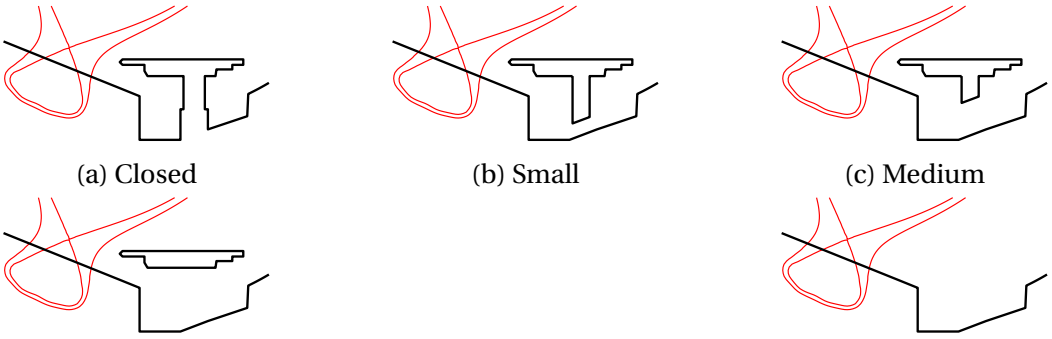

(a) Closed (b) Small (c) Medium

(d) Large (e) Open

FIGURE 4.1. : Baffle configurations considered in the SOLEDGE3X-EIRENE simulations : (a) the case with closed baffle, (b)the case with small leak under the baffle, (c) the case with medium leak, (d) the case with big leak and (e) the case with the baffle removed, in other words, open baffle.

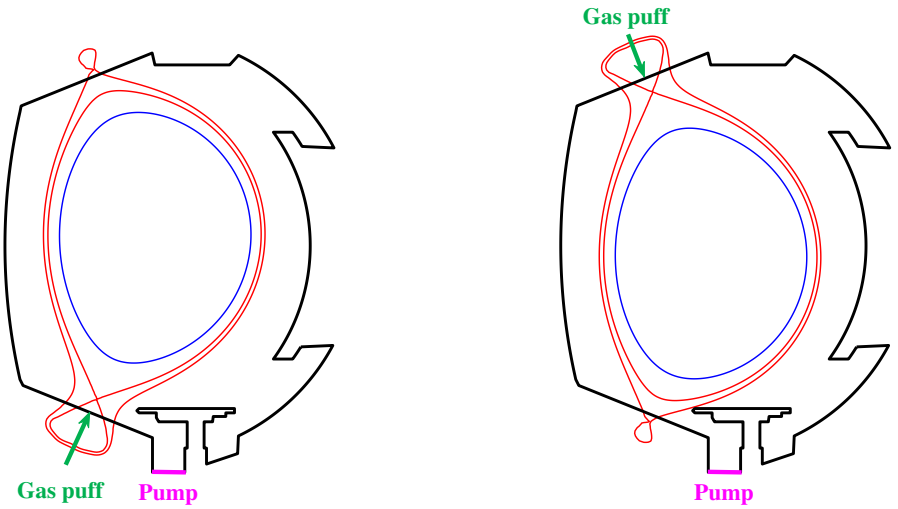

(a) LSN (b) USN

FIGURE 4.2. : (a) WEST LSN magnetic configuration comes from the experiment discharge #54903 at $t = 8\,s$, with wall geometry in the poloidal cross-section. (b) WEST USN magnetic configuration which is symmetrical with LSN magnetic configuration along the mid-plane, with the same wall geometry in the poloidal cross-section. In both sub-figures, the black solid curve represents the chamber wall, the red solid curves represent the separatrix, the blue solid curve represents the core boundary, the green arrow represents the gas puff position, the magenta line represents the pump position.

The meshes built based on different configurations (different baffle configurations, LSN and USN magnetic configurations) are not exactly the same and may have a slight

difference in partial cell size. Thus, the one-dimensional interpolation method needs to be used if we want to apply the non-constant radial transport coefficient in each configuration. However, the interpolation procedure can introduce small difference between the radial transport coefficient profiles that are finally applied in each case. To make a fair comparison between all the cases, we apply the WEST classic L-mode transport coefficient setups $D_\perp = 0.3$, $\chi_{\perp,e} = \chi_{\perp,i} = 1$ for the later simulations, as the mean value of non-constant radial transport coefficient $D_\perp$ is around 0.3, the classic value can be thought as a good choice. In this situation, we also change the input power to 0.45 MW, to keep the target profile of the baffle closed case has a good match with the experimental one (not shown here). These procedures can at least keep the main conclusion for the impact of leakage consistent with the ideal situation. From the latter comparison of the simulation results in Section 4.1.1.1, we understand that the influence of different pump positions relative to the outer strike point is small, and the USN no baffle case shows characteristics consistent with LSN no baffle case. So it is acceptable to compare LSN closed baffle discharge and USN no baffle discharge directly, and provides support for the subsequent experimental verification in Section 4.1.1.5. The influence of pump position in LSN and USN will be investigated in the future.

In order to make the simulation results cover different plasma states, from the sheath limited regime to the detached regime, the density scan is applied for a low input power case going from $n_{e,sep} = 1.0 \times 10^{19}\,m^{-3}$ to $3.0 \times 10^{19}\,m^{-3}$. As shown in Figure 4.3, the sensitivity of gas puff rate in each case can be obviously influenced by different levels of leakage, leading to a specific range of operational gas puff rate in each case. However, the range of operational upstream $n_{e,sep}$ is overall limited below $3.0 \times 10^{19}\,m^{-3}$, without degrading the core plasma or inducing a radiative collapse. All the cases share the same setups besides the differences in wall geometry and in operational gas puff rate during the upstream $n_{e,sep}$ scan.

In the next sections, we investigate the impact of the level of baffle leakage on plasma behavior and transport of neutrals. We start with the analysis of the detachment threshold.

4.1.1.1. Impact of baffle leakage on plasma behavior

The simulation result is always time-dependent in SOLEDGE3X-EIRENE. Here, we analyze only the final steady-state result. To reduce the effects of the oscillation from Monte Carlo simulation on the final results, we increase the number of particles used in EIRENE to 2×10^5. After the simulation is converged, the data set used for analysis is obtained by sampling 20 data every 1×10^4 iterations (time step dt $\approx 2 \times 10^{-8}$ s) in SOLEDGE3X. The results with error bars in some figures show the average value and the standard deviation of its data set.

In Figure 4.3, we can observe that the range of operational gas puffing rate is the broadest in the case with closed baffle. The more leakage under the baffle, the narrower the range of operational gas puffing rate. In addition, the upstream $n_{e,sep}$ ramped up with increasing gas puff rate in the simulations of each case.

In the 2PM prediction [13], the parallel electron flux at the target $\Gamma_{e,t}$ increases proportionally to $n^2_{e,sep}$ in high-recycling regime. After reaching a threshold value of $n_{e,sep}$, $\Gamma_{e,t}$ rolls over and the plasma steps into the detached regime (Section 2.6.3). The threshold value of $n_{e,sep}$ corresponding to the rollover of $\Gamma_{e,t}$ is called the detachment threshold in upstream $n_{e,sep}$. The detachment threshold can also be expressed with respect to gas puff rate. The profiles of peak $\Gamma_{e,t}$ at the outer target as a function of gas puff rate and as a function of upstream $n_{e,sep}$ are shown in Figure 4.4 and Figure 4.5 respectively. It can be observed that the lower level of baffle leakage, the higher detachment threshold in gas puff rate, but the lower detachment threshold in upstream $n_{e,sep}$. The relative decrease in upstream separatrix density threshold is much smaller than the relative increase in gas puff rate threshold with reducing leakage under the baffle.

Also, the USN open case has a very close detachment threshold compared to the LSN open one, and their peak $\Gamma_{e,t}$ profiles are matched in low upstream $n_{e,sep}$ until the detachment happens. After the rollover of peak $\Gamma_{e,t}$, the USN open case has a higher $\Gamma_{e,t}$ value at the outer target than that of the LSN open case under the same upstream $n_{e,sep}$. The USN open case shows some consistent characteristics with the LSN open case, but the USN one seems to be more open than LSN one after surpassing the detachment threshold.

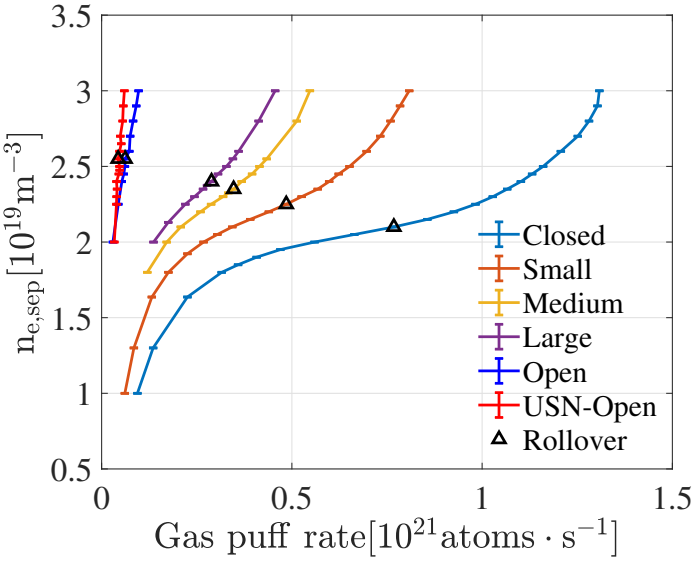

FIGURE 4.3. : Evolution of the upstream separatrix electron density $n_{e,sep}$ as a function of the gas puff rate for the six cases (five LSN cases with baffle from closed to open and one USN case with no baffle in the upper divertor) under consideration. The black triangle on each curve marks the point when the rollover of $\Gamma_{e,t}$ happens as shown in Figure 4.4.

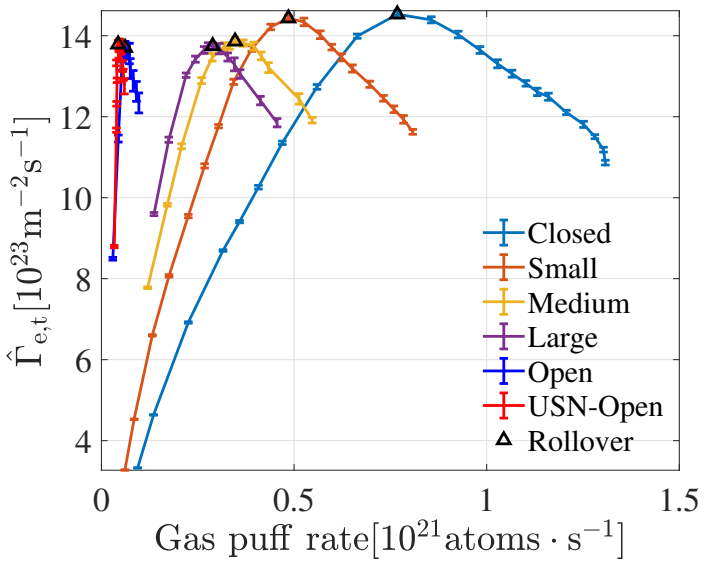

FIGURE 4.4. : Evolution of peak electron particle flux $\Gamma_{e,t}$ at the outer target as a function of gas puff rate for the six cases under consideration, the values corresponding to the rollover have been marked by black triangles.

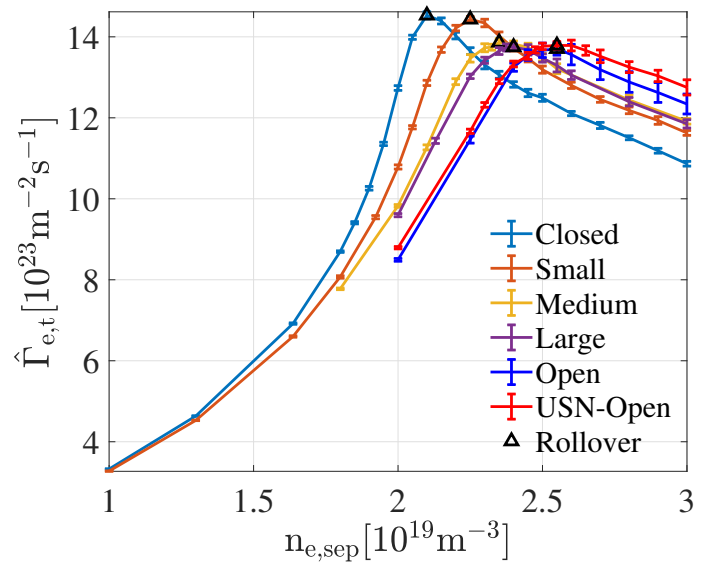

FIGURE 4.5. : Evolution of peak $\Gamma_{e,t}$ at the outer target as a function of upstream $n_{e,sep}$ for the six cases under consideration, the rollover positions have been marked by black triangles.

4.1.1.2. Transport of neutrals

For the cases with leakage under the baffle, some neutrals can escape to the low field side of the main chamber through the leak position under the outer baffle since they are not magnetized. To study more details about the transport of neutrals, we made a

2D plot comparison between two LSN cases, one with closed baffle and another with small leak under the baffle, as shown in Figure 4.6. Two cases have the same gas puff rate = 2.25×10^{20} D atoms s^{-1}. The result shows that in the presence of the leakage, the neutral density in the low field side increases by a factor from 2.5 to 6. When there are more neutral ionization sources nearby the separatrix, the upstream $n_{e,sep}$ will increase accordingly. This explains why the case with leakage has higher upstream $n_{e,sep}$ compared with the closed case under the same gas puff rate. Vice-versa, the case with closed baffle needs to increase the gas puff rate to maintain the same upstream $n_{e,sep}$ as the case with small leak. This is consistent with what we observed in Figure 4.3. In addition, for the case with leakage, overall less neutral penetration in the confined region can be observed (light blue region in Figure 4.6c), but when checking the neutral density profile at the OMP, the neutral density is slightly higher from CEI to the separatrix. Further investigations are necessary for understanding the neutral penetration under the impact of leakage.

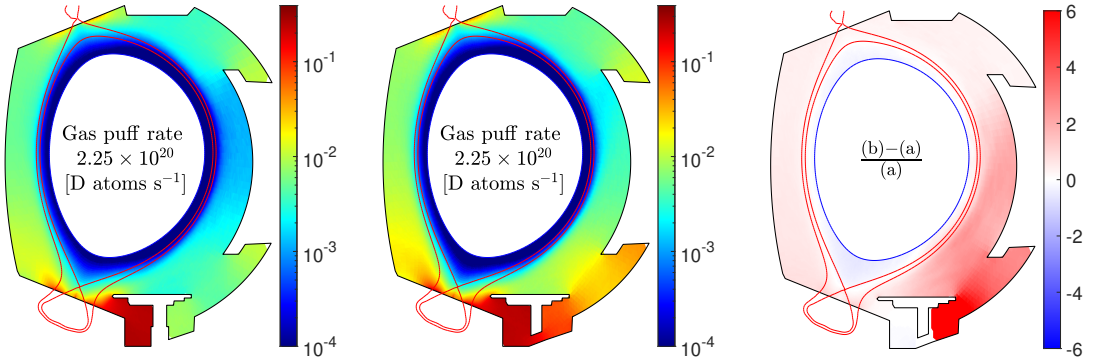

(a) $n_{neu}[10^{19} m^{-3}]$ (b) $n_{neu}[10^{19} m^{-3}]$ (c) Relative change rate

FIGURE 4.6. : (a) The neutral density n_{neu} distribution in the case with closed baffle. (b) The neutral density n_{neu} distribution in the case with small leak. Both (a) and (b) have the same setup parameters include the same gas puff rate = 2.25×10^{20} atoms s^{-1}. (c) The contour of relative change rate in neutral density n_{neu} shows that the leakage under baffle results in the increase of neutral density by a factor of 2.5–6 in the LFS and of 1.5 in the high field side of the main chamber.

The neutral compression ratio is used to analyze the impact of leakage quantitatively, it can be defined as the ratio between the neutral pressure at the outer divertor target and that at the near wall OMP (the point at the OMP and close to the antenna). Here the neutral pressure at the outer divertor target comes from the neutral pressure averaged over the outer target region. A higher neutral compression ratio can be observed in the case with a lower leakage level under the same upstream $n_{e,sep}$, corresponding to a better performance of the divertor region in trapping the neutral particles as shown in Figure 4.7. For the two cases with no baffle (LSN open case and USN open case), the compression ratio changes slightly and is around 50 in the upstream $n_{e,sep}$ range that is covered by the simulation. So we can consider that the compression

ratio is not sensitive to the variation of upstream $n_{e,sep}$ in the two cases. However, in the case with a closed baffle, the ratio is increased by a factor up to 4 and changes between 50 and 200, and the compression ratio improved significantly with increasing upstream $n_{e,sep}$ before the rollover of $\Gamma_{e,t}$. After the rollover, the compression ratio changes slightly, in the end, tends to decrease when the upstream $n_{e,sep}$ becomes very high. The different behaviors of the compression ratio before and after detachment can be explained as being affected by the different heights of the ionization front. When the plasma is attached, more and more neutrals are trapped in the divertor region with increasing upstream plasma density $n_{e,sep}$, and the compression ratio is increased simultaneously. However, when the plasma is detached, the ionization front moves up off toward the X-point. So, in this situation, it is easier for neutral particles to escape the divertor region, and the restricting effect of the baffle is weakened. Also, the recycling on the baffle tip becomes more important in high upstream $n_{e,sep}$. Both aspects can explain the decrease of the compression ratio under very high upstream $n_{e,sep}$.

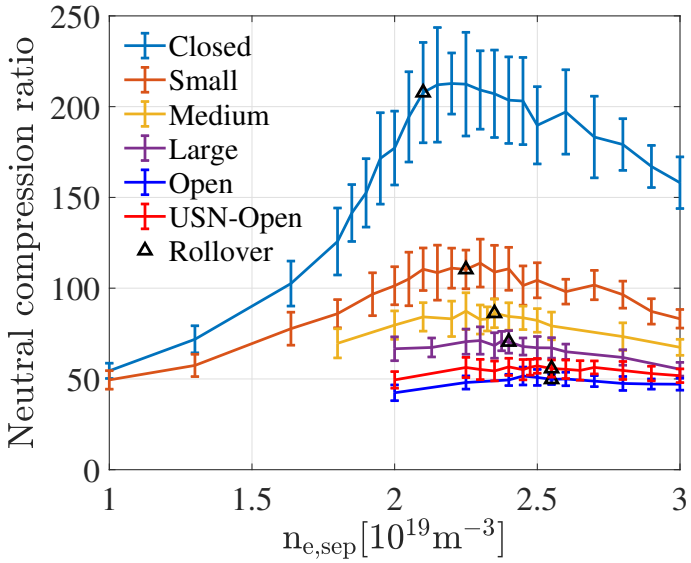

FIGURE 4.7. : The profiles of the neutral compression ratio (ratio between the average neutral pressure at the outer target and the near wall OMP position). The black triangle on each curve marks the point when the rollover of $\Gamma_{e,t}$ happens.

The evolution of peak neutral pressure at the outer target $\hat{P}_{neu,t}$ also shows a rollover characteristic (Figure 4.8) as the peak Γ_e at the outer target (Figure 4.5). The rollover of the peak neutral pressure can be attributed to reduced particle flux and the movement of the ionization front away from the divertor target after $n_{e,sep}$ exceeds a certain threshold. In Figure 4.9a–4.9c, we investigate the change in neutral pressure in the lower divertor region when there is a slight increase in upstream density, $\Delta n_{e,sep} = 2.0 \times 10^{18}\,m^{-3}$, in the cases with a closed baffle. Figure 4.9a represents the result before the rollover of $\hat{P}_{neu,t}$ with an increase of $n_{e,sep}$ by $\Delta n_{e,sep}$ from $1.80 \times 10^{19}\,m^{-3}$. Figure

4.9b represents the result at the rollover of $\hat{P}_{\mathrm{neu,t}}$ with an increase of $n_{\mathrm{e,sep}}$ by $\Delta n_{\mathrm{e,sep}}$ from 2.25×10^{19} m^{-3}. Figure 4.9c represents the result after the rollover of $\hat{P}_{\mathrm{neu,t}}$ with an increase of $n_{\mathrm{e,sep}}$ by $\Delta n_{\mathrm{e,sep}}$ from 2.80×10^{19} m^{-3}. It can be observed that the ionization front is moving up off the target with increasing upstream $n_{\mathrm{e,sep}}$ after detachment happens. At the same time, the neutral pressure in the two small regions near the strike points begins to decrease, but the neutral pressure in the larger region near the ionization front remains increased. So the peak neutral pressure at the outer target can not well represents the overall neutral pressure level in the divertor, which plays an important role in influencing the momentum and power dissipation in SOL. The workaround is to use the neutral pressure averaged over the divertor outer leg region (as shown in Figure 4.10). The evolution of averaged neutral pressure in the divertor outer leg as a function upstream $n_{\mathrm{e,sep}}$ is shown in Figure 4.11, it can be observed that the case with less leakage has an overall higher neutral pressure level in the divertor under the same upstream $n_{\mathrm{e,sep}}$, indicating greater momentum and power dissipation. Therefore, a lower detachment threshold in the upstream $n_{\mathrm{e,sep}}$ is required in the case with less leakage to reach a similar level of momentum and power dissipation.

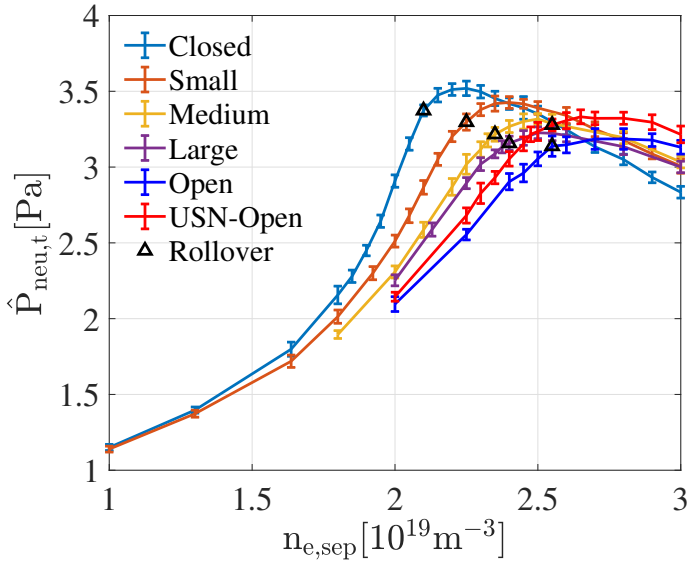

FIGURE 4.8. : Evolution of the peak neutral pressure at the divertor outer target.

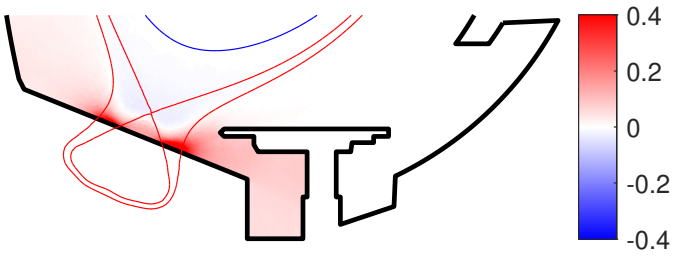

(a) ΔP_{neu}[Pa] due to increased $n_{\mathrm{e,sep}}$ before the rollover of $\hat{P}_{\mathrm{neu,t}}$

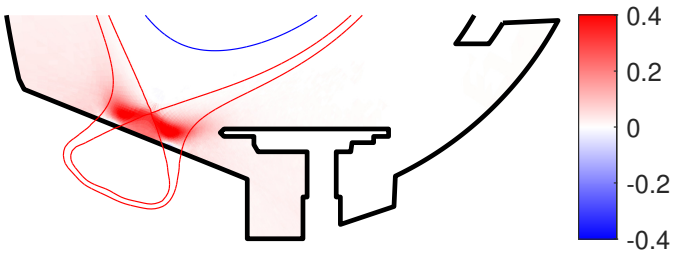

(b) ΔP_{neu}[Pa] due to increased $n_{\mathrm{e,sep}}$ at the rollover of $\hat{P}_{\mathrm{neu,t}}$

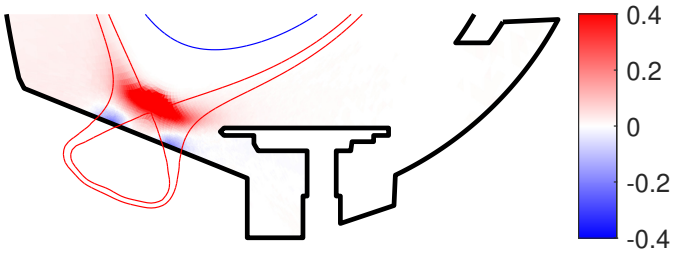

(c) ΔP_{neu}[Pa] due to increased $n_{\mathrm{e,sep}}$ after the rollover of $\hat{P}_{\mathrm{neu,t}}$

FIGURE 4.9. : The 2D maps (a)–(c) represent the change of neutral pressure ΔP_{neu} in the lower divertor when upstream density increases by a little $\Delta n_{\mathrm{e,sep}} = 2.0 \times 10^{18}\,\mathrm{m}^{-3}$ in the case with baffle closed : (a) represents the result before the rollover of peak neutral pressure at the divertor outer target $\hat{P}_{\mathrm{neu,t}}$ with an increase of $n_{\mathrm{e,sep}}$ by $\Delta n_{\mathrm{e,sep}}$ from $1.80 \times 10^{19}\,\mathrm{m}^{-3}$. (b) represents the result at the rollover of $\hat{P}_{\mathrm{neu,t}}$ with an increase of $n_{\mathrm{e,sep}}$ by $\Delta n_{\mathrm{e,sep}}$ from $2.25 \times 10^{19}\,\mathrm{m}^{-3}$. (c) represents the result after the rollover of $\hat{P}_{\mathrm{neu,t}}$ an increase of $n_{\mathrm{e,sep}}$ by $\Delta n_{\mathrm{e,sep}}$ from $2.80 \times 10^{19}\,\mathrm{m}^{-3}$.

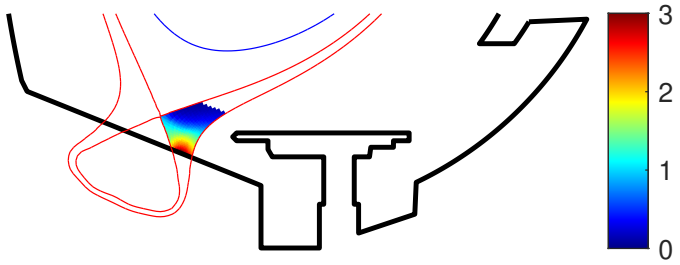

FIGURE 4.10. : The divertor outer leg region (from the outer divertor entrance to the target in the poloidal direction along SOL) that is used to calculate the average neutral pressure. The color bar in this figure represents the neutral pressure [Pa].

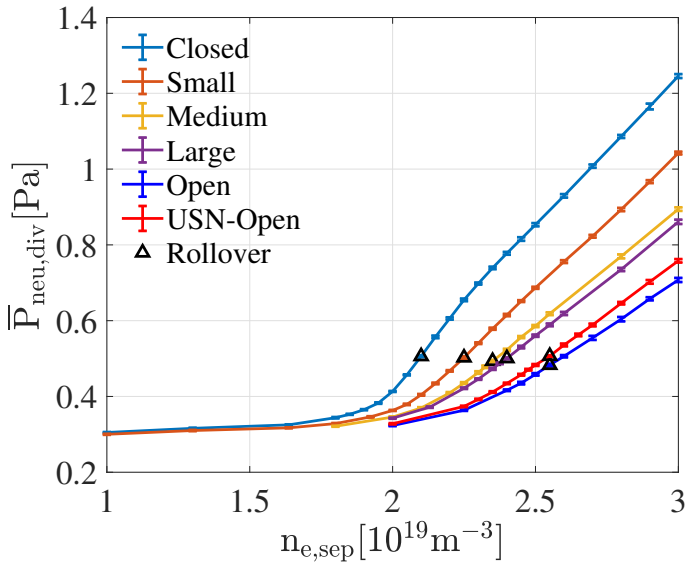

FIGURE 4.11. : Evolution of neutral pressure averaged over the divertor outer leg region as a function of upstream separatrix density. The black triangle on each curve marks the point when the rollover of Γ_e happens.

4.1.1.3. Parameters sensitivity related to the detachment

The average electron temperature inside the radiation front (Section 3.2.3) is evaluated, as shown in Figure 4.12, together with the peak electron temperature at the outer target. We can observe that the average temperature inside the radiation front is around 4.2 eV and the peak electron temperature at the outer target is around 2.2 eV when $\Gamma_{e,t}$ rollover happens in each case. The average electron temperature inside the radiation front does not change much after the radiation front detaches from the target. It means that the region inside the radiation front can maintain a relatively stable temperature of around 4.2 eV after the detachment happens, and the radiation is much more active at this characteristic temperature. In a deep detached case with $n_{e,sep} = 3 \times 10^{19}\,m^{-3}$, the radiation in the entire modeling domain is mainly from the

atom excitation (about 90%), and the volume recombination (about 10%). If we focus on the radiation from the region inside the radiation front, the contribution from the volume recombination will increase to about 24%. The volume recombination radiation mainly happens in the region near the X-point.

We also evaluated the evolution of the vertical distance between the position of the radiator (radiation peak) and the target, as shown in Figure 4.13. The distance equals 0 in the attached regime, and then it ramps up with raised upstream $n_{e,sep}$, and can even be higher than the vertical distance between X-point and target in the end. One interesting thing observed is that the radiator height corresponding to the rollover of $\Gamma_{e,t}$ is always around 1.4 cm.

Simulation results above show that there exist rollover characteristic parameters : the peak electron temperature at the outer target about 2.2 eV, the average electron temperature inside the radiation front around 4.2 eV, the vertical distance between the position of the radiator and target about 1.4 cm, on which the divertor closure has no obvious influence. This peak target temperature result is close to what has been observed in the DIII-D experiment, T_e drops to 2 eV when the rollover in peak J_{sat} happened [114]. This phenomenon is probably due to the factors : the ion-neutral interaction happens at T_e from 2 to 5 eV, and plasma recombination happens at T_e below 1 eV [115].

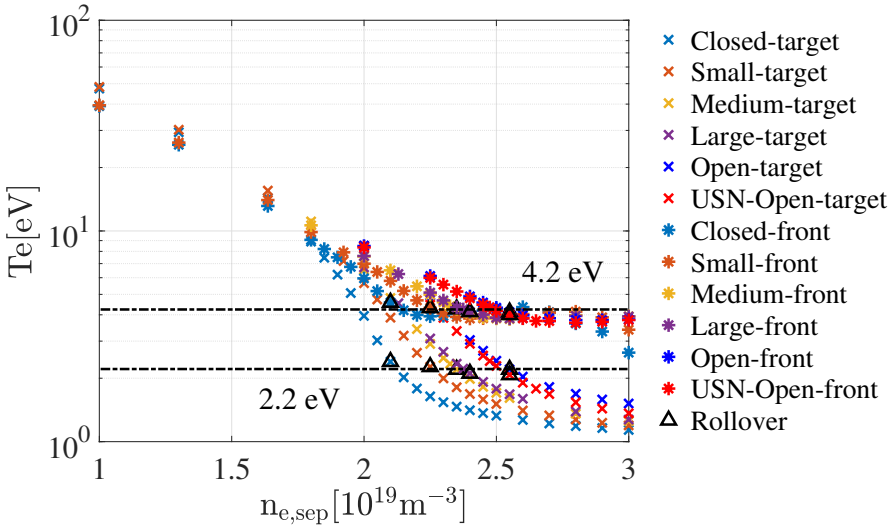

FIGURE 4.12. : The scatter points of the peak electron temperature at the outer target (marked by crosses) and the average electron temperature inside the radiation front (marked by asterisks). The black triangle on each curve marks the point when the rollover of $\Gamma_{e,t}$ happens.

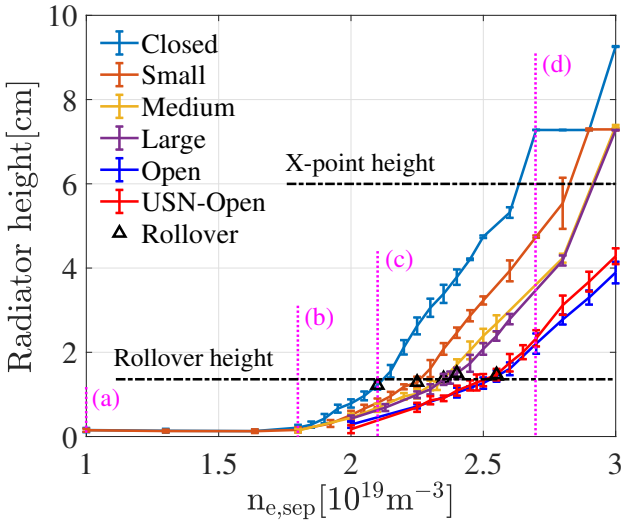

FIGURE 4.13. : The profiles of the vertical distance between the position of radiator (radiation peak) and target. When $\Gamma_{e,t}$ rollover happens in each case (marked by black triangle), the radiator height is always around 1.4 cm. The X-point height is about 6 cm. The 2D radiation maps of four LSN baffled closed cases, marked by magenta columns (a)–(d), are shown in Figure 3.37.

As we discussed in Section 4.1.1.2, the relationship between $n_{e,sep}$ and gas puff rate is indirectly influenced by the baffle configuration, which can have effects on the neutral transport. Thus we can observe a significant difference among the profiles of six cases with different levels of leakage, shown in Figure 4.3. Another obvious difference exists among the profiles of peak electron temperature at the outer target as a function of $n_{e,sep}$ shown in Figure 4.12. The target electron temperature as a downstream parameter is influenced by the upstream parameter $n_{e,sep}$ in SOL. In the process from upstream to target, for the cases with reduced leakage, the momentum and power dissipation of plasma increase due to overall higher neutral pressure near the divertor.

However, the relationship between the radiator height and the target electron temperature seems not significantly influenced by the baffle configurations with different leakage levels, as shown in Figure 4.14, those scatter points are almost distributed around the same curve. This can be explained as the temperature at the target plays a key role in setting the power and momentum dissipation factor due to these processes mainly happening in the region near divertor target. For this reason, the plasma regime is directly related to the target temperature. The levels of leakage, however, play a role in affecting the relationships between the gas fuelling, upstream and target parameters. The insensitivity of radiator height to the leakage when it is as a function of local target temperature can be useful in detachment control. During the real experimental discharge, the slight change of distance between the separatrix and the baffle tip (due to instability issues) can also lead to an obvious change in divertor closure

and presents similar effects like the baffle leakage as we discussed in this section : the transport process between upstream and downstream can be influenced by the leakage. So in the ideal situation, it is preferred to take the parameters near the target (e.g. target temperature) as the input signals when designing the feedback control system, which aims to achieve stable detachment.

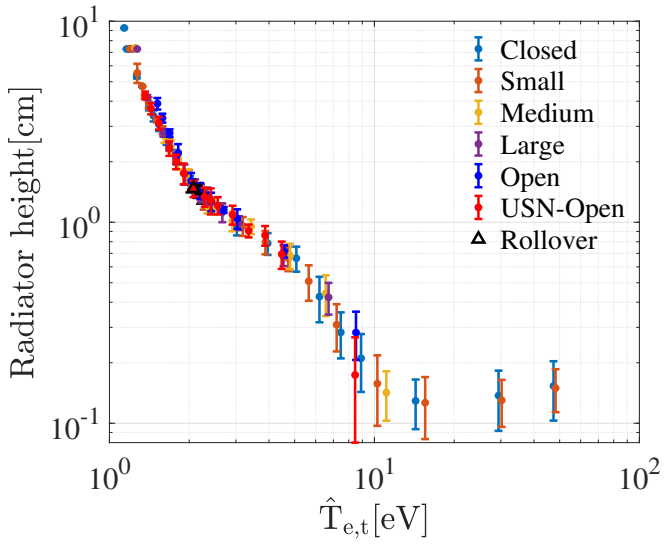

FIGURE 4.14. : The scatter points of the radiator height as a function of peak $T_{e,t}$ at the outer target.

4.1.1.4. Analyze through the extended two-point model

Here we will use the extended 2PM (Section 2.6.1) to reproduce the predictions of WEST simulation (Section 3.2.1.2, the case that takes #54903 as reference, no drift) which is used to discuss the impact of leakage (Section 4.1.1). To keep a good match between the extended 2PM and the SOLEDGE3X-EIRENE simulation, we take the simulation data as the input of the extended 2PM to help us estimate certain parameters in the model. In this way, the impact of leakage observed in the simulation can be consistently presented in the result of the extended 2PM. As the extended 2PM is composed of simple conceptual terms, the terms most associated with causing the impact of leakage in the extended 2PM can be easily identified in a quantitative way. Another reason for taking the simulation data as the input of the extended 2PM is because the simulation data with upstream density scan can give out more information in a more precise way than the experiment.

Input parameters The input parameters of the extended 2PM used here can be divided into constant and non-constant parameters.

The constant parameters include :

- $a = 0.428\,\mathrm{m}$, the minor radius of WEST.

- $R = 2.468\,\mathrm{m}$, the major radius of WEST.
- $L = 31\,\mathrm{m}$, the parallel connection length from upstream to target.
- $q_{95} = 4$, the safety factor.
- $z = 1$, the ratio of electron density and ion density, its value is one as we have no impurity in the cases simulated.
- $M_\mathrm{u} = 0, M_\mathrm{t} = 1$, the Mach number, assumed to be 0 in the upstream and 1 at the target.
- $R_\mathrm{t}/R_\mathrm{u} = 0.774$, the toroidal flux expansion value used in WEST.
- m_f, the fuel ion mass.
- $k_{0\mathrm{e}}$, the electron parallel conductivity coefficient.

The non-constant parameters are calculated based on the upstream and target data provided by the simulation results. An important fact is that the data in SOLEDGE3X-EIRENE can not be applied directly in the extended 2PM since the extended 2PM ignores radial variations of upstream and target parameters, also, it follows the particle balance assumption, but there exists perpendicular particle diffusion into the PFR in the divertor. As a result, the density and particle flux profile at the target show obvious shifting outwards from the separatrix field line and peak value reduced in the experiment and SOLEDGE3X-EIRENE. To make a fair comparison between the extended 2PM and SOLEDGE3X-EIRENE, we use the upstream separatrix density $n_{\mathrm{e,sep}}$ and upstream separatrix ion (electron) temperature $T_{\mathrm{i(e),sep}}$ from simulation data as the upstream density n_u and upstream ion (electron) temperature $T_{\mathrm{i(e),u}}$ in the extended 2PM. The target density n_t and target ion (electron) temperature $T_{\mathrm{i(e),t}}$ in the extended 2PM are obtained from the point corresponding to the peak electron particle flux Γ_e at the outer target in each simulation case. Here the upstream and target data from the simulation are just obtained to evaluate the non-constant parameters in the extended 2PM. When we apply the model to make predictions for WEST, the upstream and target conditions will no longer be used, and this part will be discussed in detail in Section 4.1.1.4. Now we introduce the non-constant parameters :

- SOL input power $P_{\mathrm{in,sol}}$. When detachment happens through raising plasma density or injecting the impurity, the power radiation in the core can become important. This means that even if the total input power is fixed, the $P_{\mathrm{in,sol}}$ can still change under certain conditions. In this section, all the simulation cases have fixed total input power $P^{\mathrm{sim}}_{\mathrm{in,edge}} = 0.449\,\mathrm{MW}$, the $P_{\mathrm{in,sol}}$ is obtained by subtracting the power radiated inside the separatrix from $P^{\mathrm{sim}}_{\mathrm{in,edge}}$. The evolution of $P_{\mathrm{in,sol}}$ as a function of $T_{\mathrm{e,t}}$ is shown in Figure 4.15a.

- Power decay length in SOL upstream λ_q (Section 2.5). This parameter can be evaluated by Equations (4.1) [13]. Here, the λ_n and the λ_T represent the decay length of density and temperature in SOL upstream, we assume $T_e = T_i$ only in the calculation of λ_q. The λ_n and λ_T can be evaluated by the OMP density and temperature profiles from simulation. As the λ_q is fully evaluated based on upstream parameters, we postulate it to be a function of upstream density n_u, the evolution of λ_q is shown in Figure 4.15b.

$$\frac{1}{\lambda_q} = \frac{1}{\lambda_n} + \frac{3}{2\lambda_T} \tag{4.1}$$

- The ratio of ion temperature and electron temperature τ. This parameter can be evaluated by Equations (2.64) as it is influenced by the collision between particles. It can be applied in two positions : the upstream and target, we marked them as τ_u and τ_t. Due to different source locations, the τ_u is postulated to be a function of upstream density n_u and the τ_t is postulated to be a function of target electron temperature $T_{e,t}$. The evolution of τ_u and τ_t is shown in Figure 4.15c and 4.15d.

- Volumetric transfer terms for power and momentum f_{power}, f_{mom}. They are evaluated by Equations (2.56) and (2.57), we use f_{power}, f_{mom} to introduce the effects of radiation, charge exchange, frictional collisions with neutrals, viscous forces and volume recombination in the SOL. As these effects is mainly happened in the region near target because of low target temperature when detachment happens, we postulate them to be a function of target electron temperature $T_{e,t}$, the evolution of f_{power}, f_{mom} is shown in Figure 4.16a and 4.16b.

- Parallel heat conduction factor f_{cond}. The parallel heat transfer in SOL is dominated by conduction, but the heat convection is no more negligible when the temperature gradient between upstream and target become important. The parallel heat conduction factor f_{cond} is defined by Equation (2.58). So the relationship between upstream and target temperature evaluated by parallel heat conduction can be written into Equation (2.59). We can observe that the profiles of f_{cond} show the minimize the presence of the impact of leakage due to different wall geometry when it is as a function of upstream density n_u as shown in Figure 4.16c and 4.16d, so we postulate it to be a function of upstream density n_u.

In the assumptions of the extended 2PM, f_{power}, f_{mom} and f_{cond} are normally close to 1 in the sheath limited regime, but their value is limited under 0.9 as shown in Figure 4.16. This is normal because, on the one hand, we have few cases in the sheath-limited regime as we focus more on detachment; on the other hand, the divertor SOL does not strictly follow the particle balance assumption under the influence of the PFR as we have discussed previously. Here, these parameters are underestimated but can still indirectly reflect the influence of perpendicular particle diffusion into the PFR in the divertor.

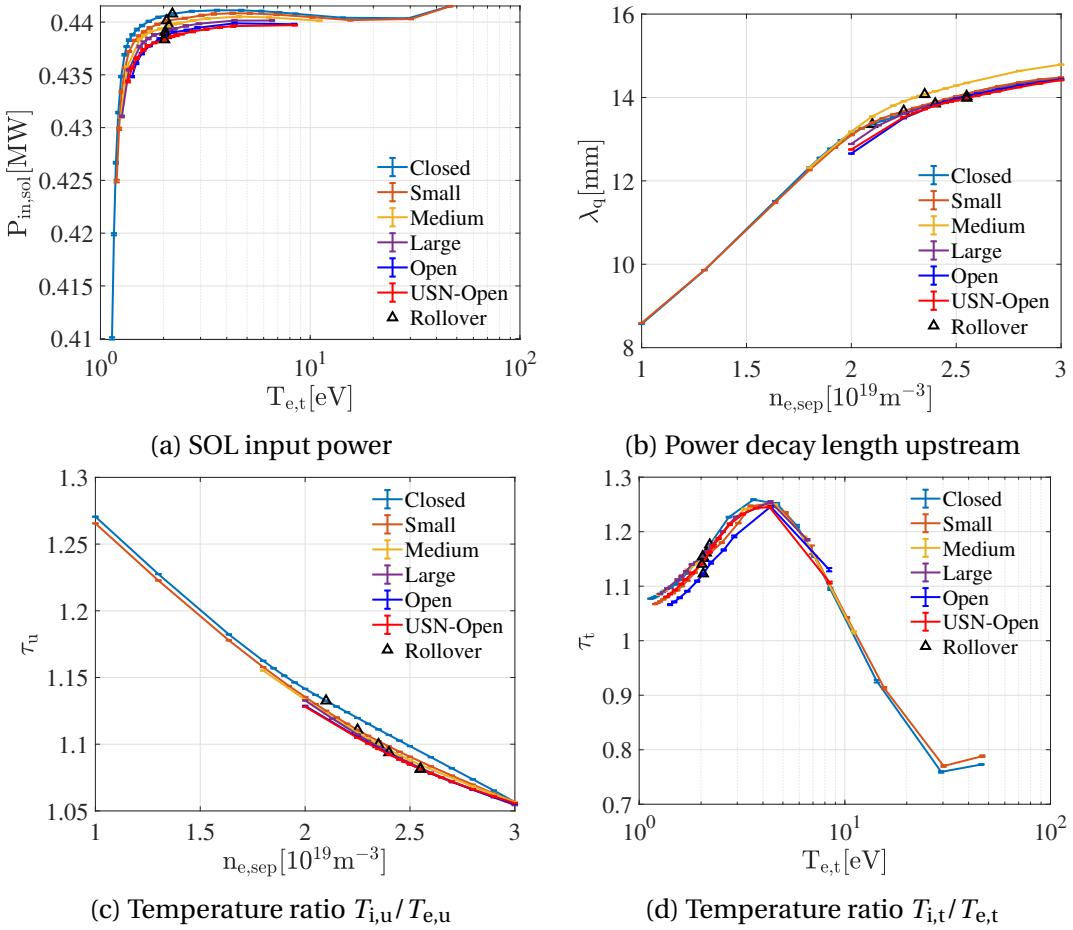

(a) SOL input power

(b) Power decay length upstream

(c) Temperature ratio $T_{i,u}/T_{e,u}$

(d) Temperature ratio $T_{i,t}/T_{e,t}$

FIGURE 4.15. : Evolution of non-constant parameters : (a) SOL input power $P_{in,sol}$, (b) power decay length in SOL upstream λ_q, (c) ratio of ion temperature and electron temperature τ in SOL upstream, (d) ratio of ion temperature and electron temperature τ at the target. They are calculated by the WEST simulation data in SOLEDGE3X-EIRENE with baffle leakage influence under consideration.

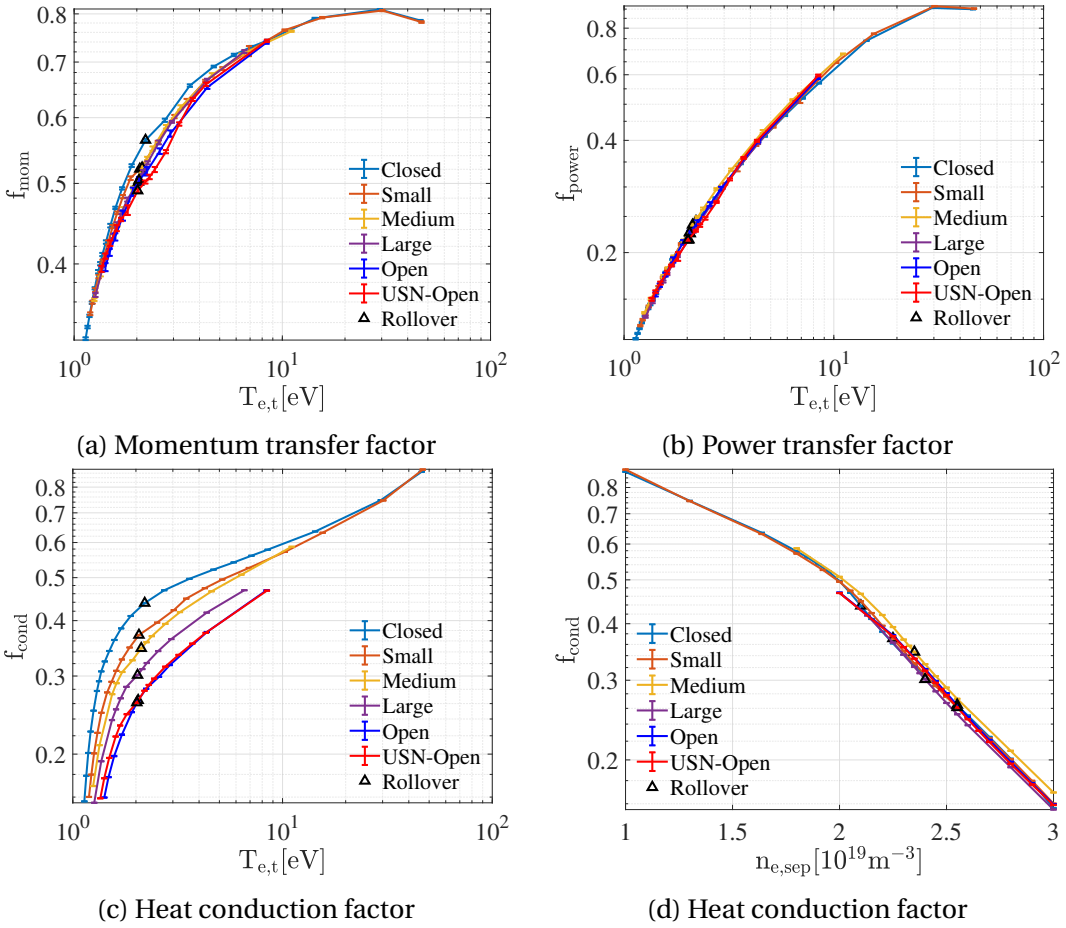

(a) Momentum transfer factor

(b) Power transfer factor

(c) Heat conduction factor

(d) Heat conduction factor

FIGURE 4.16. : Evolution of non-constant parameters : (a) volumetric transfer terms for power f_{power}, (b) volumetric transfer terms for momentum f_{mom}, (c) parallel heat conduction factor f_{cond} as a function of $T_{\text{e,t}}$, and (d) parallel heat conduction factor f_{cond} as a function of n_{u}. They are calculated by the WEST simulation data in SOLEDGE3X-EIRENE with baffle leakage influence under consideration.

Calculation process From the Equations (2.56)–(2.66), we can obtain the following Equations (4.2)–(4.4) [50]. The target temperature $T_{\text{e,t}}$ can be evaluated by Equation (4.3), however except the upstream parameters, there also includes some non-constant parameters like $P_{\text{in,sol}}$, τ_{t}, f_{mom} and f_{power} depend mainly on the divertor conditions. In order to calculate the target temperature $T_{\text{e,t}}$ with given upstream parameters, we can use the iterative method. The process is illustrated in Figure 4.17 : starting with a given value of upstream density, then corresponding λ_{q}, τ_{u} and f_{cond} can be determined through profiles in the Figure 4.15 and 4.16. Next, supposing an initial value of $T_{\text{e,t}}$ (the maximum value of $T_{\text{e,t}}$ that can be analyzed), getting the $P_{\text{in,sol}}$, τ_{t}, f_{mom} and f_{power} according to the initial $T_{\text{e,t}}$, applying all the parameters obtained into Equations (4.5), finding the $T_{\text{e,t}}$ value best match with those parameters by the help of bisection method, comparing the $T_{\text{e,t}}$ with the initial $T_{\text{e,t}}$, if the difference is too big,

using the new $T_{e,t}$ to start next iterations until the difference between two $T_{e,t}$ is small enough.

Based on the $T_{e,t}$ calculated with provided upstream conditions and appropriate non-constant parameters, we can easily evaluate other target parameters like electron density $n_{e,t}$, electron particle flux $\Gamma_{e,t}$, parallel heat flux $q_{\parallel t}$, etc.

$$p_{totu} = 2n_u k\left(1+\frac{\tau_u}{z_u}\right)\left(\frac{7f_{cond}q_{\parallel u}L}{2\kappa_{0e}}+T_{e,t}^{\frac{7}{2}}\right)^{\frac{2}{7}} \tag{4.2}$$

$$T_{e,t} = \left[\frac{8m_f}{e\gamma^2}\right]\left[\frac{q_{\parallel u}^2}{p_{totu}^2}\right]\left[\left(\frac{f_{power}}{f_{mom}}\right)^2\right]\left[\frac{1+\tau_t/z_t}{2}\right]\left[\frac{\left(1+M_t^2\right)^2}{4M_t^2}\right]\left[\left(\frac{R_u}{R_t}\right)^2\right] \tag{4.3}$$

$$\Gamma_{e\parallel t} = \left[\frac{\gamma}{8m_f}\right]\left[\frac{p_{totu}^2}{q_{\parallel u}}\right]\left[\frac{f_{mom}^2}{f_{power}}\right]\left[\frac{2}{1+\tau_t/z_t}\right]\left[\frac{4M_t^2}{\left(1+M_t^2\right)^2}\right]\left[\frac{R_t}{R_u}\right] \tag{4.4}$$

$$f(T_{e,t}) = T_{e,t} - \left[\frac{8m_f}{e\gamma^2}\right]\left[\frac{q_{\parallel u}^2}{p_{totu}^2}\right]\left[\left(\frac{f_{power}}{f_{mom}}\right)^2\right]\left[\frac{1+\tau_t/z_t}{2}\right]\left[\frac{\left(1+M_t^2\right)^2}{4M_t^2}\right]\left[\left(\frac{R_u}{R_t}\right)^2\right] \tag{4.5}$$

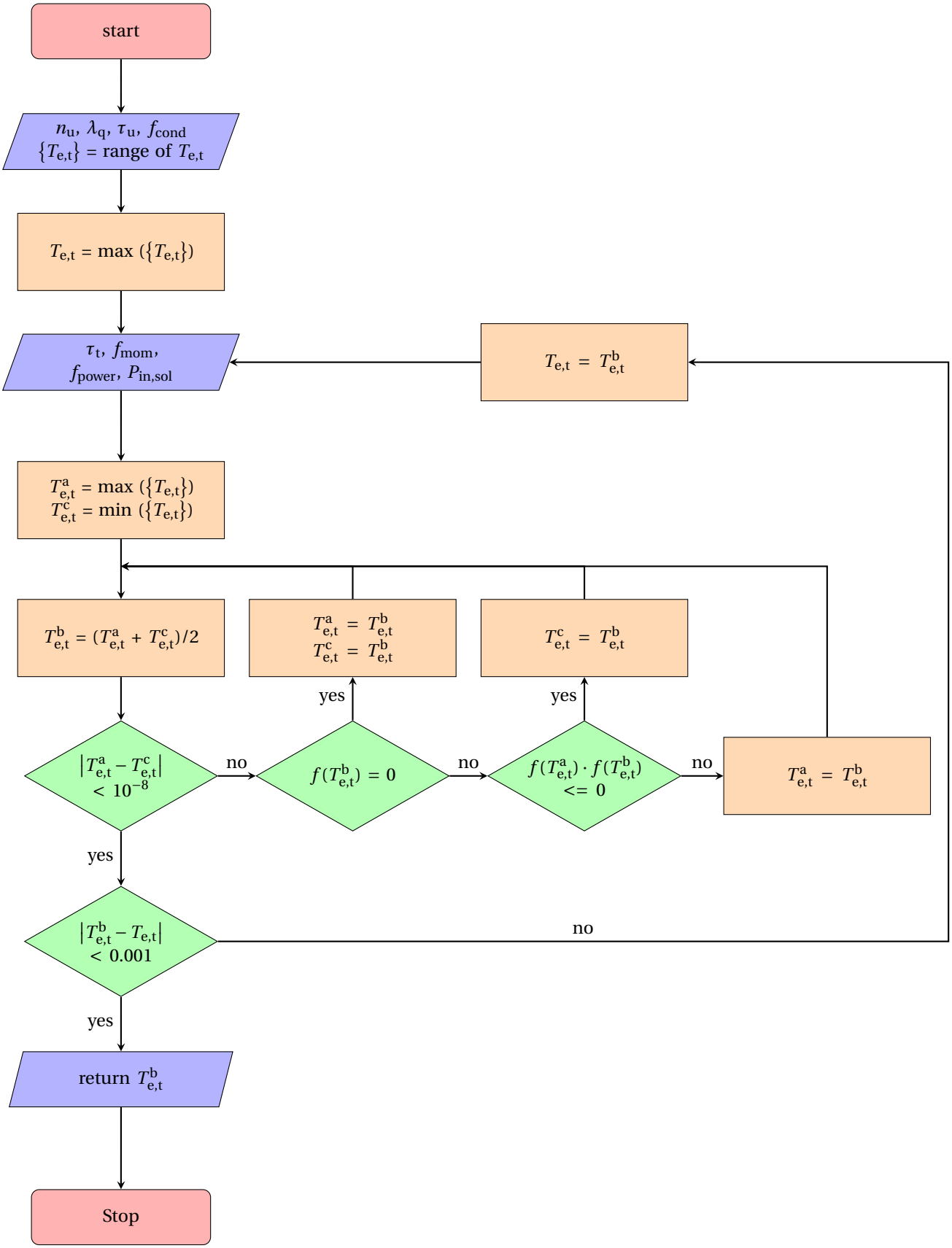

FIGURE 4.17. : The flow chart introduces the process of getting the target temperature in the extended 2PM.

Comparison with SOLEDGE simulation We can get some profiles similar to Figure 4.5 and Figure 4.12, but this time the results are from the calculation of the extended 2PM after applying the upstream $n_{e,sep}$ scan. Here we take two cases as an example, one is the case with no leak, and another one is the case with small leak. The profiles of the extended 2PM show a good match with the scatter points from SOLEDGE3X-EIRENE results as shown in Figure 4.18. The different detachment threshold in $n_{e,sep}$ can also be observed in the prediction of the extended 2PM as shown in Figure 4.18b. Due to the rapid change of some non-constant parameters and not dense enough samples in very low target temperatures, the calculation of the extended 2PM is hard to converge, so we neglect that part in our analysis.

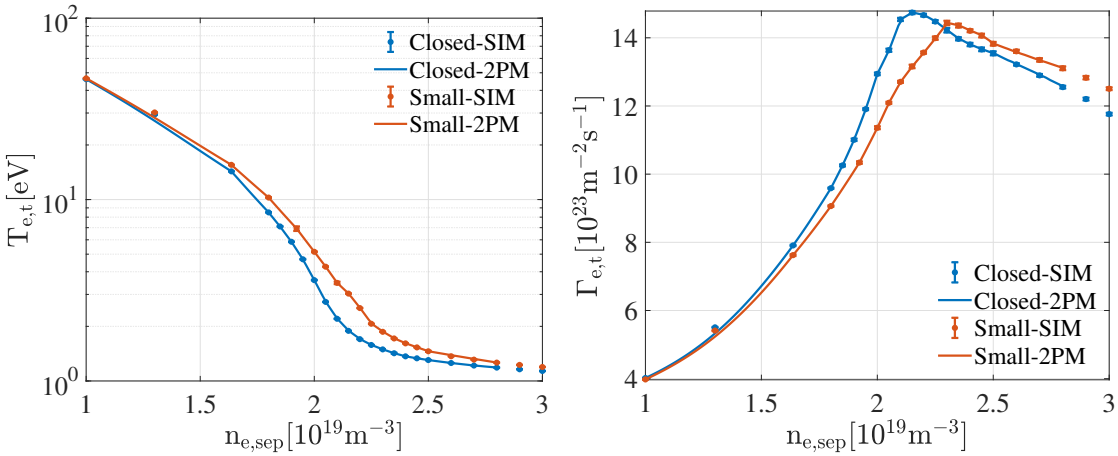

(a) T_e at the outer target

(b) Γ_e at the outer target

FIGURE 4.18. : (a) Evolution of electron temperature at the outer target $T_{e,t}$ as a function of $n_{e,sep}$. (b) Eevolution of particle flux at the outer target $\Gamma_{e,t}$ as a function of $n_{e,sep}$. Solid curves represent the result from the extended 2PM, scatter points represent the result from SOLEDGE3X-EIRENE simulation (SIM). Here we show only two cases as an example : the case with closed baffle and the case with small leakage under the baffle.

The parameters that introduce the impact of leakage Through the extended 2PM, the constant parameters are the same for all the cases, so the differences in non-constant parameters are the possible reasons for the different performance between baffle closed case and small leak case as observed in Figure 4.18. When we look at the evolution of non-constant parameters in Figure 4.15 and 4.16, most parameters appear no obvious difference between two cases with variable baffle leakage except $P_{in,sol}$, τ_t and f_{mom}. From Equation (4.3) and Equation (2.60), one can observe that $T_{e,t}$ is proportional to $P^2_{in,sol}$, f^2_{mom} and $(1+\tau_t)/2$. Comparing with $P_{in,sol}$ and f_{mom}, the small difference of τ_t has limited influence on the final results, thus we can neglect its variation in different cases. Our later results also support this point of view. As the f_{power} and the f_{cond} also play an important role in connecting the upstream and target, a minimal change in their value can also be important for the final results in

the extended 2PM, so we take them into account in the analyzing of which parameter matters to introduce the impact of leakage in the extended 2PM.

We start by defining the common parameters and independent parameters among the non-constant parameters for the two cases with variable baffle leakage. The common parameter means that the parameter is strictly the same when applied in the two cases. When finding the value of the common parameter by given $T_{e,t}$ or n_u, we interpolate the two sets of data from two cases separately and then take the average result as the input of the extended 2PM. On the contrary, the independent parameter just keeps the result unique to each case. In Section 4.1.1.4, we take all the non-constant parameters as the independent items to make the comparison. The influence of each non-constant parameter on introducing the impact of leakage in the extended 2PM can be identified easily : when changing the parameter from the independent one to the common one, if the difference between the two cases due to the impact of leakage remains the same as before, it means that the parameter has no obvious effects of introducing the impact of leakage in the extended 2PM. For the analysis process, we chose to reduce the number of independent parameters gradually but not analyze only one independent parameter each time because some parameters may be highly coupled and can cause some problems in the calculation when they are not from the same source (independent or common).

Firstly, we isolate the effects of λ_q, τ_u and τ_t from the extended 2PM, so f_{mom}, f_{power}, f_{cond}, $P_{in,sol}$ are still remained to be independent in each case. The evolution of Γ_e under new condition is shown in Figure 4.19a, comparing with the Figure 4.18b, the difference between them is quite small, and the impact of leakage still remained. So λ_q, τ_u and τ_t can be considered to have no obvious effects in introducing the impact of leakage.

Based on the first step, we continue to change the $P_{in,sol}$ from the independent to the common parameter. The result, as shown in Figure 4.19b, indicates that the effects of $P_{in,sol}$ can be ignored in introducing the impact of leakage, even if we have observed a significant difference between the two cases with variable baffle leakage for the profiles of $P_{in,sol}$ in Figure 4.15a.

Then we put f_{cond} as the common parameter. The result as shown in Figure 4.19c, compared with Figure 4.19b, a small difference can be observed. The peak $\Gamma_{e,t}$ decreases a little in the small leak case but increases slightly in the no leak case in the section right before rollover.

Next, the f_{power} is set as the common parameter. It seems to have the same tendency as the behavior of f_{cond} but presents a more significant difference this time, as shown in Figure 4.19d. The peak $\Gamma_{e,t}$ in small leak case is reduced a little. So now there is only f_{mom} remaining as the independent parameter, but we can still observe the impact of leakage from the profiles.

The f_{power} is also set as the only independent parameter to check its effects, as shown in Figure 4.19e. The two solid curves from the extended 2PM are almost similar, so no obvious impact of leakage can be observed this time.

When we finally no longer use the independent parameters, all the parameters used in both cases are exactly the same, so it is not surprising to see the Γ_e profiles from

two cases meet together, as shown in Figure 4.19f. Under this condition, the impact of leakage vanishes from the result of the extended 2PM.

Overall, from the comparison above, we can see that the independent f_{mom} tends to increase the impact of leakage, independent f_{power} and f_{cond} tend to lower the impact of leakage. The absolute influence of them in introducing the impact of leakage is in an order like : $f_{\mathrm{mom}} >> f_{\mathrm{power}} > f_{\mathrm{cond}}$. The effects of f_{power} and f_{cond} are even negligible compared with the strong influence carried by the f_{mom}.

Through the above analysis, we can see the plasma pressure balance between upstream and target in SOL is the aspect that is fundamentally influenced by the leakage under the baffle. But it is not a direct influence as the leakage influences more on the transport of neutrals as discussed in Section 4.1.1.2, and then the redistribution of neutrals can influence the plasma pressure balance by plasma-neutrals interactions.

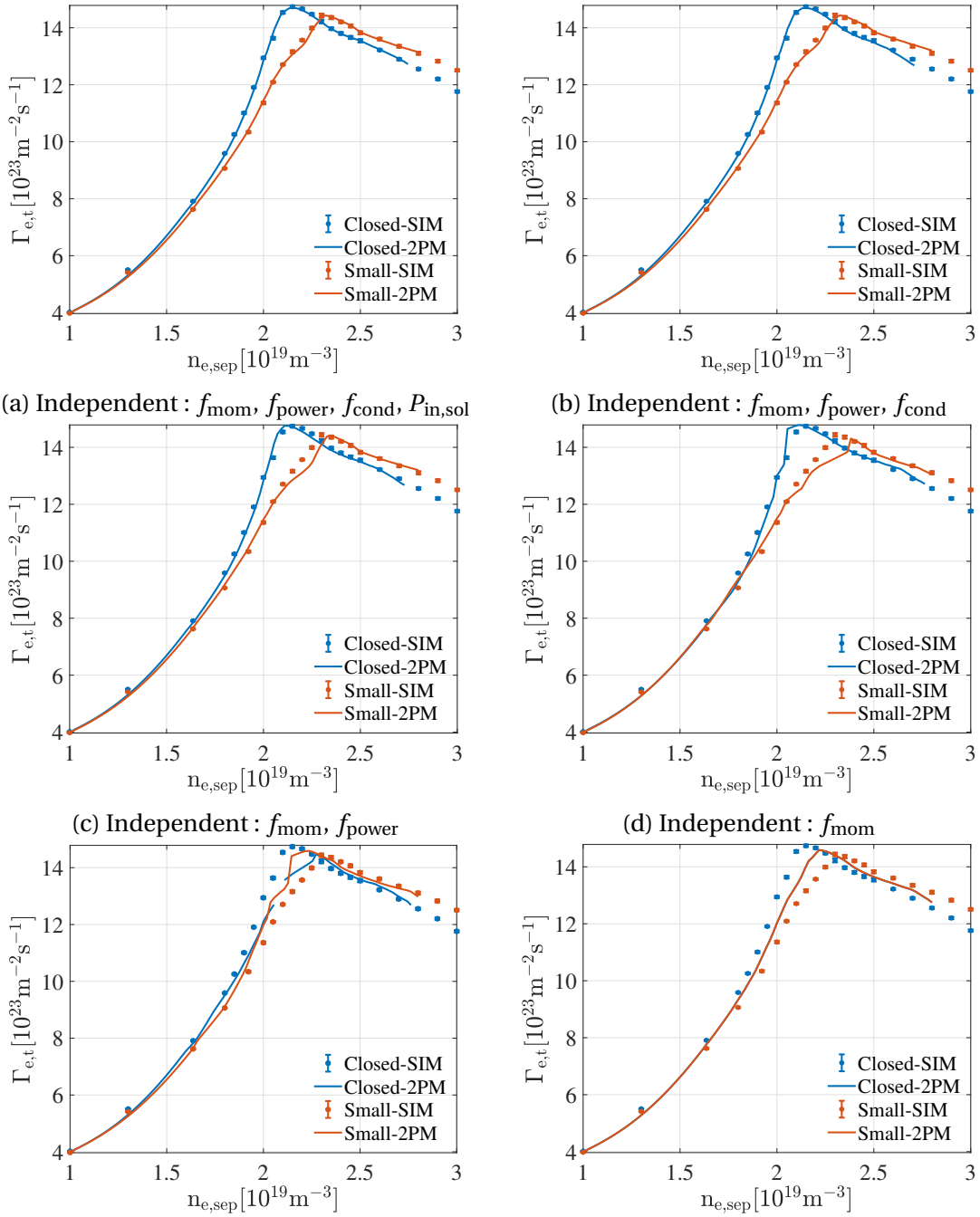

(a) Independent : f_{mom}, f_{power}, f_{cond}, $P_{in,sol}$

(b) Independent : f_{mom}, f_{power}, f_{cond}

(c) Independent : f_{mom}, f_{power}

(d) Independent : f_{mom}

(e) Independent : f_{power}

(f) No independent parameters

FIGURE 4.19. : Evolution of particle flux at the outer target $\Gamma_{e,t}$ as a function of $n_{e,sep}$. Solid curves represent the result from the extended 2PM, scatter points represent the result from SOLEDGE3X-EIRENE simulation (SIM). Here we show only two cases as an example : the case with closed baffle and the case with small leakage under the baffle. Each figure shows the result with different groups of independent input parameters in the extended 2PM. Except for the independent parameters used, other parameters are set to be the common parameters.

4.1.1.5. Comparing with experiment

Discharge	55077	56923	56726	56769
Campaign	C4	C5	C5	C5
Configuration	LSN	LSN	LSN	USN
Plasma current I_p (MA)	0.5	0.5	0.4	0.4
Toroidal field B_ϕ (T)	3.6	3.7	3.2	3
Heating power P_{in}^{exp} (kW)	150	140	365	375
Central line integrated density ($10^{19}/m^2$)	4	4.5	3	3
Upstream separatrix density $n_{e,sep}$ ($10^{19}/m^3$)	1.8 ± 0.25	2.1 ± 0.25	-	-
$P_{neu,omp}$ (mPa)	0.2	0.2	0.2	0.5
$P_{neu,baffle}$ (mPa)	10	15	6	-
Time t (s)	15	15	6	6

TABLE 4.1. : The data of experiment cases, $P_{neu,omp}$ represents the average neutral pressure at the near wall OMP position, $P_{neu,baffle}$ represents the average neutral pressure under baffle.

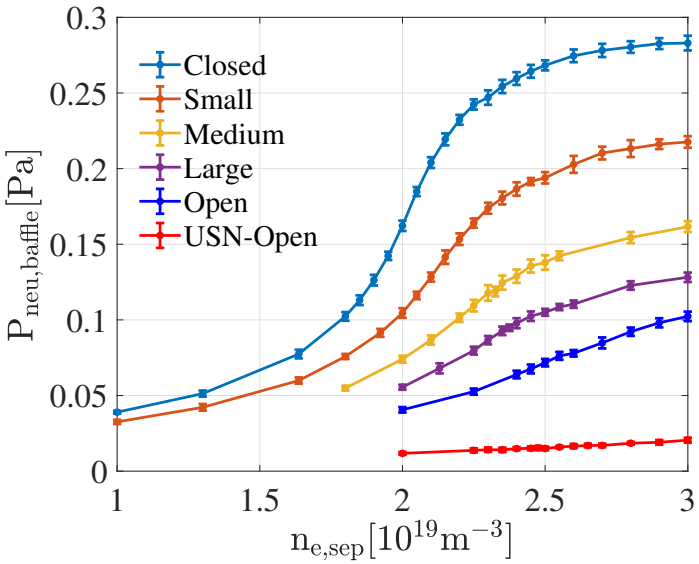

FIGURE 4.20. : Evolution of neutral pressure under baffle as a function of upstream $n_{e,sep}$.

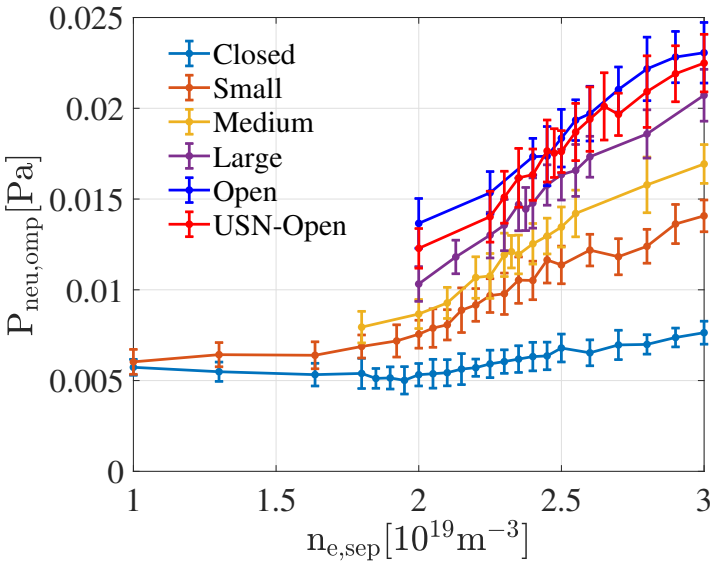

FIGURE 4.21. : Evolution of neutral pressure at the near wall OMP position as a function of upstream $n_{e,sep}$.

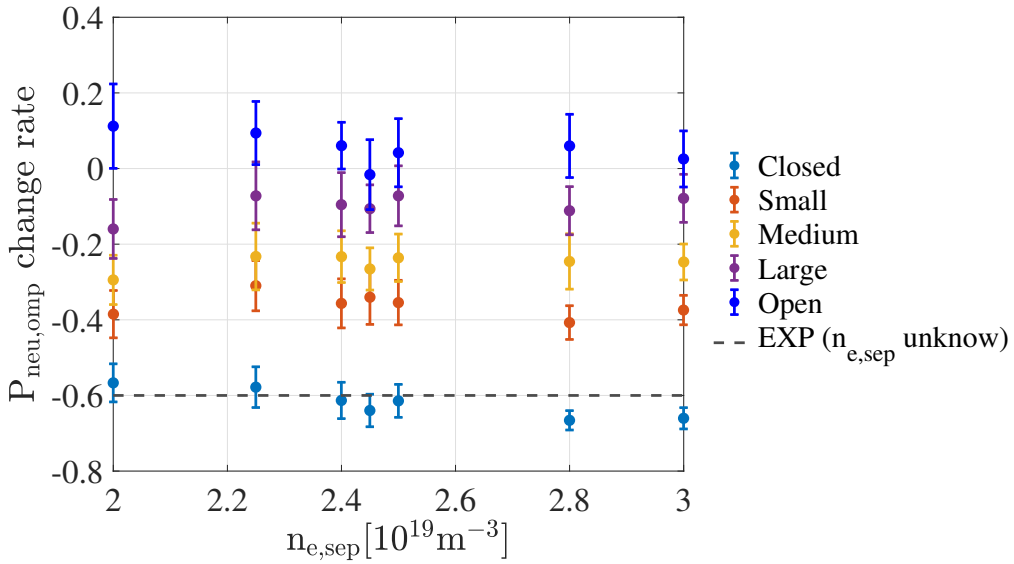

FIGURE 4.22. : The change rate of the neutral pressure at the near wall OMP : $(P^{LSN}_{neu,omp} - P^{USN}_{neu,omp})/P^{USN}_{neu,omp}$, as a function of upstream $n_{e,sep}$. The dashed line represent the $P_{neu,omp}$ change rate = −0.6, comparing between discharges #56726 and #56769.

Results from the SOLEDGE3X-EIRENE simulation are compared with four WEST discharges, as shown in Table 4.1. In WEST experimental campaign C5, the space between the divertor outer baffle and the vacuum vessel was sealed. The experimental data from the LSN discharge in C5 can be considered as baffle closed case when compared with the simulation, the one in C4 can be considered as the case with small

leakage. For the discharge #56923 in C5, we can observe about 50% higher neutral pressure under baffle $P_{\text{neu,baffle}}$, 17% higher upstream $n_{\text{e,sep}}$ and 13% higher central line integrated density compared with the discharge #55077 in C4. Both discharges have very close operational parameters. In the prediction of simulation for the neutral pressure under the baffle as shown in Figure 4.20, the LSN baffle closed case indeed has higher neutral pressure than the other LSN cases with leakage under the same upstream $n_{\text{e,sep}}$ which is consistent with the result given by experiment. However, the neutral pressure under the baffle evolves as a function of $n_{\text{e,sep}}$. For this reason, the increase of about 17% in the upstream density can also impact the neutral pressure under the baffle, making it difficult to conclude that the 50% higher neutral pressure under baffle is due to the effect of leakage sealed in the campaign C5. Moreover, other modifications implemented in WEST vacuum vessel between C4 and C5, like the change in the material of limiter bumpers, can impact the neutral density and pressure. For this reason, it is very challenging to estimate the impact of the leakage by comparing C4 and C5 discharges.

We also need to notice that the absolute values of neutral pressure under the baffle and the one at the near wall OMP are much higher in the simulations (Figure 4.20 and 4.21) than in the experiment (Table 4.1) by a factor up to 25. The neutral pressure difference between simulation and experiment is possibly due to two factors : first, different measurement positions. In experiment, the neutral pressure is measured after the pipe conduction, but in simulation, the P_{neu} is obtained directly from the locations (the region near the wall at the OMP and the region not far below the baffle). This factor can cause an underestimate of neutral pressure in the experiment and has been discussed in more detail in Section 2.7.2; second, the pure D simulation case also shows a higher P_{neu} compared to the simulation case with impurities (C or N). In pure D simulation, the neutral particles play an important role in the momentum and power dissipation of plasma. When the impurities particles are introduced into the plasma, they are much more effective in dissipating the power than the D atoms. In the case of the same energy dissipation, the pressure of D atoms and the total pressure of neutral particles required is greatly reduced under the effects of impurity. These aspects will be investigated further in future studies. So the $P_{\text{neu,omp}}$ measured in the experiment can not be compared directly with the data from simulation as they are not in the same order of magnitude.

To make a fair comparison, we choose two discharges in the same campaign C5, LSN discharge #56726, and USN discharge #56769. Both are pure Ohmic heating cases, with very close central line integrated density and operational parameters. However, there was no diagnostic available to evaluate the neutral pressure in the upper divertor, and the reflectometry density measurement (used to evaluate the $n_{\text{e,sep}}$) at the OMP was not performed in the two cases. A workaround is to compute the change rate of the neutral pressure at the near wall OMP $P_{\text{neu,omp}}$ for each LSN case, the change rate is defined as $(P^{\text{LSN}}_{\text{neu,omp}} - P^{\text{USN}}_{\text{neu,omp}})/P^{\text{USN}}_{\text{neu,omp}}$. For the cases with baffle, the change rate is normally negative. It represents the decrease of neutral pressure in the far SOL when the baffle is introduced as the baffle can limit the leakage of neutral particles from the divertor, thus lowering the neutral pressure in the far SOL as discussed in Section

4.1.1.2. The baffle with less leakage can have a better effect in limiting the neutral particles, leading to lower $P_{\text{neu,omp}}$. For this reason, we can see the baffle closed case has the lowest neutral pressure at the near wall OMP compared with other cases, as shown in Figure 4.21. Here we compare the LSN baffled closed case and USN case directly because the USN case can be considered as LSN no baffle case, and they have consistent characteristics as discussed in Section 4.1.1.1.

The reasons for using the $P_{\text{neu,omp}}$ change rate to analyze the impact of leakage in the experiment are : first, this parameter shows insensitivity to the changes of upstream $n_{\text{e,sep}}$ as shown in Figure 4.22. This is important because measurements of upstream conditions are not always available in the experimental discharges ; second, it is hard to reproduce the plasma in the simulation that has the same order of magnitude of P_{neu} as in the experiment, this part has been discussed before. The $P_{\text{neu,omp}}$ change rate can be an ideal parameter to evaluate the tendency that happened in the simulation and experiment under the effects of leakage.

Figure 4.22 shows the $P_{\text{neu,omp}}$ change rate calculated by simulation cases and the value from selected experimental cases as a reference. It can be observed that the reference value given by the experiment matches with the prediction of SOLEDGE3X-EIRENE when the $P_{\text{neu,omp}}$ change rate is calculated between the baffle closed cases and the USN case. This is consistent with the fact that we have a baffle closed divertor in campaign C5 of WEST.

The diagnostics for neutral pressure measurements have been improved since the C5 campaign, with better measurement accuracy and more measurement positions (the upper divertor is included). A more detailed comparison with simulation results will be possible for future experiments, and this aspect will be investigated further.

The impact of leakage is also analyzed via the 2PM, which shows that the plasma pressure balance between upstream and target in SOL (f_{mom}) is the aspect that is fundamentally influenced by the variable baffle leakage. More details can be found in Section 4.1.1.4.

4.1.2. Long and short baffle in TCV

The impact of divertor closure in TCV H-mode case has been investigated through the simulation via changing the length of the outer baffle. Except for the wall geometry, the short outer baffle cases keep all parameters identical to the long one presented in Section 3.2.2. The comparison between long and short baffle is shown in Figure 4.23. They are the case with D and C, no nitrogen seeding is applied.

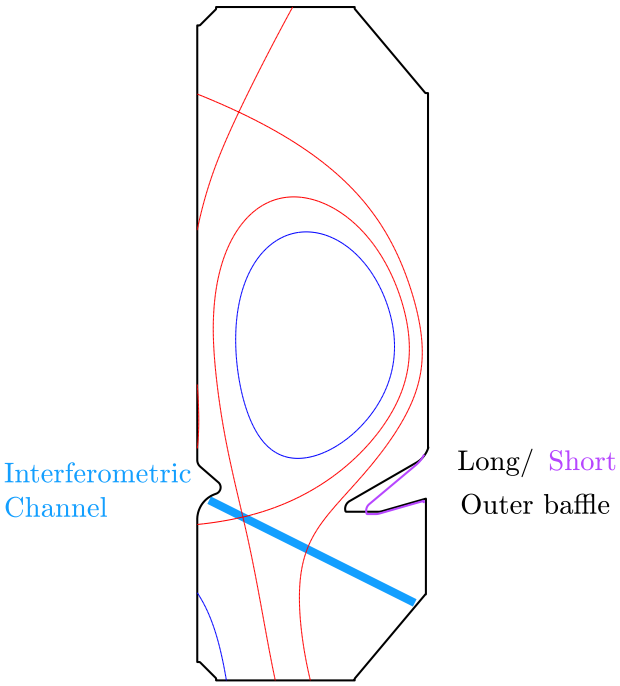

FIGURE 4.23. : Geometries with the long and short outer baffle. An interferometric channel was introduced in the simulation, to study the influence of the outer baffle length on line integral density nearby X-point.

The comparison of long and short baffle TCV cases presents similar results to WEST investigation in Section 4.1.1 : under the same upstream density, compared with long baffle case, short baffle case represents lower gas puff applied (Figure 4.24), lower neutral compression ratio (Figure 4.25), less effective in trapping neutral particles in the divertor, higher target temperature (Figure 4.26), higher detachment threshold in $n_{e,sep}$ (Figure 4.27).

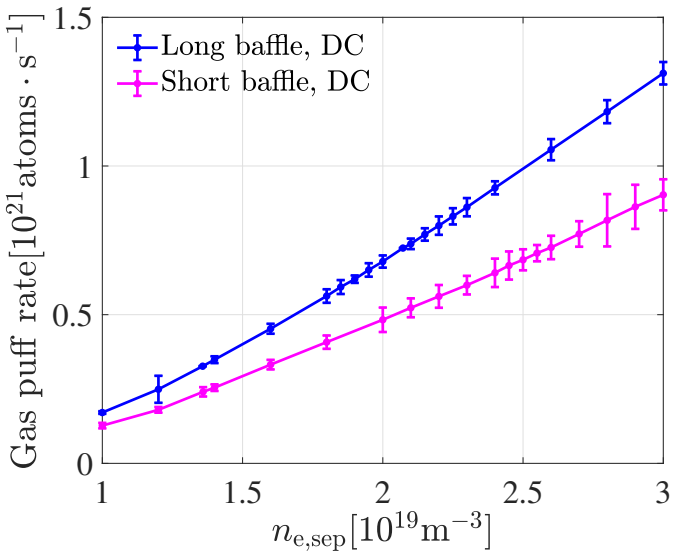

FIGURE 4.24. : Evolution of gas puff as a function of $n_{e,sep}$.

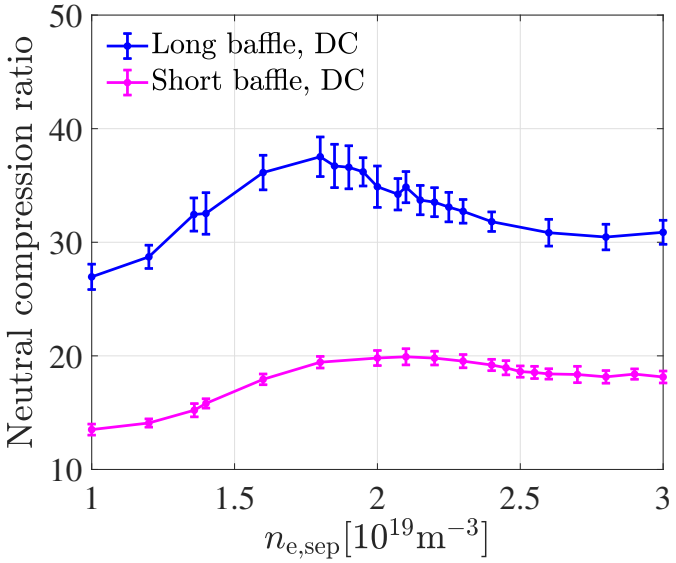

FIGURE 4.25. : Evolution of neutral compression ratio (equals to the ratio between $P_{neu,target}$ and $P_{neu,omp}$, the corresponding positions can be checked in Figure 3.28) as a function of $n_{e,sep}$.

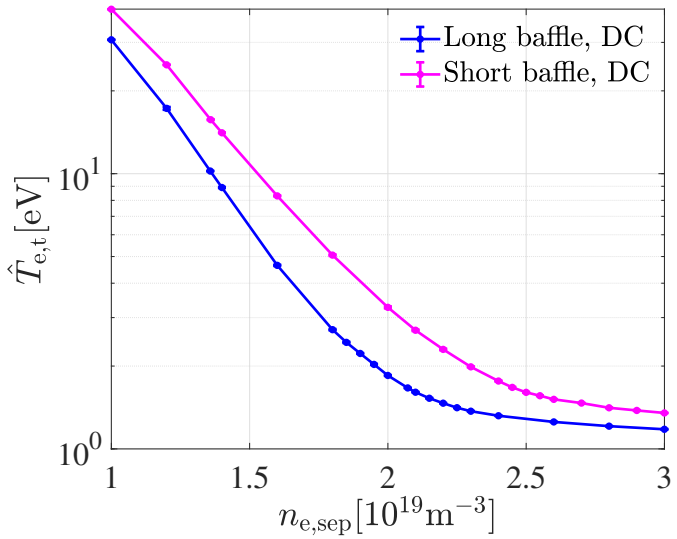

FIGURE 4.26. : Evolution of peak electron temperature at the outer target as a function of $n_{e,sep}$.

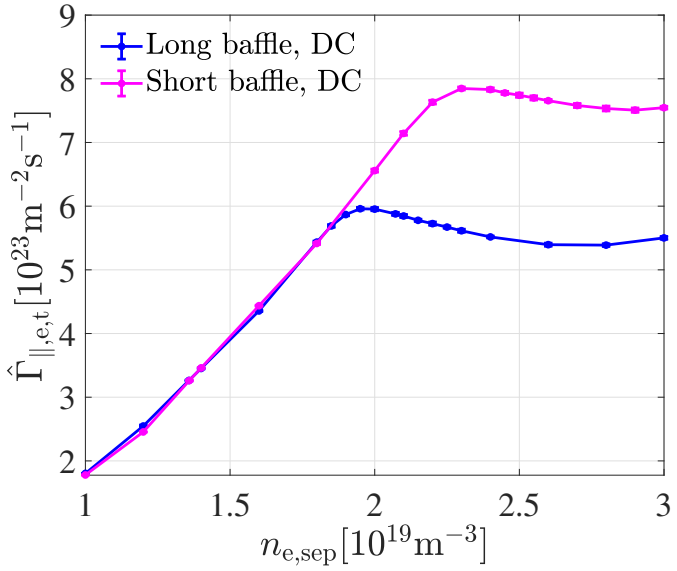

FIGURE 4.27. : Evolution of peak parallel electron flux at the outer target as a function of $n_{e,sep}$.

Because of the lower divertor closure, the case with short baffle exhibits a lower divertor neutral pressure (Figure 4.28), leading to a lower momentum and power dissipation level at the same upstream density when compared to the long baffle case. The difference in neutral pressure distribution due to the change in baffle length can thus influence the detachment.

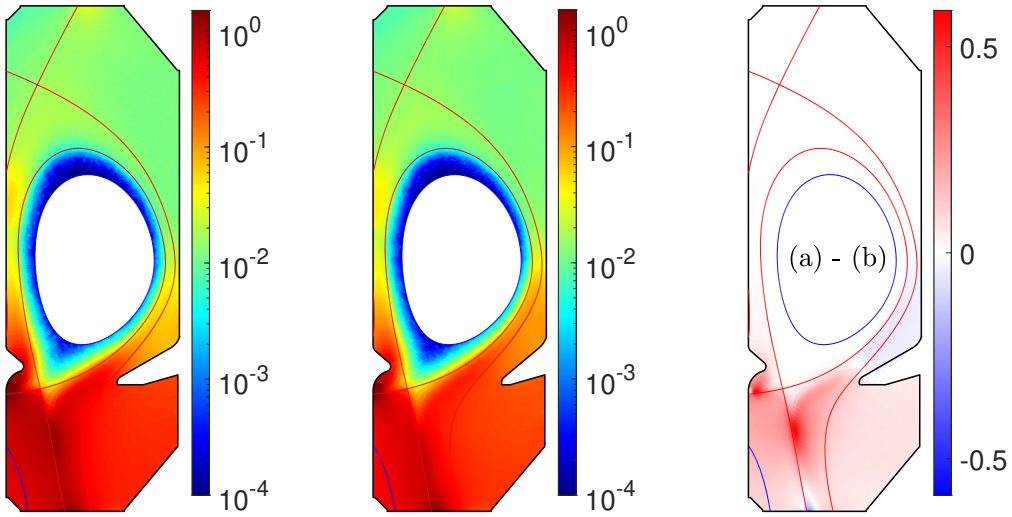

(a) Long baffle, DC (b) Short baffle, DC (c) Change of P_{neu}

FIGURE 4.28. : 2D maps of P_{neu} [Pa] are shown in (a) and (b), which have the same upstream separatrix density ($n_{\text{e,sep}} = 3 \times 10^{19}\,\text{m}^{-3}$) but different baffle lengths. Plot (c) shows the change in neutral pressure between (a) and (b) when the baffle length is increased while keeping $n_{\text{e,sep}}$ constant.

It is interesting to note that, despite the difference in divertor closure, a consistent detachment threshold is found in both TCV and WEST (Section 4.1.1) cases when considering the divertor neutral pressure (averaged along the lower part of the outer divertor leg, blue line in Figure 3.28). This is illustrated in Figure 4.29 where the detachment threshold is ≈ 0.76 Pa for TCV cases with $P^{\text{sim}}_{\text{in,edge}} = 210$ kW, and ≈ 1.21 Pa for WEST cases with $P^{\text{sim}}_{\text{in,edge}} = 450$ kW. This finding suggests that the divertor neutral pressure can be used as an ordering parameter for the divertor state when applying constant SOL input power, independently of the divertor configuration.

If we introduce an interferometric channel (Figure 4.23) in the TCV simulation, to analyze the line-integral density $n_{\text{e,int,X}}$ over the channel which is pointing in the X-point region in the same way as WEST (Channel 1 in Figure 2.13). We can find that the $n_{\text{e,int,X}}$ shows similar characteristics to the divertor neutral pressure, indicating that the divertor-averaged neutral pressure and $n_{\text{e,int,X}}$ are highly related.

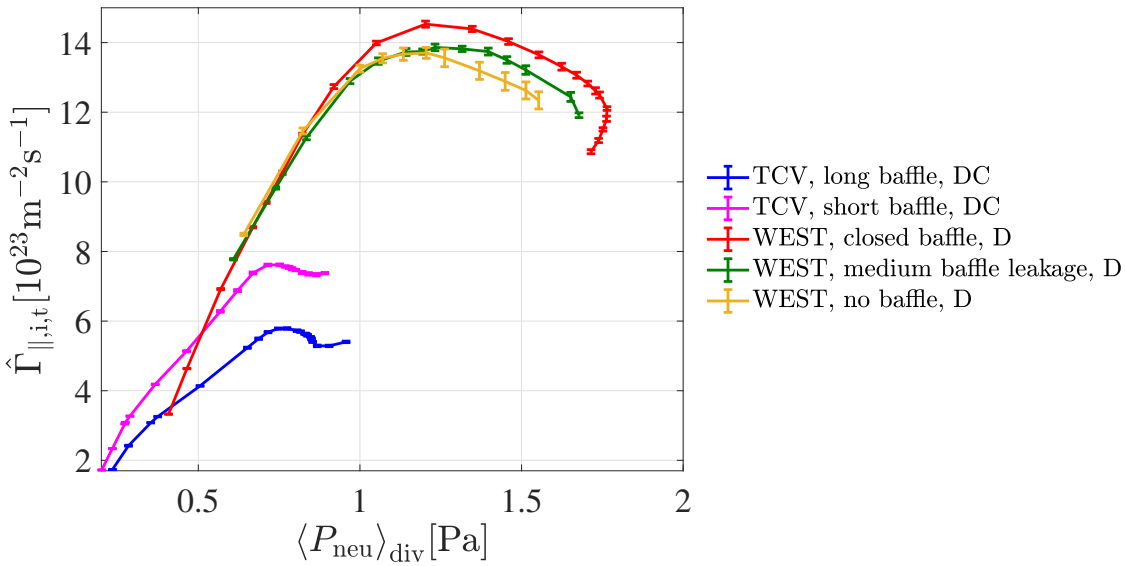

FIGURE 4.29. : Evolution of peak particle flux at the outer target as a function of divertor-averaged neutral pressure in TCV and WEST with different divertor closure levels.

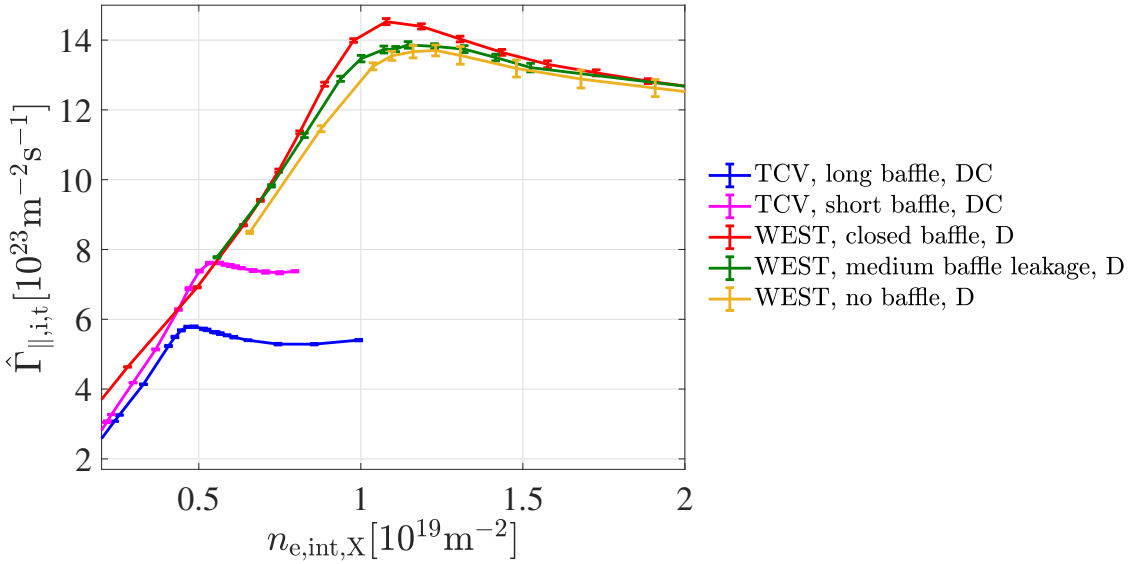

FIGURE 4.30. : Evolution of peak particle flux at the outer target as a function of line-integral density over the channel which is pointing in the X-point region in TCV and WEST with different divertor closure levels.

However, there is a noticeable contrast in the deuterium puff rate required to achieve detachment between WEST and TCV. With reduced divertor closure, the deuterium puff rate at the detachment threshold is lower by 92% in the WEST case (as shown in Figure 4.4) and by less than 5% in the TCV case. This difference can be attributed to the influence of the divertor wall recycling coefficient and the relative positioning

of the pump. In the WEST simulation cases (Section 4.1.1), the variable divertor closure is achieved by either creating a hole at the bottom of the baffle or removing the baffle entirely, to mimic divertor neutral leakage. The pump is positioned under the baffle (close to the hole), with a recycling coefficient $R_{\text{pump}} = 0.95$. The wall recycling coefficient is taken as $R_{\text{wall}} = 1$ (assuming full recycling of ions impinging the wall). With a higher level of leakage, the neutral pressure near the pump decreases substantially, even if the average divertor neutral pressure remains the same. As a result, the pumping speed decreases proportionally to the neutral pressure, which reduces the requirements for the deuterium puff rate needed to integrate the loss of neutrals and maintain the particle balance. However, in the TCV case, there is no pump. The sink of particles is dominated by the integral ion flux impinging on the target with a recycling coefficient of $R_{\text{wall}} = 0.99$. Simulation results show that the integral ion flux impinging on the target is similar ($\approx 6 \times 10^{21}\,\text{s}^{-1}$) at detachment onset, despite the difference in divertor closure. A slightly lower (less than 5%) ionization source (from deuterium gas puff) is required in a reduced divertor closure case to achieve a similar integral ion flux level at the target because the upstream density is higher. The difference between TCV and WEST emphasizes the effect of divertor wall conditioning and the relative positioning of the pump in gas fuel operation.

4.2. Impact of nitrogen seeding

Nitrogen is often used in high radiation scenarios, mainly radiating power in the SOL and divertor region in medium-sized tokamaks such as WEST and TCV [116]. The radiation increases significantly and the target heat load is largely reduced with nitrogen seeding [17]. In H-mode scenarios, nitrogen can change the ELM characteristics (reduce ELM size by a factor of 2—3 and increase the ELM frequency by a similar amount) and improve the energy confinement [117, 118]. High levels of nitrogen radiation reduce the ELM amplitude further and can cause back-transitions to L-mode [17]. However, nitrogen and carbon should be avoided in future reactors due to their chemical reactivity, for example in the presence of lithium wall coatings, and strong tritium retention [28, 119].

Based on the long and short baffle TCV cases with D and C, nitrogen seeding is introduced to investigate how it will influence the divertor state. In addition to the cases we used before, three cases are added : two have *ramped Nitrogen Seeding starting From an Attached case* (NSFA) with long and short baffle; the remaining one has *ramped Nitrogen Seeding starting From a Detached case* (NSFD) with long baffle. When ramped nitrogen seeding is applied, the deuterium puff rate remains unchanged, Figure 4.31. The two NSFA cases with long and short baffles have a similar upstream density ($n_{\text{e,sep}} \approx 1.35 \times 10^{19}\,\text{m}^{-3}$) at the start point. The long baffle NSFD case has higher upstream density ($n_{\text{e,sep}} \approx 2.07 \times 10^{19}\,\text{m}^{-3}$) at the start point. The ramped nitrogen seeding rate leads to an increase of nitrogen concentration in the divertor, which is an important variable in evaluating the impact of nitrogen. We define the impurity concentration $c_Z = P_{\text{neu,z,div}}/P_{\text{neu,total,div}}$ (the ratio of neutral pressure

between impurity species and total one, averaged along the lower part of divertor outer leg, blue line in Figure 3.28). The evolution of carbon and nitrogen concentration as a function of peak electron temperature at the outer target is shown in Figure 4.32. The achievement of detachment is usually accompanied by low temperature (below 5 eV) at the target. So the parameters here are shown as a function of peak electron temperature at the outer target to make it easier to analyze the impact of nitrogen seeding for detachment.

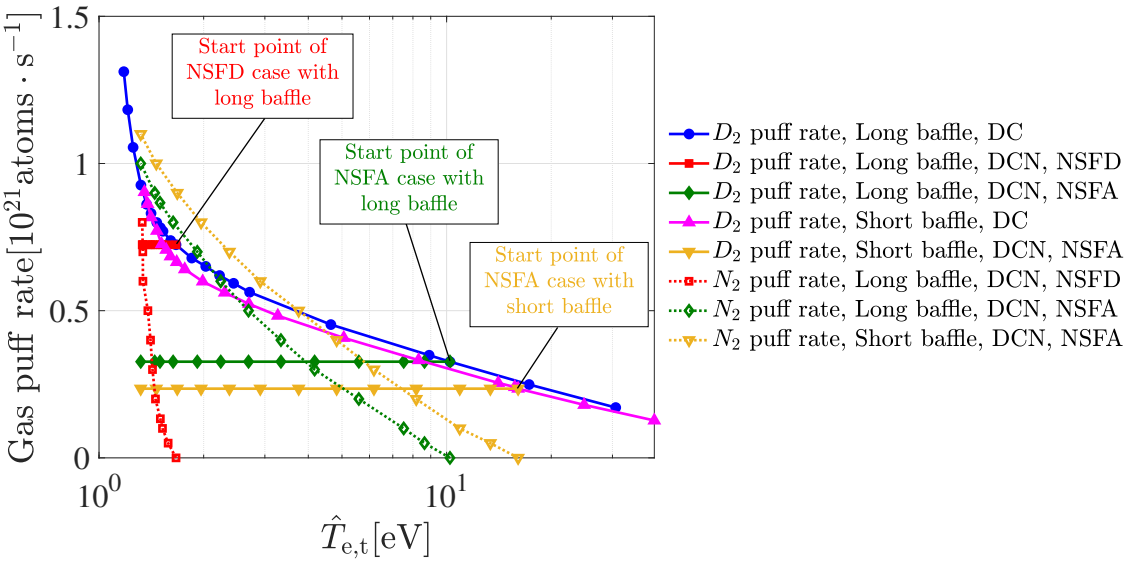

FIGURE 4.31. : Evolution of deuterium and nitrogen puff rate as a function of peak electron temperature $\hat{T}_{e,t}$ at the outer target. NSFA (NSFD) means the case with ramped Nitrogen Seeding starts From an Attached (Detached) plasma. When ramped nitrogen seeding is applied, the deuterium puff rate keeps constant as the start point.

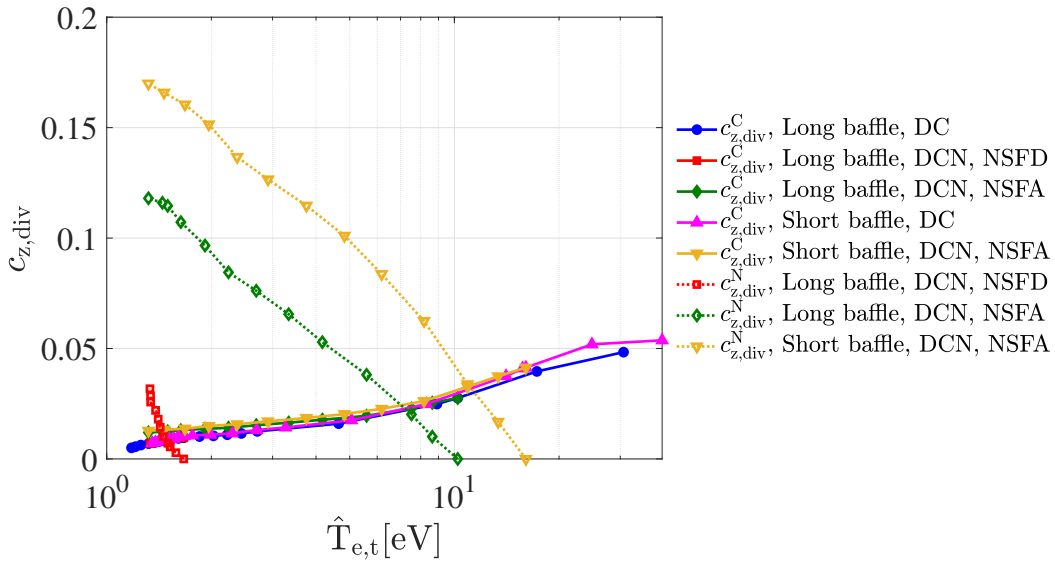

FIGURE 4.32. : Evolution of carbon and nitrogen concentration ($c^C_{z,div}$ and $c^N_{z,div}$, respectively) as a function of peak electron temperature $\hat{T}_{e,t}$ at the outer target.

4.2.1. In the cases with unchanged divertor closure

This section primarily focuses on the impact of nitrogen seeding on the divertor state. Three long baffle cases (one case without nitrogen seeding and two cases with nitrogen seeding) are compared. Figure 4.33a shows the evolution of $n_{e,sep}$ as a function of peak electron temperature at the outer target. It is evident that the case without nitrogen seeding requires a relatively high $n_{e,sep}$ to achieve a low target temperature. However, the case with nitrogen seeding starting from an attached state can achieve a similar target temperature with a lower $n_{e,sep}$, which remains relatively constant throughout the scan. This suggests that nitrogen seeding can cool the target temperature with little effect on the upstream density.

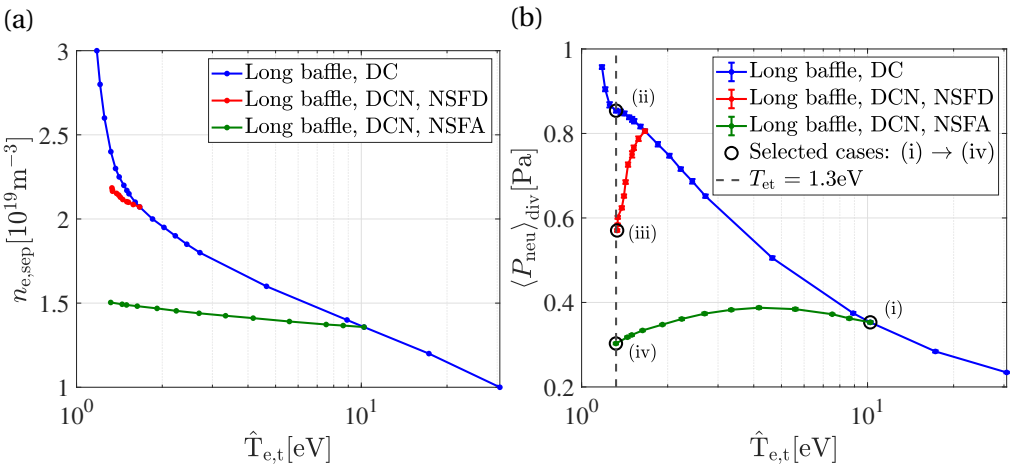

FIGURE 4.33. : (a) Evolution of upstream separatrix density $n_{e,sep}$ as a function of peak electron temperature at the outer target. (b) Evolution of divertor-averaged neutral pressure (the position of $P_{neu,div}$ is shown in Figure 3.28) as a function of peak electron temperature at the outer target. There are four cases selected : (i) represents an attached case without nitrogen seeding and with a peak target temperature $T_{e,t} = 9.6\,eV$. (ii) → (iv), represent the detached cases with increasing nitrogen concentration (from 0 to 0.12) and with approximately the same peak target temperatures $T_{e,t} = 1.3\,eV$.

The divertor neutral pressure is strongly related to the upstream density in the case without nitrogen seeding, Figure 4.33. However, when nitrogen seeding is introduced starting from the attached case, the divertor neutral pressure remains constantly lower, following a behavior similar to that of $n_{e,sep}$. This observation is consistent with the experimental results [86], indicating that the divertor neutral pressure is strongly related to the upstream electron density and insensitive to nitrogen injection. However, when nitrogen seeding is introduced starting from a detached case, the divertor neutral pressure drops rapidly. Cases (ii) and (iii) in Figure 4.33b have similar upstream density ($n^{ii}_{e,sep} \approx 2.4 \times 10^{19}\,m^{-3}$ compared to $n^{iii}_{e,sep} \approx 2.2 \times 10^{19}\,m^{-3}$) but present a significant difference in divertor neutral pressure (0.85 Pa compared to 0.57 Pa) due to nitrogen injection. Further studies show that introducing nitrogen seeding starting from the detached case rapidly decreases the target particle flux, as shown by the red curve in Figure 4.34a. Fewer neutral particles are recycled from the target, as a result, divertor neutral pressure decreases. Next, we use the 2PM (Section 2.6.1) to explain how the target particle flux is influenced by nitrogen. As the upstream heat flux $q_{\parallel,u}$ remains relatively constant throughout the scan in the simulation cases, Equation 17 in [50] can be simplified to :

$$\Gamma^{2PM}_{\parallel,e,t} \propto P^2_{total,u} \frac{\left(1 - f_{mom,loss}\right)^2}{\left(1 - f_{cooling}\right)}, \tag{4.6}$$

where the P_{total} represents the total plasma pressure, the $f_{\text{mom,loss}}$ and f_{cooling} represent the momentum loss fraction and power loss fraction. The subscripts 'u' and 't' in the parameters indicate upstream and target, respectively. As shown in Figure 4.34b, the nitrogen seeding leads to a drop in the upstream pressure ($P_{\text{total,u}}$) with little effects on the loss of momentum from upstream to the target ($P_{\text{total,u}} - P_{\text{total,t}}$). While both the upstream pressure and the loss of momentum increase with $n_{\text{e,sep}}$ by applying a ramped-up deuterium puff rate. In Figure 4.34c, the $(1-f_{\text{mom,loss}})^2/(1-f_{\text{cooling}})$ evolves with approximately the same slope, particularly the red curve is matched with the blue curve, despite the difference in nitrogen seeding. The $f_{\text{mom,loss}}$ and f_{cooling} of the red curve are slightly higher than that of the blue curve under the same peak electron temperature at the outer target. Therefore, when nitrogen is introduced, the decrease in the target particle flux is mainly driven by the drop in the upstream pressure.

Furthermore, the introduction of nitrogen seeding changes the primary factor responsible for detachment. With increased $n_{\text{e,sep}}$, detachment is primarily driven by the momentum losses, part of which are proportional to the divertor neutral pressure. However, nitrogen seeding effectively limits the increase of $n_{\text{e,sep}}$ and the upstream temperature decreases simultaneously at the same rate as the case without nitrogen seeding, as a function of the reduced target temperature. Thus, the upstream pressure drops, driving the detachment instead.

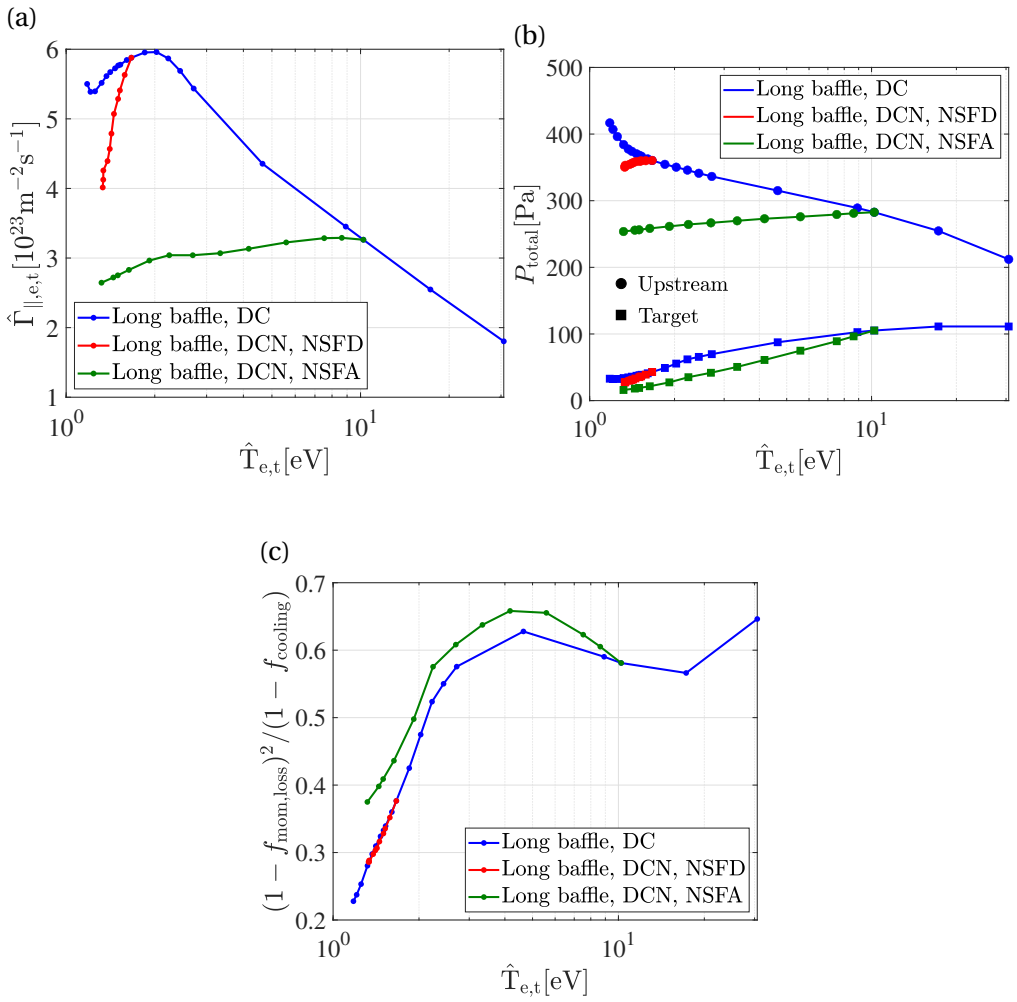

FIGURE 4.34. : (a) Evolution of peak parallel electron particle flux as a function of peak electron temperature at the outer target. (b) Evolution of total plasma pressure at the upstream and outer target. (c) Evolution of $(1-f_{\text{mom,loss}})^2/(1-f_{\text{cooling}})$, where $f_{\text{mom,loss}}$ and f_{cooling} represent momentum loss fraction and power loss fraction, respectively.

The 2D maps in Figure 4.35 show the distribution of electron temperature, total plasma pressure, and neutral pressure for each of the cases highlighted in Figure 4.33b. Case (ii) reaches detachment by increasing $n_{\text{e,sep}}$, and thus increasing the divertor neutral pressure compared with case (i). However, with increasing nitrogen concentration in cases (iii) and (iv), the required divertor neutral pressure gradually decreases. This can be explained by considering the power balance, as nitrogen is much more effective in cooling down the divertor compared to deuterium neutrals. For example, comparing cases (ii) and (iv), assuming the influence of carbon is negligible, the efficiency of nitrogen compared to deuterium f_z^{N} will lead to the general influence of neutral particles (nitrogen and deuterium) in case (iv) approximately equals to the

influence of deuterium in case (ii) in the divertor in terms of achieving same peak target temperature $\hat{T}_{e,t} = 1.3\,\text{eV}$, as expressed by the following equation :

$$f_z^N \langle P_{neu,N} \rangle_{div}^{(iv)} + \langle P_{neu,D} \rangle_{div}^{(iv)} = \langle P_{neu,D} \rangle_{div}^{(ii)} \tag{4.7}$$

Therefore, we obtain $f_z^N \approx 16.4$, close to the $f_z^N = 18$ used in the partial detachment model in [120], which will later be compared with the simulations in Section G.1.

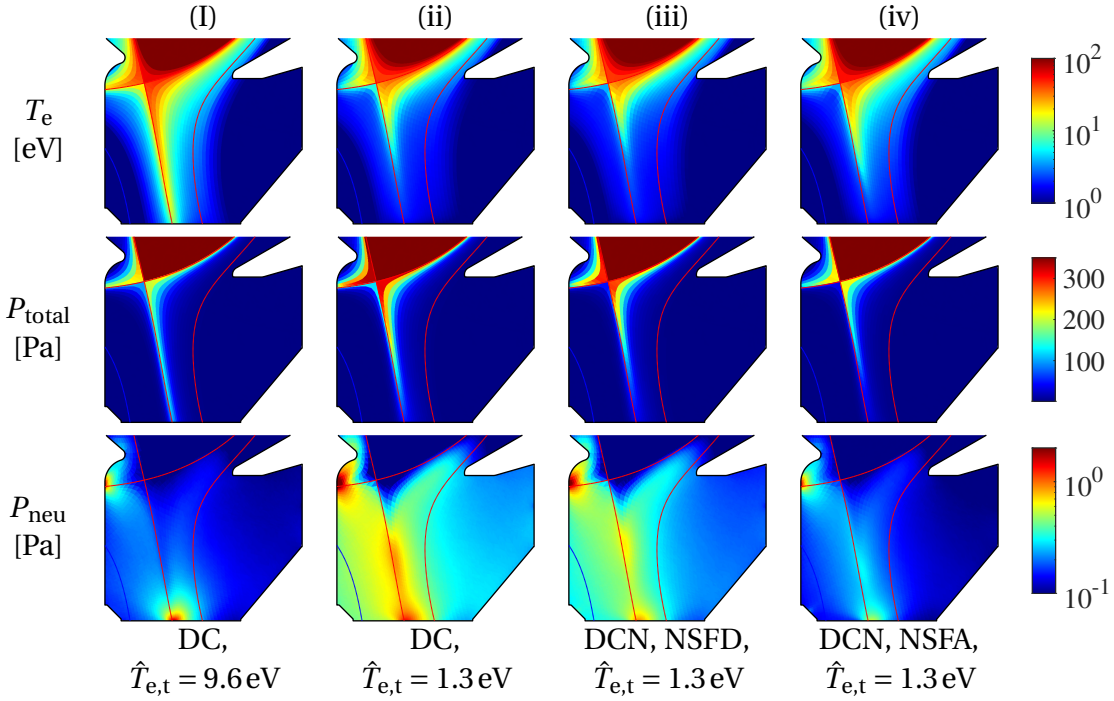

FIGURE 4.35. : 2D maps of variables for selected cases (i)–(iv) marked in Figure 4.33b : electron temperature T_e in the first row, total plasma pressure P_{total} in the second row, and neutral pressure P_{neu} in the third row.

The evolution of the ratio between radiated power and total input power in the modeling domain as a function of peak electron temperature at the outer target is shown in Figure 4.36. Nitrogen seeding leads to a higher fraction of radiated power. Figure 4.37 shows the evolution of radiated power from different species in the cases with and without nitrogen seeding. As the deuterium or nitrogen gas puff rate increases, the peak target temperature $\hat{T}_{e,t}$ decreases in both cases (from 10 eV to 1.5 eV). The radiated power from carbon remains approximately constant ($\approx 0.048\,\text{MW}$) in the $n_{e,sep}$ ramp-up case (Figure 4.37a) and is reduced (from 0.044 MW to 0.028 MW) in the nitrogen ramp-up case (Figure 4.37b) as a function of decreasing target temperature. The limited role of carbon in achieving detachment is evident since there is little change in power dissipation by carbon with reduced temperature.

In the case without nitrogen seeding (only D and C), despite more than 50% of power being radiated by carbon (Figure 4.37a), the increased power dissipation with

increasing upstream density is mainly due to deuterium emission, driven by the neutral pressure level in the divertor.

When nitrogen is seeded starting from the attached case (as shown in Figure 4.37b), it eventually replaces carbon and deuterium as the dominant radiation source, accounting for more than 65% of radiated power for $\hat{T}_{e,t} < 2\,eV$, with a nitrogen concentration lower than 0.12 in the divertor, Figure 4.32. This is consistent with previous simulation observations [87, 93]. The radiated power from deuterium remains constant with decreasing $\hat{T}_{e,t}$ due to constantly lower divertor neutral pressure.

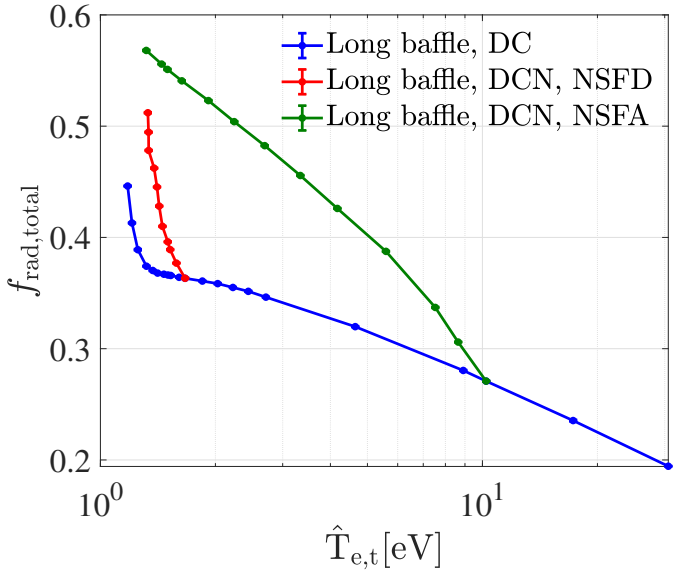

FIGURE 4.36. : Evolution of the ratio between radiated power and total input power in the modeling domain as a function of peak electron temperature at the outer target.

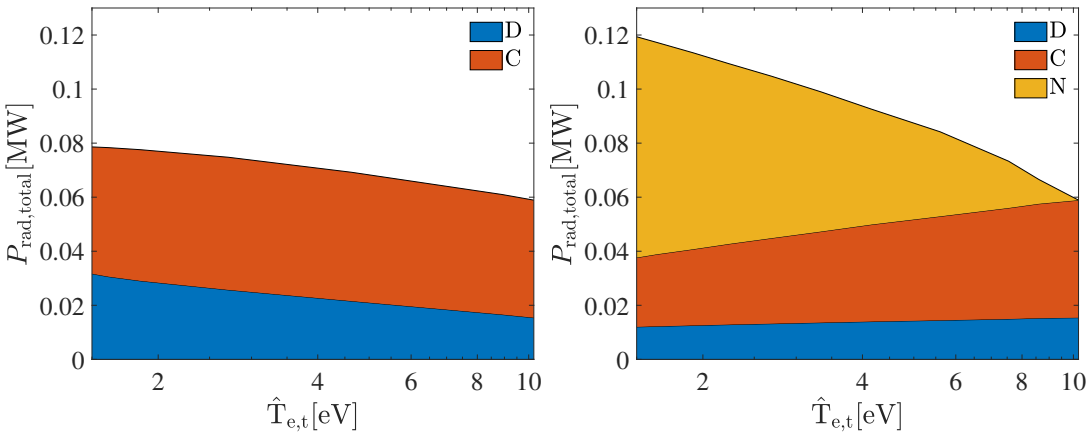

(a) Long baffle, DC (b) Long baffle, DCN, NSFA

FIGURE 4.37. : (a) Evolution of radiation from different species as a function of peak electron temperature at the outer target in DC case. (b) Evolution of radiation from different species in DCN case with nitrogen seeding starting from attached.

Nitrogen plays an important role in radiative power dissipation, and it is found localized in the region of low temperature close to the target [93]. Reaching detachment with nitrogen seeding and pure deuterium puff leads to different radiation profiles along the divertor outer leg for the same target heat flux. In particular, with nitrogen seeding, the emission front appears closer to the target, as shown in Figure 4.38.

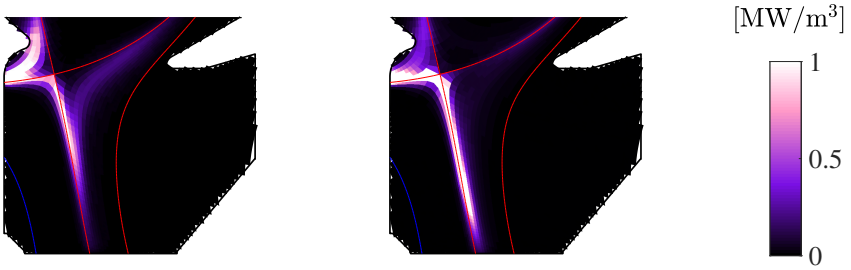

(a) Deeply detached case without nitrogen seeding (b) Deeply detached case with nitrogen seeding, NSFA

FIGURE 4.38. : 2D maps of P_{rad} for two long baffle cases with similar $\hat{q}_{\parallel,\mathrm{ot}}$ about 1.12 MW/m^2.

4.2.2. In the cases with changed divertor closure

In Section 4.1.2, we discussed that the change in baffle length can influence the neutral pressure distribution (mainly deuterium) so that the long baffle case has a lower detachment threshold in terms of upstream density $n_{\mathrm{e,sep}}$. In this section, we study if the effect of nitrogen is influenced by divertor closure. When discussing the impact of nitrogen seeding on detachment, it is more practical to consider the point

at which the radiation front starts moving upwards from the target ($H^{N}_{rad,front} \geq 0.05$, Section 4.4) as a sign of divertor detachment, particularly for identifying the threshold of detachment. This is because the ramped nitrogen seeding rate leads to a direct decrease in the target ion flux, similar to the target electron flux in Figure 4.34a, making it difficult to identify the rollover threshold. Experimental nitrogen seeding cases also show a significant decrease in particle flux with respect to the case without nitrogen [28, 86, 121].

In Figure 4.39, we observe that for the ramped nitrogen seeding cases starting from attached, the detachment threshold in $n_{e,sep}$ is almost unchanged between the two baffle lengths ($\approx 1.4 \times 10^{19}\,m^{-3}$), thus the influence of neutral pressure is equivalent in both cases. However, the detachment threshold in nitrogen concentration is lower by 50% in the long baffle case compared with the short baffle case, as visible in Figure 4.40. The effects of carbon are neglected due to low carbon concentration ($c_{C,div} \approx 0.018$ compared to $c_{N,div} \approx 0.05$–0.1 when the plasma detaches, carbon is also approximately half as effective as nitrogen in power radiation, discussed in Section G.1). This observation confirms that increased divertor closure can also facilitate the detachment process with nitrogen seeding as reduced nitrogen concentration is required.

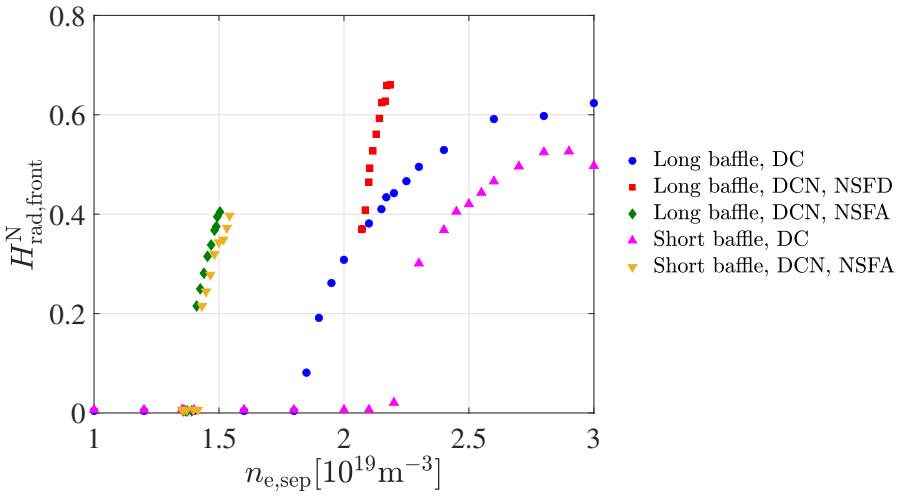

FIGURE 4.39. : Evolution of normalized radiation front height as a function of $n_{e,sep}$.

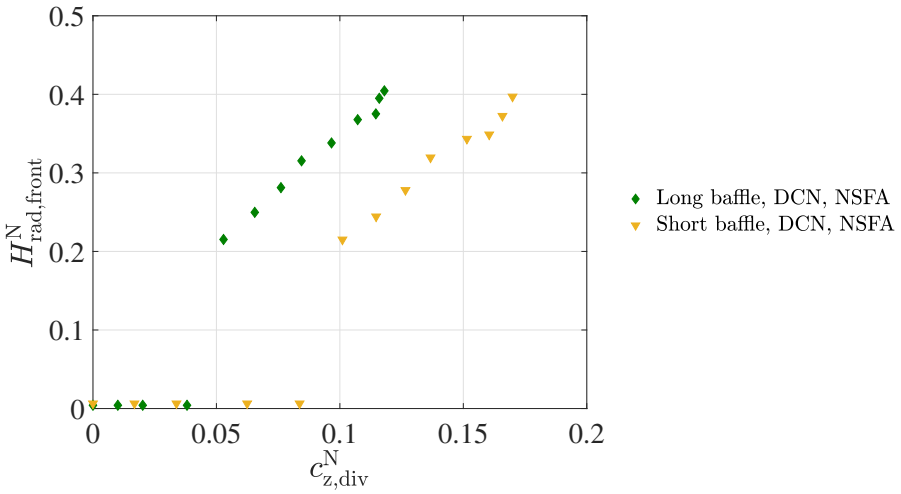

FIGURE 4.40. : Evolution of normalized radiation front height as a function of nitrogen concentration.

TCV cases with or without nitrogen seeding show different results in $\hat{T}_{e,t}$ threshold for detachment as shown in Figure 4.41a. Two cases without nitrogen seeding detach at $\hat{T}_{e,t} \approx 2.5\,eV$, while two cases with nitrogen seeding (starting from attached) detach at $\hat{T}_{e,t} \approx 5\,eV$. When a sufficient amount of nitrogen is present, it is possible to radiate enough power to achieve detachment even at higher divertor temperatures (between 5–10 eV). In contrast, if nitrogen seeding is not used, a lower divertor temperature (2.5–5 eV) is required to achieve a similar level of power dissipation. Despite the difference in target temperature threshold influenced by nitrogen, we observe approximately the same heat flux threshold $\approx 2.3\,MW/m^2$ for the radiation front to begin moving upward from the target, as shown in Figure 4.41b. Furthermore, the lower radiation front in the nitrogen seeding case (Figure 4.38) can also be verified through Figure 4.41b, where one can observe that the radiation front height in the high nitrogen concentration case is generally lower than the one with lower nitrogen concentration or without nitrogen for a given target heat load in deeply detached divertor.

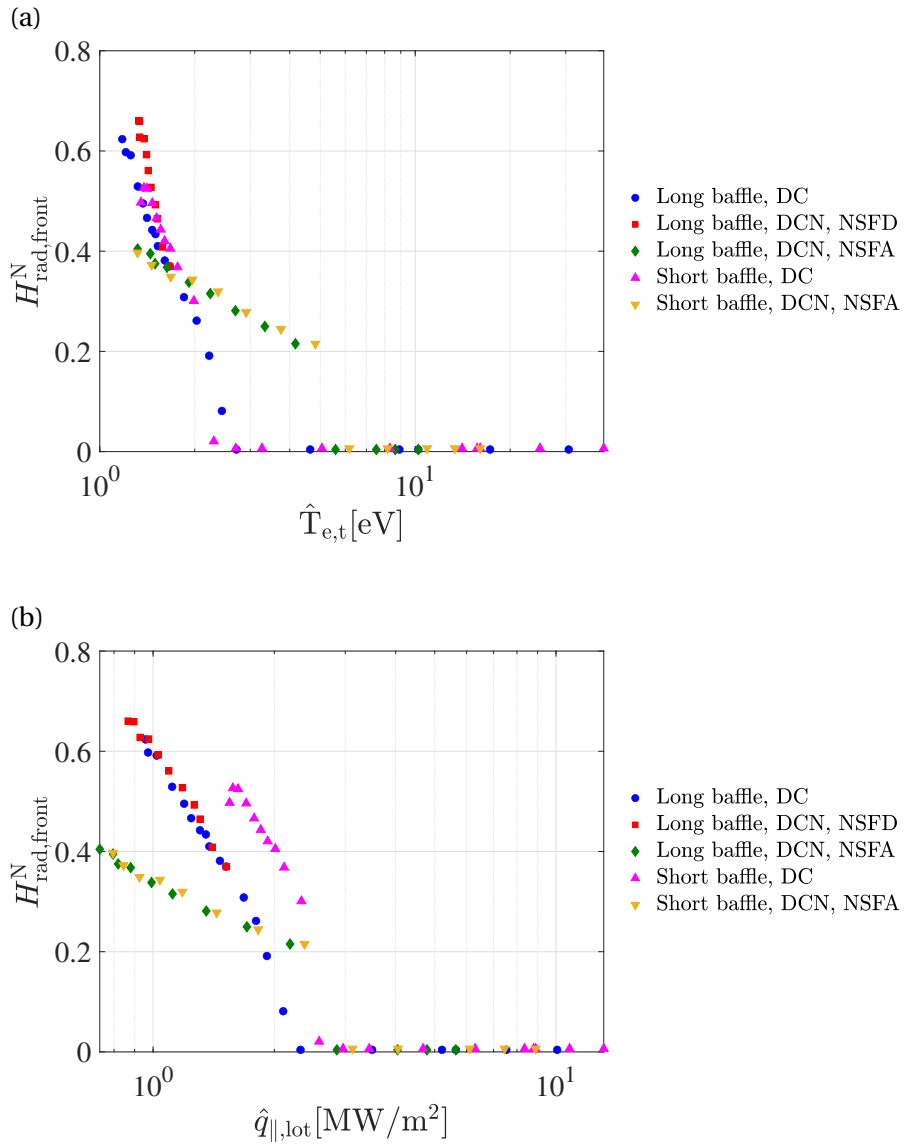

FIGURE 4.41. : (a) Evolution of normalized radiation front height as a function of peak electron temperature at the outer target, and (b) as a function of peak parallel heat flux at the outer target.

4.3. Impact of heating power

In pure ohmic discharge, the heating source is driven by the ohmic resistance and current of plasma. The resistance can decrease with increased temperature as described by Spitzer conductivity, the efficiency of ohmic heating will decrease at higher temperatures. Further auxiliary heating systems are thus needed to heat the plasma to the required ignition temperature [80]. With the influence of drifts, the higher input

power can increase the asymmetry of outer and inner energy (E_{outer} and E_{inner}, respectively) in JET simulation [78]. High power throughput is also a regular statute for actively running devices. It would be interesting to know about the characteristics of the high heating power case. There are two types of power increase : one is increasing the input power by methods like NBI, where the $\mathbf{B}_\theta$ is not obviously influenced; and the other is increasing the plasma current, which can influence the $\mathbf{B}_\theta$. Here, we will discuss the situation where $\mathbf{B}_\theta$ remains unchanged.

4.3.1. Evolution of target density profile

In this section, we will investigate the impact of input power on the evolution of the density profile at the outer target based on the WEST simulation case discussed in Section 3.2.1.3. We will also take into account the influence of drifts in the forward field. The results of the low input power case ($P^{\text{sim}}_{\text{in,edge}} = 0.45\,\text{MW}$), with and without drifts, are shown in Figure 4.42. It can be observed that the peak target density generally increases as $n_{\text{e,sep}}$ increases. However, after $n_{\text{e,sep}}$ exceeds a certain threshold ($n_{\text{e,sep}} \approx 2.70 \times 10^{19}\,\text{m}^{-3}$), the peak target density saturates or decreases. A significant decrease in target peak density is found in the case with no drifts, indicating strong plasma recombination. On the other hand, the case with drifts presents a saturated target peak density after exceeding the threshold due to a relatively higher target temperature, as illustrated in Section E.2.3.

For the radial position of the density peak, it can be observed that the density peak remains stuck at the separatrix in the case with drifts (Figure 4.42a). This is due to the radial $\mathbf{E}_\theta \times \mathbf{B}_\phi$ drift flow, which directs plasma from the outer SOL into the main plasma (and into the private plasma below the X-point). On the other hand, in the absence of drifts, the position of the density peak monotonically moves outward as $n_{\text{e,sep}}$ increases (Figure 4.42b).

When high input power ($P^{\text{sim}}_{\text{in,edge}} = 2\,\text{MW}$) is applied, the saturation of peak density in the case with drifts, and the significant decrease in peak density in the case with no drifts, after $n_{\text{e,sep}}$ exceeds a certain threshold, remain the same as in the low input power situation (Figure 4.43). The density peak positions still remain close to the separatrix in the case with drifts. However, the density peak positions in the case with no drifts exhibit different characteristics compared to the previous low power situation : the radial position of the density peak gradually moves towards the separatrix with increasing $n_{\text{e,sep}}$, and then moves away from the separatrix after $n_{\text{e,sep}}$ exceeds the threshold corresponding to the maximum target density reached.

The formation of the density peak is due to the competition of particle flux transport between parallel and perpendicular components in the divertor volume. In the cases with no drifts, as the $n_{\text{e,sep}}$ increases, the fraction of perpendicular particle flux becomes higher, leading to the monotonic outward movement of the radial position of the density peak in the low input power case. The different behavior of density peak movement in the high input power case indicates that the fraction of the perpendicular component is relatively high at low $n_{\text{e,sep}}$, then gradually decreases before reaching the maximum target density. After exceeding the threshold, the fraction of

the perpendicular component starts to increase. More work still needs to be done to understand this phenomenon. The radial position of the density peak in the cases with drifts does not seem to be obviously influenced by the varied input power, indicating that the $\mathbf{E}_\theta \times \mathbf{B}_\phi$ flow is relatively stronger than the perpendicular diffusion transport (from SOL to PFR).

In addition, the double peak is only observed in the high input power case with drifts, as shown in Figure 4.43a. The profiles exhibiting a double peak correspond to $n_{\mathrm{e,sep}}$ ranging from $3.00 \times 10^{19}\,\mathrm{m}^{-3}$ to $3.85 \times 10^{19}\,\mathrm{m}^{-3}$, which happen to be the plasma in high-recycling regimes. When the plasma detaches, the double peak will disappear. This observation highlights the importance of high input power, drifts, and high recycling regimes in obtaining the double peak profile.

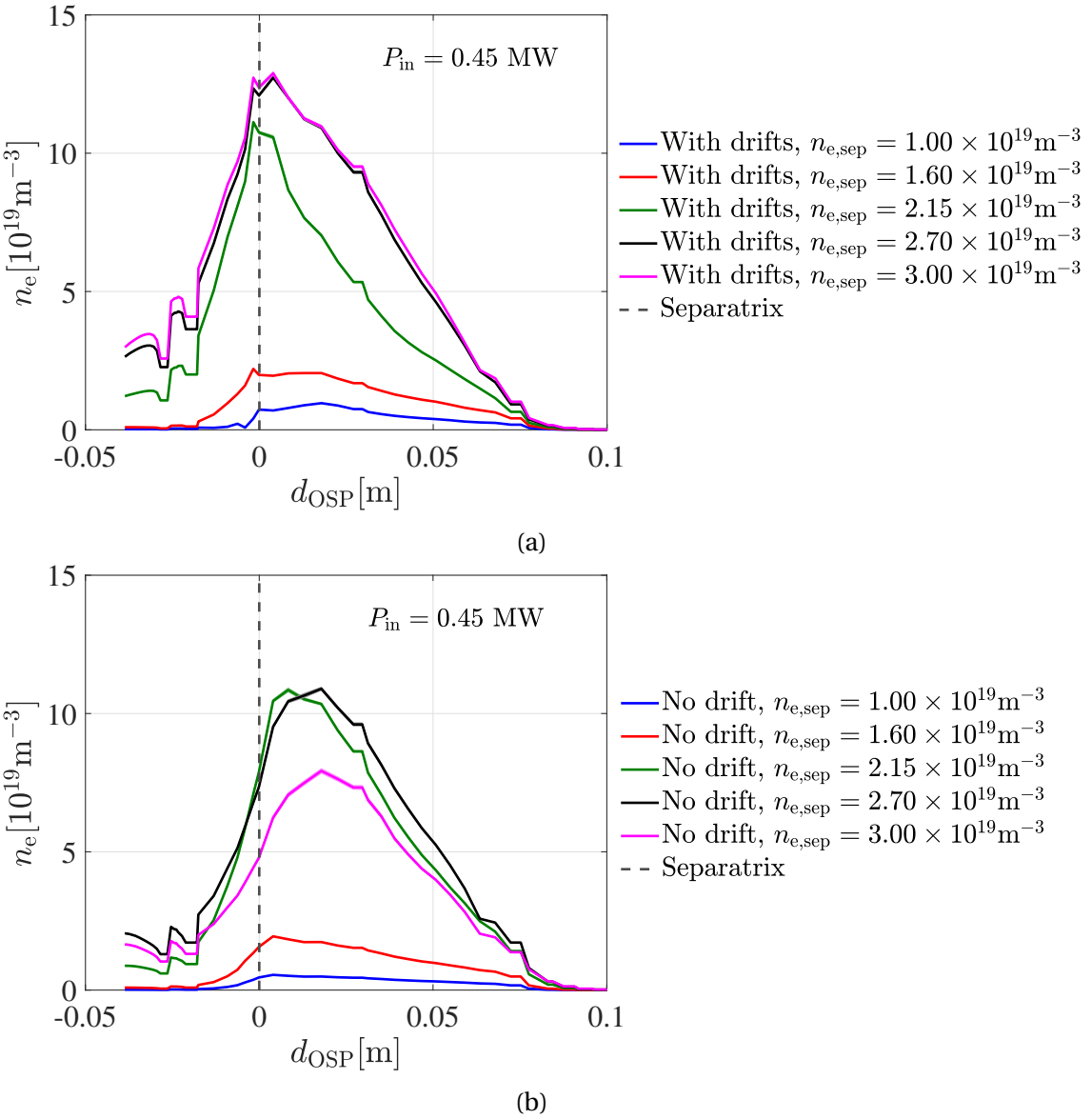

FIGURE 4.42. : (a) Evolution of density profile at the outer target with increasing $n_{e,sep}$ in the low input power case with drifts. (b) Evolution of density profile at the outer target with increasing $n_{e,sep}$ in the low input power case with no drifts. d_{OSP} is the radial distance from the outer strike point, negative values are in the PFR, positive values are in the SOL. The dashed line represents the position of separatrix.

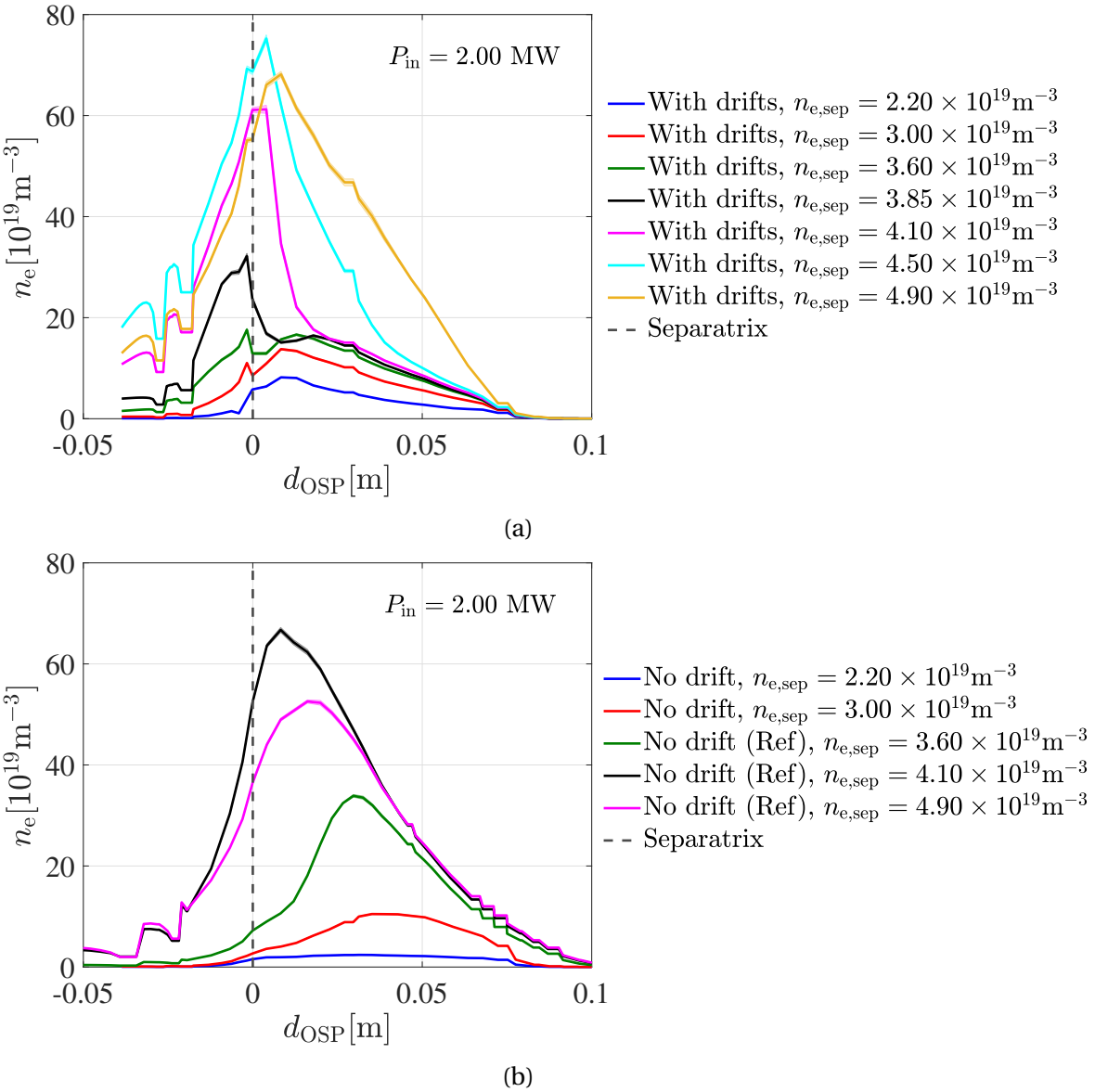

FIGURE 4.43. : (a) Evolution of density profile at the outer target with increasing $n_{e,sep}$ in the high input power case with drifts. (b) Evolution of density profile at the outer target with increasing $n_{e,sep}$ in the high input power case with no drifts. The three reference cases (with consistent simulation setups and a similar magnetic configuration) are used to give reference for the target density profiles at higher $n_{e,sep}$. d_{OSP} is the radial distance from the outer strike point, negative values are in the PFR, positive values are in the SOL. The dashed line represents the position of separatrix.

4.3.2. Impact of leakage under high heating power

The baffle leakage has been discussed in Section 4.1.1. Here, we will discuss the impact of leakage in high input power case, and compare it with the low input power one. The cases analyzed in this section are based on the simulation of discharge #54903 with no drifts (Section 4.1.1), constant diffusion coefficients, and variable input power (0.45 MW → 2 MW). For simplicity, we just make the comparison between the case with no leak and the case with small leak.

4.3.2.1. Detachment threshold

The evolution of particle flux at the outer target as a function of $n_{e,sep}$ is shown in Figure 4.44, we can see that the range of both the particle flux at the outer target and upstream density $n_{e,sep}$ is generally increased when higher heating power is applied. The impact of leakage on detachment is still the same despite a higher heating power applied : lower $n_{e,sep}$ required to achieve detachment. The peak target density is found to be nearly saturated in both cases after the rollover of particle flux happens as shown in 4.45. From the evolution of the target peak temperature as a function of upstream density $n_{e,sep}$ shown in Figure 4.46, one can see that high and low heating power cases have a similar operational range of target temperature from 40 eV to 1 eV, in the range of $n_{e,sep}$ studied. However, the higher heating power case presents a sharper temperature decrease when it starts to detach. For the evolution of radiator height as a function of target temperature as shown in Figure 4.47, the detachment process in the higher heating power case seems to be slower and more difficult to reach the same height compare to low heating power case. The leakage still shows no influence on the relationship between radiator height and target temperature for cases with the same input power.

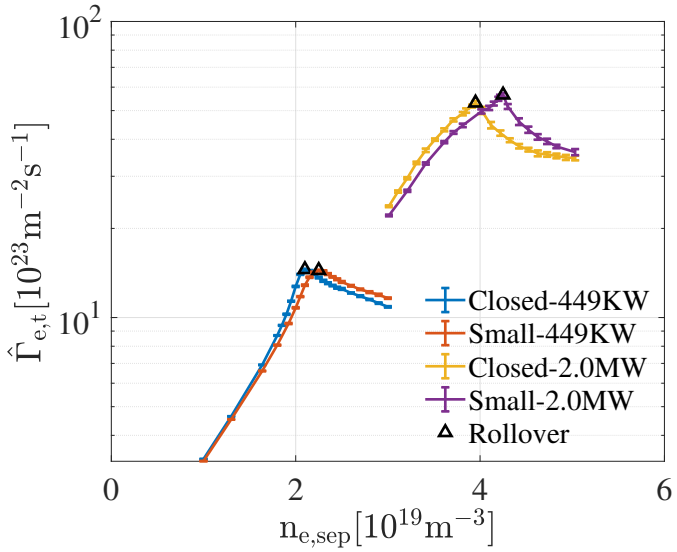

FIGURE 4.44. : Evolution of peak electron particle flux Γ_e at the outer target as a function of upstream $n_{e,sep}$. The black triangle on each curve marks the point when the rollover of Γ_e happens.

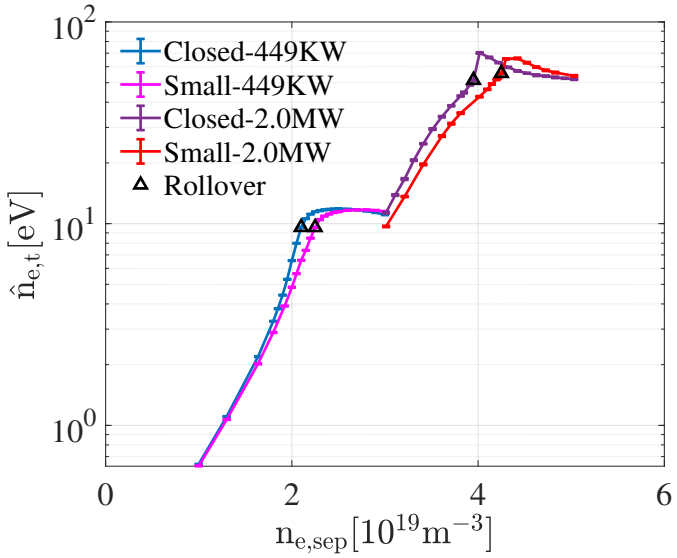

FIGURE 4.45. : Evolution of peak electron density at the outer target as a function of upstream $n_{e,sep}$. The black triangle on each curve marks the point when the rollover of Γ_e happens.

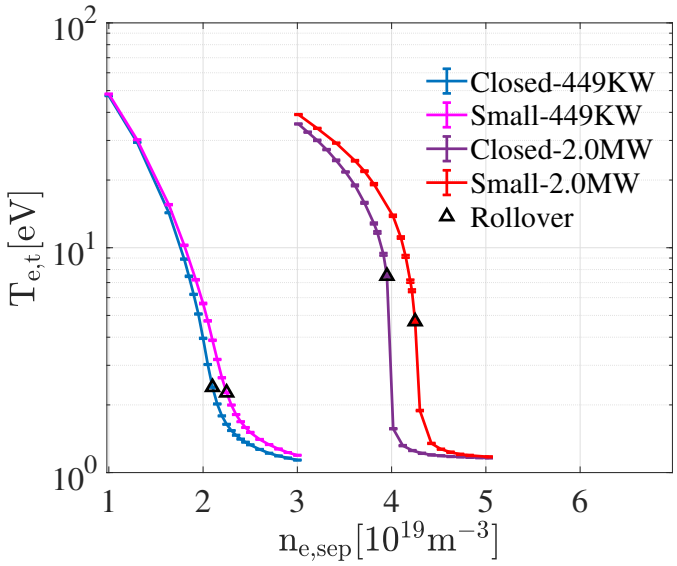

FIGURE 4.46. : Evolution of peak electron temperature T_e at the outer target as a function of upstream $n_{e,sep}$. The black triangle on each curve marks the point when the rollover of Γ_e happens.

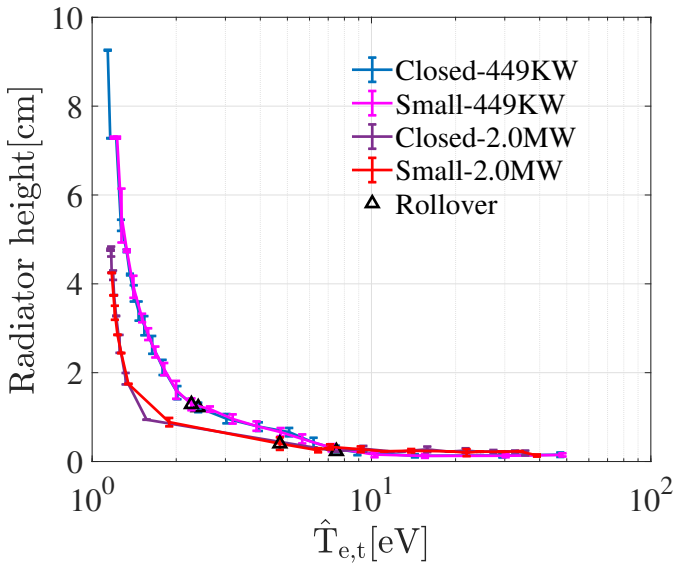

FIGURE 4.47. : Evolution of the vertical distance between the position of radiator (radiation peak) and target. The black triangle on each curve marks the point when the rollover of Γ_e happens.

4.3.2.2. Neutral transport

In Figure 4.48, we can see that the case with less leakage corresponds to a higher compression ratio. Nevertheless, higher heating power can further increase the neutral compression ratio. The neutral compression ratio is defined as the ratio between the

average neutral pressure at the outer target and that on the near-wall OMP position. We can check the relative change of these two components : Figure 4.49 shows that when higher heating power is applied, the neutral pressure at the target can increase by a factor of about 5 for both baffle closed and small leak cases. However, the situation of neutral pressure on the near-wall OMP is a little different, as shown in Figure 4.50. The baffle closed case shows a slight change of neutral pressure with higher input power, but the case with a small leak presents an obvious increase due to the function of leakage under the baffle. Generally, the influence of high heating power on the neutral confinement in the divertor region is stronger than that in the upstream region because of better capability in trapping neutral particles in the divertor when heating power increases. This can be explained by the fact that a smaller fraction of neutral particles can escape from the divertor in a higher heating case, attributed to the shorter ionization mean-free path of D_0 [80].

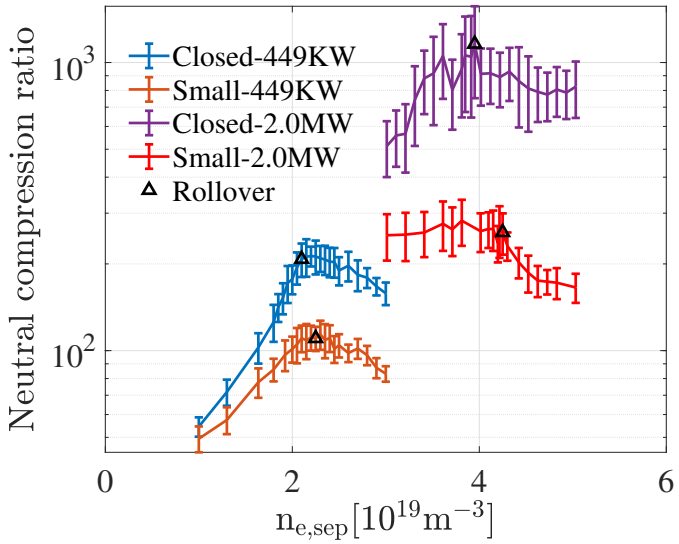

FIGURE 4.48. : Evolution of the neutral compression ratio (ratio between the average neutral pressure at the outer target and the near-wall OMP position). The black triangle on each curve marks the point when the rollover of Γ_e happens.

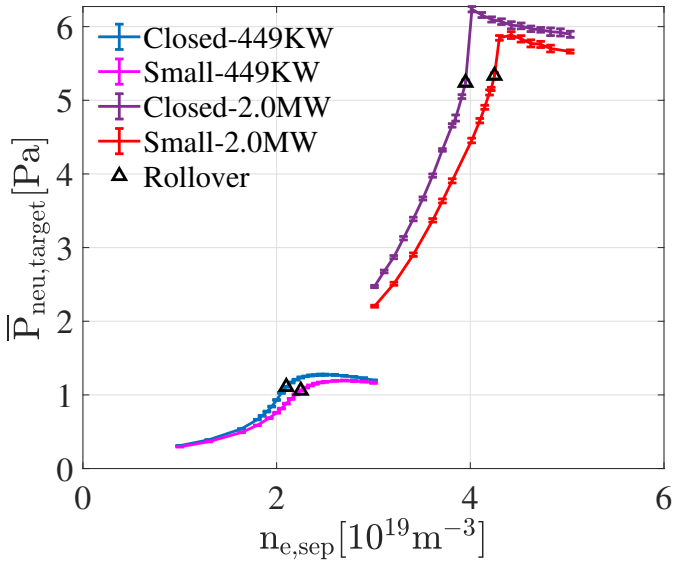

FIGURE 4.49. : Evolution of the average neutral pressure at the outer target. The black triangle on each curve marks the point when the rollover of Γ_e happens.

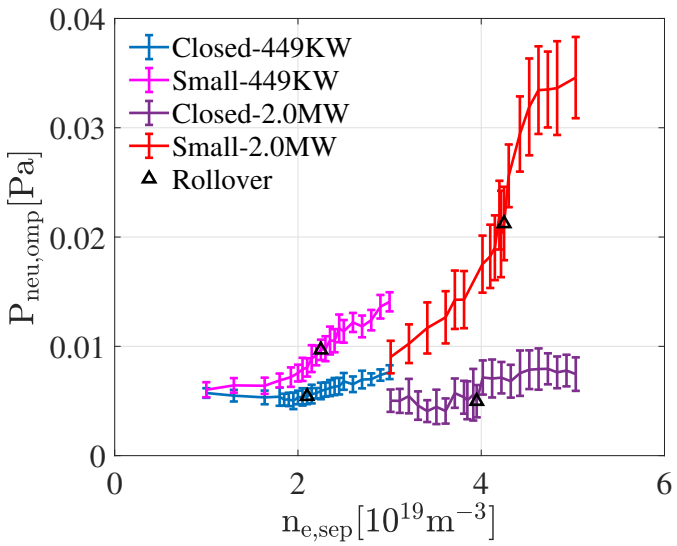

FIGURE 4.50. : Evolution of the average neutral pressure the near-wall OMP. The black triangle on each curve marks the point when the rollover of Γ_e happens.

4.4. Summary of the impacts on detachment threshold

The impacts of divertor closure, nitrogen, and heating power on detachment have been studied. The rollover of particle flux is usually used as the criterion for detachment. However, simulations with nitrogen in Section 4.2 show that the ramped nitrogen

seeding rate leads to a direct decrease in the target particle flux, even if it is still far from the detached regime, making it difficult to identify the threshold of particle flux rollover and divertor detachment.

The detachment of the radiation front from the divertor target is a straightforward indicator of detached plasma, which can replace the rollover of particle flux as a more general criterion for detachment, particularly when nitrogen seeding is involved. We found that the detachment of the radiation front usually occurs earlier than the rollover of particle flux (Figure 3.40), so the detachment threshold may correspond to a situation when the radiation front has a certain distance from the target plate. We can use the normalized radiation front height $H^{\mathrm{N}}_{\mathrm{rad}}$ (Section 3.2.3) to describe the relative distance between the radiation front and the target plate.

Figure 4.51 shows the evolution of the normalized radiation front height as a function of the outer target peak temperature, including five cases : TCV case with long and short baffle (Section 4.1.2), WEST low input power case with and without baffle ($P^{\mathrm{sim}}_{\mathrm{in,edge}} = 0.45\,\mathrm{MW}$, Section 4.1.1), and WEST high input power case ($P^{\mathrm{sim}}_{\mathrm{in,edge}} = 2\,\mathrm{MW}$, Section 4.3.2). These cases have low impurity concentration or pure deuterium, showing the rollover of particle flux. The black circle marks the point when the rollover of particle flux happens. It can be observed that the rollover of particle flux may occur at different $H^{\mathrm{N}}_{\mathrm{rad}}$ values. The higher input power case has a lower $H^{\mathrm{N}}_{\mathrm{rad}}$ when the rollover happens. However, the rollover of particle flux does not always correspond to a lower target temperature. For example, $T_{\mathrm{e,t}}$ can be 7.5 eV when the rollover happens in the high input power case, but a relatively higher $H^{\mathrm{N}}_{\mathrm{rad}}$ always corresponds to a low target temperature. When $H^{\mathrm{N}}_{\mathrm{rad}} \geq 0.05$, $T_{\mathrm{e,t}}$ is generally lower than 3 eV.

Thus, we can approximately set $H^{\mathrm{N}}_{\mathrm{rad}} = 0.05$ as a criterion for detachment, which provides more reliable performance in determining whether the target has been protected compared with the detachment criterion based on the rollover of particle flux.

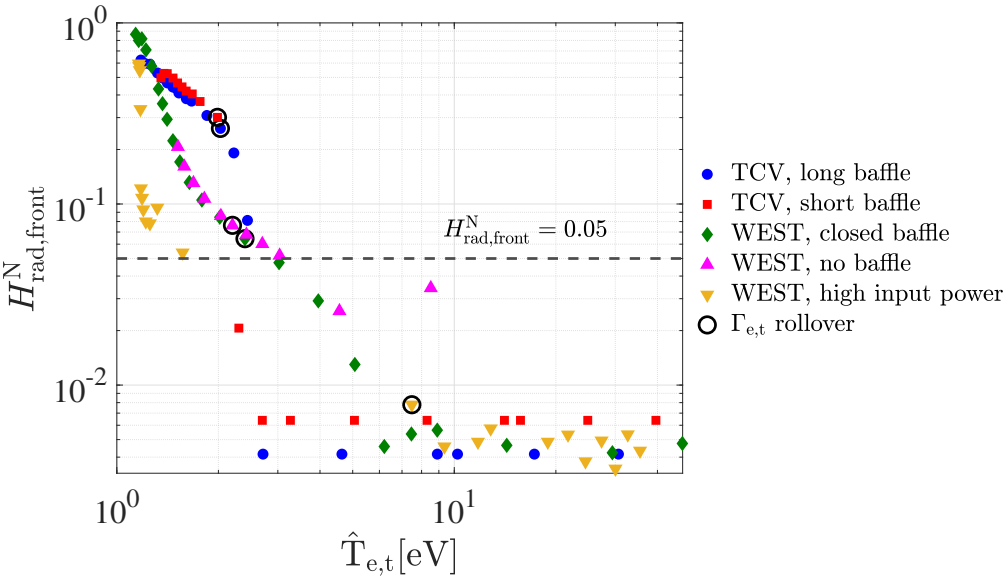

FIGURE 4.51. : Evolution of normalized radiation front height as a function of outer target peak temperature. The black circle marks the point when the rollover of Γ_e happens in the corresponding case.

Based on the analysis conducted in this chapter, we can summarize the impact of wall geometry, particles, and energy sources on the radiation front detachment threshold of several variables, as illustrated in Table 4.2. The target temperature, target heat flux, divertor neutral pressure, line integral density near X-point, and normalized radiation front height exhibit potential for identifying or controlling detached plasma, due to the consistent threshold observed in situations involving variable divertor closure, impurity concentration, and input power. However, reliable measurements of the target temperature and target heat flux become challenging when the plasma is detached due to limitations in diagnostic methods. The divertor neutral pressure diagnostic also shows significant time delays and instabilities when estimated using the Baratron gauge. In complex scenarios, a more practical solution to control detachment might be to employ the line integral density near X-point and normalized radiation front.

Variables	**Diagnostics**	**Impact on detachment threshold (behavior) of variables**		
		Better divertor closure WEST & TCV	**Higher impurities concentration TCV**	**Higher input power P_{in} WEST**
Upstream separatrix density $n_{e,sep}$	Reflectometer	Up to 15% lower threshold	Up to 24% lower threshold	Up to 96% higher threshold
D_2 puff rate	Gas valve	Up to 1100% higher threshold in WEST/ Consistent threshold in TCV	Up to 45% lower threshold	Up to 520% higher threshold
Divertor radiation $P_{rad,div}$	Bolometry	Up to 17% higher threshold in WEST/ Consistent threshold in TCV	Up to 36% higher threshold	Up to 470% higher threshold
Target temperature T_{et}	Langmuir probe not reliable when $T_{et} < 5$ eV	Consistent threshold $2-3$ eV	Up to 71% higher threshold 2.4 eV in pure D	Consistent threshold $2-3$ eV
Target heat flux $q_{\parallel,t}$	Infrared thermography not reliable when detached	Consistent threshold	Consistent threshold	Up to 160% higher threshold
Divertor neutral pressure $P_{neu,div}$	Baratron gauge relatively big oscillation	Consistent threshold	Up to 43% lower threshold	Up to 470% higher threshold
Line integral density near X-point $n_{e,int,X}$	Interfermetry	Consistent threshold	Up to 38% lower threshold	Up to 360% higher threshold
Rollover of particle flux $\Gamma_{\parallel,t}$	Langmuir probe	Rollover happens with Cst. P_{in}	Direct decrease of $\Gamma_{\parallel,t}$ with ramped nitrogen seeding	Rollover happens with Cst. P_{in}
Normalized radiation front height H^{N}_{rad}	Visible camera Spectroscopy	Consistent threshold: $H^{N}_{rad} = 0.05$ the straightforward appearance of detached plasma		

TABLE 4.2. : Impact of divertor closure, impurities concentration, and input power on detachment threshold of several variables in WEST and TCV. Consistent threshold (in green block) indicates the change of threshold is less than 5%.

5. Detachment control strategy

Sommaire

Several detachment control methods have been developed based on analyzing the target particle flux, radiation front or radiation center, and radiated power (Section 1.6). However, there will be challenges in controlling detachment in future high-power devices such as DEMO. This is because DEMO will inevitably require very high input power to achieve ignition. Following the control strategies based on analyzing the rollover of particle flux, the high input power needs to be provided from the beginning during the transition from the attached regime (with high heat flux) to the detached regime (with low heat flux). The transition state, which can last for a certain duration with nearly constant high input power, is dangerous and can potentially damage the device or reduce the lifetime of DEMO, particularly when considering that detachment control will be frequently performed. This is because each pulse has a limited duration (up to 30 minutes in ITER) at the moment.

A better way to reach ignition in DEMO is to first start the discharge with relatively low input power, control the plasma to reach detachment, and then gradually increase the input power while keeping the radiation front at a certain distance from the target. This should be done until the ignition is reached. This strategy can maintain the erosion of the target tile by plasma heat load at a low level, even in the transition phase, and provide a higher level of protection for the target tile. This process requires maintaining the detachment level unchanged with increasing input power and possibly involving impurity seeding to facilitate detachment maintenance at high input power. Additionally, divertor closure can be influenced by the distance from separatrix to the baffle tip. Instabilities in the magnetic configuration can trigger the variable divertor closure, thus increasing the difficulties in stable detachment control. Therefore, it is important to find a proper detachment control strategy based on variables that are highly related to the detachment level and are not influenced by complex situations such as variable input power, impurity concentration, and divertor closure.

5.1. A general criterion for detachment

We understand that detachment occurs when the power entering the divertor is largely radiated, causing the temperature of the target to become very low. This results in neutral particles recycled from the target being less likely to be ionized in the vicinity of their origin. As a result, the ionization front can move away from the target, achieving the so-called detachment. Therefore, we can attempt to assess the balance between the power entering (from upstream) and the power radiated in the divertor to establish a criterion for detachment.

It can be assumed that the power entering the divertor is primarily transported through thermal conduction until the divertor detachment is achieved. To evaluate the heating power transported by thermal conduction, one can refer to the heat conductivity equation from the 2PM (Section 2.6.1), as shown below :

$$T_{\mathrm{eu}}^{7/2} - T_{\mathrm{e,div}}^{7/2} = \frac{7 q_{\parallel \mathrm{cond}} L}{2 k_{0\mathrm{e}}}, \tag{5.1}$$

where T_{eu} represents the upstream temperature, $T_{\mathrm{e,div}}$ represents the divertor temperature. When the plasma is attached, $T_{\mathrm{e,div}}$ is approximately equal to the target temperature T_{et}. When the plasma is detached, $T_{\mathrm{e,div}}$ is approximately equal to the averaged temperature in the radiation front, allowing for a reasonable estimation of conduction power. $q_{\parallel \mathrm{cond}}$ represents the parallel heat flux carried by thermal conduction, L is the parallel connection length between the upstream and the target, and $k_{0\mathrm{e}}$ is the electron conductivity coefficient. The heat power P_{cond} that enters the divertor carried by thermal conduction, can be obtained by multiplying $q_{\parallel \mathrm{cond}}$ by the effective poloidal area A_{eff} :

$$\begin{aligned} P_{\mathrm{cond}} &= q_{\parallel \mathrm{cond}} A_{\mathrm{eff}} \\ &\approx (T_{\mathrm{eu}}^{7/2} - T_{\mathrm{e,div}}^{7/2}) \times \frac{2 k_{0\mathrm{e}}}{7 L} \times \frac{2 \pi a \lambda_{\mathrm{q}}}{q_{\mathrm{s}}}, \end{aligned} \tag{5.2}$$

where λ_{q} represents the decay length of the parallel heat flux, a is the minor radius, and q_{s} denotes the safety factor. Considering that in our simulation cases (Section 3), the outer target requires slightly higher $n_{\mathrm{e,sep}}$ to achieve detachment compared with the inner target in WEST, while only the outer target detaches in TCV in the range of $n_{\mathrm{e,sep}}$ investigated, the outer target in both devices presents the importance in investigating detachment. Thus, we will focus on comparing the power carried by thermal conduction P_{cond}, and the power radiation P_{rad}, in the LFS. The radiation power P_{rad} is estimated in the outer target region and denoted as $P_{\mathrm{rad,ot}}$ (integrated power radiation in the cyan polygon shown in Figure 5.1).

Based on the WEST simulation cases with drifts in Section 3.2.1.3, the evolution of conductive power P_{cond}, and radiation power $P_{\mathrm{rad,ot}}$, as a function of $n_{\mathrm{e,sep}}$ are shown in Figure 5.2. The figure includes cases with low input power ($P_{\mathrm{in,edge}}^{\mathrm{sim}} = 0.45\,\mathrm{MW}$) and high input power ($P_{\mathrm{in,edge}}^{\mathrm{sim}} = 2.00\,\mathrm{MW}$). It can be observed that the power carried by thermal conduction continuously decreases while the power radiated increases. There

are two intersections ($P_{\text{cond}} = P_{\text{rad,ot}}$), which correspond to two threshold values : $n_{\text{e,sep}} = 2.03 \times 10^{19}\ \text{m}^{-3}$ for the low input power case, and $n_{\text{e,sep}} = 4.59 \times 10^{19}\ \text{m}^{-3}$ for the high input power case.

Next, the evolution of normalized radiation front height of the two cases is plotted in Figure 5.3, with the threshold values for detachment marked by dashed lines. It can be observed that the normalized radiation front height is approximately 0.05 when reaching the threshold value in both cases, indicating the divertor detachment. The 2D maps of radiation in the two cases corresponding to the $P_{\text{cond}} = P_{\text{rad,ot}}$ threshold are shown in Figure 5.4.

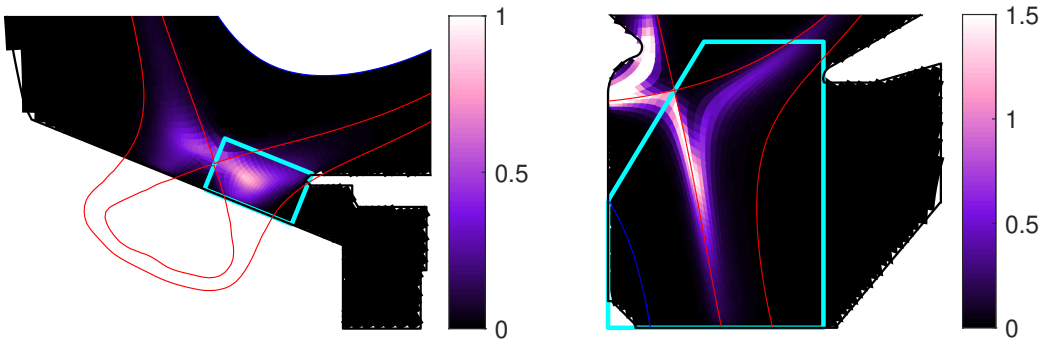

(a) $P_{\text{rad}}[\text{MW/m}^3]$ in WEST case (b) $P_{\text{rad}}[\text{MW/m}^3]$ in TCV case

FIGURE 5.1. : 2D maps of power radiation in WEST and TCV, the cyan polygon in each figure encloses the outer target region where P_{rad} or $P_{\text{rad,ot}}$ that mentioned in this section is integrated.

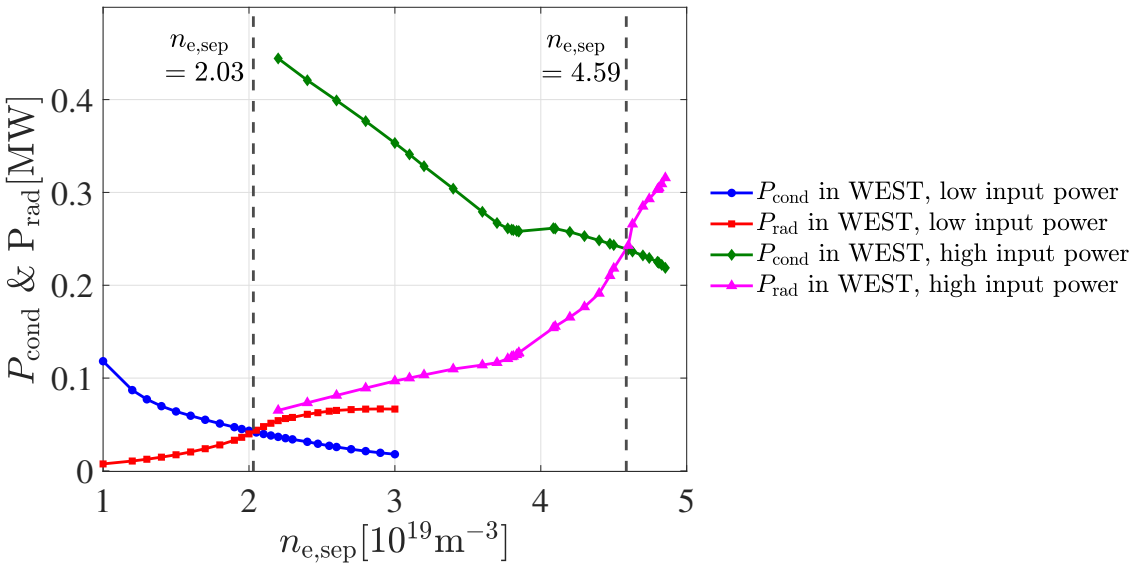

FIGURE 5.2. : Evolution of radiation and conductive power at divertor outer leg in WEST as a function of $n_{\text{e,sep}}$.

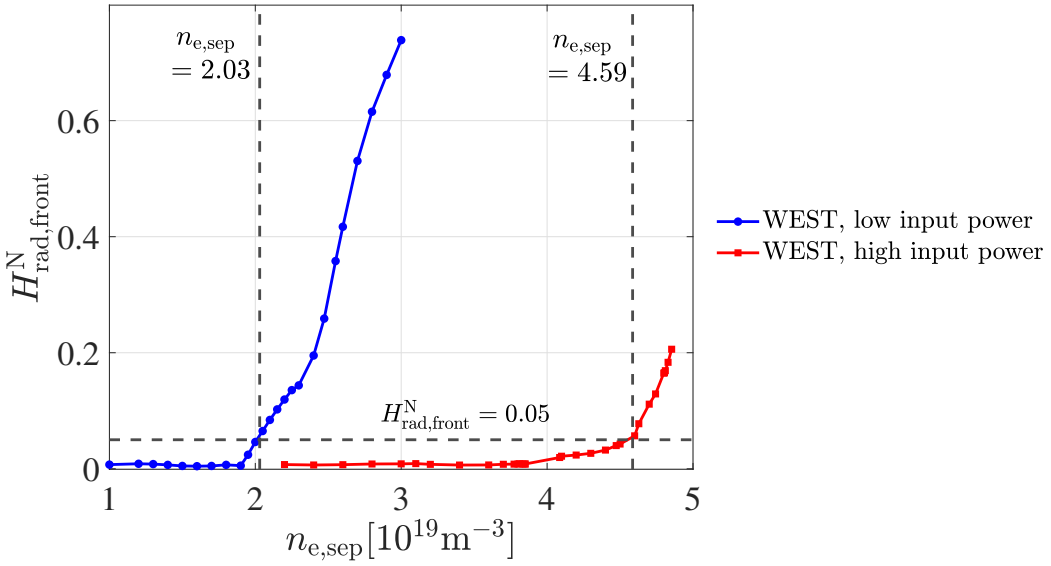

FIGURE 5.3. : Evolution of normalized radiation front height as a function of $n_{e,sep}$. The dashed lines correspond to the threshold values where $P_{cond} = P_{rad}$ in low and high input power cases.

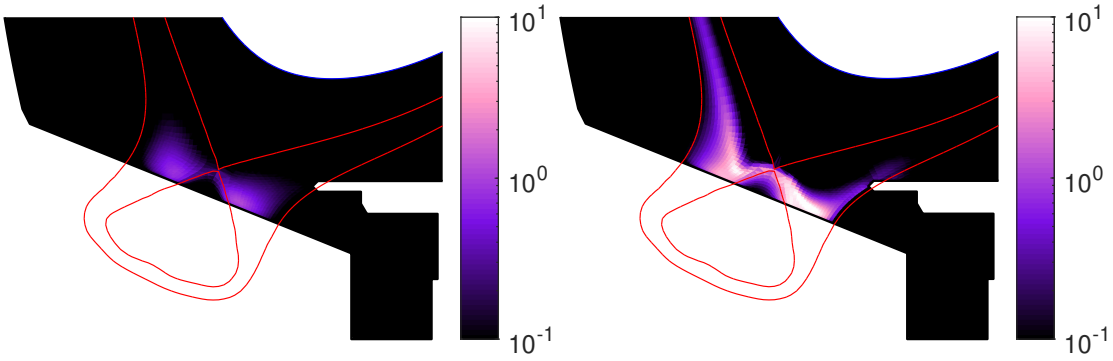

(a) P_{rad}[MW/m^3] in WEST case with $P^{sim}_{in,edge}$ = 0.45 MW, $n_{e,sep}$ = 2.00 × 10^{19} m^{-3}

(b) P_{rad}[MW/m^3] in WEST case with $P^{sim}_{in,edge}$ = 2.00 MW, $n_{e,sep}$ = 4.60 × 10^{19} m^{-3}

FIGURE 5.4. : 2D maps of power radiation, corresponding to the threshold value of low and high input power cases in Figure 5.2.

From the WEST simulation results above, it has been preliminarily verified that the detachment threshold is related to the moment when $P_{cond} = P_{rad}$. The ratio between P_{rad} and P_{cond}, denoted as R_D, is of interest for detachment control. Since the connection length is approximately $L \approx \pi R q_s$ (where R is the major radius), and $T_{e,div}$ is only a few eV (4–6 eV) when the plasma is detached and much smaller than T_{eu}, $T_{e,div}$ can be neglected. Therefore, R_D can be evaluated using the following equation :

$$R_D = \frac{7 R q_s^2 P_{rad}}{4 a k_{0e} \lambda_q T_{eu}^{7/2}}, \tag{5.3}$$

where the decay length of heat flux λ_q is obtained by :

$$\lambda_q \sim \frac{2}{7}\lambda_T \tag{5.4}$$

The reason for evaluating λ_q using Equation 5.4 is that this approach provides a reasonable estimation of λ_q that is not influenced by the divertor condition (as discussed in Section 2.5.2). Most of the inputs of R_D are approximately constant parameters, as shown in Table 5.1. It should be noted that the decay length of heat flux, λ_q, slightly increases as a function of $n_{e,sep}$. When calculating R_D in each simulation case in this section, λ_q is evaluated using Equation 5.4, despite the fact that using a constant λ_q does not significantly affect the performance of R_D. As a reference, in Table 5.1, we provide the value of λ_q when the plasma starts to detach.

Discharge	WEST #56420	TCV #70690
Major radius R[m]	2.50	0.88
Minor radius a [m]	0.44	0.22
Safety factor q_s (at $\psi_N = 0.95$)	3.71	3.72
Decay length of heat flux λ_q [mm]	10.00	2.34
Electron conductivity coefficient k_{0e}	2000	

TABLE 5.1. : The inputs of R_D in WEST and TCV discharges.

Some representative simulation cases (Table 5.2) discussed in this thesis were selected to assess the reliability of R_D in various situations, such as different machine sizes, with or without drifts, and variable divertor closure, impurity concentration, and input power. The evolution of the normalized radiation front height as a function of R_D is shown in Figure 5.5 and 5.6. It can be observed that when $R_D = 1$, all the cases reach initiate detachment, which is consistent with our prediction. This robust threshold remains unaffected by varying impurity concentration, divertor closure, and input power, as it follows the principle of power balance, assuming that most of the conducted power is radiated when detachment is achieved. Additionally, the monotonic evolution of R_D as a function of target temperature (Figure 5.7) proves the reliability of using R_D to control divertor detachment during the transitions from the attached to the detached regime.

Simulation cases	Magnetic configuration	Baffle closure level	Divertor impurities concentration [%]	Input power [MW]	Drifts
WEST, closed baffle	#54903	High	0	0.45	No
WEST, medium baffle leakage	#54903	Medium	0	0.45	No
WEST, no baffle	#54903	Low	0	0.45	No
WEST, no drifts	#56420	High	0	0.45	No
WEST, with drifts	#56420	High	0	0.45	Yes
WEST, high input power	#56420	High	0	2	Yes
TCV, long baffle, no N seeding	#70690	High	0 (N)	0.21	No
TCV, long baffle, with N seeding	#70690	High	7 (N)	0.21	No
TCV, long baffle, high input power	#70690	High	7 (N)	0.5	No
TCV, short baffle, no N seeding	#70690	Medium	0 (N)	0.21	No
TCV, short baffle, with N seeding	#70690	Medium	10 (N)	0.21	No

TABLE 5.2. : Details about the simulation cases referred to in Figure 5.5–5.8 : The impurity concentration in the TCV cases mentioned in the table corresponds to the concentration of nitrogen when the plasma starts to detach. Additionally, the TCV cases exhibit carbon impurities resulting from sputtering, with concentration levels ranging from 1% to 2% when the plasma starts to detach.

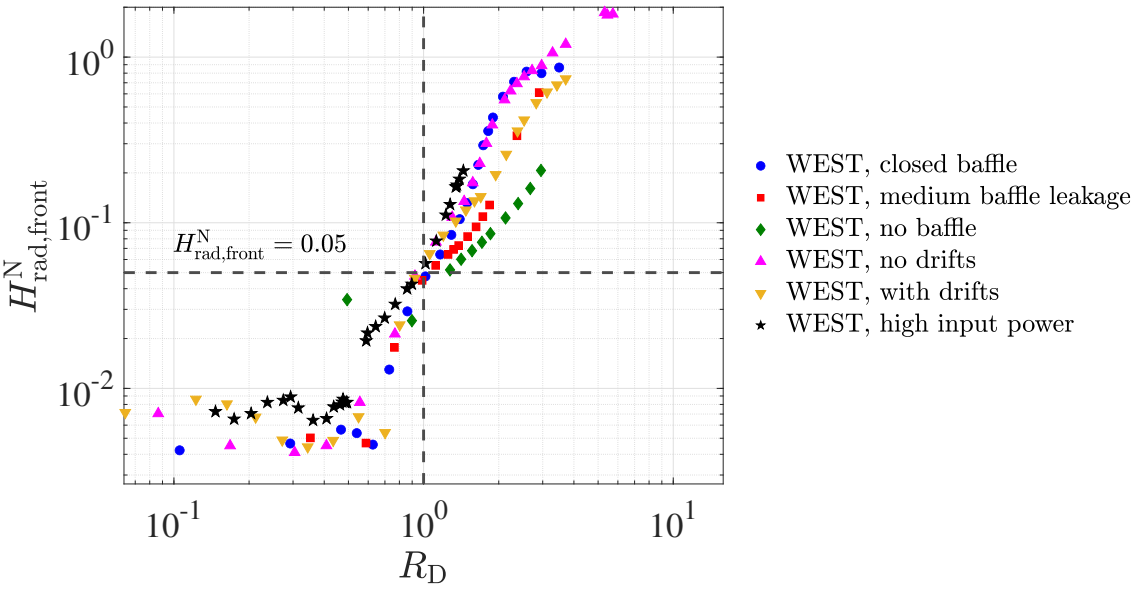

FIGURE 5.5. : Evolution of normalized radiation front height as a function of the ratio of detachment R_{D} in WEST.

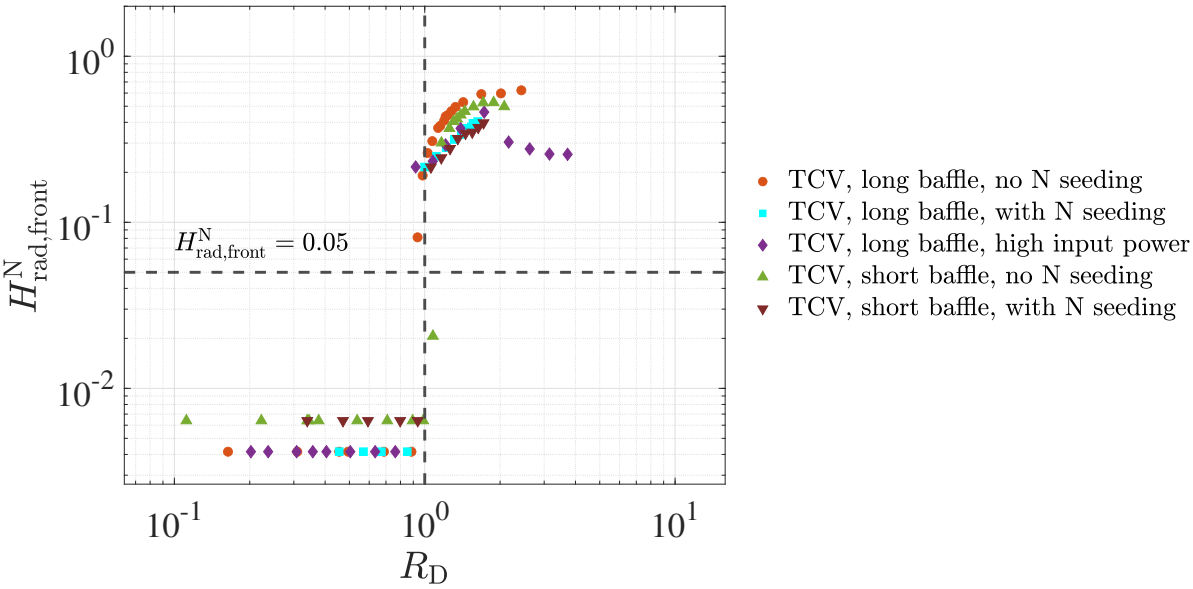

FIGURE 5.6. : Evolution of normalized radiation front height as a function of the ratio of detachment R_{D} in TCV.

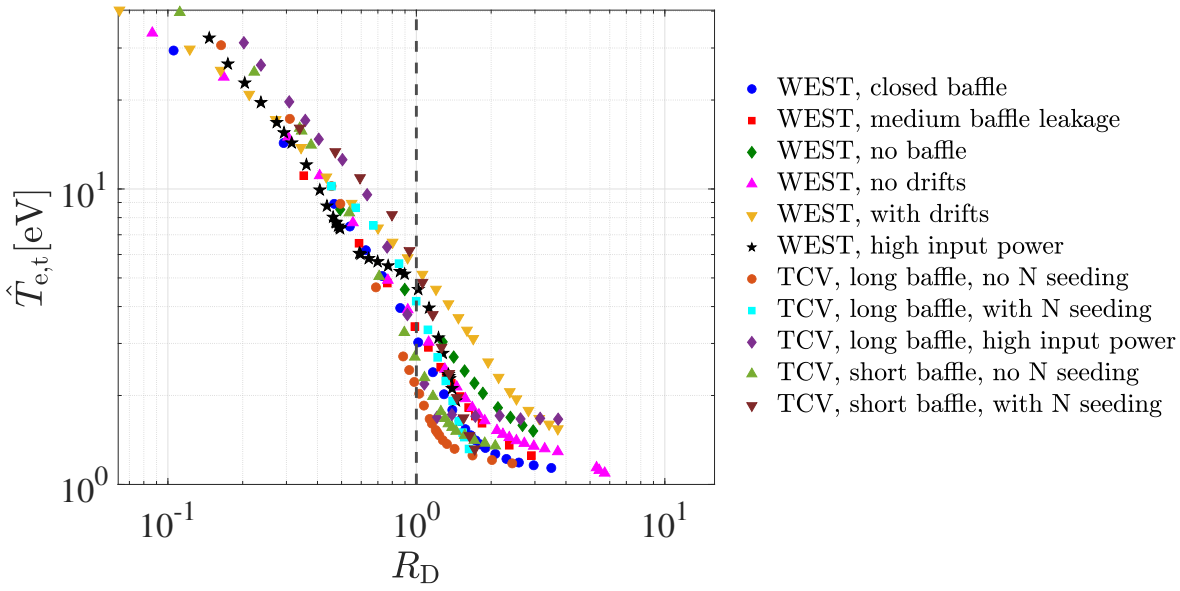

FIGURE 5.7. : Evolution of peak target temperature as a function of the ratio of detachment R_D in WEST and TCV.

It is possible to estimate the items in R_D (Equation 5.3) in the experiments :

- The outer divertor power radiation P_{rad}, it can be evaluated by bolometry signal (Section 3.2.1.5) returned from channel 2 as this line of sight covers the outer divertor region in WEST, Figure 3.20. The bolometry signal represents the radiated power integrated along the line of sight. There exist differences between the outer divertor region that is covered by channel 2 and the one covered by cyan polygon in Figure 5.1a; also, the signal from channel 2 is usually in a magnitude of 1×10^{-4} W, which is much smaller than the P_{rad} integrated in the outer divertor region, in a magnitude of 1×10^5 W. So the bolometry channel 2 signal needs to be scaled to replace P_{rad} to calculate R_D. To know the value of scaling factor, we calculated R_D in two ways, one is based on P_{rad} integrated in the outer divertor region, and another one is based on scaling factor times bolometry channel 2 signal obtained by SYNDI function, which relates the 2D power radiation in simulation to the experimental like bolometry diagnostic. It has been found that scaling factor = 6.5×10^8 can make R_D calculated from two ways have a good match. The comparison between two R_D values of WEST cases is shown in Figure 5.8. One can observe that the R_D calculated based on scaled bolometry channel 2 signal is approximately matched with the one calculated based on P_{rad} integrated in the outer divertor region from the attached regime to detached regime. The presence of XPR and high input power cases can slightly influence the consistency between the two R_D, but the monotonic evolution of R_D when plasma transits from attached to detached is not influenced. Overall, it is no doubt a good choice to replace P_{rad} by scaled bolometry channel 2 signal in real experimental detachment control of WEST.

- The upstream temperature T_{eu} can be measured by TS or reciprocating Langmuir probe or can be estimated by $T_{eu} \propto P_{in,sol}^{4/9} n_{e,sep}^{-2/9}$ (Equation 16.34 in [122]). For WEST simulations, scale the $P_{in,sol}^{4/9} n_{e,sep}^{-2/9}$ by a factor of 2.2×10^3 shows a good match with T_{eu} when plasma is attached, Figure 5.9.
- The heat flux decay length λ_q can be evaluated in real-time through experimental profiles, such as the radial temperature profile measured by TS at the OMP, or by measuring the heat flux profile at the target using LPs and IR (Section 2.5). Alternatively, λ_q can be replaced by a suitable constant value, such as the value in Table 5.1), if it is not significantly influenced by variable divertor closure, impurity concentration, and input power when the plasma is detached.
- The conductivity coefficients k_{0e} is a constant number and set as 2000 in a tokamak plasma.
- The safety factor q_s is dependent on the configuration and tokamak size.

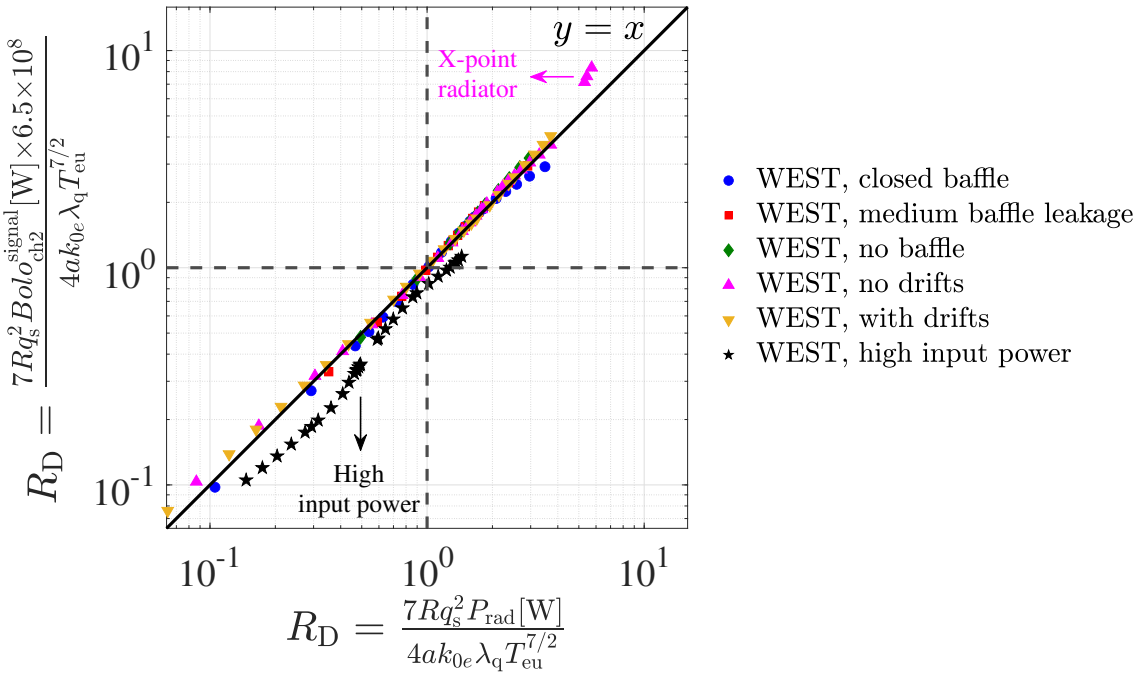

FIGURE 5.8. : The comparison between two R_D values of WEST cases : In X-axis, R_D is calculated based on integral power radiation P_{rad} [W] in the outer target region. In Y-axis, R_D is calculated based on replacing P_{rad} with Bolometry signal [W] (from Channel 2 that covers the outer target region) times 6.5×10^8.

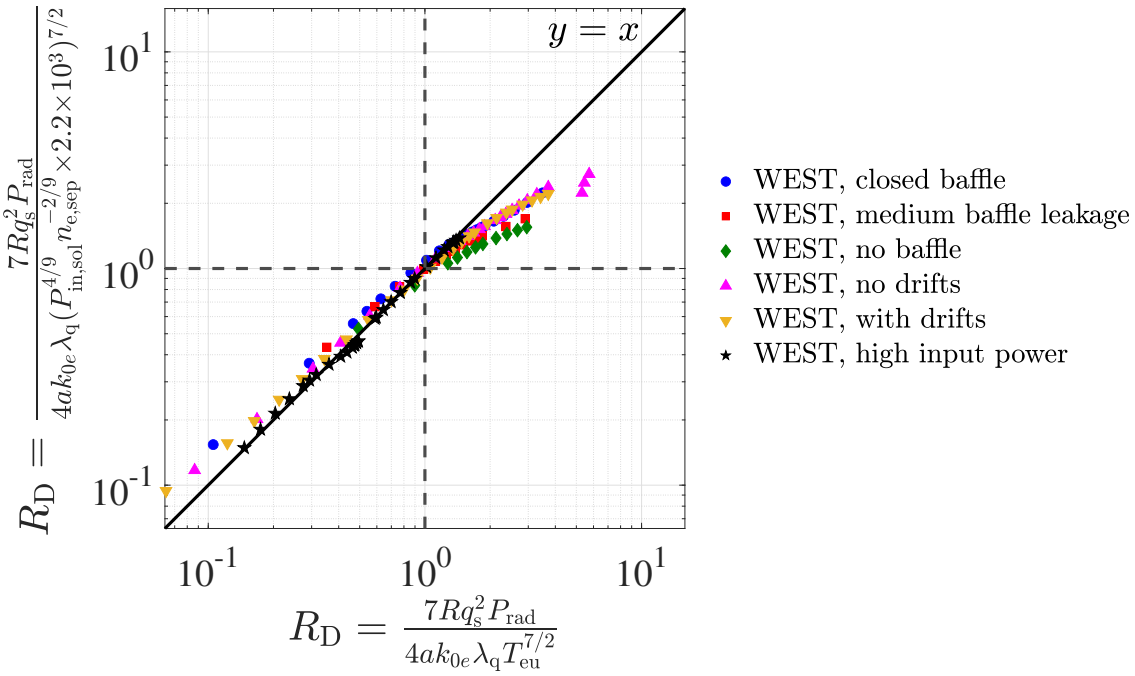

FIGURE 5.9. : The comparison between two R_D values of WEST cases : In X-axis, R_D is calculated based on the upstream separatrix temperature T_{eu}. In Y-axis, R_D is calculated based on replacing T_{eu} with $P_{in,sol}^{4/9} n_{e,sep}^{-2/9} \times 2.2 \times 10^3$.

5.2. Detachment control strategies

In general, a control strategy for detachment consists of two main components : the detachment criterion and the divertor state indicator. The detachment criterion serves to help the control system identify whether the divertor is in a detached or attached state. An example of detachment criteria is the rollover of particle flux. The divertor state indicator is used to provide information about whether the divertor is approaching or moving away from the desired detached state. Ideally, the divertor state indicator should be reliable, sensitive, and exhibit a monotonic evolution during the transitions from the attached to the detached regimes. An example of the divertor state indicator is the line integral density nearby the X-point.

When the detachment control relies on the parallel ion saturation current density $J_{\parallel,i}$. The rollover of $J_{\parallel,i}$ serves as the detachment criterion, indicating the moment when plasma starts to detach. The evolution of $J_{\parallel,i}$ itself acts as the divertor state indicator. However, $J_{\parallel,i}$ exhibits different tendencies before and after detachment, requiring the control factor k_n to switch signs before and after detachment (as discussed in Section C). This sign-switching artificially ensures that $J_{\parallel,i}$ behaves as a monotonically evolving variable for the control system.

Through the simulations and analyses presented in this thesis, we can summarize and propose several control strategies for the tokamak operation.

The candidates of criterion for detachment

- **Rollover of particle flux** The rollover of particle flux serves as an effective criterion for detachment control. The parallel ion saturation current density, denoted as $J_{\parallel,\mathrm{i}}$, at the divertor target is a suitable parameter for this purpose as it can be easily and reliably measured using LPs. Experimental studies have observed a reduction in the target $J_{\parallel,\mathrm{i}}$ as the divertor progresses into detachment, either through increased core density or ramped nitrogen seeding [28, 86, 121]. This observation is consistent with experimental cases. Identifying the rollover point of $J_{\parallel,\mathrm{i}}$ is crucial for effective detachment control. The control factor k_{n} needs to switch its sign appropriately to ensure that the divertor detachment remains under control when the rollover occurs. However, it is important to note that the rollover point of $J_{\parallel,\mathrm{i}}$ can potentially be influenced by variable scrape-off layer (SOL) input power and impurity concentration. For instance, as shown in Figure 5.10, from point A to point B, ramped nitrogen seeding results in a significant reduction in $J_{\parallel,\mathrm{i}}$. However, starting from point B, if we keep the nitrogen seeding rate fixed and increase only the deuterium puff rate, the $J_{\parallel,\mathrm{i}}$ increases again, despite reaching a higher level of divertor detachment with the heat flux at the target continuing to decrease until point C. Thus, the heat flux threshold for $J_{\parallel,\mathrm{i}}$ rollover can increase due to increased impurity concentration. The detachment can still be controlled in the realistic time-dependent simulations by only adjusting the nitrogen puff rate, and simultaneously keeping a constant deuterium puff rate, to maintain the monotonic increase of impurity concentration as a function of the level of detachment. However, in long-duration experimental discharges, the nonmonotonic evolution of impurity concentration with the level of detachment usually occurs due to reduced sputtering when detachment is achieved, particles retention on the wall, as well as the flexible ratio of deuterium and impurities gas puff rate that may be applied in advanced control scenarios. The change in the rollover threshold can present a significant challenge for detachment control.

- **Normalized radiation front height = 0.05** When the radiation front has a certain distance from the target, we can consider the detachment happens. It is a straightforward criterion of detached plasma, as this behavior can be helpful in spreading power to a larger surface through radiation. Thus, it can be used in general situations despite the differences in baffle closure and nitrogen seeding. However, the real-time measurements of the radiation front position have challenges in some tokamak devices with short divertor legs such as WEST.

- $\boldsymbol{R_{\mathrm{D}} = 1}$ R_{D} shows a robust threshold for nearly all the simulation cases discussed in this thesis, thus can be an ideal criterion for detachment as discussed in Section 5.1. In addition, it is easier to be diagnosed than the radiation front height in tokamak devices such as WEST.

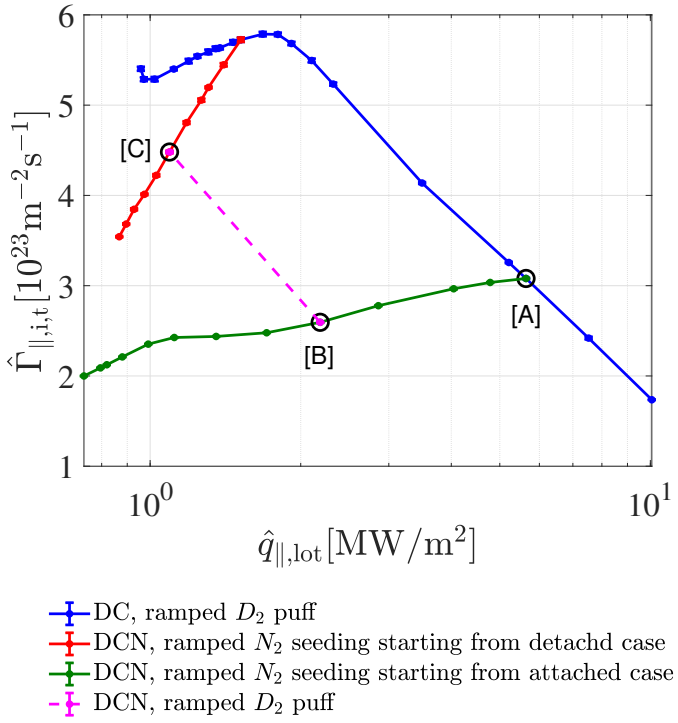

FIGURE 5.10. : Evolution of parallel ion particle flux as a function of peak parallel heat flux at the outer target. The solid curves are from the TCV cases introduced in Section 4.2. The dashed magenta line represents the possible evolution of parallel ion particle flux in the case with ramped deuterium gas puff rate, and fixed nitrogen seeding rate. The setup of deuterium and nitrogen puff rate is shown in Table 5.3.

Cases	D_2 puff rate $[10^{21}\mathrm{atoms}\cdot\mathrm{s}^{-1}]$	N_2 seeding rate $[10^{21}\mathrm{atoms}\cdot\mathrm{s}^{-1}]$
DC, ramped D_2 puff	$0.17 \rightarrow 1.31$	0
DCN, NSFD	0.72	$0 \rightarrow 0.8$
DCN, NSFA	0.33	$0 \rightarrow 1.0$
DCN, ramped D_2 puff	$0.33 \rightarrow 0.72$	0.3

TABLE 5.3. : The deuterium and nitrogen puff rate applied in the simulation cases in Figure 5.10.

The candidates of divertor state indicator

- **Particle flux** In the attached plasma with constant input power and without impurity seeding, the increase of particle flux indicates the plasma is approaching the detachment, while after exceeding the detachment threshold, we need to

have a reduced particle flux to reach a deeper level of detachment. The transition state before and after rollover needs to be carefully treated.

- **Line integral density nearby the X-point** It shows a mono-increasing evolution during the transitions from the attached to the detached regime. There is no rollover that needs to be considered, making it simpler for the system to treat the data compared with the particle flux. However, it still has the same disadvantage as particle flux, as its reliability can be strongly influenced by variable input power and impurity concentration. Additionally, when the plasma is deeply detached, the plasma density in the divertor is close to the saturation state due to strong plasma recombination, as a result, the line integral density near the X-point may no longer be sensitive to the detachment level.

- **Bolometry signal** This variable can show the level of radiation in the divertor. In the case with fixed input power, more power radiation means a colder divertor target, thus facilitating the detachment. The bolometry signal will also show a mono-increasing evolution when plasma transit from attached to detached, and its mono-increasing evolution would not be strongly influenced by the impurity seeding. However, when plasma is deeply detached, the power radiation will also reach a saturation state. Thus like the line integral density near X-point, it can not be directly used to control deeply detached plasma.

- **Radiation front height** The height of the radiation front is found to increase steadily as the level of detachment becomes higher in most simulation cases of this thesis. While in a TCV case with high input power (green diamonds in Figure 5.6), the rollover of radiation front height can be observed when plasma is deeply detached. Thus it is probably not quite reliable to be used in high input power cases. The normalized radiation front height is nearly zero when plasma is in an attached state. So we need to consider analyzing the particle flux, line integral density near the X-point, or bolometry signal in the attached plasma as a supplement reference to know if the plasma is approaching detachment.

- $\boldsymbol{R}_{\mathrm{D}}$ This valuable tool shows ideal characteristics for estimating divertor states. As shown in Figure 5.7, the radiative power fraction R_{D} exhibits a monotonically increasing evolution during the transitions from attached to detached (with decreasing target temperature). Specifically, in the case of high input power for the TCV, when the radiation front height shows a rollover, the R_{D} still maintains a monotonically increasing trend. Therefore, compared to other divertor state indicators, R_{D} demonstrates the most reliable performance and can be applied to control detachment even in complex situations involving variable divertor closure, impurity concentration, and input power.

Summary of detachment control strategies

The detachment control strategies based on some possible combinations of criteria for detachment and divertor state indicators are discussed and summarized in

Table 5.4. The block with green color represents that the method is applicable in the corresponding situation, while the block with orange color represents that it is not fully applicable. All the listed control strategies are predicted to work properly in the situation with fixed input power, fixed divertor closure, and relatively low impurities concentration. When there is a variable impurities concentration and input power, the particle flux and line integral density may be significantly influenced. Taking normalized radiation front height as the criterion of detachment, and using radiation front height and/or bolometry as the divertor state indicator can be a more reliable choice. The detachment control strategy based on R_{D} is also an ideal choice. It can not only handle the situation with fixed input power and fixed divertor closure but can also handle more complex situations including variable divertor closure, impurities concentration, and input power.

Control strategies		Fixed input power & divertor closure		Variable input power & divertor closure & impurities concentration
Criterion of detachment	Plasma state indicator	Negligible influence of impurity or significant influence of impurity with a monotonic increase in impurity concentration with the level of detachment	Significant influence of impurity with monotonic decrease or non-monotonic evolution in impurity concentration with the level of detachment	
Rollover of particle flux	Particle flux/ Bolometry/ Line integral density/ Radiation front height			
Normalized radiation front height = 0.05	Line integral density/ Particle flux			
	Bolometry/ Radiation front height			
$R_D = 1$	R_D			

TABLE 5.4. : Detachment control strategies summarize and comparison. The block with green color represents that the method is applicable in the corresponding situation, while the block with orange color represents that it is not fully applicable.

5.3. Real-time detachment control based on R_D

In this section, we designed a real-time detachment control application scenario based on R_D to verify the reliable performance of R_D in complex situations with variable impurity concentration and input power. This work also investigated a possible operation way to realize control of detachment in future high input power devices (e.g. DEMO).

The plasma can initially be controlled to make R_D value oscillates around a proper value above one (target value) with relatively low input power. Then, the input power

can be gradually increased until the plasma reaches ignition. In this process, R_D tends to decrease, but we can still pull R_D back to the target value by increasing the deuterium gas puff or impurity seeding or mixing of both. It is necessary to use the feedback method to make R_D automatically controlled. We tried to test this scenario with the help of SOLEDGE3X-EIRENE simulation and figure out the reliability of this detachment control strategy with the influence of increased input power and impurity seeding.

A WEST case was tested in realistic time-dependent simulation, Figure 5.11, following the steps below :

- From $t = 0\,\text{s}$ to $t = 0.1\,\text{s}$, the input power was kept constant, and the divertor plasma was attached.
- From $t = 0.1\,\text{s}$ to $t = 0.2\,\text{s}$, the input power was still constant, but feedback control was activated to adjust the pure deuterium puff rate. The target R_D was set to reach 1.2, and as a result, the plasma started to detach.
- From $t = 0.2\,\text{s}$ to $t = 0.3\,\text{s}$, the input power was constant, and the pure deuterium puff rate was adjusted to reach target $R_D = 2.0$, resulting in a deeper detachment of the plasma.
- From $t = 0.3\,\text{s}$ to $t = 0.4\,\text{s}$, the input power gradually increased. The detachment was maintained by adjusting the deuterium puff rate.
- From $t = 0.4\,\text{s}$ to $t = 0.5\,\text{s}$, the input power gradually increased. The detachment was maintained by keeping the deuterium puff rate constant and adjusting the nitrogen puff rate.
- From $t = 0.5\,\text{s}$ to $t = 0.6\,\text{s}$, the input power remained constant at a high value. The detachment was maintained by adjusting the mixed gas injection rate (with a fixed ratio of deuterium and nitrogen).

A similar test was also done for TCV case, as shown in Figure 5.12. The detachment was maintained successfully in the WEST and TCV simulations with complex situations, thus proving the reliability of R_D in detachment control. This strategy is also worth to be verified through the experiment and possibly provides higher reliability in detachment control. This work will be done in the near future.

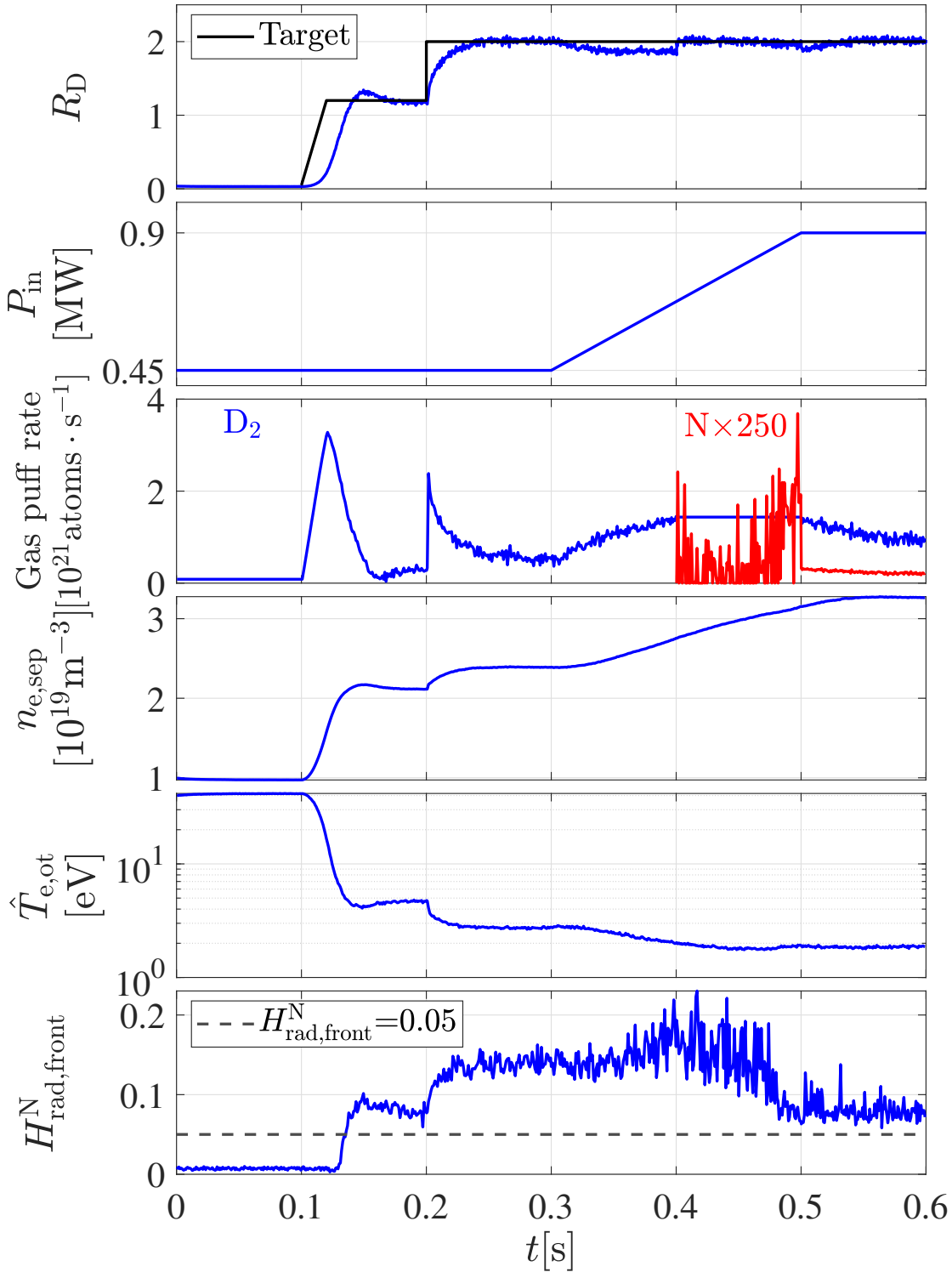

FIGURE 5.11. : Detachment maintained in WEST case with R_D controlled by feedback, the evolution of several simulated fields as a function of time.

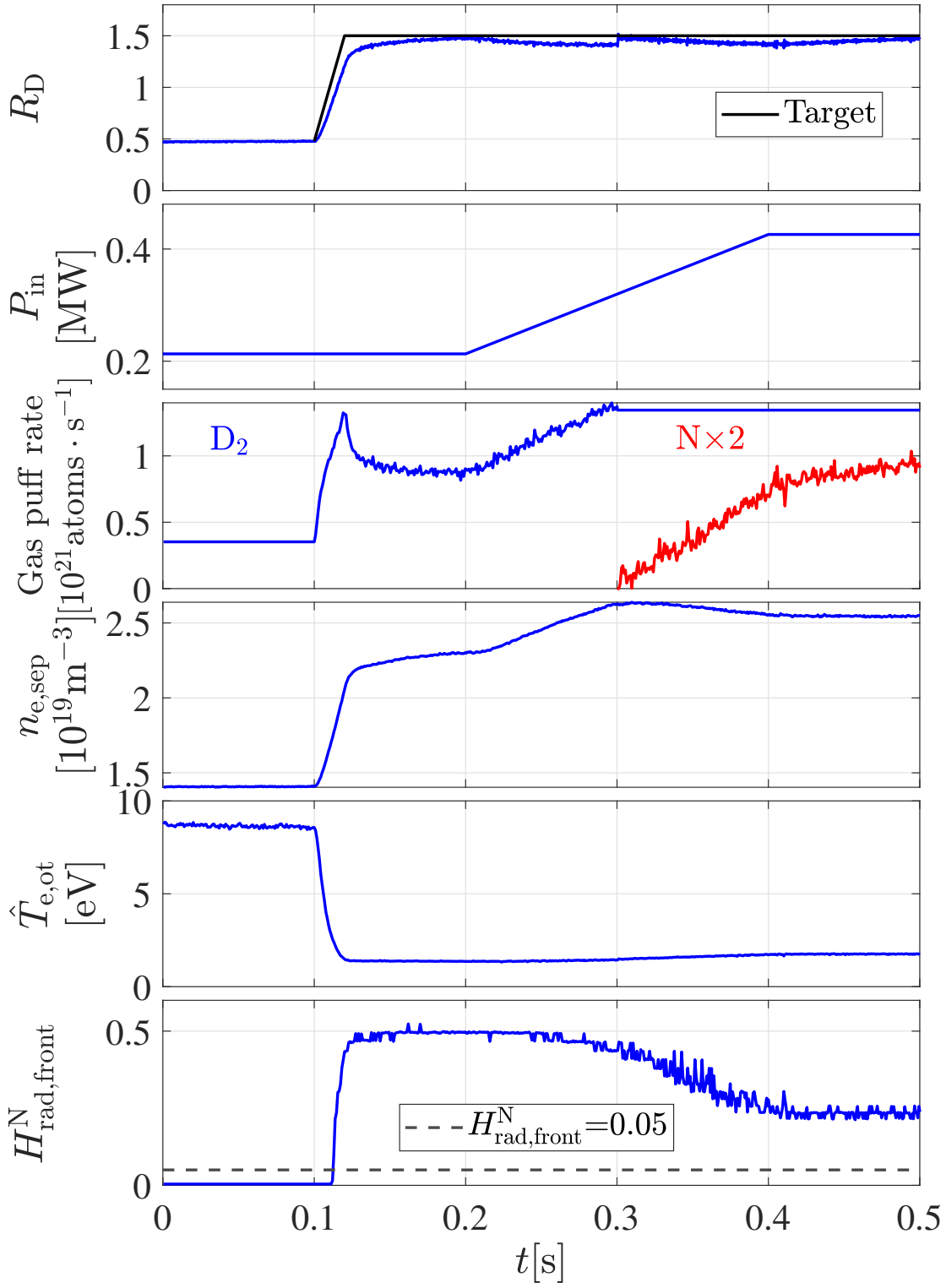

FIGURE 5.12. : Detachment maintained in TCV case with R_D controlled by feedback, the evolution of several simulated fields as a function of time.

Conclusion

This thesis mainly focuses on investigating detachment control strategies based on the study of edge physics through the combination of simulation and experiment analysis.

In Chapter 1 and Chapter 2. We introduced the general aspects of thermonuclear fusion, tokamak, edge plasma, plasma regimes, and experimental diagnostics. A systematic approach towards maintaining a proper level of detachment in real-time through feedback control is necessary to ensure the continuous production of energy by the reactor and the long life of the plasma-facing components. There are some challenges such as the difficulties in finding appropriate control variables that are highly related to the level of detachment despite the influence of the variable impurity concentration in the divertor, input power, and divertor closure. We try to solve this challenge by employing numerical simulations as the high collisionality in edge plasma provides the possibility to simulate edge plasma with fluid equations and as they can give more details than the experimental data. The 2PM is also used to relate the upstream and target conditions in SOL, giving us an easier way to understand the basic physics in it.

In Chapter 3. Several promising basic simulation cases (WEST and TCV) are obtained by using SOLEDGE3X-EIRENE, with input parameters specially defined to reproduce the experiments. Profile feedback control has been developed as an interpretive tool to extract edge transport coefficients from experimental data. The plasma density scan has been applied to investigate the plasma characteristics of different regimes, from attached to detached. The detachment of the radiation front is found to occur slightly earlier than the rollover of particle flux in the constant input power cases without impurity seeding.

In Chapter 4. The impact of wall geometry (divertor closure), impurity seeding, and heating power on detachment has been discussed. Divertor closure (divertor leakage in WEST, long and short baffle in TCV) mainly affects the neutral pressure distribution in the divertor. As the divertor closure increases with the same upstream density, we expect to have higher divertor neutral pressure (up to a limit, as neutral recycling on the baffles can occur), leading to a higher momentum and power dissipation level, which facilitates detachment. When detachment is achieved in constant input power cases without impurity seeding, the divertor presents a robust neutral pressure threshold, despite the difference in divertor closure, emphasizing the strong relationship between neutral pressure and divertor states. The impact of divertor closure on the detachment gas puff rate threshold differs significantly between TCV and WEST simulations. With reduced divertor closure, the detachment deuterium puff rate threshold in WEST reduced by up to 92%, whereas in TCV, it reduced by less than 5%. This highlights

the influence of the first wall recycling properties and the relative positioning of the pump in gas fuel operation. When introducing nitrogen seeding, it can cool the target temperature with little effect on the upstream density and momentum loss but drops the upstream pressure, leading to a decrease in the target particle flux and divertor neutral pressure. Nitrogen with concentration ≈ 0.12 in the divertor can replace deuterium and carbon as the primary radiation source (radiate $\approx 65\%$ of power). Sufficient power can be dissipated to achieve radiation front detachment at a higher target temperature threshold since nitrogen is a more effective radiator in the higher temperature range of 5–10 eV. When maintaining the same heat load is required in a detached divertor with constant SOL input power, the case with higher nitrogen concentration allows for a lower radiation front height because nitrogen radiation is mainly localized near the target. Higher input power is found to generally increase the threshold value of some discussed variables (e.g. upstream separatrix density, target temperature, divertor radiation, target particle flux) for achieving divertor detachment.

In Chapter 5. A variable R_D has been proposed based on the competition between heat conduction (from upstream to divertor) and power radiation in the divertor. $R_D = 1$ can be used as an ideal criterion for detachment in devices of different sizes and shows an almost consistent threshold for the case with different levels of divertor closure, impurities concentration, and input power (verified in WEST and TCV). Based on the analysis of available diagnostics in the experiment and general criterion for detachment $R_D = 1$, new strategies for controlling the divertor detachment have been proposed. The robustness of a control strategy for WEST tokamak has been investigated by numerical simulations and it will be tested in future experiments.

Bibliographie

[1] H. YANG, G. CIRAOLO, J. BUCALOSSI et al. « Numerical modeling of the impact of leakage under divertor baffle in WEST ». In : *Nuclear Materials and Energy* (2022), p. 101302. ISSN : 2352-1791. DOI : https://doi.org/10.1016/j.nme.2022.101302. URL : https://www.sciencedirect.com/science/article/pii/S2352179122001831 (cf. p. 3).

[2] H. BUFFERAND, J. BUCALOSSI, G. CIRAOLO et al. « Progress in edge plasma turbulence modelling—hierarchy of models from 2D transport application to 3D fluid simulations in realistic tokamak geometry ». In : *Nuclear Fusion* 61.11 (oct. 2021), p. 116052. DOI : 10.1088/1741-4326/ac2873. URL : https://dx.doi.org/10.1088/1741-4326/ac2873 (cf. p. 3).

[3] J. BUCALOSSI, J. ACHARD, O. AGULLO et al. « Operating a full tungsten actively cooled tokamak : overview of WEST first phase of operation ». In : *Nuclear Fusion* 62.4 (fév. 2022), p. 042007. DOI : 10.1088/1741-4326/ac2525. URL : https://dx.doi.org/10.1088/1741-4326/ac2525 (cf. p. 3, 58).

[4] S. Di GENOVA, A. GALLO, N. FEDORCZAK et al. « Modelling of tungsten contamination and screening in WEST plasma discharges ». In : *Nuclear Fusion* 61.10 (sept. 2021), p. 106019. DOI : 10.1088/1741-4326/ac2026. URL : https://dx.doi.org/10.1088/1741-4326/ac2026 (cf. p. 3).

[5] H BUFFERAND, J BALBIN, S BASCHETTI et al. « Implementation of multi-component Zhdanov closure in SOLEDGE3X ». In : *Plasma Physics and Controlled Fusion* 64.5 (mars 2022), p. 055001. DOI : 10.1088/1361-6587/ac4fac. URL : https://dx.doi.org/10.1088/1361-6587/ac4fac (cf. p. 3, 32).

[6] Nicolas RIVALS, Patrick TAMAIN, Yannick MARANDET et al. « SOLEDGE3X full vessel plasma simulations for computation of ITER first-wall fluxes ». In : *Contributions to Plasma Physics* 62.5-6 (2022), e202100182. DOI : https://doi.org/10.1002/ctpp.202100182. eprint : https://onlinelibrary.wiley.com/doi/pdf/10.1002/ctpp.202100182. URL : https://onlinelibrary.wiley.com/doi/abs/10.1002/ctpp.202100182 (cf. p. 3).

[7] Rémi DELAPORTE-MATHURIN, Hao YANG, Julien DENIS et al. « Fuel retention in WEST and ITER divertors based on FESTIM monoblock simulations ». In : *Nuclear Fusion* 61.12 (oct. 2021), p. 126001. DOI : 10.1088/1741-4326/ac2bbd. URL : https://dx.doi.org/10.1088/1741-4326/ac2bbd (cf. p. 4).

[8] E. LARIBI, E. SERRE, P. TAMAIN et al. « Impact of negative triangularity on edge plasma transport and turbulence in TOKAM3X simulations ». In : *Nuclear Materials and Energy* 27 (2021), p. 101012. ISSN : 2352-1791. DOI : https://doi.org/10.1016/j.nme.2021.101012. URL : https://www.sciencedirect.com/science/article/pii/S2352179121000880 (cf. p. 4).

[9] Nicolas RIVALS, Patrick TAMAIN, Yannick MARANDET et al. « Impact of enhanced far-SOL transport on first wall fluxes in ITER from full vessel edge-plasma simulations ». In : *Nuclear Materials and Energy* 33 (2022), p. 101293. ISSN : 2352-1791. DOI : https://doi.org/10.1016/j.nme.2022.101293. URL : https://www.sciencedirect.com/science/article/pii/S2352179122001740 (cf. p. 4).

[10] G. CIRAOLO, S. Di GENOVA, H. YANG et al. « Interpretative modeling of impurity transport and tungsten sources in WEST boundary plasma ». In : *Nuclear Fusion* 61.12 (oct. 2021), p. 126015. DOI : 10.1088/1741-4326/ac2439. URL : https://dx.doi.org/10.1088/1741-4326/ac2439 (cf. p. 4).

[11] John WESSON et David J CAMPBELL. *Tokamaks*. T. 149. Oxford university press, 2011 (cf. p. 19, 20, 23, 31, 199, 200).

[12] Shunjie LI, H JIANG, Zhigang REN et al. « Optimal tracking for a divergent-type parabolic PDE system in current profile control ». In : *Abstract and Applied Analysis*. T. 2014. Hindawi. 2014 (cf. p. 22).

[13] Peter C STANGEBY et al. *The plasma boundary of magnetic fusion devices*. T. 224. Institute of Physics Pub. Philadelphia, Pennsylvania, 2000 (cf. p. 23, 40, 41, 45, 46, 49, 106, 117, 219).

[14] F WAGNER. « A quarter-century of H-mode studies ». In : *Plasma Physics and Controlled Fusion* 49.12B (nov. 2007), B1. DOI : 10.1088/0741-3335/49/12B/S01. URL : https://dx.doi.org/10.1088/0741-3335/49/12B/S01 (cf. p. 24).

[15] M BERNERT, T EICH, A KALLENBACH et al. « The H-mode density limit in the full tungsten ASDEX Upgrade tokamak ». In : *Plasma Physics and Controlled Fusion* 57.1 (nov. 2014), p. 014038. DOI : 10.1088/0741-3335/57/1/014038. URL : https://dx.doi.org/10.1088/0741-3335/57/1/014038 (cf. p. 24).

[16] R BEHN, B LABIT, B P DUVAL et al. « Threshold power for the transition into H-mode for H, D, and He plasmas in TCV ». In : *Plasma Physics and Controlled Fusion* 57.2 (déc. 2014), p. 025007. DOI : 10.1088/0741-3335/57/2/025007. URL : https://doi.org/10.1088/0741-3335/57/2/025007 (cf. p. 24).

[17] J R HARRISON, C THEILER, O FÉVRIER et al. « Progress toward divertor detachment on TCV within H-mode operating parameters ». In : *Plasma Physics and Controlled Fusion* 61.6 (mai 2019), p. 065024. DOI : 10.1088/1361-6587/ab140e. URL : https://dx.doi.org/10.1088/1361-6587/ab140e (cf. p. 24, 82, 135).

[18] P.T. LANG, A. LOARTE, G. SAIBENE et al. « ELM control strategies and tools : status and potential for ITER ». In : *Nuclear Fusion* 53.4 (mars 2013), p. 043004. DOI : 10.1088/0029-5515/53/4/043004. URL : https://dx.doi.org/10.1088/0029-5515/53/4/043004 (cf. p. 24).

[19] D.G. WHYTE, A.E. HUBBARD, J.W. HUGHES et al. « I-mode : an H-mode energy confinement regime with L-mode particle transport in Alcator C-Mod ». In : *Nuclear Fusion* 50.10 (oct. 2010), p. 105005. DOI : 10.1088/0029-5515/50/10/105005. URL : https://dx.doi.org/10.1088/0029-5515/50/10/105005 (cf. p. 25).

[20] T. HAPPEL, M. GRIENER, D. SILVAGNI et al. « Stationarity of I-mode operation and I-mode divertor heat fluxes on the ASDEX Upgrade tokamak ». In : *Nuclear Materials and Energy* 18 (2019), p. 159-165. ISSN : 2352-1791. DOI : https://doi.org/10.1016/j.nme.2018.12.022. URL : https://www.sciencedirect.com/science/article/pii/S2352179118301017 (cf. p. 25).

[21] Y.J. LIU, Z.X. LIU, A.D. LIU et al. « Power threshold and confinement of the I-mode in the EAST tokamak ». In : *Nuclear Fusion* 60.8 (juill. 2020), p. 082003. DOI : 10.1088/1741-4326/ab88e0. URL : https://dx.doi.org/10.1088/1741-4326/ab88e0 (cf. p. 25).

[22] R.A. PITTS, S. BARDIN, B. BAZYLEV et al. « Physics conclusions in support of ITER W divertor monoblock shaping ». In : *Nuclear Materials and Energy* 12 (2017). Proceedings of the 22nd International Conference on Plasma Surface Interactions 2016, 22nd PSI, p. 60-74. ISSN : 2352-1791. DOI : https://doi.org/10.1016/j.nme.2017.03.005. URL : https://www.sciencedirect.com/science/article/pii/S2352179116302885 (cf. p. 25).

[23] Y. SHIMOMURA, M. KEILHACKER, K. LACKNER et al. « Characteristics of the divertor plasma in neutral-beam-heated ASDEX discharges ». In : *Nuclear Fusion* 23.7 (juill. 1983), p. 869. DOI : 10.1088/0029-5515/23/7/002. URL : https://dx.doi.org/10.1088/0029-5515/23/7/002 (cf. p. 26).

[24] M. WISCHMEIER. « High density operation for reactor-relevant power exhaust ». In : *Journal of Nuclear Materials* 463 (2015). PLASMA-SURFACE INTERACTIONS 21, p. 22-29. ISSN : 0022-3115. DOI : https://doi.org/10.1016/j.jnucmat.2014.12.078. URL : https://www.sciencedirect.com/science/article/pii/S0022311514010216 (cf. p. 26).

[25] J. BUCALOSSI, J.P. GUNN, A. GÉRAUD et al. « Feedback control on edge plasma parameters with ergodic divertor in Tore Supra ». In : *Journal of Nuclear Materials* 290-293 (2001). 14th Int. Conf. on Plasma-Surface Interactions in Controlled Fusion D evices, p. 566-570. ISSN : 0022-3115. DOI : https://doi.org/10.1016/S0022-3115(00)00588-2. URL : https://www.sciencedirect.com/science/article/pii/S0022311500005882 (cf. p. 26).

[26] C GUILLEMAUT, M LENNHOLM, J HARRISON et al. « Real-time control of divertor detachment in H-mode with impurity seeding using Langmuir probe feedback in JET-ITER-like wall ». In : *Plasma Physics and Controlled Fusion* 59.4 (fév. 2017), p. 045001. DOI : 10.1088/1361-6587/aa5951. URL : https://doi.org/10.1088/1361-6587/aa5951 (cf. p. 26).

[27] Q.P. YUAN, K. WU, L. WANG et al. « The first implementation of active detachment feedback control in EAST PCS ». In : *Fusion Engineering and Design* 154 (2020), p. 111557. ISSN : 0920-3796. DOI : https://doi.org/10.1016/j.fusengdes.2020.111557. URL : https://www.sciencedirect.com/science/article/pii/S0920379620301058 (cf. p. 26).

[28] D. ELDON, H.Q. WANG, L. WANG et al. « An analysis of controlled detachment by seeding various impurity species in high performance scenarios on DIII-D and EAST ». In : *Nuclear Materials and Energy* 27 (2021), p. 100963. ISSN : 2352-1791. DOI : https://doi.org/10.1016/j.nme.2021.100963. URL : https://www.sciencedirect.com/science/article/pii/S235217912100048X (cf. p. 26, 52, 135, 144, 169).

[29] D ELDON, H ANAND, J-G BAK et al. « Enhancement of detachment control with simplified real-time modelling on the KSTAR tokamak ». In : *Plasma Physics and Controlled Fusion* 64.7 (mai 2022), p. 075002. DOI : 10.1088/1361-6587/ac6ff9. URL : https://dx.doi.org/10.1088/1361-6587/ac6ff9 (cf. p. 26).

[30] A. LOARTE, R.D. MONK, J.R. MARTÍN-SOLÍS et al. « Plasma detachment in JET Mark I divertor experiments ». In : *Nuclear Fusion* 38.3 (mars 1998), p. 331. DOI : 10.1088/0029-5515/38/3/303. URL : https://dx.doi.org/10.1088/0029-5515/38/3/303 (cf. p. 27).

[31] Timo RAVENSBERGEN, Matthijs van BERKEL, Artur PEREK et al. « Real-time feedback control of the impurity emission front in tokamak divertor plasmas ». In : *Nature communications* 12.1 (2021), p. 1105 (cf. p. 27, 202).

[32] M BERNERT, F JANKY, B SIEGLIN et al. « X-point radiation, its control and an ELM suppressed radiating regime at the ASDEX Upgrade tokamak ». In : *Nuclear Fusion* 61.2 (2020), p. 024001 (cf. p. 27).

[33] A. PEREK, W. A. J. VIJVERS, Y. ANDREBE et al. « MANTIS : A real-time quantitative multispectral imaging system for fusion plasmas ». In : *Review of Scientific Instruments* 90.12 (2019), p. 123514. DOI : 10.1063/1.5115569. eprint : https://doi.org/10.1063/1.5115569. URL : https://doi.org/10.1063/1.5115569 (cf. p. 27).

[34] A. KALLENBACH, R. DUX, V. MERTENS et al. « H mode discharges with feedback controlled radiative boundary in the ASDEX Upgrade tokamak ». In : *Nuclear Fusion* 35.10 (oct. 1995), p. 1231. DOI : 10.1088/0029-5515/35/10/I07. URL : https://dx.doi.org/10.1088/0029-5515/35/10/I07 (cf. p. 28).

[35] N. ASAKURA, T. NAKANO, N. OYAMA et al. « Investigations of impurity seeding and radiation control for long-pulse and high-density H-mode plasmas in JT-60U ». In : *Nuclear Fusion* 49.11 (sept. 2009), p. 115010. DOI : 10.1088/0029-5515/49/11/115010. URL : https://dx.doi.org/10.1088/0029-5515/49/11/115010 (cf. p. 28).

[36] K. WU, Q.P. YUAN, B.J. XIAO et al. « Achievement of radiative feedback control for long-pulse operation on EAST ». In : *Nuclear Fusion* 58.5 (mars 2018), p. 056019. DOI : 10.1088/1741-4326/aab506. URL : https://dx.doi.org/10.1088/1741-4326/aab506 (cf. p. 28).

[37] Yanmin DUAN, Liqun HU, Songtao MAO et al. « Measurement of radiated power loss on EAST ». In : *Plasma Science and Technology* 13.5 (2011), p. 546. DOI : 10.1088/1009-0630/13/5/07. URL : https://dx.doi.org/10.1088/1009-0630/13/5/07 (cf. p. 28).

[38] S I KRASHENINNIKOV, A S KUKUSHKIN et A A PSHENOV. « Divertor plasma detachment : roles of plasma momentum, energy, and particle balances ». In : *Plasma Physics and Controlled Fusion* 64.12 (nov. 2022), p. 125011. DOI : 10.1088/1361-6587/ac9a6f. URL : https://dx.doi.org/10.1088/1361-6587/ac9a6f (cf. p. 28).

[39] T.W. PETRIE, T.E. EVANS, N.H. BROOKS et al. « Results from radiating divertor experiments with RMP ELM suppression and mitigation ». In : *Nuclear Fusion* 51.7 (mai 2011), p. 073003. DOI : 10.1088/0029-5515/51/7/073003. URL : https://doi.org/10.1088/0029-5515/51/7/073003 (cf. p. 28).

[40] Xingwei ZHENG, Jiangang LI, Jiansheng HU et al. « Comparison between gas puffing and supersonic molecular beam injection in plasma density feedback experiments in EAST ». In : *Plasma Physics and Controlled Fusion* 55.11 (oct. 2013), p. 115010. DOI : 10.1088/0741-3335/55/11/115010. URL : https://dx.doi.org/10.1088/0741-3335/55/11/115010 (cf. p. 28).

[41] V M ZHDANOV. *Transport processes in multicomponent plasma*. CRC Press, 2002 (cf. p. 33, 57).

[42] S. I. BRAGINSKII. « Transport Processes in Plasma ». In : *Review of Plasma Physics* (1 1965) (cf. p. 33).

[43] P. HELANDER et D. SIGMAR. *Collisional Transport in Magnetized Plasmas*. Cambridge, UK : Cambridge University Press, 2002 (cf. p. 33).

[44] A. ZEILER. *Tokamak Edge Turbulence, IPP 5/88*. Rapp. tech. Max-Planck-Institut für Plasmaphysik, 1999 (cf. p. 33).

[45] O. FÉVRIER, C. THEILER, H. DE OLIVEIRA et al. « Analysis of wall-embedded Langmuir probe signals in different conditions on the Tokamak à Configuration Variable ». In : *Review of Scientific Instruments* 89.5 (2018), p. 053502. DOI : 10.1063/1.5022459. eprint : https://doi.org/10.1063/1.5022459. URL : https://doi.org/10.1063/1.5022459 (cf. p. 37, 91).

[46] C. GRISOLIA, L.D. HORTON et J.K. EHRENBERG. « Modelling of hydrogen conditioning, retention and release in Tore Supra ». In : *Journal of Nuclear Materials* 220-222 (1995). Plasma-Surface Interactions in Controlled Fusion Devices, p. 516-520. ISSN : 0022-3115. DOI : https://doi.org/10.1016/0022-3115(94)00514-1. URL : https://www.sciencedirect.com/science/article/pii/0022311594005141 (cf. p. 39).

[47] Eric M JONES. *Atomic collision processes in plasma physics experiments : analytic expressions for selected cross-sections and Maxwellian rate coefficients 2*. Rapp. tech. UKAEA, 1977 (cf. p. 40).

[48] T. EICH, B. SIEGLIN, A. SCARABOSIO et al. « Inter-ELM Power Decay Length for JET and ASDEX Upgrade : Measurement and Comparison with Heuristic Drift-Based Model ». In : *Phys. Rev. Lett.* 107 (21 nov. 2011), p. 215001. DOI : 10.1103/PhysRevLett.107.215001. URL : https://link.aps.org/doi/10.1103/PhysRevLett.107.215001 (cf. p. 42, 87).

[49] A.V. CHANKIN, W. FUNDAMENSKI, M. GROTH et al. « Effect of neutrals on the power decay length at the divertor target ». In : *Journal of Nuclear Materials* 415.1, Supplement (2011). Proceedings of the 19th International Conference on Plasma-Surface Interactions in Controlled Fusion, S562-S565. ISSN : 0022-3115. DOI : https://doi.org/10.1016/j.jnucmat.2010.12.039. URL : https://www.sciencedirect.com/science/article/pii/S0022311510008615 (cf. p. 44).

[50] P C STANGEBY. « Basic physical processes and reduced models for plasma detachment ». In : *Plasma Physics and Controlled Fusion* 60.4 (mars 2018), p. 044022. DOI : 10.1088/1361-6587/aaacf6. URL : https://doi.org/10.1088/1361-6587/aaacf6 (cf. p. 47, 119, 138).

[51] A. KALLENBACH, M. BERNERT, M. BEURSKENS et al. « Partial detachment of high power discharges in ASDEX Upgrade ». In : *Nuclear Fusion* 55.5 (avr. 2015), p. 053026. DOI : 10.1088/0029-5515/55/5/053026. URL : https://dx.doi.org/10.1088/0029-5515/55/5/053026 (cf. p. 49).

[52] R. DEJARNAC, D. SESTAK, J.P. GUNN et al. « Flush-mounted Langmuir probes in the WEST tokamak divertor ». In : *Fusion Engineering and Design* 163 (2021), p. 112120. ISSN : 0920-3796. DOI : https://doi.org/10.1016/j.fusengdes.2020.112120. URL : https://www.sciencedirect.com/science/article/pii/S0920379620306682 (cf. p. 52).

[53] H REIMERDES, G P CANAL, B P DUVAL et al. « Power distribution in the snowflake divertor in TCV ». In : *Plasma Physics and Controlled Fusion* 55.12 (nov. 2013), p. 124027. DOI : 10.1088/0741-3335/55/12/124027. URL : https://doi.org/10.1088/0741-3335/55/12/124027 (cf. p. 52).

[54] P C STANGEBY. « A problem in the interpretation of tokamak Langmuir probes when a fast electron component is present ». In : *Plasma Physics and Controlled Fusion* 37.9 (sept. 1995), p. 1031-1037. DOI : 10.1088/0741-3335/37/9/008. URL : https://doi.org/10.1088/0741-3335/37/9/008 (cf. p. 52).

[55] C. THEILER, B. LIPSCHULTZ, J. HARRISON et al. « Results from recent detachment experiments in alternative divertor configurations on TCV ». In : *Nuclear Fusion* 57.7 (mars 2017), p. 072008. DOI : 10.1088/1741-4326/aa5fb7. URL : https://doi.org/10.1088/1741-4326/aa5fb7 (cf. p. 53, 91, 92).

[56] M WENSING, B P DUVAL, O FÉVRIER et al. « SOLPS-ITER simulations of the TCV divertor upgrade ». In : *Plasma Physics and Controlled Fusion* 61.8 (juill. 2019), p. 085029. DOI : 10.1088/1361-6587/ab2b1f. URL : https://doi.org/10.1088/1361-6587/ab2b1f (cf. p. 53, 83).

[57] NIEMCZEWSKI. « Neutral particle dynamics in the Alcator C-Mod tokamak, PhD Thesis MIT, Cambridge ». Thèse de doct. 1995 (cf. p. 53).

[58] P DEVYNCK, N FEDORCZAK, R MAO et al. « Calculation of the radiated power in WEST ». In : *Journal of Physics Communications* 5.9 (sept. 2021), p. 095008. DOI : 10.1088/2399-6528/ac2370. URL : https://dx.doi.org/10.1088/2399-6528/ac2370 (cf. p. 54, 77).

[59] C. GIL, G. COLLEDANI, M. DOMENES et al. « Renewal of the interfero-polarimeter diagnostic for WEST ». In : *Fusion Engineering and Design* 140 (mars 2019). Co-Authors : The West Team, p. 81-91. DOI : 10.1016/j.fusengdes.2019.02.003. URL : https://hal-cea.archives-ouvertes.fr/cea-02045950 (cf. p. 55).

[60] H. BUFFERAND, G. CIRAOLO, Y. MARANDET et al. « Numerical modelling for divertor design of the WEST device with a focus on plasma–wall interactions ». In : *Nuclear Fusion* 55.5 (avr. 2015), p. 053025. DOI : 10.1088/0029-5515/55/5/053025. URL : https://doi.org/10.1088/0029-5515/55/5/053025 (cf. p. 57).

[61] Xavier BONNIN, Wouter DEKEYSER, Richard PITTS et al. « Presentation of the New SOLPS-ITER Code Package for Tokamak Plasma Edge Modelling ». In : *Plasma and Fusion Research* 11 (2016), p. 1403102-1403102. DOI : 10.1585/pfr.11.1403102 (cf. p. 57).

[62] S. WIESEN, D. REITER, V. KOTOV et al. « The new SOLPS-ITER code package ». In : *Journal of Nuclear Materials* 463 (2015). PLASMA-SURFACE INTERACTIONS 21, p. 480-484. ISSN : 0022-3115. DOI : https://doi.org/10.1016/j.jnucmat.2014.10.012. URL : https://www.sciencedirect.com/science/article/pii/S0022311514006965 (cf. p. 57).

[63] R. SCHNEIDER, X. BONNIN, K. BORRASS et al. « Plasma Edge Physics with B2-Eirene ». In : *Contributions to Plasma Physics* 46.1-2 (2006), p. 3-191. DOI : https://doi.org/10.1002/ctpp.200610001. eprint : https://onlinelibrary.wiley.com/doi/pdf/10.1002/ctpp.200610001. URL : https://onlinelibrary.wiley.com/doi/abs/10.1002/ctpp.200610001 (cf. p. 57).

[64] T. D. ROGNLIEN, P. N. BROWN, R. B. CAMPBELL et al. « 2-D Fluid Transport Simulations of Gaseous/Radiative Divertors ». In : *Contributions to Plasma Physics* 34.2-3 (1994), p. 362-367. DOI : https://doi.org/10.1002/ctpp.2150340241. eprint : https://onlinelibrary.wiley.com/doi/pdf/10.1002/ctpp.2150340241. URL : https://onlinelibrary.wiley.com/doi/abs/10.1002/ctpp.2150340241 (cf. p. 57).

[65] T. D. ROGNLIEN, D. D. RYUTOV, N. MATTOR et al. « Two-dimensional electric fields and drifts near the magnetic separatrix in divertor tokamaks ». In : *Physics of Plasmas* 6.5 (1999), p. 1851-1857. DOI : 10.1063/1.873488. eprint : https://doi.org/10.1063/1.873488. URL : https://doi.org/10.1063/1.873488 (cf. p. 57).

[66] R SIMONINI, G CORRIGAN, G RADFORD et al. « Models and Numerics in the Multi-Fluid 2-D Edge Plasma Code EDGE2D/U ». In : *Contributions to Plasma Physics* 34.2-3 (1994), p. 368-373. DOI : https://doi.org/10.1002/ctpp.2150340242. eprint : https://onlinelibrary.wiley.com/doi/pdf/10.1002/ctpp.2150340242. URL : https://onlinelibrary.wiley.com/doi/abs/10.1002/ctpp.2150340242 (cf. p. 57).

[67] G. J. RADFORD, A. V. CHANKIN, G. CORRIGAN et al. « The Particle and Heat Drift Fluxes and their Implementation into the EDGE2D Transport Code ». In : *Contributions to Plasma Physics* 36.2-3 (1996), p. 187-191. DOI : https://doi.org/10.1002/ctpp.2150360217. eprint : https://onlinelibrary.wiley.com/doi/pdf/10.1002/ctpp.2150360217. URL : https://onlinelibrary.wiley.com/doi/abs/10.1002/ctpp.2150360217 (cf. p. 57).

[68] P. TAMAIN, H. BUFFERAND, G. CIRAOLO et al. « The TOKAM3X code for edge turbulence fluid simulations of tokamak plasmas in versatile magnetic geometries ». In : *Journal of Computational Physics* 321 (2016), p. 606-623. ISSN : 0021-9991. DOI : https://doi.org/10.1016/j.jcp.2016.05.038. URL : https://www.sciencedirect.com/science/article/pii/S0021999116301838 (cf. p. 57).

[69] L. EASY, F. MILITELLO, J. OMOTANI et al. « Three dimensional simulations of plasma filaments in the scrape off layer : A comparison with models of reduced dimensionality ». In : *Physics of Plasmas* 21.12 (2014), p. 122515. DOI : 10.1063/1.4904207. eprint : https://doi.org/10.1063/1.4904207. URL : https://doi.org/10.1063/1.4904207 (cf. p. 57).

[70] Fabio RIVA, Fulvio MILITELLO, Sarah ELMORE et al. « Three-dimensional plasma edge turbulence simulations of the Mega Ampere Spherical Tokamak and comparison with experimental measurements ». In : *Plasma Physics and Controlled Fusion* 61.9 (août 2019), p. 095013. DOI : 10.1088/1361-6587/ab3561. URL : https://dx.doi.org/10.1088/1361-6587/ab3561 (cf. p. 57).

[71] H. BUFFERAND, P. TAMAIN, S. BASCHETTI et al. « Three-dimensional modelling of edge multi-component plasma taking into account realistic wall geometry ». In : *Nuclear Materials and Energy* 18 (2019), p. 82-86. ISSN : 2352-1791. DOI : https://doi.org/10.1016/j.nme.2018.11.025. URL : https://www.sciencedirect.com/science/article/pii/S2352179118302035 (cf. p. 57).

[72] J. BUCALOSSI, M. MISSIRLIAN, P. MOREAU et al. « The WEST project : Testing ITER divertor high heat flux component technology in a steady state tokamak environment ». In : *Fusion Engineering and Design* 89.7-8 (oct. 2014), p. 907-912. DOI : 10.1016/j.fusengdes.2014.01.062 (cf. p. 58, 59).

[73] G. CIRAOLO, A. THIN, H. BUFFERAND et al. « First modeling of strongly radiating WEST plasmas with SOLEDGE-EIRENE ». In : *Nuclear Materials and Energy* 20 (2019), p. 100685. ISSN : 2352-1791. DOI : https://doi.org/10.1016/j.nme.2019.100685. URL : https://www.sciencedirect.com/science/article/pii/S2352179118302461 (cf. p. 62, 68).

[74] Guido CIRAOLO, Hugo BUFFERAND, Pierfrancesco Di CINTIO et al. « Fluid and kinetic modelling for non-local heat transport in magnetic fusion devices ». In : *Contributions to Plasma Physics* 58.6-8 (mai 2018), p. 457-464. DOI : https://doi.org/10.1002/ctpp.201700222. URL : https://onlinelibrary.wiley.com/doi/abs/10.1002/ctpp.201700222 (cf. p. 63, 66).

[75] J.P. GUNN, C. BOUCHER, M. DIONNE et al. « Evidence for a poloidally localized enhancement of radial transport in the scrape-off layer of the Tore Supra tokamak ». In : *Journal of Nuclear Materials* 363-365 (2007). Plasma-Surface Interactions-17, p. 484-490. ISSN : 0022-3115. DOI : https://doi.org/10.1016/j.jnucmat.2007.01.195. URL : https://www.sciencedirect.com/science/article/pii/S0022311507000943 (cf. p. 70).

[76] B. LABOMBARD, J.E. RICE, A.E. HUBBARD et al. « Transport-driven Scrape-Off-Layer flows and the boundary conditions imposed at the magnetic separatrix in a tokamak plasma ». In : *Nuclear Fusion* 44.10 (sept. 2004), p. 1047. DOI : 10.1088/0029-5515/44/10/001. URL : https://dx.doi.org/10.1088/0029-5515/44/10/001 (cf. p. 70).

[77] G.S. KIRNEV, G. CORRIGAN, D. COSTER et al. « EDGE2D code simulations of SOL flows and in–out divertor asymmetries in JET ». In : *Journal of Nuclear Materials* 337-339 (2005). PSI-16, p. 271-275. ISSN : 0022-3115. DOI : https://doi.org/10.1016/j.jnucmat.2004.09.032. URL : https://www.sciencedirect.com/science/article/pii/S0022311504008967 (cf. p. 70).

[78] R.A. PITTS, P. ANDREW, X. BONNIN et al. « Edge and divertor physics with reversed toroidal field in JET ». In : *Journal of Nuclear Materials* 337-339 (2005). PSI-16, p. 146-153. ISSN : 0022-3115. DOI : https://doi.org/10.1016/j.jnucmat.2004.10.111. URL : https://www.sciencedirect.com/science/article/pii/S0022311504008487 (cf. p. 70, 147, 209, 213-217).

[79] A GALLO, N FEDORCZAK, S ELMORE et al. « Impact of the plasma geometry on divertor power exhaust : experimental evidence from TCV and simulations with SolEdge2D and TOKAM3X ». In : *Plasma Physics and Controlled Fusion* 60.1 (oct. 2017), p. 014007. DOI : 10.1088/1361-6587/aa857b. URL : https://doi.org/10.1088/1361-6587/aa857b (cf. p. 70).

[80] Mirko WENSING. « Drift-related transport and plasma-neutral interaction in the TCV divertor ». Thèse de doct. Lausanne, 2021, p. 263. DOI : 10.5075/epfl-thesis-8447. URL : http://infoscience.epfl.ch/record/285066 (cf. p. 70, 90, 146, 154, 214).

[81] S. CODA, J. AHN, R. ALBANESE et al. « Overview of the TCV tokamak program : scientific progress and facility upgrades ». In : *Nuclear Fusion* 57.10 (juin 2017), p. 102011. DOI : 10.1088/1741-4326/aa6412. URL : https://dx.doi.org/10.1088/1741-4326/aa6412 (cf. p. 82).

[82] H. REIMERDES, M. AGOSTINI, E. ALESSI et al. « Overview of the TCV tokamak experimental programme ». In : *Nuclear Fusion* 62.4 (mars 2022), p. 042018. DOI : 10.1088/1741-4326/ac369b. URL : https://dx.doi.org/10.1088/1741-4326/ac369b (cf. p. 82).

[83] Rion A CAUSEY. « Hydrogen isotope retention and recycling in fusion reactor plasma-facing components ». In : *Journal of Nuclear Materials* 300.2 (2002), p. 91-117. ISSN : 0022-3115. DOI : https://doi.org/10.1016/S0022-3115(01)00732-2. URL : https://www.sciencedirect.com/science/article/pii/S0022311501007322 (cf. p. 82).

[84] O. FÉVRIER, H. REIMERDES, C. THEILER et al. « Divertor closure effects on the TCV boundary plasma ». In : *Nuclear Materials and Energy* 27 (2021), p. 100977. ISSN : 2352-1791. DOI : https://doi.org/10.1016/j.nme.2021.100977. URL : https://www.sciencedirect.com/science/article/pii/S2352179121000600 (cf. p. 82, 103).

[85] H. REIMERDES, B.P. DUVAL, H. ELAIAN et al. « Initial TCV operation with a baffled divertor ». In : *Nuclear Fusion* 61.2 (jan. 2021), p. 024002. DOI : 10.1088/1741-4326/abd196. URL : https://doi.org/10.1088/1741-4326/abd196 (cf. p. 82, 83, 103).

[86] O FÉVRIER, C THEILER, J R HARRISON et al. « Nitrogen-seeded divertor detachment in TCV L-mode plasmas ». In : *Plasma Physics and Controlled Fusion* 62.3 (fév. 2020), p. 035017. DOI : 10.1088/1361-6587/ab6b00. URL : https://dx.doi.org/10.1088/1361-6587/ab6b00 (cf. p. 82, 89, 138, 144, 169).

[87] A SMOLDERS, M WENSING, S CARLI et al. « Comparison of high density and nitrogen seeded detachment using SOLPS-ITER simulations of the tokamak á configuration variable ». In : *Plasma Physics and Controlled Fusion* 62.12 (oct. 2020), p. 125006. DOI : 10.1088/1361-6587/abbcc5. URL : https://dx.doi.org/10.1088/1361-6587/abbcc5 (cf. p. 83, 142).

[88] D GALASSI, H REIMERDES, C THEILER et al. « Numerical investigation of optimal divertor gas baffle closure on TCV ». In : *Plasma Physics and Controlled Fusion* 62.11 (sept. 2020), p. 115009. DOI : 10.1088/1361-6587/abb24f. URL : https://doi.org/10.1088/1361-6587/abb24f (cf. p. 83, 102, 103).

[89] Joachim ROTH. « Chemical erosion of carbon based materials in fusion devices ». In : *Journal of Nuclear Materials* 266-269 (1999), p. 51-57. ISSN : 0022-3115. DOI : https://doi.org/10.1016/S0022-3115(98)00658-8. URL : https://www.sciencedirect.com/science/article/pii/S0022311598006588 (cf. p. 84).

[90] J. HAWKE, Y. ANDREBE, R. BERTIZZOLO et al. « Improving spatial and spectral resolution of TCV Thomson scattering ». In : *Journal of Instrumentation* 12.12 (déc. 2017), p. C12005. DOI : 10.1088/1748-0221/12/12/C12005. URL : https://dx.doi.org/10.1088/1748-0221/12/12/C12005 (cf. p. 86).

[91] B. P. DUVAL, A. BORTOLON, A. KARPUSHOV et al. « Spontaneous L-mode plasma rotation scaling in the TCV tokamak ». In : *Physics of Plasmas* 15.5 (2008), p. 056113. DOI : 10.1063/1.2841528. eprint : https://doi.org/10.1063/1.2841528. URL : https://doi.org/10.1063/1.2841528 (cf. p. 86).

[92] M KOČAN, J P GUNN, J-Y PASCAL et al. « Edge ion-to-electron temperature ratio in the Tore Supra tokamak ». In : *Plasma Physics and Controlled Fusion* 50.12 (nov. 2008), p. 125009. DOI : 10.1088/0741-3335/50/12/125009. URL : https://doi.org/10.1088/0741-3335/50/12/125009 (cf. p. 86, 208).

[93] L. CASALI, D. ELDON, A. MCLEAN et al. « Impurity leakage and radiative cooling in the first nitrogen and neon seeding study in the closed DIII-D SAS configuration ». In : *Nuclear Fusion* 62.2 (jan. 2022), p. 026021. DOI : 10.1088/1741-4326/ac3e84. URL : https://dx.doi.org/10.1088/1741-4326/ac3e84 (cf. p. 87, 142, 143).

[94] E.T. MEIER, R.J. GOLDSTON, E.G. KAVEEVA et al. « Drifts, currents, and power scrape-off width in SOLPS-ITER modeling of DIII-D ». In : *Nuclear Materials and Energy* 12 (2017). Proceedings of the 22nd International Conference on Plasma Surface Interactions 2016, 22nd PSI, p. 973-977. ISSN : 2352-1791. DOI : https://doi.org/10.1016/j.nme.2016.12.016. URL : https://www.sciencedirect.com/science/article/pii/S2352179116301545 (cf. p. 87).

[95] A V CHANKIN, D P COSTER, R DUX et al. « SOLPS modelling of ASDEX upgrade H-mode plasma ». In : *Plasma Physics and Controlled Fusion* 48.6 (mai 2006), p. 839. DOI : 10.1088/0741-3335/48/6/010. URL : https://dx.doi.org/10.1088/0741-3335/48/6/010 (cf. p. 87).

[96] N CHRISTEN, C THEILER, TD ROGNLIEN et al. « Exploring drift effects in TCV single-null plasmas with the UEDGE code ». In : *Plasma Physics and Controlled Fusion* 59.10 (août 2017), p. 105004. DOI : 10.1088/1361-6587/aa7c8e. URL : https://doi.org/10.1088/1361-6587/aa7c8e (cf. p. 89, 214, 215).

[97] H. DE OLIVEIRA, P. MARMILLOD, C. THEILER et al. « Langmuir probe electronics upgrade on the tokamak à configuration variable ». In : *Review of Scientific Instruments* 90.8 (2019), p. 083502. DOI : 10.1063/1.5108876. eprint : https://doi.org/10.1063/1.5108876. URL : https://doi.org/10.1063/1.5108876 (cf. p. 91).

[98] K. VERHAEGH, B. LIPSCHULTZ, J.R. HARRISON et al. « The role of plasma-molecule interactions on power and particle balance during detachment on the TCV tokamak ». In : *Nuclear Fusion* 61.10 (sept. 2021), p. 106014. DOI : 10.1088/1741-4326/ac1dc5. URL : https://dx.doi.org/10.1088/1741-4326/ac1dc5 (cf. p. 94).

[99] A W LEONARD. « Plasma detachment in divertor tokamaks ». In : *Plasma Physics and Controlled Fusion* 60.4 (fév. 2018), p. 044001. DOI : 10.1088/1361-6587/aaa7a9. URL : https://doi.org/10.1088/1361-6587/aaa7a9 (cf. p. 102).

[100] A LOARTE, R.D MONK, J.R MARTÍN-SOLÍS et al. « Plasma detachment in JET Mark I divertor experiments ». In : *Nuclear Fusion* 38.3 (mars 1998), p. 331-371. DOI : 10.1088/0029-5515/38/3/303. URL : https://doi.org/10.1088/0029-5515/38/3/303 (cf. p. 103, 215).

[101] JET Team (prepared by R.D MONK). « Recent results from divertor and scrape-off layer studies at JET ». In : *Nuclear Fusion* 39.11Y (nov. 1999), p. 1751-1762. DOI : 10.1088/0029-5515/39/11y/315. URL : https://doi.org/10.1088/0029-5515/39/11y/315 (cf. p. 103).

[102] L.D HORTON, G.C VLASES, P ANDREW et al. « Studies in JET divertors of varied geometry. I : Non-seeded plasma operation ». In : *Nuclear Fusion* 39.1 (jan. 1999), p. 1-17. DOI : 10.1088/0029-5515/39/1/301. URL : https://doi.org/10.1088/0029-5515/39/1/301 (cf. p. 103).

[103] N ASAKURA, S SAKURAI, N HOSOGANE et al. « Heat and particle transport of SOL and divertor plasmas in the W shaped divertor on JT-60U ». In : *Nuclear Fusion* 39.11Y (nov. 1999), p. 1983-1994. DOI : 10.1088/0029-5515/39/11y/344. URL : https://doi.org/10.1088/0029-5515/39/11y/344 (cf. p. 103).

[104] R NEU, J.C FUCHS, A KALLENBACH et al. « The ASDEX Upgrade divertor IIb—a closed divertor for strongly shaped plasmas ». In : *Nuclear Fusion* 43.10 (sept. 2003), p. 1191-1196. DOI : 10.1088/0029-5515/43/10/021. URL : https://doi.org/10.1088/0029-5515/43/10/021 (cf. p. 103).

[105] L. CASALI, C. SANG, A.L. MOSER et al. *Modelling the effect of divertor closure on detachment onset in DIII-D with the SOLPS code*. Avr. 2018. DOI : 10.1002/ctpp.201700215 (cf. p. 103).

[106] H.Y. GUO, H.Q. WANG, J.G. WATKINS et al. « First experimental tests of a new small angle slot divertor on DIII-D ». In : *Nuclear Fusion* 59.8 (juill. 2019), p. 086054. DOI : 10.1088/1741-4326/ab26ee. URL : https://doi.org/10.1088/1741-4326/ab26ee (cf. p. 103).

[107] M.W. SHAFER, B. COVELE, J.M. CANIK et al. « Dependence of neutral pressure on detachment in the small angle slot divertor at DIII-D ». In : *Nuclear Materials and Energy* 19 (mai 2019), p. 487-492. ISSN : 2352-1791. DOI : https://doi.org/10.1016/j.nme.2019.04.003. URL : https://www.sciencedirect.com/science/article/pii/S2352179118302588 (cf. p. 103).

[108] A.L. MOSER, A.W. LEONARD, A.G. MCLEAN et al. « The effect of divertor closure on detachment onset in DIII-D ». In : *Nuclear Materials and Energy* 19 (mai 2019), p. 67-71. DOI : 10.1016/j.nme.2019.01.017 (cf. p. 103).

[109] L. CASALI, B.M. COVELE et H.Y. GUO. « The effect of neutrals in the new SAS divertor at DIII-D as modelled by SOLPS ». In : *Nuclear Materials and Energy* 19 (mai 2019), p. 537-543. ISSN : 2352-1791. DOI : https://doi.org/10.1016/j.nme.2019.03.021. URL : https://www.sciencedirect.com/science/article/pii/S2352179118301753 (cf. p. 103).

[110] L. CASALI, D. ELDON, J.A. BOEDO et al. « Neutral leakage, power dissipation and pedestal fueling in open vs closed divertors ». In : *Nuclear Fusion* 60.7 (juin 2020), p. 076011. DOI : 10.1088/1741-4326/ab8d06. URL : https://doi.org/10.1088/1741-4326/ab8d06 (cf. p. 103).

[111] H SI, H Y GUO, G S XU et al. « Modeling the effect of divertor closure on plasma detachment for new divertor design of EAST by SOLPS ». In : *Plasma Physics and Controlled Fusion* 61.9 (août 2019), p. 095007. DOI : 10.1088/1361-6587/ab348f. URL : https://doi.org/10.1088/1361-6587/ab348f (cf. p. 103).

[112] Y Q TAO, G S XU, Q Q YANG et al. « Impact of divertor closure on edge plasma behavior in EAST H-mode plasmas ». In : *Plasma Physics and Controlled Fusion* 63.6 (avr. 2021), p. 065004. DOI : 10.1088/1361-6587/abf447. URL : https://doi.org/10.1088/1361-6587/abf447 (cf. p. 103).

[113] Alberto LOARTE. « Effects of divertor geometry on tokamak plasmas ». In : *Plasma Physics and Controlled Fusion* 43.6 (mai 2001), R183-R224. DOI : 10.1088/0741-3335/43/6/201. URL : https://doi.org/10.1088/0741-3335/43/6/201 (cf. p. 103).

[114] AL MOSER, L CASALI, BM COVELE et al. « Separating divertor closure effects on divertor detachment and pedestal shape in DIII-D ». In : *Physics of Plasmas* 27.3 (2020), p. 032506. DOI : 10.1063/1.5109027 (cf. p. 113).

[115] SL ALLEN, NH BROOKS, R BASTASZ et al. « Radiative divertor and scrape-off layer experiments in open and baffled divertors on DIII-D ». In : *Nuclear Fusion* 39.11Y (1999), p. 2015. DOI : 10.1088/0029-5515/39/11y/348 (cf. p. 113).

[116] M. BERNERT, M. WISCHMEIER, A. HUBER et al. « Power exhaust by SOL and pedestal radiation at ASDEX Upgrade and JET ». In : *Nuclear Materials and Energy* 12 (2017). Proceedings of the 22nd International Conference on Plasma Surface Interactions 2016, 22nd PSI, p. 111-118. ISSN : 2352-1791. DOI : https://doi.org/10.1016/j.nme.2016.12.029. URL : https://www.sciencedirect.com/science/article/pii/S2352179116302174 (cf. p. 135).

[117] P A SCHNEIDER, E WOLFRUM, M G. DUNNE et al. « Observation of different phases during an ELM crash with the help of nitrogen seeding ». In : *Plasma Physics and Controlled Fusion* 56.2 (jan. 2014), p. 025011. DOI : 10.1088/0741-3335/56/2/025011. URL : https://dx.doi.org/10.1088/0741-3335/56/2/025011 (cf. p. 135).

[118] M N A BEURSKENS, J SCHWEINZER, C ANGIONI et al. « The effect of a metal wall on confinement in JET and ASDEX Upgrade ». In : *Plasma Physics and Controlled Fusion* 55.12 (nov. 2013), p. 124043. DOI : 10.1088/0741-3335/55/12/124043. URL : https://dx.doi.org/10.1088/0741-3335/55/12/124043 (cf. p. 135).

[119] L. WANG, H.Y. GUO, F. DING et al. « Advances in plasma–wall interaction control for H-mode operation over 100 s with ITER-like tungsten divertor on EAST ». In : *Nuclear Fusion* 59.8 (juill. 2019), p. 086036. DOI : 10.1088/1741-4326/ab1ed4. URL : https://doi.org/10.1088/1741-4326/ab1ed4 (cf. p. 135).

[120] A KALLENBACH, M BERNERT, R DUX et al. « Analytical calculations for impurity seeded partially detached divertor conditions ». In : *Plasma Physics and Controlled Fusion* 58.4 (fév. 2016), p. 045013. DOI : 10.1088/0741-3335/58/4/045013. URL : https://dx.doi.org/10.1088/0741-3335/58/4/045013 (cf. p. 141, 232).

[121] C THEILER, J HARRISON, O FÉVRIER et al. « SOL transport and detachment in alternative divertor configurations in TCV L-and H-mode plasmas ». In : *27th IAEA Fusion Energy Conference (FEC 2018)*. CONF. 2018 (cf. p. 144, 169).

[122] Ulrich STROTH. « Prozesse am Plasmarand ». In : *Plasmaphysik : Phänomene, Grundlagen und Anwendungen*. Berlin, Heidelberg : Springer Berlin Heidelberg, 2018, p. 511-541. ISBN : 978-3-662-55236-0. DOI : 10.1007/978-3-662-55236-0_16. URL : https://doi.org/10.1007/978-3-662-55236-0_16 (cf. p. 167).

[123] Karl J ASTROM. « PID controllers : theory, design, and tuning ». In : *The International Society of Measurement and Control* (1995) (cf. p. 202).

[124] E. KOLEMEN, D.A. GATES, C.W. ROWLEY et al. « Strike point control for the National Spherical Torus Experiment (NSTX) ». In : *Nuclear Fusion* 50.10 (sept. 2010), p. 105010. DOI : 10.1088/0029-5515/50/10/105010. URL : https://doi.org/10.1088/0029-5515/50/10/105010 (cf. p. 202).

[125] Sigurd SKOGESTAD et Ian POSTLETHWAITE. *Multivariable feedback control : analysis and design*. john Wiley & sons, 2005 (cf. p. 202).

[126] G.P. CANAL, T. LUNT, H. REIMERDES et al. « Enhanced drift effects in the TCV snowflake divertor ». In : *Nuclear Fusion* 55.12 (nov. 2015), p. 123023. DOI : 10.1088/0029-5515/55/12/123023. URL : https://dx.doi.org/10.1088/0029-5515/55/12/123023 (cf. p. 215).

[127] S K ERENTS, R A PITTS, W FUNDAMENSKI et al. « A comparison of experimental measurements and code results to determine flows in the JET SOL ». In : *Plasma Physics and Controlled Fusion* 46.11 (sept. 2004), p. 1757. DOI : 10.1088/0741-3335/46/11/006. URL : https://dx.doi.org/10.1088/0741-3335/46/11/006 (cf. p. 216, 217).

[128] Nobuyuki ASAKURA. « Understanding the SOL flow in L-mode plasma on divertor tokamaks, and its influence on the plasma transport ». In : *Journal of Nuclear Materials* 363-365 (2007). Plasma-Surface Interactions-17, p. 41-51. ISSN : 0022-3115. DOI : https://doi.org/10.1016/j.jnucmat.2006.12.029. URL : https://www.sciencedirect.com/science/article/pii/S0022311506006325 (cf. p. 219).

[129] A KALLENBACH et S HENDERSON. personal communication. November, 2022 (cf. p. 232).

[130] A LOARTE, S BOSCH, A CHANKIN et al. « Multi-machine scaling of the divertor peak heat flux and width for L-mode and H-mode discharges ». In : *Journal of Nuclear Materials* 266-269 (1999), p. 587-592. ISSN : 0022-3115. DOI : https://doi.org/10.1016/S0022-3115(98)00590-X. URL : https://www.sciencedirect.com/science/article/pii/S002231159800590X (cf. p. 232).

[131] T. EICH, A.W. LEONARD, R.A. PITTS et al. « Scaling of the tokamak near the scrape-off layer H-mode power width and implications for ITER ». In : *Nuclear Fusion* 53.9 (août 2013), p. 093031. DOI : 10.1088/0029-5515/53/9/093031. URL : https://dx.doi.org/10.1088/0029-5515/53/9/093031 (cf. p. 232).

[132] U. STROTH, M. BERNERT, D. BRIDA et al. « Model for access and stability of the X-point radiator and the threshold for marfes in tokamak plasmas ». In : *Nuclear Fusion* 62.7 (avr. 2022), p. 076008. DOI : 10.1088/1741-4326/ac613a. URL : https://dx.doi.org/10.1088/1741-4326/ac613a (cf. p. 233).

[133] O. PAN, M. BERNERT, T. LUNT et al. « SOLPS-ITER simulations of an X-point radiator in the ASDEX Upgrade tokamak ». In : *Nuclear Fusion* 63.1 (nov. 2022), p. 016001. DOI : 10.1088/1741-4326/ac9742. URL : https://dx.doi.org/10.1088/1741-4326/ac9742 (cf. p. 233, 234).

ANNEXES

A. Maxwellian velocity distribution

Maxwellian distribution describes the ratio between the number of particles (dN) with a velocity close to $\boldsymbol{v}$ ($= v_x + v_y + v_z$) in the unit velocity volume ($dv_x\,dv_y\,dv_z$) and the total number of particles (N) in the system with a given temperature (T), as shown in Equations A.1 and A.2. Where the Boltzmann constant $k = 1.38 \times 10^{-23}\,\mathrm{JK}^{-1}$. It is suitable to be used for idealized gases or plasma in a steady state (thermodynamic equilibrium) where the particles can move freely without particle lost from the system, nor the presence of outer force, except for the collision that exchanges energy and momentum with each other or with the thermal environment.

$$\frac{dN}{N} = f^{\mathrm{Max}}(\boldsymbol{v})\,dv_x\,dv_y\,dv_z \tag{A.1}$$

$$f^{\mathrm{Max}}(\boldsymbol{v}) = \left(\frac{m}{2\pi kT}\right)^{3/2} \exp\left(-\frac{m}{2kT}\left(v_x^2 + v_y^2 + v_z^2\right)\right) \tag{A.2}$$

Because particles have equal rights to move in all directions, $f^{\mathrm{Max}}(\boldsymbol{v})$ can be written to be dependent only on the magnitude of the velocity v :

$$\frac{dN}{N} = f^{\mathrm{Max}}(v)4\pi v^2\,dv \tag{A.3}$$

$$v \equiv \left(v_x^2 + v_y^2 + v_z^2\right)^{1/2} \tag{A.4}$$

A.1. Typical speeds

Three typical speeds can be obtained based on Maxwellian distribution :

The mean velocity $\langle v \rangle$

$$\langle v \rangle = \frac{\int v\,dN}{N} = \int v\frac{dN}{N} = \int_0^\infty v f^{\mathrm{Max}}(v)4\pi v^2\,dv = \sqrt{\frac{8kT}{\pi m}} \tag{A.5}$$

The root mean square velocity v_{rms}

$$\langle v^2 \rangle = \frac{\int v^2\,dN}{N} = \int v^2\frac{dN}{N} = \int_0^\infty v^2 f^{\mathrm{Max}}(v)4\pi v^2\,dv = \frac{3kT}{\pi m} \tag{A.6}$$

$$v_{\mathrm{rms}} = \sqrt{\langle v^2 \rangle} = \sqrt{\frac{3kT}{m}} \tag{A.7}$$

The most probable velocity v_{mp}

To find v_{mp}, which corresponds to the maximum value of $f(v)$, we calculate its derivative result and set it to zero

$$\left.\frac{df(v)}{dv}\right|_{v=v_{\mathrm{mp}}} = 0 \tag{A.8}$$

So we obtain v_{mp} as follow

$$v_{\mathrm{mp}} = \sqrt{\frac{2kT}{m}} \tag{A.9}$$

A.2. One-way parameters

Next, we discuss the one-way velocity $v_{\text{one-way}}$ that describes the averaged velocity of random particles heading to one direction (or to the wall). We suppose it is in the x direction.

$$\begin{aligned} v^{\mathrm{Max}}_{\text{one-way}} &= \int_{v_{\mathrm{x}}=0}^{+\infty} f^{\mathrm{Max}}(\boldsymbol{v})\, v_{\mathrm{x}}\, dv_{\mathrm{x}} \int_{v_{\mathrm{y}}=-\infty}^{+\infty} dv_{\mathrm{y}} \int_{v_{\mathrm{z}}=-\infty}^{+\infty} dv_{\mathrm{z}} \\ &= \sqrt{\frac{kT}{2\pi m}} = \frac{1}{4}\langle v\rangle \end{aligned} \tag{A.10}$$

So we have one-way particle flux, n represents the particle density :

$$\Gamma^{\mathrm{Max}}_{\text{one-way}} = \frac{1}{4} n\langle v\rangle \tag{A.11}$$

The one-way heat flux can be written as

$$\begin{aligned} q^{Max}_{\text{one-way}} &= \int_{v_{\mathrm{x}}=0}^{+\infty} \frac{1}{2} nm\left(v_{\mathrm{x}}^2 + v_{\mathrm{y}}^2 + v_{\mathrm{z}}^2\right) v_{\mathrm{x}} f^{\mathrm{Max}}(\boldsymbol{v})\, dv_{\mathrm{x}} \int_{v_{\mathrm{y}}=-\infty}^{+\infty} dv_{\mathrm{y}} \int_{v_{\mathrm{z}}=-\infty}^{+\infty} dv_{\mathrm{z}} \\ &= 2kT\Gamma^{\mathrm{Max}}_{\text{one-way}} \end{aligned} \tag{A.12}$$

A.3. Drift Maxwellian distribution

The previous equations are related to ordinary Maxwellian distribution with no drift velocity. In the presence of mean drift velocity $\mathbf{a} = a_{\mathrm{x}} + a_{\mathrm{y}} + a_{\mathrm{z}}$, we use drift Maxwellian distribution and the Equation A.2 can be written as

$$f^{\mathrm{drift,Max}}(\boldsymbol{v}) = \left(\frac{m}{2\pi kT}\right)^{3/2} \exp\left(-\frac{m}{2kT}\left((v_{\mathrm{x}}-a_{\mathrm{x}})^2 + (v_{\mathrm{y}}-a_{\mathrm{y}})^2 + (v_{\mathrm{z}}-a_{\mathrm{z}})^2\right)\right) \tag{A.13}$$

Firstly, we calculate the mean drift velocity in the x-direction :

$$\begin{aligned} v_{\mathrm{x}}^{\mathrm{drift,Max}} &= \int_{v_{\mathrm{x}}=-\infty}^{+\infty} f^{\mathrm{drift,Max}}(\boldsymbol{v})\, v_{\mathrm{x}}\, \mathrm{d}v_{\mathrm{x}} \int_{v_{\mathrm{y}}=-\infty}^{+\infty} dv_{\mathrm{y}} \int_{v_{\mathrm{z}}=-\infty}^{+\infty} dv_{\mathrm{z}} \\ &= \langle v_{\mathrm{x}}\rangle = a_{\mathrm{x}} \end{aligned} \tag{A.14}$$

Due to the mean drift velocity, we can discuss the net flux in the x-direction :

$$\begin{aligned}\Gamma_{\mathrm{x}}^{\mathrm{drift,Max}} &= \int_{v_{\mathrm{x}}=-\infty}^{+\infty} n f^{\mathrm{drift,Max}}(\boldsymbol{v})\, v_{\mathrm{x}}\, \mathrm{d}v_{\mathrm{x}} \int_{v_{\mathrm{y}}=-\infty}^{+\infty} dv_{\mathrm{y}} \int_{v_{\mathrm{z}}=-\infty}^{+\infty} dv_{\mathrm{z}} \\ &= n\langle v_{\mathrm{x}}\rangle = n a_{\mathrm{x}}\end{aligned} \tag{A.15}$$

Therefore, the total (net) heat flux in the x-direction :

$$\begin{aligned}q_{\mathrm{x}}^{\mathrm{drift,Max}} &= \int_{v_{\mathrm{x}}=-\infty}^{+\infty} \frac{1}{2} nm\left(v_{\mathrm{x}}^2 + v_{\mathrm{y}}^2 + v_{\mathrm{z}}^2\right) v_{\mathrm{x}} f^{\mathrm{drift,Max}}(\boldsymbol{v})\, dv_{\mathrm{x}} \int_{v_{\mathrm{y}}=-\infty}^{+\infty} dv_{\mathrm{y}} \int_{v_{\mathrm{z}}=-\infty}^{+\infty} dv_{\mathrm{z}} \\ &= \left(\frac{5}{2}kT + \frac{1}{2}ma_{\mathrm{x}}^2\right)\Gamma_{\mathrm{x}}^{\mathrm{drift,Max}}\end{aligned} \tag{A.16}$$

A.4. Boltzmann factor

When an external conservative force field, for example, gravity or an electrostatic force, has effects on the particles. The particle distribution remains Maxwellian, but the density changes, which is related to the Boltzmann factor.

$$dn(\boldsymbol{v}, x) = n_0 f^{\mathrm{Max}}(\boldsymbol{v}) \exp(-\Phi(x)/kT)\, dv_{\mathrm{x}}\, dv_{\mathrm{y}}\, dv_{\mathrm{z}}, \tag{A.17}$$

where $\exp(-\Phi(x)/kT)$ is the Boltzmann factor, n_0 is the reference value of density at potential $\Phi = 0$. For an electric potential $\Phi = q\phi$, it becomes $\exp\left(-q\phi/kT\right)$. Here, q is the charge on the particle. When it refers to ions, the Boltzmann factor is $\exp\left(-e\phi/kT\right)$. When it refers to electrons, with charge $-e$, the Boltzmann factor is $\exp\left(e\phi/kT\right)$.

B. Particle drifts

The motion of plasma particles confined by the uniform magnetic field **B** follows circular Larmor orbits. Their motion can be influenced by several factors, represented as perpendicular drifts. The factors include gravity perpendicular to the **B**, electric field perpendicular to the **B**, gradient of magnetic field perpendicular to the **B**, curved magnetic field and also the pressure gradient perpendicular to the **B**, etc.

For the non-relativistic particles in the uniform magnetic field **B**, its equation of motion is

$$m\frac{d\mathbf{v}}{dt} = q\mathbf{v}\times\mathbf{B} \tag{B.1}$$

When external force **F** is applied, its equation of motion becomes

$$m\frac{d(\mathbf{v}+\mathbf{v}_{\parallel}^{'}+\mathbf{v}_{\perp}^{'})}{dt} = q(\mathbf{v}+\mathbf{v}_{\parallel}^{'}+\mathbf{v}_{\perp}^{'})\times\mathbf{B}+\mathbf{F}_{\parallel}+\mathbf{F}_{\perp}, \tag{B.2}$$

where $\mathbf{v}$ is the particles original gyromotion velocity, $\mathbf{v}^{'}$ is the change of velocity due to external force. The components parallel with the **B** are marked with "$\parallel$", and the components perpendicular to the **B** are marked with "$\perp$". Subtracting Equation B.1 from Equation B.2 gives :

$$m\frac{d(\mathbf{v}_{\parallel}^{'}+\mathbf{v}_{\perp}^{'})}{dt} = q(\mathbf{v}_{\parallel}^{'}+\mathbf{v}_{\perp}^{'})\times\mathbf{B}+\mathbf{F}_{\parallel}+\mathbf{F}_{\perp} \tag{B.3}$$

We need to notice that $\mathbf{v}_{\parallel}^{'}\times\mathbf{B}=\mathbf{0}$. The $\mathbf{F}_{\parallel}$ only leads to an acceleration of particle along **B**, which can be written as : $m\,d\mathbf{v}_{\parallel}^{'}/dt = \mathbf{F}_{\parallel}$. With the drift velocity perpendicular to the **B**, the Lorentz fore will appear to balance with the constant $\mathbf{F}_{\perp}$, so $d\mathbf{v}_{\perp}^{'}/dt = \mathbf{0}$. Finally, we have

$$q\mathbf{v}_{\perp}^{'}\times\mathbf{B}+\mathbf{F}_{\perp}=\mathbf{0} \tag{B.4}$$

The drift velocity $\mathbf{v}_{\mathrm{d}}$ due to the external force is defined as Equation B.5, the direction of velocity is perpendicular to external force $\mathbf{F}_{\perp}$ and **B**.

$$\mathbf{v}_{\mathrm{d}} = \frac{\mathbf{F}_{\perp}\times\mathbf{B}}{qB^2} \tag{B.5}$$

B.0.1. Gravitational drift

When Gravity is perpendicular to the magnetic field, the $\mathbf{F}_{\perp} = m\mathbf{g}$ in Equation B.5, the gravitational drift is written as Equation B.6. The gravitational drift is negligible for fusion experiments but becomes important for the astrophysical plasmas.

$$\mathbf{v}_{\mathrm{d,grav}} = \frac{m\mathbf{g}\times\mathbf{B}}{qB^2} \tag{B.6}$$

B.0.2. E × B drift

In the presence of an electric field perpendicular to the magnetic field, the $\mathbf{F}_\perp = q\mathbf{E}$ in Equation B.5, the **E × B** drift perpendicular to both fields is written as Equation B.7. This drift is independent of the charge, mass, and energy of the particle. So, there is no electric current driven by this drift, but it can influence the movement of the whole plasma. As illustrated in Figure 1.

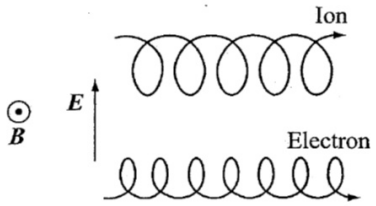

FIGURE 1. : **E × B** drift. Figure from reference [11].

$$\mathbf{v}_{E\times B} = \frac{\mathbf{E}\times\mathbf{B}}{B^2} \tag{B.7}$$

B.0.3. ∇B drift

When there is a transverse gradient in a magnetic field, the curvature radius of the particle orbit can be changed due to the varied magnetic field. As a result, the particle orbits undergo a ∇B drift perpendicular to both the magnetic field and its gradient. Assuming the ∇B to be small so that the magnetic field variation across the Larmor radius is small compared to B. The magnetic moment of particles is $\mu = m v_\perp^2/(2B)$, a force $\mathbf{F}_{\nabla B} = -\mu\nabla_\perp B$ is produced due to the gradient of the magnetic field, it tends to pull particles from strong magnetic fields back to weak magnetic fields, so it is in the reversed direction of ∇B. The $\mathbf{F}_\perp = \mathbf{F}_{\nabla B}$ in Equation B.5, the ∇B drift is written as Equation B.8. Figure 2 shows the trajectories of an ion and an electron under the influence of **E × B** drift. In a tokamak, the magnetic field decreases with increasing major radius R, leading to the ∇B drift being directed along the Z-direction. Its direction upward or downward depends on the $\mathbf{B}_\phi$ direction and the charge sign.

$$\mathbf{v}_{\nabla B} = \frac{m v_\perp^2}{2q}\frac{\mathbf{B}\times\nabla B}{B^3} \tag{B.8}$$

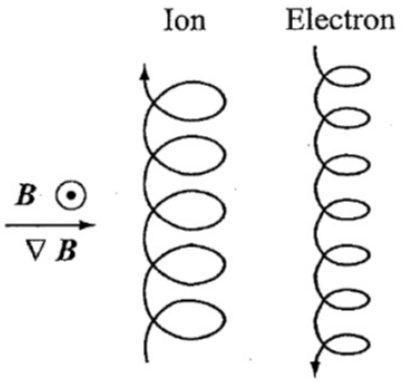

FIGURE 2. : ∇B drift. Figure from reference [11].

B.0.4. Curvature drift

The toroidal magnetic field in Tokamak is curved field lines with curvature radius R. In this case, the particles are subject to the centrifugal force $\mathbf{F}_\perp = m v_\parallel^2 / R$, and $\nabla B = B/R$. So the curvature drift is written as Equation B.9. We need to note that this centrifugal force $\mathbf{F}_\perp$ is also charge sign independent, similar to $\mathbf{F}_{\nabla B}$. The curvature drift and ∇B drift have the same direction for ions and electrons in Tokamak.

$$\mathbf{v}_{\text{curv}} = \frac{m v_\parallel^2}{q} \frac{\mathbf{B} \times \nabla B}{B^3} \tag{B.9}$$

B.0.5. ∇P drift

In the presence of a pressure gradient ∇P due to density or temperature gradients in the plasma, the $\mathbf{F}_\perp = -\nabla p_\alpha / n_\alpha$ in Equation B.5. The so-called diamagnetic drift is written as Equation B.10.

$$\mathbf{v}_{\nabla P} = \frac{\mathbf{B} \times \nabla p_{\text{a}}}{q_{\text{a}} n_\alpha B^2} \tag{B.10}$$

In contrast to the particle drifts above, the diamagnetic drift is a fluid drift in magnetized plasmas. The diamagnetic drift has no contribution to the displacement of guiding centers in the homogeneous magnetic field, so there is no net transport of particles.

C. Parameter feedback control

A classic PID controller is used to control plasma in realistic time-dependent simulations with the control function :

$$u(t) = k_{\mathrm{n}}\left(k_{\mathrm{p}} \cdot e(t) + k_{\mathrm{i}} \cdot \int e(t)\,dt + k_{\mathrm{d}} \cdot \frac{d}{dt}e(t)\right) + BG, \tag{C.1}$$

where $u(t)$ is the manipulated variable (e.g. gas puff, input power) that can be employed to change the plasma state. k_{n} is the normalized factor, being adjusted to make the control of certain parameters (e.g. density, temperature, particle flux) have similar gain factors (k_{p}, k_{i}, and k_{d}). The error item $e(t)$ = measured value – target value, evaluating the difference between the current state and desired state. k_{p} is the proportional gain. k_{i} is the integral gain. k_{d} is the derivative gain. BG is the background value. Applying the PID controller with proper k_{n} and gain factors can make plasma evolve toward the wanted state smoothly. k_{d} is set to zero, due to k_{d} can trigger instability issues during control process. For WEST and TCV simulation cases in Section 3.2, the control of upstream or downstream parameters has been realized successfully by manipulating the gas puff rate. The proper setup of factors is shown in Table 1.

Target	$n_{\mathrm{e,sep}}$ $[\mathrm{m}^{-3}]$	T_{et} [eV]	$q_{\parallel,\mathrm{t}}$ $[\mathrm{W m}^{-2}]$	$H_{\mathrm{rad,front}}$ [m]	$\Gamma_{\parallel,\mathrm{t}}$ $[\mathrm{m}^{-2}\,\mathrm{s}^{-1}]$
k_{n}	-1.0	2.0×10^{17}	1.0×10^{5}	-2.0×10^{20}	-/+2.2×10^{-5} (before/after rollover)
k_{p}	2300–1000 (from attached to detached)				
k_{i}	4.0×10^{4}–2.0×10^{4} (from attached to detached)				

TABLE 1. : The setup of gain factors of different target parameters.

The $n_{\mathrm{e,sep}}$, T_{et}, $q_{\parallel,\mathrm{t}}$, $H_{\mathrm{rad,front}}$ evolve monotonically with the level of detachment. Thus, k_{n} can remain unchanged in the process from attached to detached. However, the particle flux at the target can roll over when detachment is achieved in the cases with constant input power. When controlling detachment by particle flux, we need to pay attention to the rollover threshold. Before the rollover, k_{n} is a negative value, and the target value needs to be higher than the highest particle flux that can be reached. While, after the rollover, the sign of k_{n} needs to be changed from negative to positive, the target value needs to be lower than the highest value simultaneously, and maintain plasma stability at the desired level of detachment.

In the control process, there are limitations to the gas puff rate. For the control of the parameters shown above, the lower limit of gas puff rate is zero, and the upper limit is set as 5.0×10^{22} atoms s^{-1} to avoid a too high gas puff rate making plasma collapse.

When controlling detachment through rollover of particle flux, the lower limit of gas puff rate needs to be renewed after rollover happens. The lower limit value depends on the gas puff rate threshold for the rollover of particle flux. One needs to notice that this kind of strategy is based on the assumption that there is no net sink or stable sink of particles on the wall, leading to an immediate change in the divertor state with a variable gas puff rate. In real experiments, the lower limit of gas puff is hard to define.

Due to the low capability of the pump, the plasma density in SOL decreases slowly even when the gas puff rate is zero. The plasma density does not have the same sensitivity to an immediate equal increase or decrease in gas puff rate. For this reason, when the divertor state (e.g. $n_{\mathrm{e,sep}}$) is much higher than the target value because of too high gas puff rate applied or other reasons, the integral factor k_{i} will be temporally increased by a factor of 10, to fast decrease the gas puff rate, thus pull $n_{\mathrm{e,sep}}$ back to target as quickly as possible. In this process, the gas puff rate is usually decreased to zero quickly. The integral term will stop accumulating when the gas puff rate is zero due to the accumulation of the integral term does not make sense anymore. It starts to accumulate again when the gas puff is non-zero. Increasing the total pump speed (e.g. increasing the number of pumps) can also be considered at the same time.

The example cases are shown in Figure 3, it used the setup as shown in Table 1, $k_{\mathrm{p}} = 2300$, $k_{\mathrm{i}} = 4.0 \times 10^4$. Two cases start from the same point and eventually converge to the nearly same state, but the red case used $n_{\mathrm{e,sep}}$ feedback control via adjusting the gas puff, and the blue case used a constant gas puff rate. The control process can reach convergence much quicker than the one with a constant puff rate by a factor of about 10. It has been found that when we want to control the plasma to reach a higher $n_{\mathrm{e,sep}}$, lower gain factors can be helpful in smoothing the control process and maintaining a stable divertor state. From attached to detached plasma, the proper gain factors can vary in a range from 2300 to 1000 for k_{p}, from 4.0×10^4 to 2.0×10^4 for k_{i}. The gain factors can be tuned by identifying system dynamic responses via methods such as the *First-Order Plus Dead Time* (FOPDT) model [123, 124] and *Frequency Response Function* (FRF) [31, 125]. More work focuses on developing an advanced controller capable of identifying system dynamic responses, autotuning gain values will be done in the next steps.

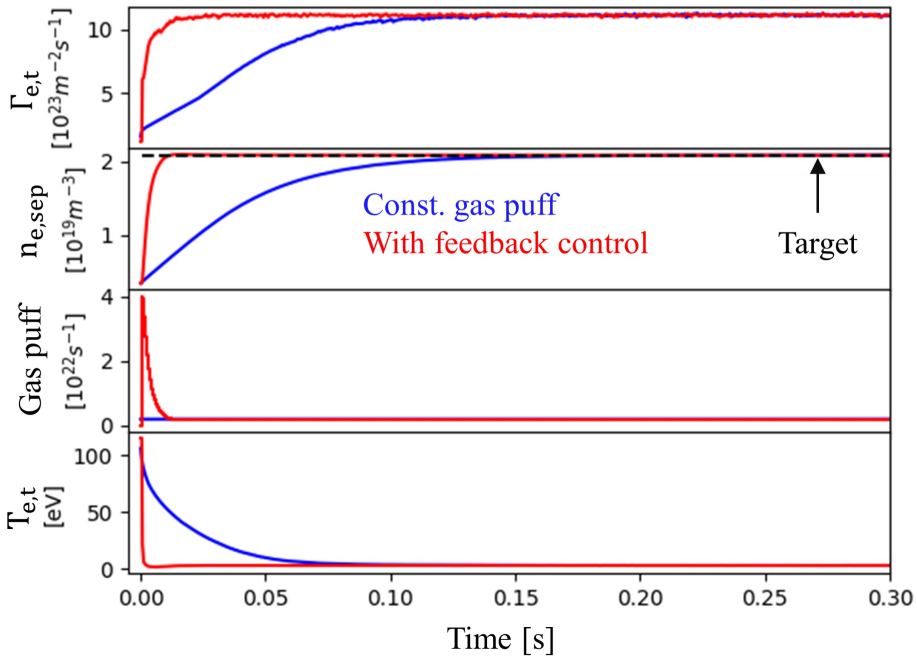

FIGURE 3. : The comparison between the case with feedback control and the case with constant gas puff applied.

Time delay influence is considered in the feedback control. The time delay (TD) ≈ 2 ms has been applied in the cases with variable k_p values as shown in Figure 4. It has been found that if the time delay is less than 2 ms, the plasma can still be controlled with the setup shown in Table 1. If the time delay is bigger (more than 2 ms), decreasing the gain factors or using ramped target as a buffering can be a good solution to make plasma still under control.

The PID feedback control method can give a solution to control certain plasma parameters to reach the desired value.

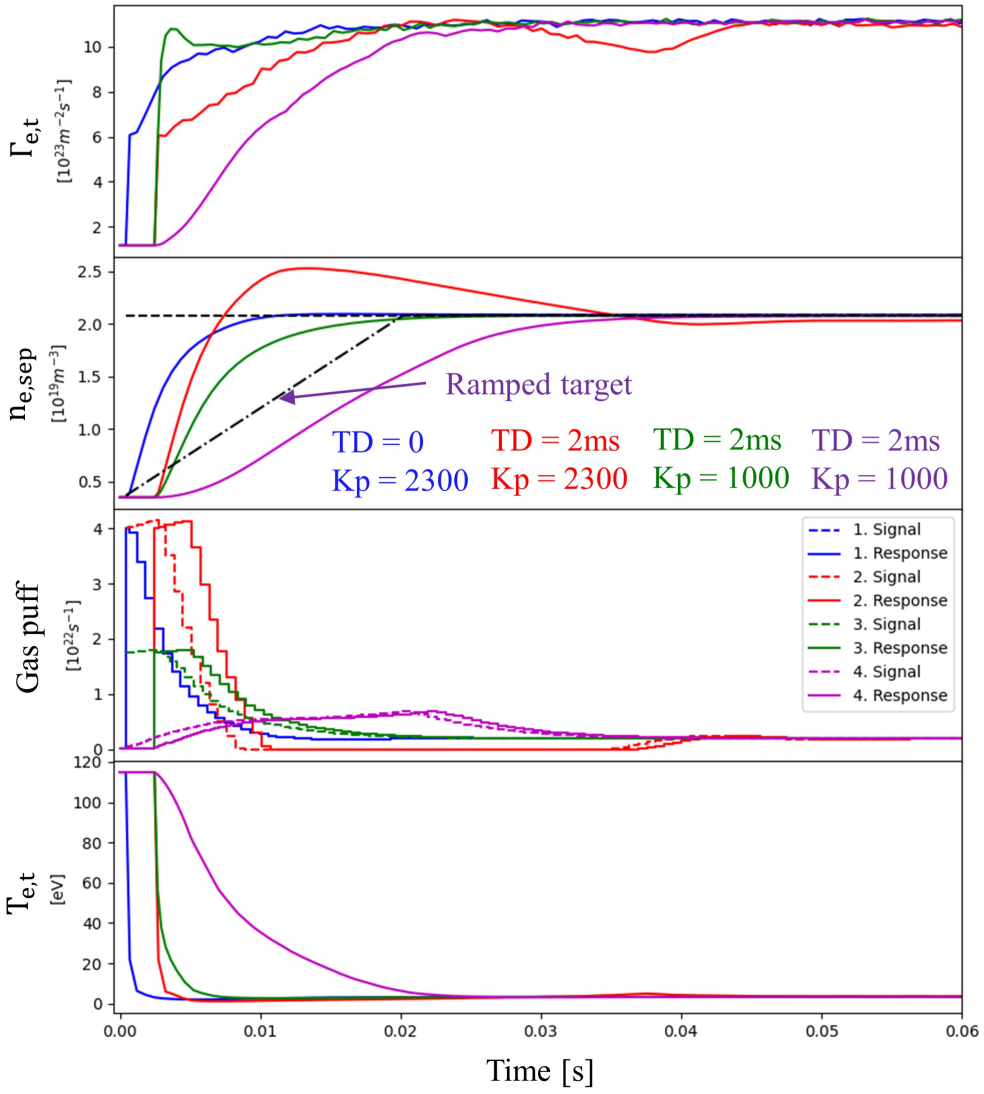

FIGURE 4. : The influence of time delay in feedback control : The $n_{e,sep}$ is controlled by adjusting the gas puff rate through the PID controller. The case with the purple color was performed with a ramped target, while the other cases were performed with a constant target value.

D. Profile feedback control

The profile feedback control can be used to control the radial density and temperature profile at the OMP via adjusting the transport coefficients. For the mesh used in the simulation, there are multiple cells distributed at the OMP in the radial direction from CEI to the wall. As shown in Equation D.1 and D.2.

$$\nabla f(r^n) = \frac{f(r^n - dr) - f(r^n + dr)}{2\,dr} \tag{D.1}$$

$$dr = \min(\left|r^{\mathrm{n}-1} - r^n\right|, \left|r^{\mathrm{n}+1} - r^{\mathrm{n}}\right|) \tag{D.2}$$

The radial position of a cell with index n is defined as r^n. $f(r)$ represents the value of density or temperature at position r. The measured value here becomes $\nabla f(r^n)$, the manipulated variable is $D_\perp$, $\chi_{\perp,\mathrm{e}}$ or $\chi_{\perp,\mathrm{i}}$.

The density and temperature profiles can be controlled at the same time if enough experimental data can be provided. $k_{\mathrm{n}} = -3.33 \times 10^{-22}$ and -1.00×10^{-4} for density and temperature, k_{p} in the range of 0–10, and k_{i} in the range of 10–20 can be proper setup for the profile feedback control. To guarantee the agreements between simulation and experiment for the radial profile at the OMP, the parameter feedback control of $n_{\mathrm{e,sep}}$ or $T_{\mathrm{e,sep}}$ needs to be activated at the same time. When the diffusion coefficients at the OMP are determined by the feedback controller, they will be propagated into the whole simulation domain following the method illustrated in Section 3.

E. Simulation setup sensitivity studies

In this chapter, we will study the influence of different simulation setups. When investigating the effects of a setup, other setups are the same or deactivated to isolate their effects, as shown in Table 2. The setups not mentioned in this table keep consistent with the choices in Section 3, depending on the machine (WEST or TCV) used to do the investigation. Here, Diff OMP represents the transport coefficients at the OMP. Its impact will be introduced in Section E.1.1. $\chi_{\perp,\mathrm{i}}/\chi_{\perp,\mathrm{e}}$ represents the ratio of $\chi_{\perp,\mathrm{i}}$ and $\chi_{\perp,\mathrm{e}}$ in the pedestal. Its impact will be introduced in Section E.1.2. The impact of ballooning, drifts, and recycling coefficients on the wall (R_{wall}) will be introduced in Sections E.1.3, E.2, and E.3.

Cases	Diff OMP	Ratio $\chi_{\perp,\mathrm{i}}/\chi_{\perp,\mathrm{e}}$	Ballooning	Drifts	R_{wall}
Case 1	Cst, Non-Cst	1	b = 0	No	1
Case 2	Non-Cst	1, 2	b = 0	No	1
Case 3	Non-Cst	1	b = 0,1,2,3	No	1
Case 4	Non-Cst	1	b = 0	No, FB, RB	1
Case 5	Non-Cst	1	b = 0	No	0.99, 1

TABLE 2. : The setups of each case in this section.

E.1. Transport coefficients

E.1.1. Radial transport coefficients

In this section, we study the impacts of transport coefficients at the OMP by the setup of Case 1 in Table 2. Two subcases of WEST are used, one with constant transport coefficients at the OMP : classic WEST L-mode setups $D_\perp = 0.3, \chi_{\perp,e} = \chi_{\perp,i} = 1$. Another one with non-constant transport coefficients at the OMP : $D_\perp$ is consistent with the coefficients shown in Figure 3.13 and suppose $\chi_{\perp,e} = \chi_{\perp,i} = D_\perp/0.3$, to maintain the proportional relationship with the WEST classic L-mode setups. The radial momentum diffusivity is constant as $\nu_\perp = 0.3$ for both cases. The transport coefficients in other positions are homogeneously propagated in the poloidal direction. The purpose is to see how the changes in diffusion coefficient can influence the results. Except for the diffusion coefficients, other setups are the same for both subcases, other possible impacts (e.g. drifts, ballooning) in Section E are excluded.

One can observe that based on the simulation setups here, the difference between constant transport coefficients case and non-constant one is mainly the temperature and density inside separatrix as shown in Figures 5 and 6. The plasma in SOL shows pretty close characteristics. From Figure 7, one can observe no big difference for the

target profiles. This indicates the classic L-mode setups in WEST can give a reasonable estimation for the transport coefficients outside separatrix, but inside separatrix, the transport coefficients are overestimated.

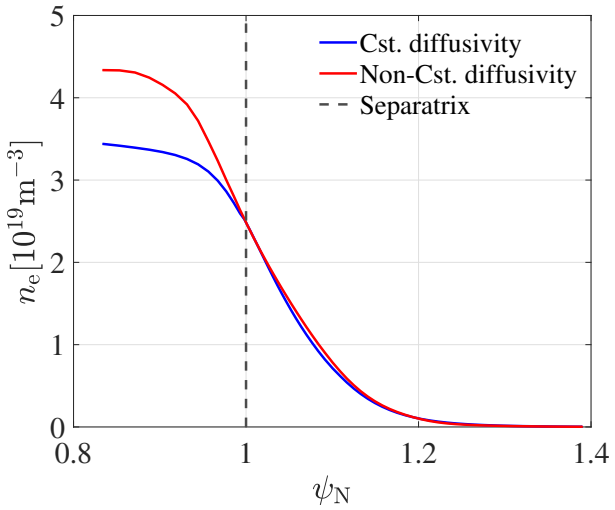

FIGURE 5. : Radial profile of upstream density in the simulation cases with constant diffusivity (blue curve) and non-constant diffusivity (red curve), the dashed line represents the position of separatrix.

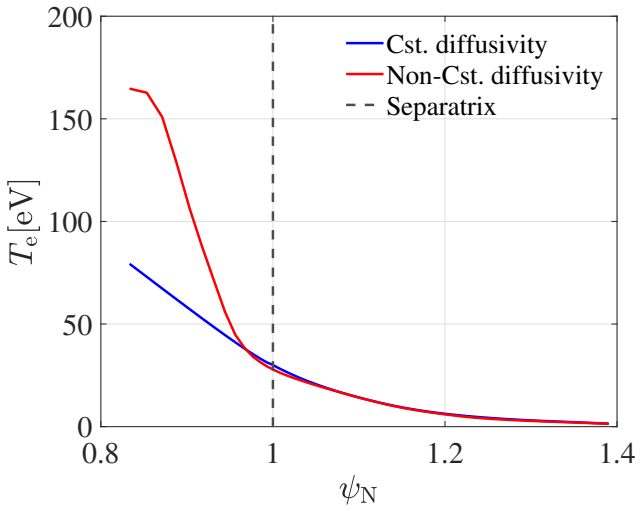

FIGURE 6. : Radial profile of upstream electron temperature in the simulation cases with constant diffusivity (blue curve) and non-constant diffusivity (red curve), the dashed line represents the position of separatrix.

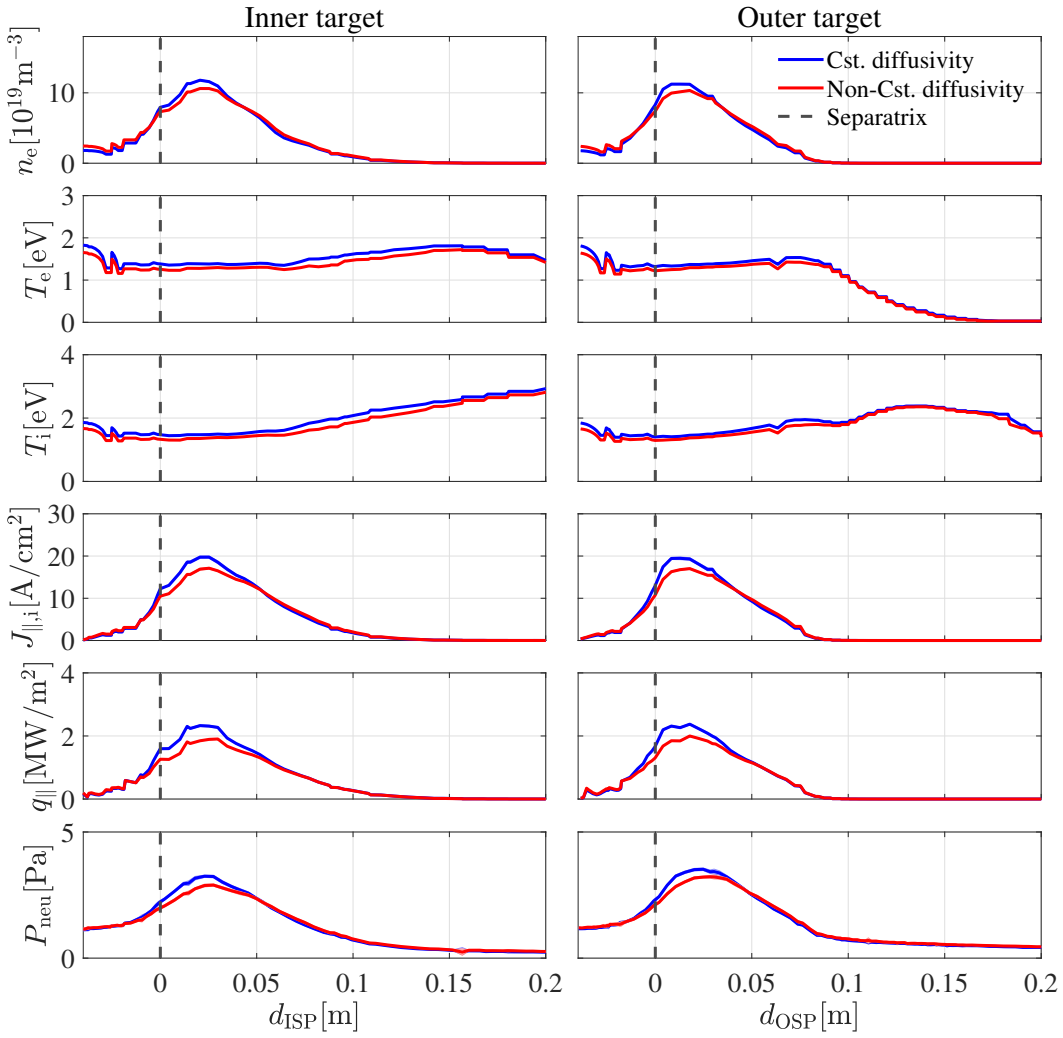

FIGURE 7. : Target profiles of multiple parameters in the simulation cases with constant diffusivity (blue curve) and non-constant diffusivity (red curve) at the inner and outer parts. d_{ISP} (d_{OSP}) is the radial distance from the inner (outer) strike point, negative values are in the PFR, positive values are in the SOL. The dashed line represents the position of separatrix.

E.1.2. Ratio of heat flux diffusivity

In this section, the impacts of the ratio between $\chi_{\perp,i}$ and $\chi_{\perp,e}$ in the pedestal will be investigated. The experimental data from several machines (Figure 7 in [92]) show that the ion-to-electron temperature ratio $\tau = T_i/T_e$ increases with radius, with $\tau = 1 \rightarrow 2.5$ in the edge plasma ($0.64 < \psi_N < 1$). To reproduce τ profile coarsely matched with experiment, the $\chi_{\perp,i}$ is supposed to be higher than $\chi_{\perp,e}$ in the pedestal. Three subcases with ratio values ($\chi_{\perp,i}/\chi_{\perp,e}$) from 1 to 3 have been applied in Case 2 (Table 2) based on TCV simulation from Section 3.2.2.

The electron and ion temperature profile in Figure 8 show that the ratio has no big impact on electron temperature, but separatrix ion temperature would increase with

a higher ratio value. For the TCV simulation in Section 3.2.2, the ratio is supposed to be 2, as it can allow a reasonable ion temperature profile.

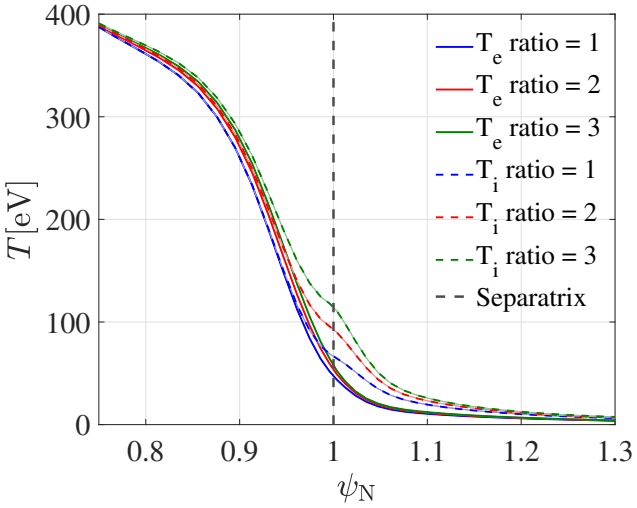

FIGURE 8. : Radial profiles of T_e and T_i at the OMP in TCV simulation cases. The dashed line represents the position of separatrix.

E.1.3. Ballooning

We discuss the value of b factor (in Equation 3.1) that describes the impact of ballooning. The b value was changed from 1 to 3, and the other setups are consistent following Case 3 in Table 2. Ballooning is applied in the simulation of WEST and TCV, we discuss the impacts of ballooning in the simulation of two devices not only due to their inherent difference (wall structure, magnetic configuration), but more importantly they are driven by different setups : WEST simulation suppose to have same input power for all the case, but TCV simulation has fixed pedestal temperature.

Ballooning in WEST In the WEST simulations with fixed input power and the same $n_{e,sep}$, one can observe no significant impact of the b value on the radial density profile at the OMP, as shown in Figure 9. However, the radial temperature profile shows a significant difference : a higher b value corresponds to a higher upstream temperature, as shown in Figure 10. Ballooning also has impacts on both targets : a higher b value leads to higher particles and heat flux at the targets, as shown in Figure 11. The study in JET shows that more power goes into the SOL on the LFS than the HFS due to the influence of ballooning [78]. In WEST simulations, one can observe that the heat deposition at the outer target increases faster than the inner one. This is because a higher b value makes the HFS have lower diffusivities as the diffusion coefficients at the OMP are fixed, thus causing more power to flow into the LFS and increasing the $T_{e,sep}$ at the OMP.

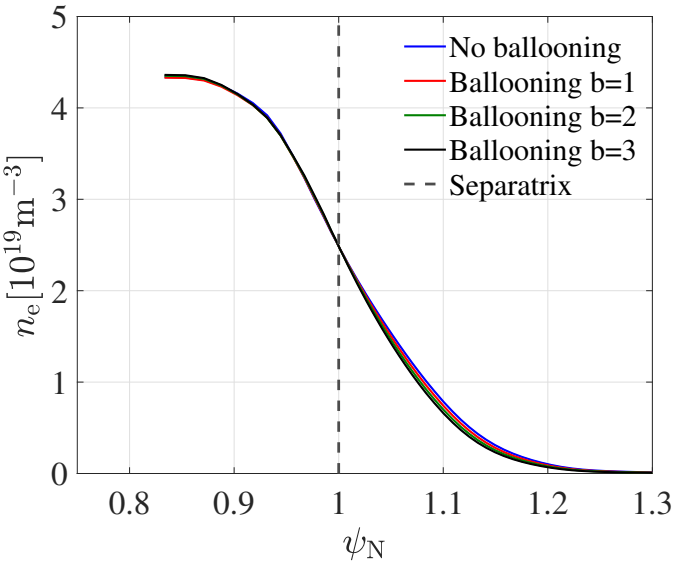

FIGURE 9. : Radial profiles of n_e at the OMP in WEST case. The dashed line represents the position of separatrix.

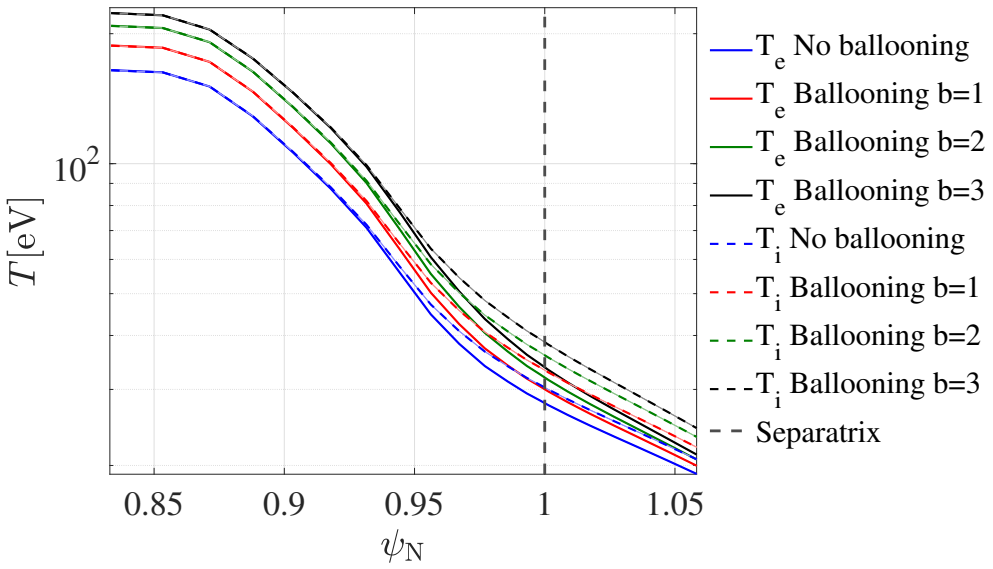

FIGURE 10. : Radial profiles of T_e and T_i at the OMP in WEST case. The dashed line represents the position of separatrix.

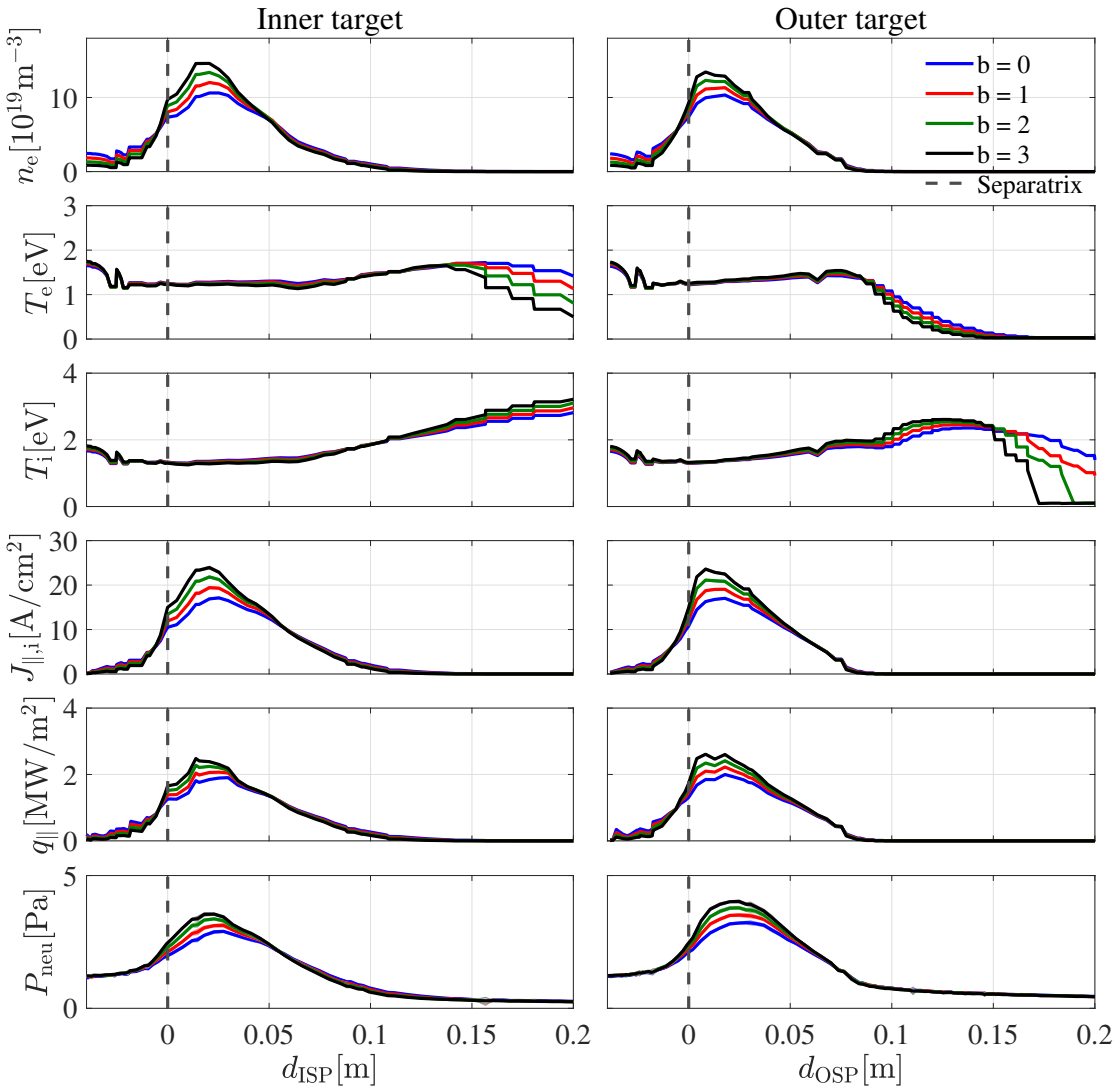

FIGURE 11. : The impact of ballooning at the target profiles in WEST case.

Ballooning in TCV For TCV case with fixed pedestal temperature and the same $n_{e,sep}$, ballooning shows no big impact on the radial density and temperature profiles at the OMP, Figure 12 and 13, but can impact the peak temperature and integral particle flux at the targets, Figure 14. A higher value of b results in a lower peak temperature at the inner target and a higher peak temperature at the outer target. Additionally, it leads to a narrower width while maintaining a similar peak particle flux at both targets. These effects have an impact on the carbon sputtering rate. The result of Figure 14 was obtained with no enhancement of diffusivities in the divertor. If considering the enhancement of diffusivities in the divertor as interoduced in Section 3.2.2.2 and scanning ballooning exponent b from 0 to 3, $b = 1$ was found to result in a good match between the experiment and simulation with respect to the C^{6+} density at OMP, Figure 3.31.

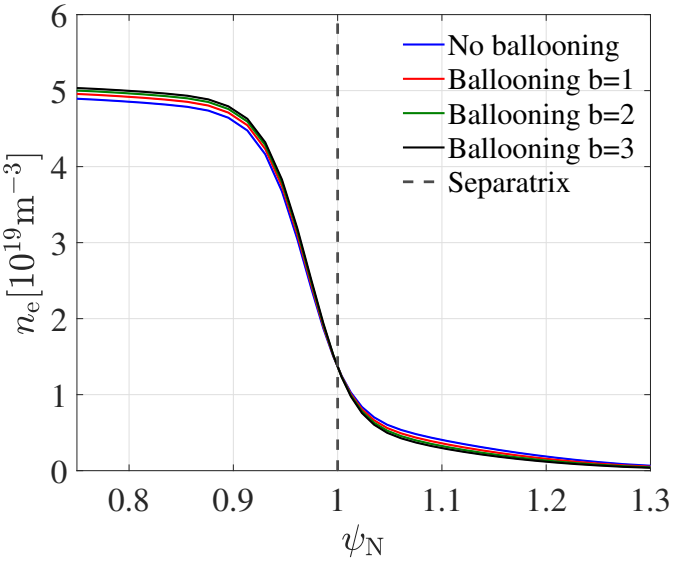

FIGURE 12. : Radial profiles of n_e at the OMP in TCV case. The dashed line represents the position of separatrix.

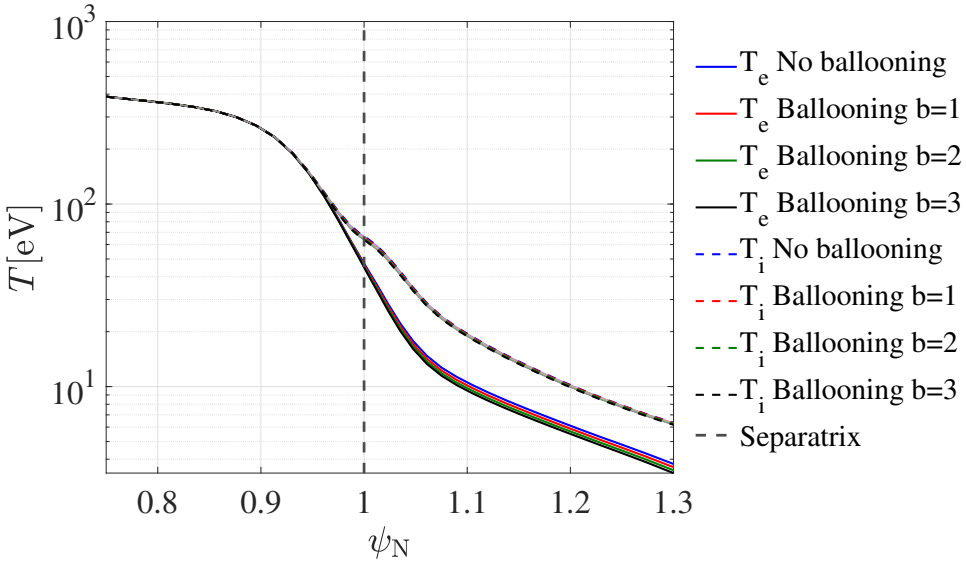

FIGURE 13. : Radial profiles of T_e and T_i at the OMP in TCV case. The dashed line represents the position of separatrix.

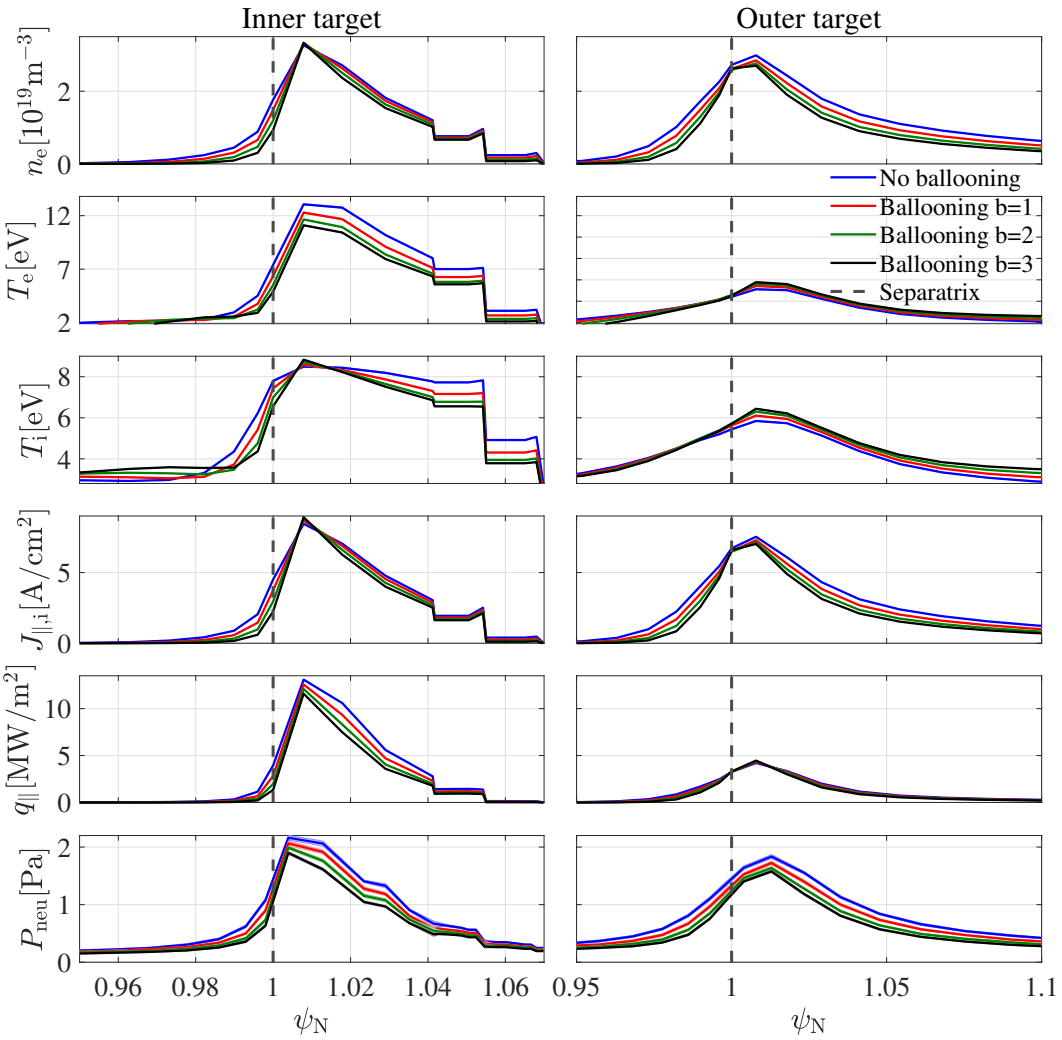

FIGURE 14. : The impact of ballooning at the target profiles in TCV case.

E.2. Simulation with drifts

Particle transport in the SOL can be contributed by anomalous cross-field transport, parallel transport, and drifts ($\mathbf{E}\times\mathbf{B}$, ∇B, and Curvature). The effects of drifts are dependent on the direction of the toroidal magnetic field $\mathbf{B}_\phi$. Normally we use the right-handed cylindrical coordinate system (r, ϕ, z) to define the magnetic geometry. Negative $\mathbf{B}_\phi$ represents a toroidal magnetic field pointing clockwise when looking down at the torus from above, with the z pointing vertically downwards. The negative $\mathbf{B}_\phi$ within LSN configuration is usually referred to as the forward field. In the forward field, the ∇B drift of ion points downward. When we refer to the reversed magnetic field, the $\mathbf{B}_\phi$ is reversed, and the plasma current $\mathbf{I}_\mathrm{p}$ is reversed simultaneously to make the field line impact the target tile always from the same direction [78]. But for the simulation, $\mathbf{I}_\mathrm{p}$ direction does not influence the final result. For all the cases (experiment and simulation) in this thesis, the plasma current $\mathbf{I}_\mathrm{p}$ is always in the same

direction as $\mathbf{B}_\phi$.

E.2.1. Drifts in forward field

The **E × B** drift plays an important role in influencing the target profile [96]. The **E × B** drift can be decomposed into $\mathbf{E}_\psi \times \mathbf{B}_\phi$ (poloidal), $\mathbf{E}_\theta \times \mathbf{B}_\phi$ (radial) and $\mathbf{E}_\psi \times \mathbf{B}_\theta$ (toroidal). We use the subscript 'ψ', 'ϕ', and 'θ' to indicate the radial, toroidal, and poloidal directions, respectively. The effect among the three components from large to low is poloidal $\mathbf{E}_\psi \times \mathbf{B}_\phi >$ radial $\mathbf{E}_\theta \times \mathbf{B}_\phi \gg$ toroidal $\mathbf{E}_\psi \times \mathbf{B}_\theta$ [80]. So we neglect the influence from $\mathbf{E}_\psi \times \mathbf{B}_\theta$. The electric potential in the SOL is expected to be proportional to the local electron temperature. For this reason, $\mathbf{E}_\psi$ points radially outward in the main SOL (but oppositely in the private plasma and core), leading to the $\mathbf{E}_\psi \times \mathbf{B}_\phi$ drift in the poloidal direction, from HFS to LFS for the forward field. The $\mathbf{E}_\theta$ is weak in the upstream, but can be important in the divertor region. It points towards the targets. The $\mathbf{E}_\theta \times \mathbf{B}_\phi$ drift points radially from the outer SOL into the main plasma (and into the private plasma below the X-point), also from the main plasma (or private plasma) into the inner SOL.

The ∇B drift of ion points downward in the forward field. These drifts and transport processes are summarised as shown in Figure 15.

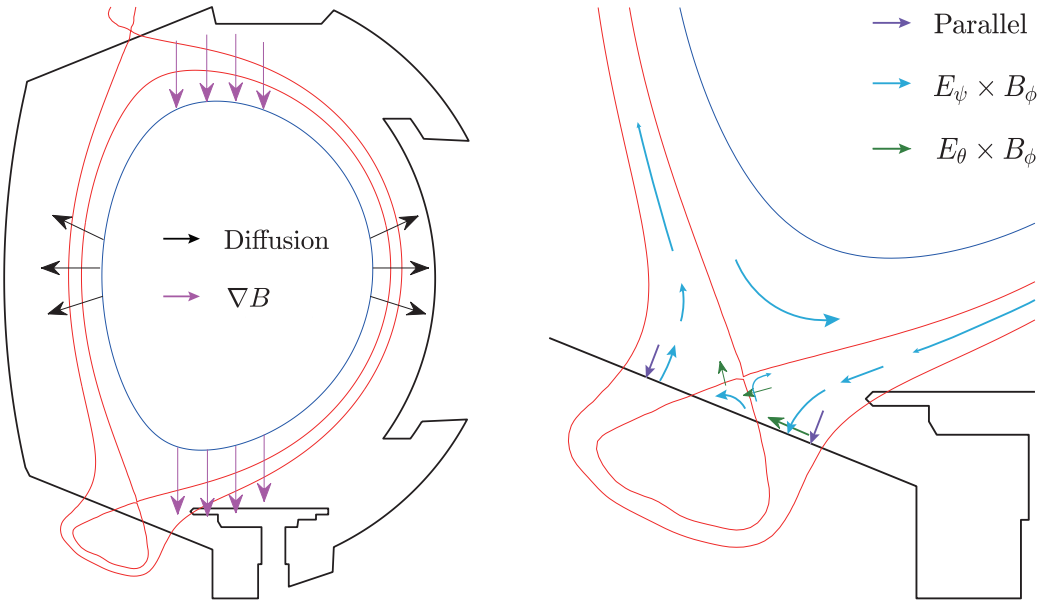

FIGURE 15. : The schematic diagram of different ion transport in the forward field.

E.2.2. Drifts in reversed field

When **B** is reversed, all the drifts transport will go in reversed direction. In some simulations, the reversed field is found to have more symmetric inner and outer target temperatures compared with the forward field [78].

E.2.3. Impact of drifts

Drifts play an important role in influencing particle and energy transport. Some phenomenons like the double-peaked ion flux profile at the target are observed and considered to be caused by drifts [100, 126], this feature can be helpful in reducing heat flux at the target [96]. The inner target in JET is a region of net deposition in the forward field [78].

Now, we study the impact of drifts through Case 4 in Table 2. It includes three subcases : one without drifts, one with drifts in the forward direction, and one with drifts in reversed direction. They have the same $n_{e,sep} = 2.47 \times 10^{19}\ m^{-3}$, leading to a detached regime. The target profiles of three cases are shown in Figure 16. d_{ISP} and d_{OSP} represent the radial distance from the inner and outer strike points, negative values are in the PFR, positive values are in the SOL. One can observe that compared with the no drift case, the case with drifts in the forward magnetic direction shows no significant difference for the profiles at the inner target, but increases the temperature, particle flux, and heat flux at the outer target. When the magnetic direction is reversed, the results are also reversed : the temperature, particle flux, and heat flux increase at the inner target, with very slight changes for the outer target. In detached plasma, the density profile at the target seems to have a smaller change compared to the temperature profile. Therefore, the drifts in different magnetic directions play a role in influencing the target temperature.

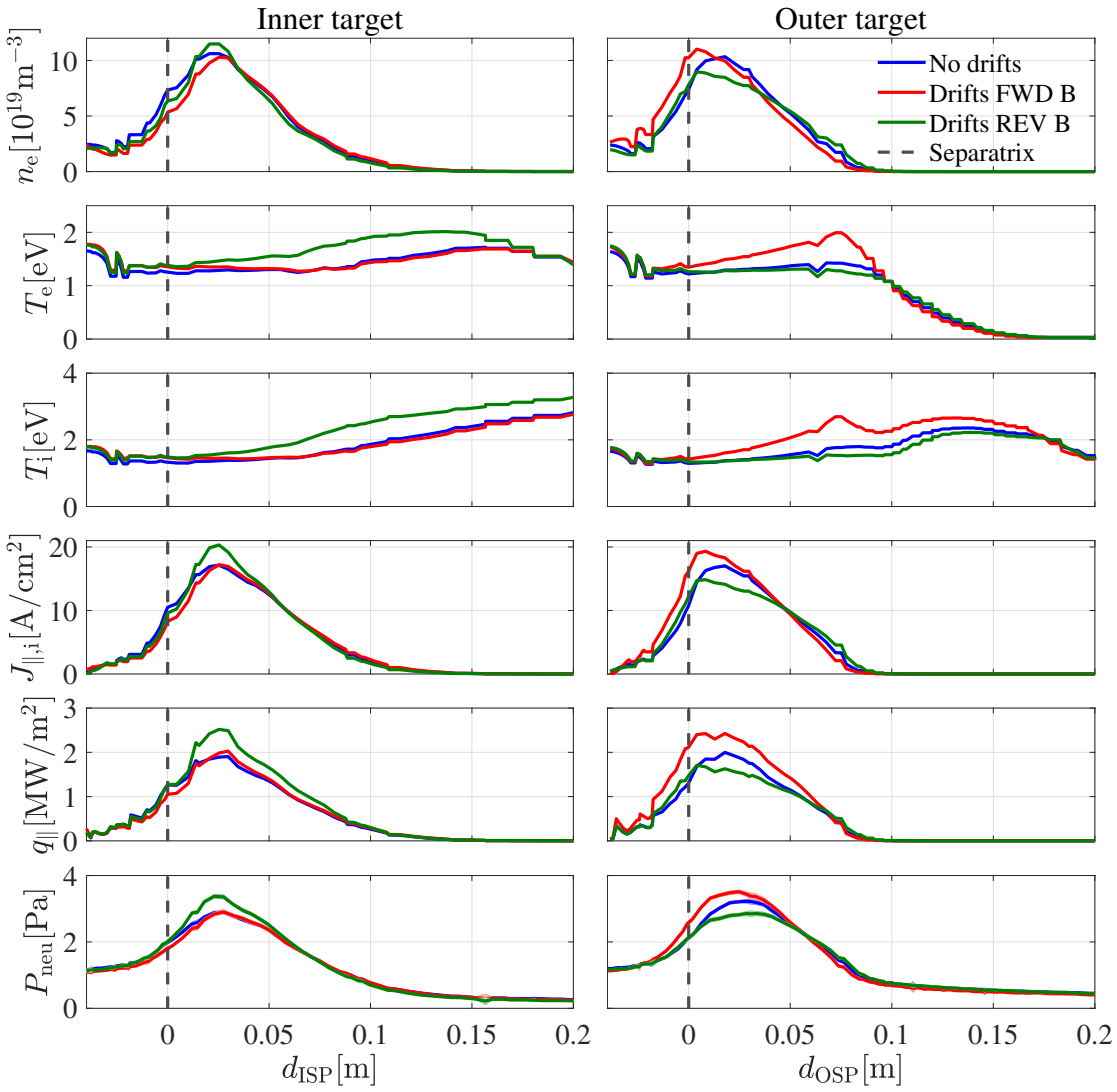

FIGURE 16. : The impact of drifts at the target profiles.

Figure 17 shows the radial dependence of Mach number measured at the top of JET in closely matched forward and reversed $\mathbf{B}_\phi$ discharges (L-mode, ohmic, low plasma density) [78, 127]. One can observe that in the forward field the flow is always positive (directed toward the inner divertor), and raised from a low positive value close to the separatrix to a higher value in the main SOL. In the reversed field, the flow has similar value to the forward one close to the separatrix but then decreases to zero which indicates mostly stagnant in the main SOL.

A consistent result can be seen in our WEST simulation case with low density ($n_{e,sep}$ = 1.4×10^{19} m^{-3}) by Figure 18. Except that, the Mach number inside separatrix and further away from the main SOL is also provided. The cases with increased $n_{e,sep}$ are put together to compare with low-density cases. One can observe that the profile in forward and reversed fields are almost symmetrical along the one with no drifts. The profile in the cases with no drifts is not influenced by the increasing $n_{e,sep}$ and has a

negative value in the main SOL, however, the cases with drifts show sensitivities in $n_{e,sep}$ level. In the main SOL, the profile of reversed $\mathbf{B}_\phi$ case keeps moving up with increasing $n_{e,sep}$, remaining negative Mach number. However the one of forward $\mathbf{B}_\phi$ case keeps moving down, and Mach number transit from positive to negative. The transition of flow direction in the main SOL indicates the moving of the stagnant point in SOL : the stagnant point moves toward the inner target in the forward field, and moves toward the outer target in the reversed field. Thus field reversal can influence the stagnant point position and flow direction, which can have impacts on the energy and particle distribution in the HFS and in the LFS.

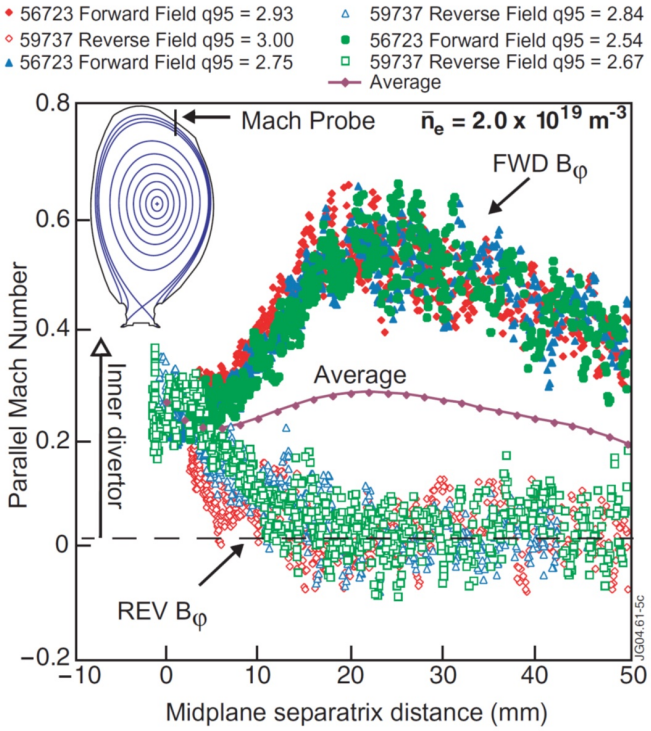

FIGURE 17. : Radial dependence of $M_\parallel$ measured by the RFA probe at the top of JET, comparing between forward $\mathbf{B}_\phi$ and reversed $\mathbf{B}_\phi$. Figure from references [78, 127].

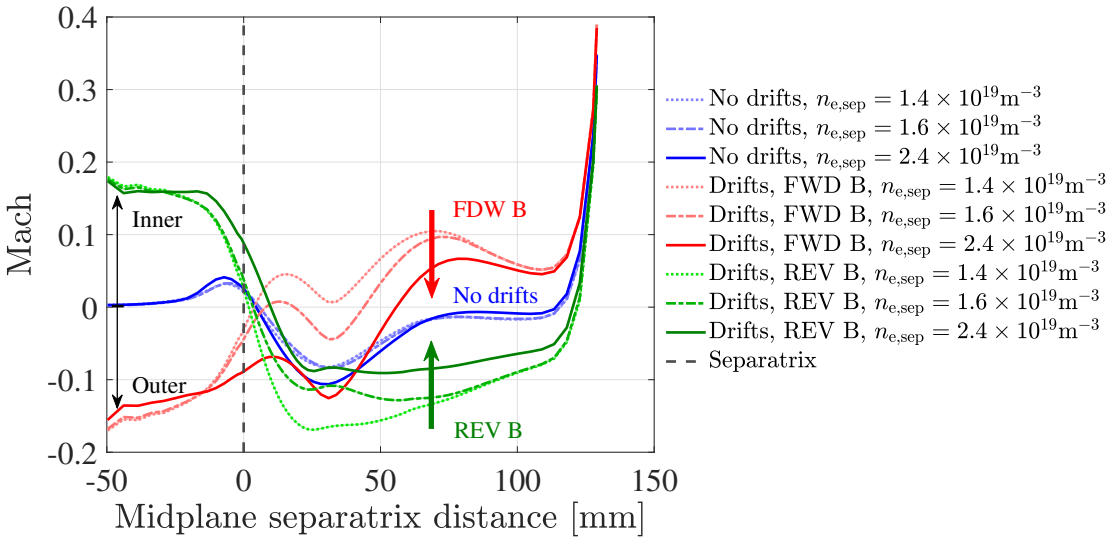

FIGURE 18. : Radial profile of $M_{\parallel}$ at the OMP in WEST simulation, comparing among no drifts, forward $\mathbf{B}_{\phi}$ and reversed $\mathbf{B}_{\phi}$ cases with increasing $n_{e,sep}$.

To understand better how drifts influence particle and energy transport, we evaluated the Mach number along SOL at $\psi_N = 1.02$ (layer nearby the separatrix, midplane separatrix distance = 6 mm) from inner target to outer target. Three values of $n_{e,sep}$ from low to high are applied to see the evolution of Mach number in different plasma regimes as shown in Figure 19. Positive value means the flow is heading for the inner target, negative value means the flow is heading for the outer target. One can observe that, when drifts are activated in the simulation, the Mach number will be strongly influenced in the poloidal direction. Forward and reversed magnetic fields show opposite effects, for example, in the HFS the Mach number has equally increased and decreased in reversed and forward fields compared with no drift case. However, one needs to notice that drifts always exist in the experiments, we compare drifts cases with no drift case is for the aim of evaluating how big influence will be caused by drifts, and if it is necessary to include drifts in the simulation when analyzing certain issues, such as the heat deposits at the inner and outer targets.

The interesting thing is that the change of $n_{e,sep}$ seems to have no impact on the Mach number at the HFS in the three cases, but in the LFS, the Mach number at the OMP is gradually reduced from positive to negative in the drift case with forward $\mathbf{B}_{\phi}$. The reversed $\mathbf{B}_{\phi}$ case shows opposite results. This indicates that the stagnant point can be influenced by increasing $n_{e,sep}$, and their moving direction is also influenced by the direction of magnetic field. In the forward $\mathbf{B}_{\phi}$ case, with increasing $n_{e,sep}$, the stagnant point tends to move toward the inner target. This point is consistent with the conclusion made from Figure 18, and verified this time through poloidal analysis.

For low $n_{e,sep}$ case with no drifts (blue curve in Figure 19a), the stagnant point can be estimated to be located between the top and OMP. However, when drifts are introduced, for example, in the forward field, the stagnant point would be below the OMP in the LFS. The switch of stagnant point position due to the introduction of drifts

can be explained by the presence of Pfirsch-Schlüter (PS) flow. For toroidal plasma, the poloidal $\mathbf{E}_\psi \times \mathbf{B}_\phi$ drift flux and diamagnetic flux are partly non-divergence free due to R-dependence of the magnetic field $B \propto 1/R$ (for both) and ∇B (for diamagnetic flux). The non-divergence-free part can contribute to the production of the so-called PS flow, which can be described as follow [13].

$$\boldsymbol{v}_\parallel^{\mathrm{PS}} = 2q\cos\theta\left(\boldsymbol{E}_r\frac{-\boldsymbol{\nabla}_r p}{en}\right)\times\frac{\boldsymbol{B}_0}{B_0^2} \tag{E.1}$$

The PS flow is much higher at the LFS than HFS, zero at the top and bottom. Its flow direction in poloidal projection is against the ion ∇B drift direction. The presence of PS flow can move the stagnant point downward along LFS, and lead to an increase in Mach number approximately 0.1 at the OMP in the forward field in the case with $n_{\mathrm{e,sep}}$ = $1.40\times10^{19}\,\mathrm{m}^{-3}$ (Figure 18). Vice-versa, the opposite effects occur in the reversed field. With increasing $n_{\mathrm{e,sep}}$, the stagnant point of the case with drifts is observed to move closer to that of no drift case due to the reduction of $v_\parallel^{\mathrm{PS}}/C_\mathrm{s}$ which is caused by lower E_r and $\nabla_r p$ [128]. The more significant PS flow at the LFS can also explain why the Mach number is $n_{\mathrm{e,sep}}$ dependent in the LFS but the Mach number in the HFS is not sensitive to the change in $n_{\mathrm{e,sep}}$ as shown in Figure 19.

Figure 20 and 21 show that the target density and temperature profiles corresponding to three $n_{\mathrm{e,sep}}$ from low to high. One can observe that the forward $\mathbf{B}_\phi$ case has a relatively higher density and temperature at the outer target and lower density and temperature at the inner target than other cases (no drift, reversed $\mathbf{B}_\phi$) at $n_{\mathrm{e,sep}}$ = $2.40\times10^{19}\,\mathrm{m}^{-3}$ (detached plasma, Figure 20c and 21c). When plasma is attached, the reversal of the $\mathbf{B}_\phi$ field shows a big impact on plasma density at the inner target (Figure 20a and 20b), but its temperature shows no sensitivity for $\mathbf{B}_\phi$ direction.

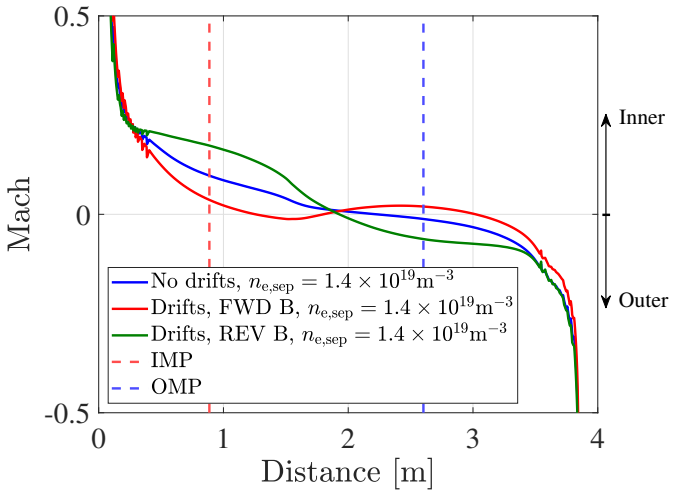

(a) Low $n_{e,sep}$

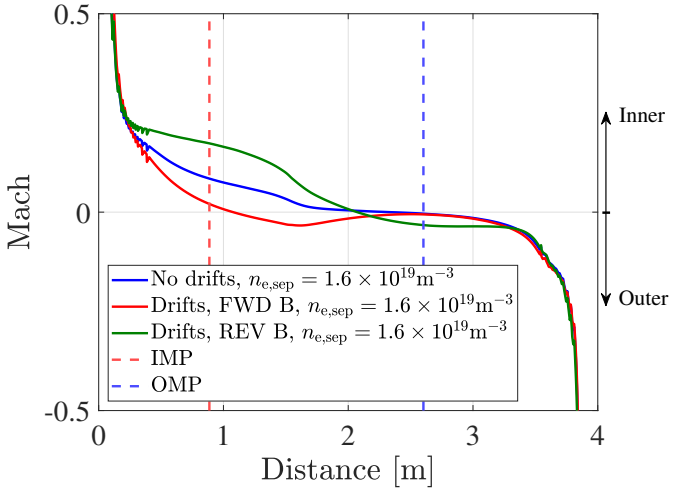

(b) Medium $n_{e,sep}$

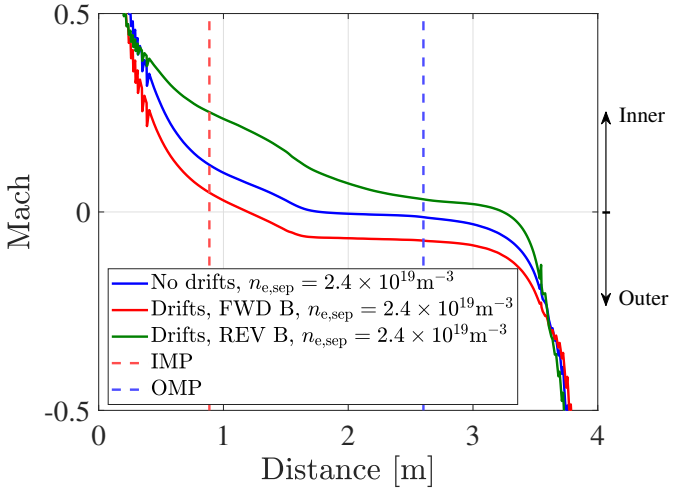

(c) High $n_{e,sep}$

FIGURE 19. : The Mach number near separatrix in poloidal direction (only show the part $-0.5 < \text{Mach} < 0.5$).

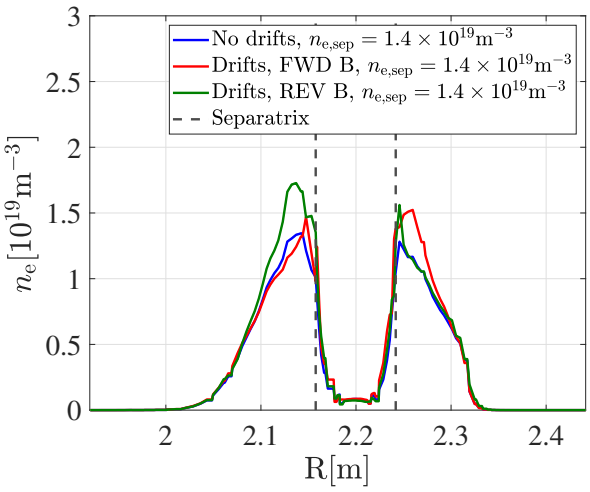

(a) Low $n_{e,sep}$

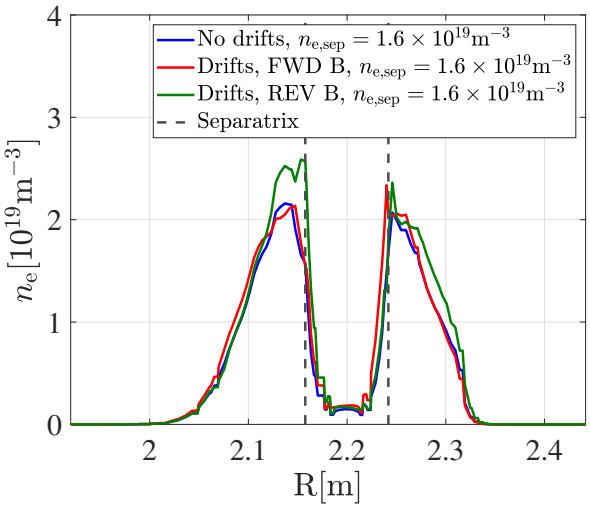

(b) Medium $n_{e,sep}$

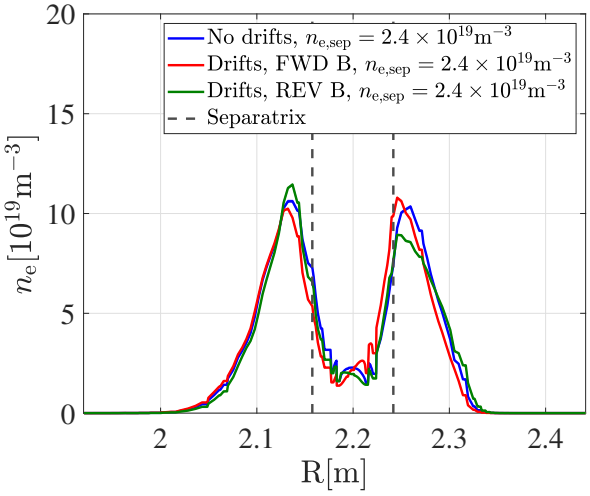

(c) High $n_{e,sep}$

FIGURE 20. : Target density profiles corresponding to three $n_{e,sep}$ from low to high.

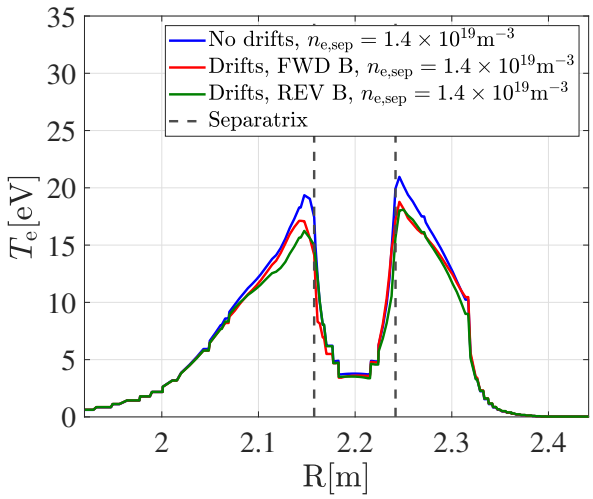

(a) Low $n_{e,sep}$

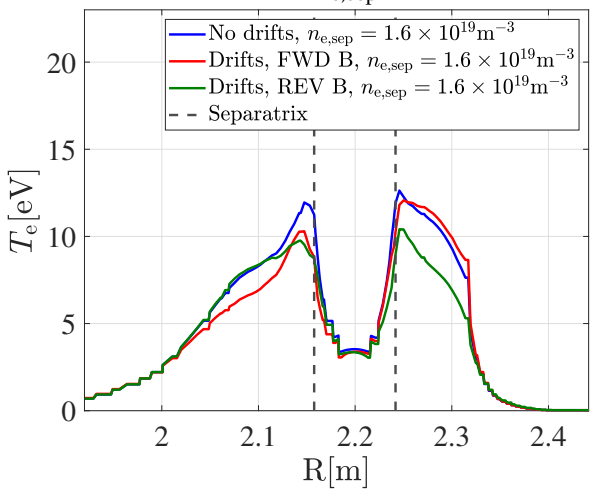

(b) Medium $n_{e,sep}$

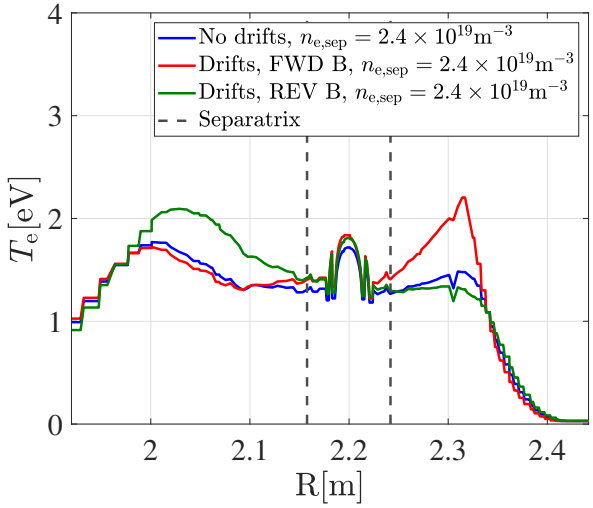

(c) High $n_{e,sep}$

FIGURE 21. : Target temperature profiles corresponding to three $n_{e,sep}$ from low to high.

The scan of $n_{\mathrm{e,sep}}$ has been performed for no drifts, forward $\mathbf{B}_\phi$, and reversed $\mathbf{B}_\phi$ cases. Figure 22 and 23 show the evolution of integral parallel heat flux and peak parallel particle flux at the inner and outer targets as a function of $n_{\mathrm{e,sep}}$. One can observe that the forward $\mathbf{B}_\phi$ case shows higher particle and heat flux deposits at the outer target than the reversed one. This can be explained by the influence of poloidal $\mathbf{E}_\psi \times \mathbf{B}_\phi$ drift flux, which moves from the inner target to the outer target poloidally. As discussed before, the PS flow can influence the stagnant point in the LFS, however, PS flow can only reach Maximum at OMP, zero at top and bottom, so it has limited influence for the transport in entire SOL.

In detached plasma, the outer target temperature is usually high in the forward $\mathbf{B}_\phi$ case (Figure 21c). A higher temperature can delay the detachment process since detachment relies mainly on the cooling down of plasma in the divertor. So, it is easy to understand why the forward $\mathbf{B}_\phi$ case has a higher $n_{\mathrm{e,sep}}$ threshold for particle flux rollover at the outer target (Figure 23b) as the rollover of particle flux is usually relevant to the beginning of detachment. The higher temperature at the outer target in forward $\mathbf{B}_\phi$ case can be explained by higher heat deposit caused by drifts, particularly the $\mathbf{E}_\psi \times \mathbf{B}_\phi$. The PS flow can offset part of $\mathbf{E}_\psi \times \mathbf{B}_\phi$ impacts, but the flow is reduced in detached plasma. In more detail, poloidal $\mathbf{E}_\psi \times \mathbf{B}_\phi$ drift can have an obvious impact on redistributing the fraction of energy flow into the inner and outer targets of the lower divertor in WEST. In the forward $\mathbf{B}_\phi$ field, poloidal $\mathbf{E}_\psi \times \mathbf{B}_\phi$ drift flow can increase the heat deposit at the outer target but slightly reduce the heat deposit at the inner one. Thus delay the rollover of particle flux at the outer target, but have no obvious influence on the rollover threshold of particle flux at the inner target (the difference of heat power deposit at the inner target between the no drifts case and forward $\mathbf{B}_\phi$ case becomes smaller with increasing $n_{\mathrm{e,sep}}$ and nearly the same after rollover happens, but the heat power deposit at the outer target is always higher than that in no drifts case. Maybe due to the stronger $\mathbf{E} \times \mathbf{B}$ drift at LFS, due to larger R).

The $\mathbf{E}_\theta \times \mathbf{B}_\phi$ drift can cause radial transport of particles from the outer to the inner target in the PFR, resulting in a noticeable shift of the radial position of peak density towards the separatrix at the outer target. Conversely, the radial position of peak density at the inner target shifts away from the separatrix.

The no drifts case shows a sudden decrease of particle flux and heat flux at both targets when $n_{\mathrm{e,sep}}$ is higher than 2.60×10^{19} m^{-3}. This can be explained as the formation of XPR in no drifts case with very low temperature at X-point and strong plasma recombination. However, the XPR is hard to observe in the cases with drifts. Probably due to the simulation with drifts introducing high poloidal velocity inside separatrix, making neutral particles hard to penetrate into the X-point region (part of neutrals are blown away by strong plasma wind), thus making the XPR hard to simulate in the case with drifts.

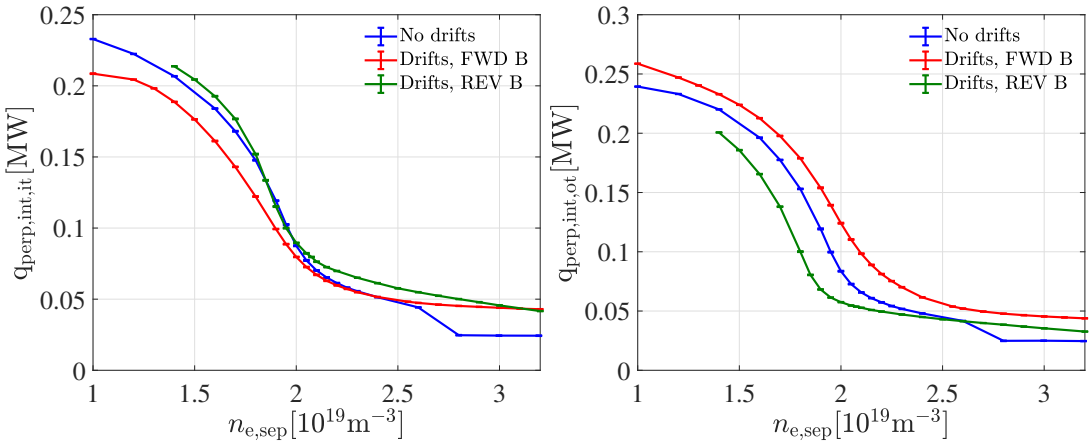

(a) Inner target (b) Outer target

FIGURE 22. : Evolution of integral parallel heat flux at inner (outer) target as a function of $n_{\mathrm{e,sep}}$ in no drifts, forward $\mathbf{B}_\phi$, and reversed $\mathbf{B}_\phi$ cases.

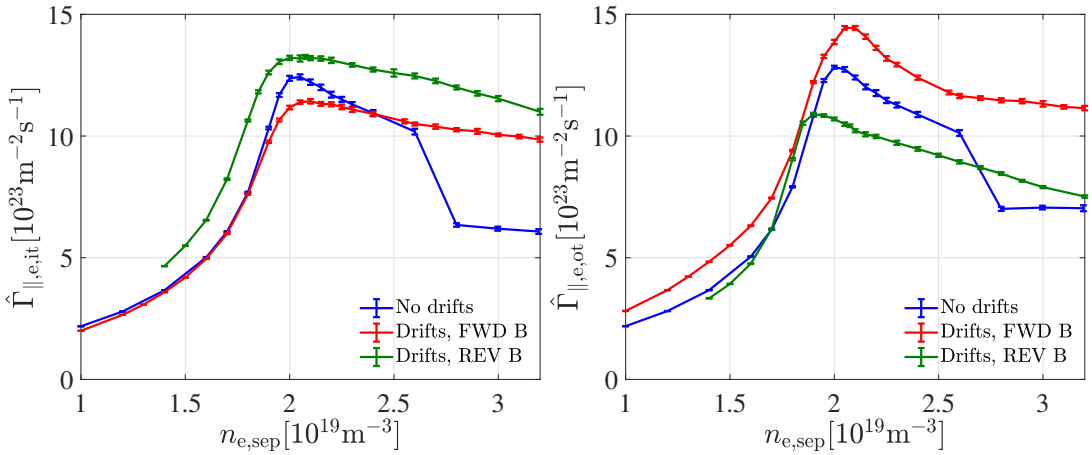

(a) Inner target (b) Outer target

FIGURE 23. : Evolution of peak parallel particle flux at inner (outer) target as a function of $n_{\mathrm{e,sep}}$ in no drifts, forward $\mathbf{B}_\phi$, and reversed $\mathbf{B}_\phi$ cases.

E.3. Recycling coefficient

In this section, we discuss the impacts of recycling coefficient on the wall (R_{wall}) which is defined as the ratio of the recycled neutral flux over the outgoing ion flux (Section 2.3.2). When W is used as plasma facing material, it behaves almost like a mirror : nearly all the incident D atoms are reflected as neutrals. Therefore, in the idealized case of a pure W wall, $R_{\mathrm{wall}} = 1$ is what one would assume in modeling. However, there are some reasons to use R_{wall} slightly < 1. In reality, the wall will never be pure pristine W but will be covered with redeposited (amorphous W instead of crystalline W) and co-deposited (W-O-C-B compounds instead of just W) layers of eroded material. These

layers can trap D and therefore reduce recycling. Ideally, the older (and therefore the dirtier) a machine is, the lower R_{wall} should be used in a simulation. Also right after a glow discharge boronization, when B layers are intentionally deposited on top of W surfaces, R_{wall} will be lower as B traps D. A proper setup of R_{wall} and pump rate can help in obtaining experiment-like plasma with reasonable gas puff rate. Numerical stability sometimes is lost if $R_{\text{wall}} = 1$ as the simulation domain is filled with plasma and neutrals and the albedo pump struggles to ensure balance.

Following the simulation setups of Case 6 in Table 2, we have two cases with almost the same setups (same pumping speed, same wall, same input power, etc.), except the different R_{wall} : one with $R_{\text{wall}} = 1$, another with $R_{\text{wall}} = 0.99$. They are feedback controlled to have the same $n_{\text{e,sep}}$. For steady-state plasma, the corresponding gas puff rate is significantly higher in the case with lower R_{wall}. Deuterium puff rate = 3.59×10^{21} D atoms s^{-1} when $R_{\text{wall}} = 0.99$, puff rate = 0.92×10^{21} D atoms s^{-1} when $R_{\text{wall}} = 1$. The comparison of radial profiles of upstream density (temperature) can be seen in Figure 24 (Figure 25). It can be observed that the density in the main SOL ($\psi_{\text{N}} \in [1, 1.2)$) is slightly higher in the case with lower R_{wall}. However, the lower R_{wall} case also presents slightly higher parallel heat flux at both targets than the one with $R_{\text{wall}} = 1$ as shown in Figure 26. Considering the fact that the two cases have the same input power, normally higher upstream density can help in decreasing target temperature when input power is fixed. The observation indicates that the case with a lower R_{wall} also has a lower power dissipation level, which is due to a slightly lower neutral pressure in the divertor leg region (defined as Figure 4.10). The averaged neutral pressure in the divertor outer leg region $\overline{P}_{\text{neu,div}} = 2.01$ Pa in the case with $R_{\text{wall}} = 1$, $\overline{P}_{\text{neu,div}} = 1.95$ Pa in the case with $R_{\text{wall}} = 0.99$.

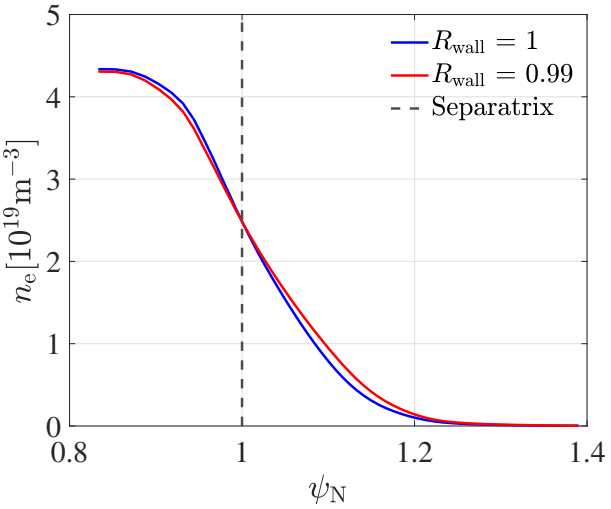

FIGURE 24. : Radial profile of upstream density in the simulation cases with $R_{\text{wall}} = 1$ (blue curve) and $R_{\text{wall}} = 0.99$ (red curve), the dashed line represents the position of separatrix.

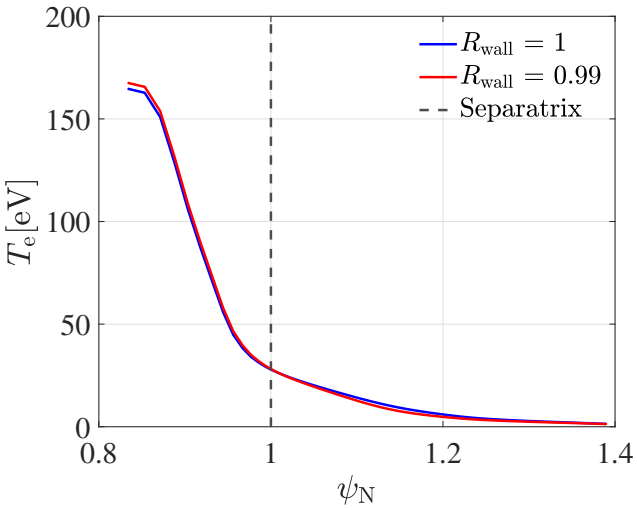

FIGURE 25. : Radial profile of upstream electron temperature in the simulation cases with $R_{wall} = 1$ (blue curve) and $R_{wall} = 0.99$ (red curve), the dashed line represents the position of separatrix.

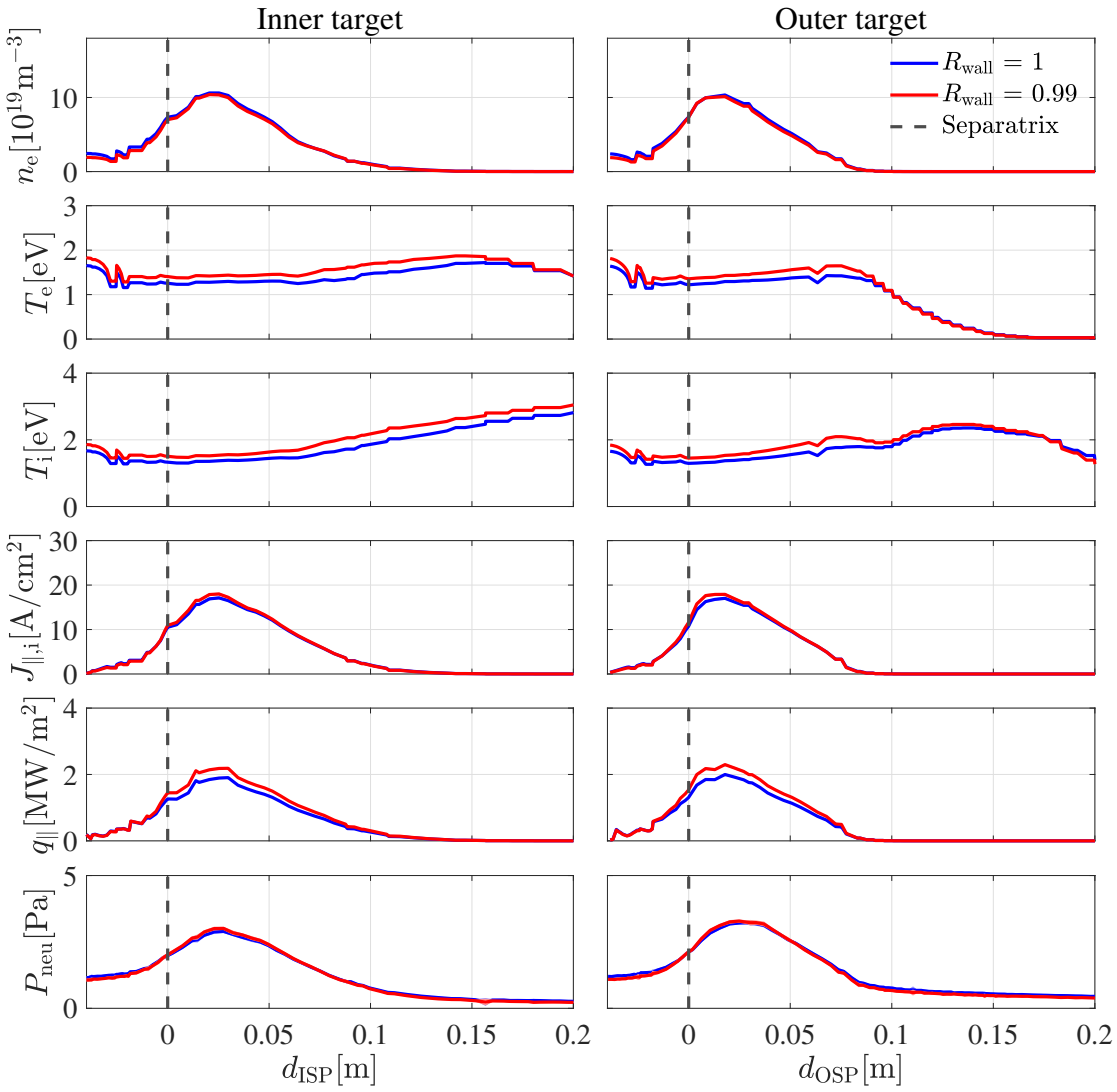

FIGURE 26. : Target profiles of multiple parameters in the simulation cases with $R_{\mathrm{wall}} = 1$ (blue curve) and $R_{\mathrm{wall}} = 0.99$ (red curve) at the inner and outer part. d_{ISP} (d_{OSP}) is the radial distance from the inner (outer) strike point, negative values are in the PFR, positive values are in the SOL. The dashed line represents the position of separatrix.

F. Difference between simulation and experiment

In Section 3.2.1.3, we made the basic WEST simulation case that has good agreement with WEST discharge #56420 at $t = 7.3\,\mathrm{s}$. Based on this basic case, we try to perform realistic time-dependent simulations, which have consistent time evolution of input parameters (gas puff rate and $n_{\mathrm{e,sep}}$) as the discharge. The purpose is to see the difference between simulation and experiment in the time transition process. The time period from $t = 5\,\mathrm{s}$ to $t = 8.5\,\mathrm{s}$ is chosen in discharge #56420 due to the plasma current and input power being approximately constant in this period, and it covers the divertor detachment. For each realistic time-dependent simulation, we only operate the gas puff rate (consistent with discharge) or $n_{\mathrm{e,sep}}$ (controlled by feedback adjustments of the D_2 gas puff rate), all the other setup (e.g. diffusion coefficients, input power) in the simulation remain untouched. The results of the realistic time-dependent simulations which have consistent time evolution of deuterium gas puff rate and $n_{\mathrm{e,sep}}$ as discharge #56420 are shown in Figure 27 and Figure 28, include the comparison with experimental data in :

- Gas puff rate.
- Upstream separatrix density $n_{\mathrm{e,sep}}$.
- Line integral density $n_{\mathrm{e,int,X}}$ of channel 1 (Figure 3.24) pointing into the X-point region.
- Peak parallel ion flux at the outer target $\hat{\Gamma}_{\parallel,\mathrm{i,ot}}$.
- Peak electron temperature at the outer target $\hat{T}_{\mathrm{e,ot}}$.
- Peak electron density at the outer target $\hat{n}_{\mathrm{e,ot}}$.
- Peak parallel heat flux at the outer target $\hat{q}_{\parallel,\mathrm{ot}}$.
- Neutral pressure under baffle $P_{\mathrm{neu,baffle}}$ which has been recalculated by 0D-model in Section 2.7.2 to make the neutral pressure can be compared to the experimental one.
- Input power P_{in} and radiated power in edge region $P_{\mathrm{rad,edge}}$. In the experimental data, the $P^{\mathrm{exp}}_{\mathrm{in}} = P^{\mathrm{exp}}_{\mathrm{rad,core}} + P^{\mathrm{exp}}_{\mathrm{in,edge}}$, the $P^{\mathrm{exp}}_{\mathrm{rad,edge}} = P^{\mathrm{exp}}_{\mathrm{rad,edge,D}} + P^{\mathrm{exp}}_{\mathrm{rad,edge,imp}}$.

There exists some difference between experimental and simulational results. The possible reason can be :

- The difference in input power. The total input power in experiments is varied and has 100 kW difference comparing between the peak and lowest value. Thus the input power of SOL in the experiment is varied, which is different from the simulation setup.

- The difference in diffusion coefficients. The diffusion coefficients can change significantly in different divertor regimes, from sheath-limited to detached. But the simulation assumes no change in diffusion coefficients and applies the diffusion coefficients extracted from experimental data at $t = 7.3\,\mathrm{s}$ through profile feedback.

- The difference in wall saturation states. In Figure 27, we can see that if the simulation case has a consistent gas puff rate with the experimental one as a function of time, the $n_{\mathrm{e,sep}}$ will be higher from 5 s to 6.5 s, and $n_{\mathrm{e,sep}}$ will be lower from 7.8 s to 8 s compared with experimental data. In simulation, the wall recycling coefficient is set as 1, but in real experiments, the wall will play as a sink of particles. After it is saturated, it can become a source of particles. At the initial stage, part of the particles is trapped in the wall, represented as lower $n_{\mathrm{e,sep}}$ in the experiment, at the end stage, the puff rate decreases, the particles release rate is higher than the sink rate, can make the $n_{\mathrm{e,sep}}$ decrease slowly.

- The difference in impurities. The simulation is with pure D, with no obvious radiation when the target temperature is high. But, in the experiment, one can observe significant radiation in the attached regime due to the effects of tungsten. The line integral density pointing to the X-point is found to be overestimated in the pure D case due to the lack of impurities.

- The limitation of LPs measurements for target temperature below 5 eV. LPs can not give reliable measurements for temperature lower than 5 eV. When plasma is detached, the target density, temperature, and heat flux from LPs are not reliable.

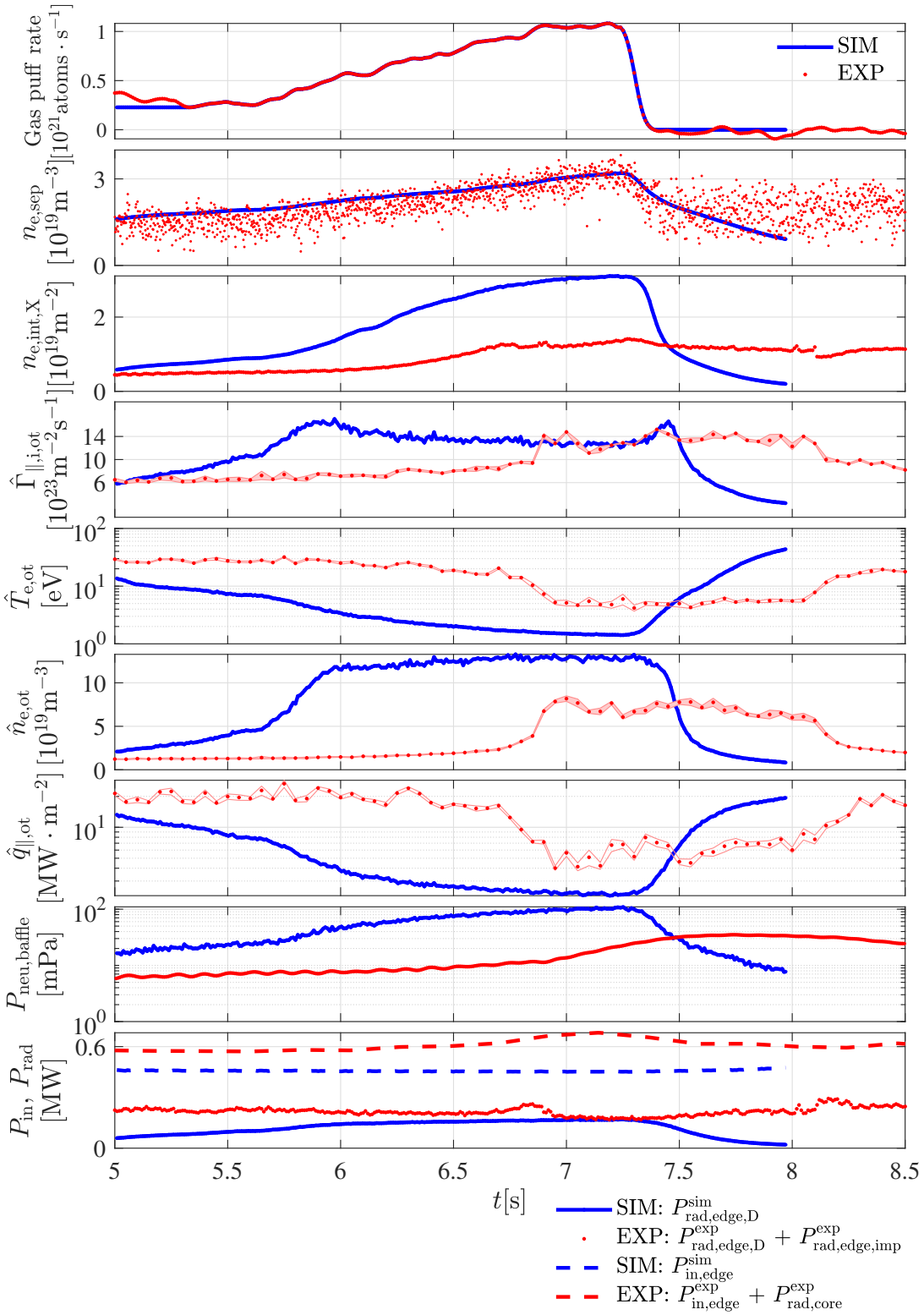

FIGURE 27. : Evolution of variables as a function of time maintains a consistent trace with the experimental gas puff rate. The simulation setup is carefully defined to reproduce experimental conditions at 7.3 s. The setup (input power, diffusion coefficients, etc.) remains unchanged throughout the simulation scan.

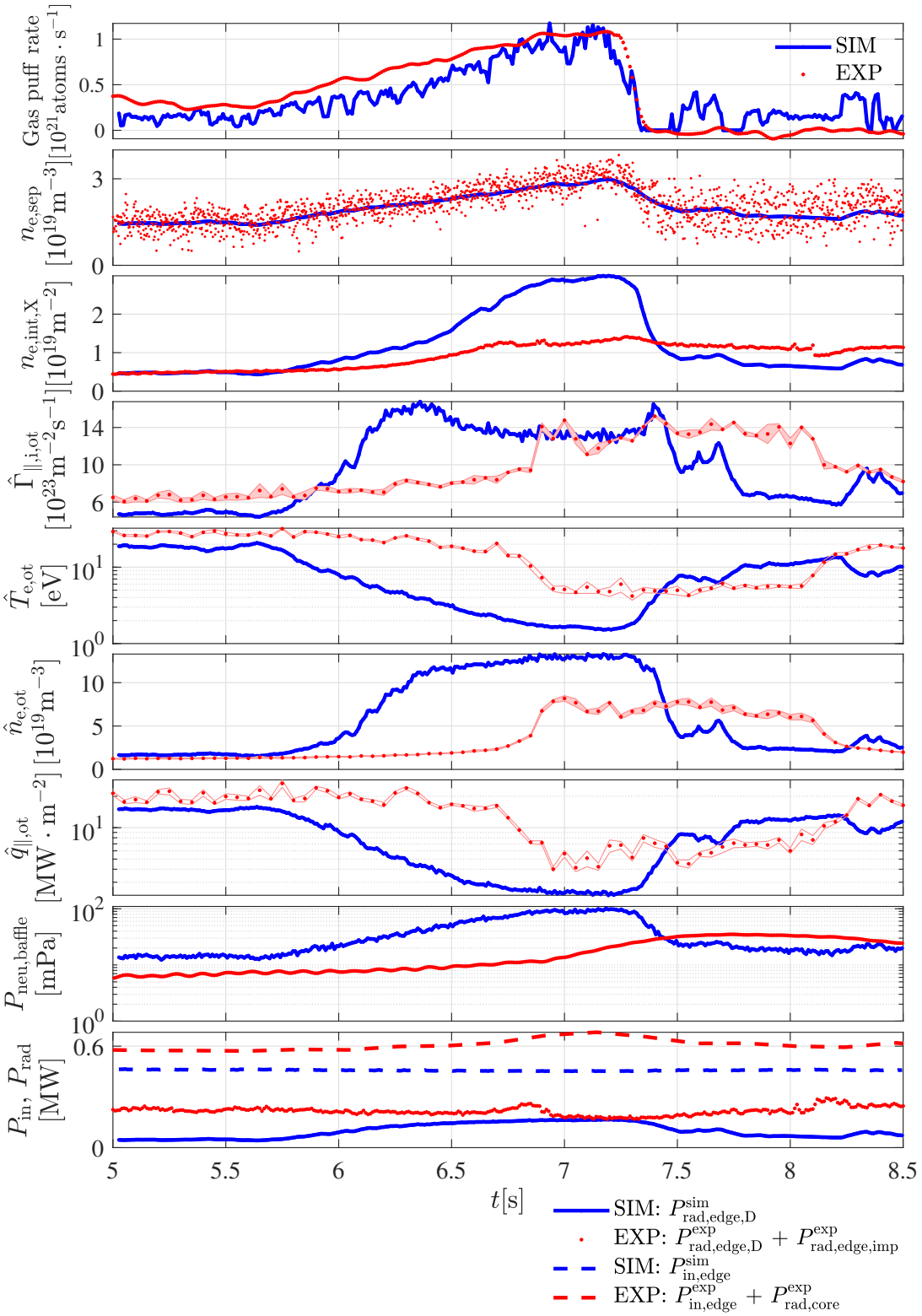

FIGURE 28. : Evolution of variables as a function of time maintains a consistent trace with the experimental $n_{e,sep}$. The simulation setup is carefully defined to reproduce experimental conditions at 7.3 s. The setup (input power, diffusion coefficients, etc.) remains unchanged throughout the simulation scan.

G. Using reduced models for characterising detached plasma

G.1. Partial detachment model

To predict the relation between input power, divertor neutral pressure, and impurity concentration under partially detached conditions (detachment of the first few power widths in the SOL) in arbitrarily sized machines, a simplified model based on an empirical formula has been proposed [120]. This model was calibrated on AUG experimental data and is currently assumed to only be relevant for divertors of similar geometry. The model is shown in Equation G.1.

$$q_{\mathrm{det}} = \frac{P_{\mathrm{sep}}}{R}\left[p_0\left(1+f_{\mathrm{z}}c_{\mathrm{z}}\right)\cdot\left(\frac{\lambda_{\mathrm{int}}}{0.005}\right)\cdot\left(\frac{R}{1.65}\right)^{r_{\mathrm{z}}}\right]^{-1}\times 1.3\ \mathrm{Pa\ m\ MW^{-1}}, \tag{G.1}$$

where $q_{\mathrm{det}} = 1$ corresponds to the partial detachment state. We now explain the terms in Equation G.1 and try to apply this model to the TCV simulation data.

- P_{sep} represents the input power across the separatrix.
- $R = 0.88\,\mathrm{m}$, the major radius.
- p_0 the average total neutral pressure under the baffle ($P_{\mathrm{neu,baffle}}$ in Figure 3.28).
- f_{z} the relative efficiency of impurity to achieve detachment compared to deuterium. For nitrogen $f_{\mathrm{z}}^{\mathrm{N}} = 18$ [120], $f_{\mathrm{z}}^{\mathrm{C}}$ is estimated to be 10 since higher concentration (by a factor 1.83) is required to obtain the same upstream power for given target parameters, when replacing N by C [129]. The influence of $f_{\mathrm{z}}^{\mathrm{C}}$ value is quite small since the carbon concentration is low (less than 5%).
- $f_{\mathrm{z}}c_{\mathrm{z}}$ in this article is calculated as $f_{\mathrm{z}}c_{\mathrm{z}} = f_{\mathrm{z}}^{\mathrm{C}}c_{\mathrm{z}}^{\mathrm{C}} + f_{\mathrm{z}}^{\mathrm{N}}c_{\mathrm{z}}^{\mathrm{N}}$.
- $\lambda_{\mathrm{int}} = \lambda_{\mathrm{q}} + 1.64S$, represents the integral power decay length [130] inside which the divertor power spreading factor S is about $\lambda_{\mathrm{q}}/2$ based on the experimental data in [131]. Checking in the simulation, the ratio λ_{q}/S increases with increasing upstream density from 1 at low densities to approximately 2 in detached states. λ_{q} is evaluated based on the target heat flux profile remapped at the OMP.
- $r_{\mathrm{z}} = 0.1$ is a weak exponent assuming that the distance where the λ step occurs scales with the major radius.

The evolution of the normalized radiation front height as a function of q_{det} is shown in Figure 29. The green and yellow symbols correspond to the long and short baffle cases with nitrogen seeding starting from the attached, indicating the onset of detachment when $q_{\mathrm{det}} \approx 1$. The model correctly predicts the partial detachment when the case has a high level of divertor radiation due to nitrogen, while it predicts a different value at which the detachment starts in the cases without seeded impurities. The

red symbols correspond to the case with nitrogen seeding can not be used to verify the agreements between the qualifier and simulation as it starts directly from the detached case with $q_{\mathrm{det}} \leq 1$. The two cases with nitrogen seeding starting from the attached state have significantly higher total impurity concentration values than other cases when the plasma detaches (Figure 4.32), indicating that high enough c_z^N in the divertor can effectively radiate most of the power that enters the divertor, despite a reduction in divertor closure.

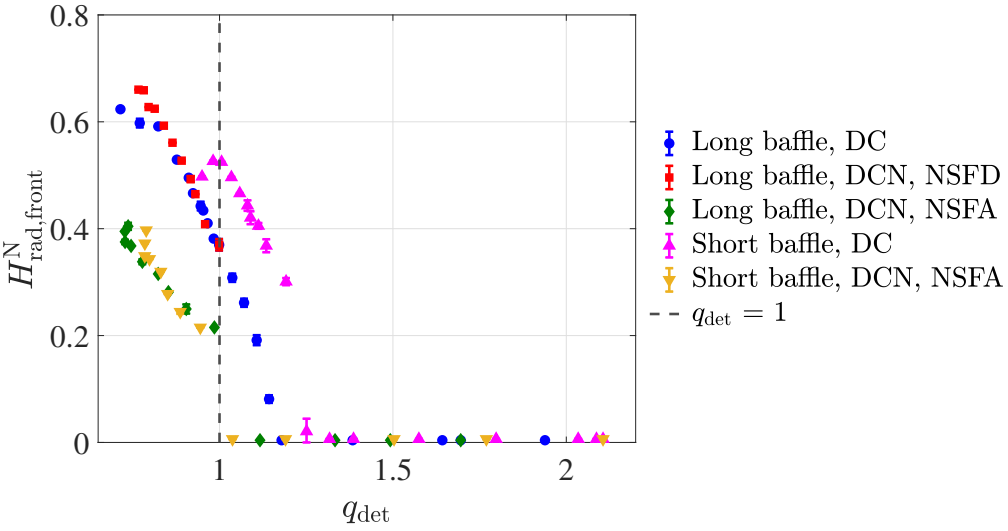

FIGURE 29. : Evolution of normalized radiation front height as a function of q_{det}.

G.2. Reduced model for prediction of X-point radiator threshold

XPR is an interesting part of detachment study, usually occurring when a deep detached level is reached. Based on the balance between energy loss (charge exchange and ionization) and thermal conduction, a reduced model which aims to explain the physical mechanisms of XPR was derived in [132] as :

$$X_{\mathrm{A}} = \frac{P_{\mathrm{ion}} + P_{\mathrm{CX}}}{P_{\mathrm{cond}}} \sim R_0^2 q_{\mathrm{s}}^2 n_{0,\mathrm{X}} n_{\mathrm{e,u}} f_{\mathrm{exp}} / \left(a T_{\mathrm{e,u}}^{2.5}\right), \tag{G.2}$$

where $n_{0,\mathrm{x}}$ is the neutral density at the X-point, $n_{\mathrm{e,u}}$ and $T_{\mathrm{e,u}}$ is the electron density and temperature at the OMP, f_{exp} is the flux expansion between the OMP and the X-point, q_{s} is the safety factor (Equation 1.4), and a is the minor radius. This model highlights the function of the safety factor, neutral density, and flux expansion factor in the formation of XPR. Equation G.2 can be reformatted [133] as :

$$X_{\mathrm{A}} \sim n_{0,\mathrm{X}} n_{\mathrm{e,u}} f_{\mathrm{exp}} B_{\mathrm{t,u}}^2 / \left(T_{\mathrm{e,u}}^{2.5} B_{\theta,\mathrm{u}}^2\right), \tag{G.3}$$

where $B_{\mathrm{t,u}}$ and $B_{\theta,\mathrm{u}}$ are the toroidal and poloidal magnetic fields at the OMP. This model has been applied to analyze the AUG simulation through SOLPS. The simula-

tion data (with no drifts) were used as input for this X-point model, and the results are shown in Figure 30. Various normalized radii (ρ = 0.9998 → 0.9889) inside the separatrix were analyzed separately for cases with different magnetic strengths ($\mathbf{B}_\phi$ = 1.8 or 2.5 T). It was found that XPR with a cold core ($T_{e,X} < 5$ eV) only occurs when X_A exceeds a certain threshold. This threshold of X_A remains robust across different toroidal field strengths and radii [133].

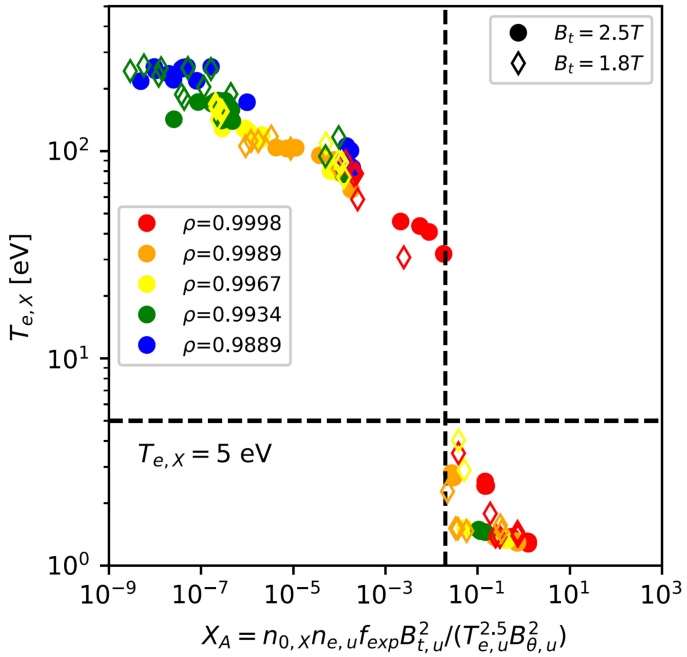

FIGURE 30. : Evolution of the electron temperature near the X-point with the X_A parameter in the flux tubes at various normalized radii. Figure from reference [133].

We will use this model by taking the simulation data from WEST simulation introduced in Section 3.2.1.3 as input to study the formation process of XPR. By changing the drift setup, we obtain two groups of cases : one with drifts and another without drifts. Other settings remain unchanged, and the $n_{e,sep}$ scan is then performed. The evolution of $T_{e,X}$ as a function of X_A is shown in Figure 31. It can be observed that the case with drifts exhibits a smooth transition, whereas the case without drifts shows a gap between (c) and (d). However, the decrease in $T_{e,X}$ is not evident in all WEST cases, which differs from Figure 30. We can further analyze the evolution of XPR in a more directly way through 2D radiation maps in Figure 32. It can be observed that the radiation in the X-point region is not significant when the plasma first detaches (Figure 32a). As X_A increases, the radiation in the X-point region starts to increase (Figure 32b). When the X_A value approaches a certain threshold, the radiation center moves into the X-point region, but radiation is still noticeable in the SOL inner and outer legs (Figure 32c). After X_A suddenly exceeds the threshold, the radiation primarily occurs in the X-point region, with approximately no radiation outside the separatrix (Figure

32d).

It has also been observed that the divertor state can change quickly near the X_A gap. A slight change of $n_{e,sep}$ as $\Delta n_{e,sep} = 0.05 \times 10^{19}$ m^{-3} can trigger the sudden appearance of XPR as shown in Figure 32 (c) → (d). In the case with drifts, the plasma appears to be relatively stable even with extremely high $n_{e,sep}$. The radiation saturates close to the X-point position, as shown in Figure 33. Combining this analysis with the discussion in Section E.2.3, we understand that drifts in the simulation can somehow prevent the formation of XPR, regardless of the forward or reversed $\mathbf{B}_\phi$, due to the increased cross-field flow speed within the separatrix. However, experimental results show a tendency closer to the case without drifts in terms of XPR, which will be further discussed in Section 3.2.1.5.

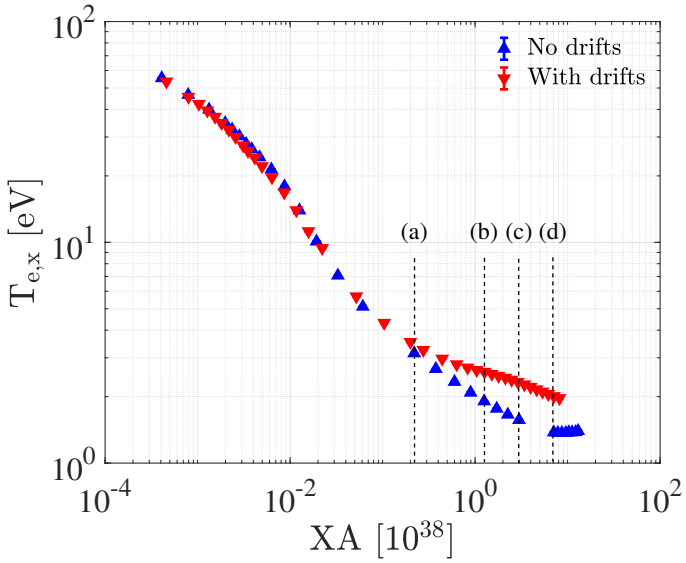

FIGURE 31. : Evolution of the electron temperature near the X-point with the X_A parameter in the outermost layer inside separatrix from WEST simulation.

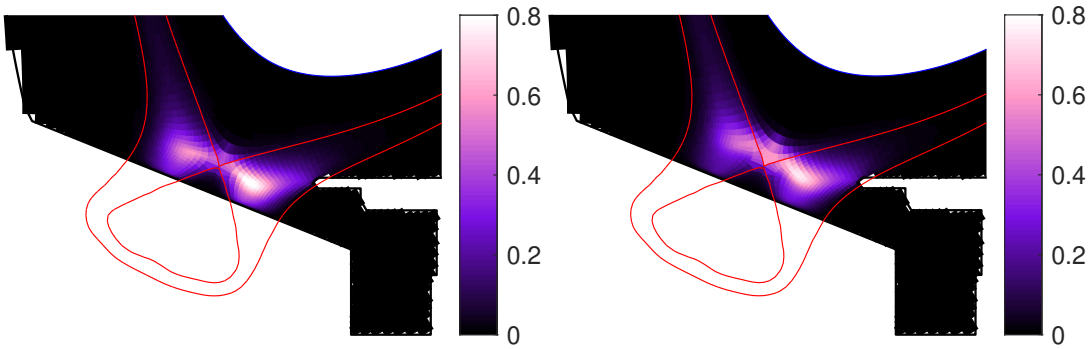

(a) $n_{e,sep} = 2.40 \times 10^{19}\,m^{-3}$ (b) $n_{e,sep} = 2.60 \times 10^{19}\,m^{-3}$

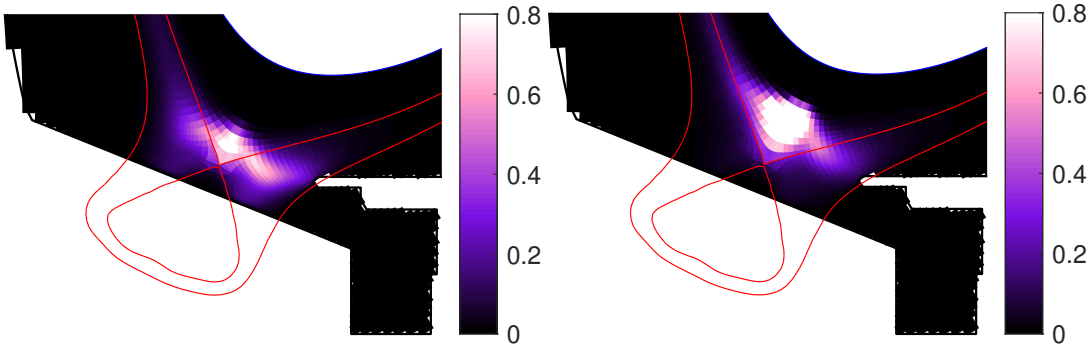

(c) $n_{e,sep} = 2.75 \times 10^{19}\,m^{-3}$ (d) $n_{e,sep} = 2.80 \times 10^{19}\,m^{-3}$

FIGURE 32. : 2D maps of radiation [MW/m^3] in the WEST simulations without drifts, (a)–(d) corresponds to the blue points marked in Figure 31.

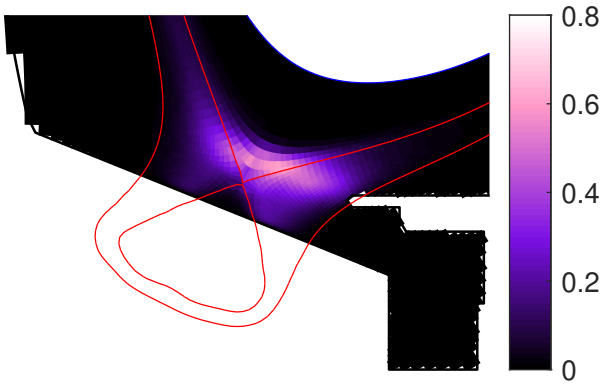

FIGURE 33. : 2D maps of radiation [MW/m^3] in the WEST simulations with drifts, $n_{e,sep} = 4.30 \times 10^{19}\,m^{-3}$.